Motions of Galaxies in the Nearby Universe with 2MASS

by

Aidan Christopher Crook

M.Phys., University of Oxford (2004)

Submitted to the Department of Physics
in partial fulfillment of the requirements for the degree of

Doctor of Philosophy

at the

MASSACHUSETTS INSTITUTE OF TECHNOLOGY

September 2009

ARCHIVES
MASSACHUSETTS INSTITUTE OF TECHNOLOGY
NOV 18 2010
LIBRARIES

© Aidan Christopher Crook, MMIX. All rights reserved.

The author hereby grants to MIT permission to reproduce and distribute publicly paper and electronic copies of this thesis document in whole or in part.

Author ....
Department of Physics
August 7, 2009

Certified by ....
John P. Huchra
Robert O. & Holly Thomis Doyle Professor of Cosmology
Harvard-Smithsonian Center for Astrophysics
Thesis Supervisor

Certified by ....
Paul L. Schechter
William A. M. Burden Professor of Astrophysics
Thesis Co-Supervisor

Accepted by ....
Thomas J. Greytak
Lester Wolfe Professor of Physics
Associate Department Head for Education

Motions of Galaxies in the Nearby Universe with 2MASS

by

Aidan Christopher Crook

Submitted to the Department of Physics
on August 7, 2009, in partial fulfillment of the
requirements for the degree of
Doctor of Philosophy

Abstract

I present the first model of a flow-field in the nearby Universe ($cz < 12,000$ km s^{-1}) constructed from groups of galaxies identified in an all-sky flux-limited survey. The Two Micron All-Sky Redshift Survey (2MRS), upon which the model is based, represents the most complete survey of its class and, with near-IR fluxes, provides the optimal method for tracing baryonic matter in the nearby Universe. Peculiar velocities are reconstructed self-consistently with a density-field based upon groups identified in the 2MRS $K_s < 11.75$ catalog. The model predicts infall toward Virgo, Perseus-Pisces, Hydra-Centaurus, Norma, Coma, Shapley and Hercules, and most notably predicts backside-infall into the Norma Cluster. I discuss the application of the model as a predictor of galaxy distances using only angular position and redshift measurements. By calibrating the model using measured distances to galaxies inside 3000 km s^{-1}, I show that, for a randomly-sampled 2MRS galaxy, improvement in the estimated distance over the application of Hubble's law is expected to be $\sim 30\%$, and considerably better in the proximity of clusters. I test the model using distance estimates from the *SFI++* sample, and find evidence for improvement over the application of Hubble's law to galaxies inside 4000 km s^{-1}, although the performance varies depending on the location of the target. I compute the peculiar velocity of the Local Group, predicted from the density-field, and find that less than 70% of the expected magnitude can be accounted for; the discrepancy between the predicted direction and the dipole in the Cosmic Microwave Background is significant at the 90%-confidence level. I demonstrate that a bulk flow of over 300 km s^{-1} in a direction close to the galactic plane is necessary to account for the remaining motion. The results suggest that one or more massive structures beyond $120/h$ Mpc are likely to be key contributors to the local dynamics. Although, with the direction of the bulk flow coincident with the Zone of Avoidance, incomplete sampling behind the galactic plane may be a factor in the discrepancy.

Thesis Supervisor: John P. Huchra
Title: Robert O. & Holly Thomis Doyle Professor of Cosmology
Harvard-Smithsonian Center for Astrophysics

Thesis Co-Supervisor: Paul L. Schechter
Title: William A. M. Burden Professor of Astrophysics

Acknowledgments

First and foremost I thank my wife, Genevieve, for her support over the past five years. The completion of this thesis marks the end of a chapter of our lives that began with our arrival into Boston with nothing more than what we could carry onto an airplane, but ends with more dreams fulfilled than I could have imagined possible.

Secondly, I want to thank my advisor, John Huchra. John's enthusiasm, guidance and encouragement has shaped the way I now look at the Universe. The opportunity to work with such an inspiring astronomer was second to none, and I thank John for giving me the chance to work on such a fascinating project.

A special thanks goes to Lucas Macri and Karen Masters, both for being great observing partners on multiple trips to the Parkes and Green Bank observatories, as well as for all the useful discussions and feedback on my work.

I want to thank Alessandra Silvestri and Phillip Zukin, with whom I worked closely to probe deeper into the mysteries unraveled in this thesis. I would also like to thank Paul Schechter, Rob Simcoe and Alan Guth for their expert advice throughout my time at MIT.

A wide-field thank-you to the members of the 2MASS and 2MRS teams, without whom this project would not have been possible, especially Tom Jarret, Nathalie Martimbeau, Perry Berlind, Mike Calkins and Susan Tokarz.

I thank my family for their encouragement, and for believing in me throughout. And finally, I want to thank my fellow degree candidates at MIT, both past and present, for making MIT much more than just an academic institution.

This work makes use of data products from the Two Micron All Sky Survey, which is a joint project of the University of Massachusetts and the Infrared Processing and Analysis Center/California Institute of Technology, funded by the National Aeronautics and Space Administration and the National Science Foundation. This work also makes use of data products from the 6dF Survey of the AATO. This research has made use of source code available at http://www.dfanning.com/. The work has been supported by NSF grant AST 0406906 and the Massachusetts Institute of Technology Bruno Rossi and Whiteman Fellowships.

Contents

List of Figures

List of Tables

Chapter 1

Introduction

Understanding the dynamics of galaxies in the nearby Universe has been a problem for the better part of a century. While the theoretical frameworks and experimental tools have advanced rapidly since Vesto Slipher first detected a galaxy rotation curve, the puzzle still contains many unsolved pieces.

1.1 Motivation

In the 1950s, Rubin (1951) first suggested the possibility that the Local Group (LG) of galaxies had a peculiar motion in a paper describing the "differential rotation of the inner metagalaxy". De Vaucouleurs (1953) proposed that its motion was influenced by the "Local Supergalaxy", or Local Supercluster (De Vaucouleurs, 1958) as it is known today, and measurements by Rubin et al. (1976) implied that the Local Group (LG) of galaxies had a velocity that deviated from the Hubble flow by more than 400 km s^{-1}.

In 1965, Penzias & Wilson (1965) reported the discovery of radiation from the Cosmic Microwave Background (CMB), and in the 70s efforts were underway to measure the anisotropy in its spatial temperature distribution. In 1976, Corey & Wilkinson (1976) reported a dipole anisotropy in the CMB, which was corroborated by Fabbri et al. (1980). The dipole represents a direct measure of the peculiar velocity of the Sun with respect to the rest frame of the CMB (Peebles & Wilkinson, 1968; Conklin, 1969; Henry, 1971) , and was later measured to exquisite accuracy by the COsmic Background Explorer (COBE) (Smoot et al., 1992; Bennett et al., 1993; Lineweaver et al., 1996). Combined with the more recent measurements from the Wilkinson Microwave Anistropy Probe (WMAP), the implication is a heliocentric velocity with respect to the CMB of 369.0 ± 0.9 km s^{-1} (Hinshaw et al., 2009). When combining the motion of the Sun around the Milky Way with the motion of our galaxy with respect to the centroid of the LG (e.g., Yahil et al., 1977; Courteau & van den Bergh, 1999; Karachentsev et al., 2009) , the LG is found to have a motion in excess of 600 km s^{-1} with respect to the rest frame of the CMB.

In the late 1960s, the idea that galaxies and clusters of galaxies develop from the small density perturbations in the early Universe was formulated by a number of authors (e.g., Peebles, 1967; Silk, 1968; Peebles & Yu, 1970; Gunn & Gott, 1972). Inhomogeneities in the gravitational potential cause mass to flow away from underdense regions and toward overdense regions. Peebles (1976b) first presented a framework (known as *gravitational instability theory*) relating the underlying mass distribution to the expected motions of galaxies. Large-scale flows were first convincingly detected in the early 1980s (e.g., Schechter, 1980; Yahil et al., 1980; Aaronson et al., 1980; Tonry & Davis, 1981; Aaronson et al., 1982) where measurements of peculiar velocities were used to model the velocity-field in the Local Supercluster. The results indicated that the LG was flowing toward the Virgo cluster, although estimates of its velocity varied from 125–480 km s^{-1}. It was clear, however, that the LG infall toward Virgo could not account for the motion with respect to the CMB, which lies more than 40° from the direction of Virgo on the sky; the necessity for additional infall toward the Hydra-Centaurus supercluster was suggested by Shaya (1984), Tammann & Sandage (1985), and Aaronson et al. (1986), but the lack of redshift-independent distance estimates initially made it difficult to map this region.

The field grew rapidly following the realization that a spiral galaxy's rotation velocity could be related to its luminosity (the Tully-Fisher relation, Tully & Fisher, 1977); a similar relation was observed for elliptical galaxies (the Faber-Jackson law Faber & Jackson, 1976). In the late 80s, the D_n-σ relation (Dressler et al., 1987; Djorgovski & Davis, 1987) for ellipticals further reduced uncertainties in distance estimates. Burstein et al. (1986) presented evidence suggesting a bulk motion toward a region known commonly as the "Great Attractor" (GA). Lynden-Bell et al. (1988) used a sample of distance estimates to over 400 elliptical galaxies to fit a model of the largest structures (Virgo, Perseus-Pisces, and the GA) and showed that the best fit required an attractor close to the galactic plane at a distance of $\sim$ 4300 km s^{-1} with a mass 50 times larger than Virgo; a similar model was constructed by Han & Mould (1990). Measurements by Dressler & Faber (1990) showed a distinctive infall pattern to a region coincident with the GA, however the contradictory results of Mathewson et al. (1992) showed no evidence for backside-infall. In fact, they provided further weight to the suggestion of Scaramella et al. (1989) that the attractor at the supposed GA location was not sufficiently massive to account for the LG velocity, necessitating a second attractor as far as $200/h$ Mpc from us. Willick (1990) showed that the entire Perseus-Pisces region was also moving in a similar direction to the GA, with a velocity similar to that expected of the LG, suggesting that an attractor at $\sim 50/h$ Mpc could not explain this bulk motion. A moment of enlightenment struck the astronomy community when Kraan-Korteweg et al. (1996) showed that the Norma Cluster (Abell 3627) was much more massive than previously anticipated — close to the galactic plane and at a redshift of $\sim$ 4700 km s^{-1}, it is now believed to be the GA originally modeled by Lynden-Bell et al. (1988). The mass, however, was estimated to be $\sim 5 \times 10^{15} M_{\odot}$, an order of magnitude less than required to explain the motion of the LG.

The field was revolutionized following the completion of the first flux-limited redshift surveys that covered almost the entire sky. The Optical Redshift Survey (ORS, Santiago et al., 1995) was a redshift survey of optically-selected targets from the Uppsala Galaxy Catalogue (UGC), the European Southern Observatory Galaxy Catalog

(ESO), and the Extension to the Southern Galaxy Catalog (ESGC). It contains two subcatalogs: one flux-limited to $B < 14.5$, the other complete to a B-band major-axis diameter of $1.9'$. The sample consists of 8457 objects, with redshifts available for 8286, and is 98% complete above $|b| > 20°$.

The Infrared Astronomical Satellite (*IRAS*) was launched in January of 1983 and ceased operations in November the same year after having surveyed more than 96% of the sky in four wavebands centered at 12, 25, 60, and 100 μm (Beichman et al., 1988). Approximately 250,000 points sources and 20,000 small extended sources down to a limiting flux density of 0.5 Jy (at 12, 25, 60 μm) and 1.5 Jy at 100μm were identified. With a resolution of $\sim 2'$, galaxies generally appeared in the catalog of point sources (PSC). Redshift surveys based on the *IRAS* PSC (Strauss et al., 1990; Fisher et al., 1995) formed the basis for much of the subsequent analysis, although other catalogs containing optically-selected galaxies were also used (e.g., Shaya et al., 1992; Hudson, 1993; Baker et al., 1998). With the inclusion of redshift measurements, the construction of a three-dimensional density-field became possible (e.g., Strauss et al., 1992; Branchini et al., 1999), however there remained significant discrepancies with the density-field reconstructed from peculiar velocity measurements (e.g., see Dressler, 1991), which can only be removed by smoothing the reconstructed field over large scales such that only the largest density peaks remain (e.g., Dekel et al., 1993). Dressler (1991) suggested that galaxies may trace the mass poorly and in a way that might not be easily predictable.

Clinging to the assumption that galaxies do in fact trace the mass, efforts to reconstruct the peculiar velocity of the LG became more complex than a model containing two or three attractors. Earlier efforts had used the angular positions of galaxies to estimate the LG peculiar velocity from *IRAS* surveys (Yahil et al., 1986; Meiksin & Davis, 1986; Harmon et al., 1987; Villumsen & Strauss, 1987; Lahav et al., 1988). Including redshift measurements and weighting galaxies according to the selection function instead of their flux, reconstructions of the LG peculiar velocity were performed by Strauss et al. (1992) and Webster et al. (1997) using *IRAS*-selected samples, Lynden-Bell et al. (1989) using an optically-selected sample, and da Costa et al. (2000) using a sample of early-type galaxies. All found that the dipole appeared to converge once sources inside $\sim 50/h$ Mpc had been included, although the direction was still offset from dipole in the CMB. Scaramella et al. (1991) and Branchini & Plionis (1996) performed similar analyses using Abell/ACO cluster samples (Abell, 1958; Abell et al., 1989), claiming significant contribution to the LG peculiar velocity from depths out to $\sim 200/h$ Mpc. These findings were more recently corroborated by Kocevski et al. (2004) and Kocevski & Ebeling (2006) using analyses of X-ray clusters, suggesting the Shapley concentration at $\sim 140/h$ Mpc may be responsible for a significant contribution to the flow.

More recently, the Extended Source Catalog from the Two Micron All-Sky Survey (2MASS, Skrutskie et al., 2006) has been used to reconstruct the LG peculiar velocity. (Maller et al., 2003) applied a flux-weighted method to the sample, and Erdoğdu et al. (2006b) and Lavaux et al. (2008) performed reconstructions that include galaxy redshifts identified in the 2MASS Redshift Survey (Huchra et al., 2009). The efforts of Maller et al. (2003) and Erdoğdu et al. (2006b) find the LG peculiar velocity lies

10–20° from the CMB direction, depending on the assumptions of the reconstruction. Erdoğdu et al. (2006b) find that the dipole appears to have converged by $\sim 60/h$ Mpc, but subsequently diverges from the CMB direction as galaxies inside shells of increasing distance are sampled, which the authors argue is likely due to increased shot noise. Lavaux et al. (2008), however, who use a method that extends into the non-linear regime, find the reconstructed dipole lies $\sim 50°$ from the CMB, and do not find evidence for convergence near $\sim 60/h$ Mpc, suggesting the dipole does in fact *not* converge inside $120/h$ Mpc. While studies of peculiar velocities in the *SFI++* sample (Springob et al., 2007) have shown that a multi-attractor model constructed inside the survey volume is consistent with the data (Masters, 2005), the recent work of Watkins et al. (2009), combining data from multiple peculiar velocity surveys, find evidence for bulk flows on $100/h$ Mpc scales. It is clear that the puzzle is far from solved, and further analysis is essential to improve our understanding of the dynamics of galaxies in the nearby Universe.

In the 1930s Zwicky (1937) noticed that the dynamical mass of the Coma Cluster was inconsistent with the mass associated with stars. Later studies of galactic rotation curves demonstrated that dark matter extended well beyond the light of galaxies (e.g., Rubin et al., 1965; Persic et al., 1996), however not in sufficient quantity to explain the "missing mass" seen on larger scales. The mass associated with stars in the Coma Cluster has found to be an order of magnitude smaller than the mass associated with hot gas, and virial analyses (Colless & Dunn, 1996) as well as X-ray data (Hughes, 1989) suggest the total mass of the cluster is almost an order of magnitude higher again (also see White et al., 1993). Gravitational lensing of background sources by galaxy clusters has provided direct evidence for dark matter in galaxy clusters (e.g., Tyson et al., 1990; Kaiser & Squires, 1993), so it seems appropriate to question the assumption that galaxies trace the underlying mass distribution accurately, either in number-density or luminosity.

In this thesis I present a new approach to the problem: instead of relying on galaxies as point tracers of the mass, I construct a model of the flow-field from galaxy groups and (where possible) their associated dynamical masses. This approach does not rely as heavily on the assumption of an intrinsic mass-to-light ratio, nor require that the number density of galaxies traces the mass density of the underlying matter distribution, but models the masses of groups and clusters according to the response of their member galaxies to the enclosed dark matter. Until now, a sufficiently complete all-sky redshift survey necessary to produce such a model has not been available, but with the recent completion of the 2MASS Redshift Survey, the construction of a group-based flow-field model is now possible.

While understanding the flows in the nearby Universe is the primary objective, by comparing the predicted peculiar velocities with observed values, it is possible to place constraints on the matter density parameter and the bias parameter for clusters. An accurate model of the velocity-field is also a powerful tool for estimating distances to astrophysical objects. Improved distance estimates will allow for a better understanding of the galaxy luminosity and mass functions (e.g., Masters et al., 2004), as well as more precise estimates of physical separations, luminosities, dynamical mass estimates, and their derived quantities.

1.2 Overview

This thesis comprises of 7 chapters. In the remainder of this chapter, I will present a brief overview of gravitational instability theory (§1.3), and introduce the Two Micron All-Sky Survey and subsequent redshift survey (§1.4).

In Chapter 2, I present a catalog of groups, constructed from 2MRS. Here, I discuss the algorithm used to identify groups (§2.1), modifications to the data set (§2.2) and present a discussion on the choice of parameters used in the group-identification algorithm (§2.3). The group catalogs and their properties are discussed in §2.4, and I summarize the implications of the catalog and discuss its potential applications in §2.5. Chapter 2 forms a portion of the article published in Crook et al. (2007, 2008).

In Chapter 3, I present a model of the flow-field, constructed from groups of galaxies in 2MRS. I begin with a discussion on the catalog of groups (§3.1); the method implemented to construct the flow-field from observational data is presented in §3.2, and the velocity-field is discussed in §3.3. I compare the flow-field with two existing models in §3.4, and summarize the main points in §3.5.

In Chapter 4, I briefly digress from the 2MRS analysis to study the $z = 0$ snapshot of the ΛCDM Hubble Volume simulation (Colberg et al., 2000; Jenkins et al., 2001) in order to assess the limitations of the suggested method for reconstructing the peculiar velocities of galaxy groups. The simulation and associated caveats are discussed in §4.1. In §4.2 I assess the limits to which gravitational instability theory can be applied in the context of the presented flow-field model, and in §4.3, I estimate the uncertainties in reconstructed peculiar velocities of galaxy groups, both in magnitude and direction. In §4.4, I discuss the effect of dynamical mass estimates and the absence of redshift-independent distance estimates on the results; the conclusions are summarized in §4.5.

In Chapter 5, I discuss the use of the flow-field model to estimate distances to galaxies from only redshift and angular position information. I begin by discussing the issue of degeneracy in the redshifts of test masses in the vicinity of galaxy clusters (§5.1). In §5.2, I present the method used to invert the flow-field into a tool that can be used to estimate distances and show the results of applying this to the flow-field model in §5.3. The method is then utilized to calibrate the model with estimated distances to nearby galaxies in §5.4, where I discuss constrains on the bias parameter. In §5.5, I apply the method of this section to obtain distance estimates to galaxies in 2MRS. I compare the predictions of the model to a sample of galaxy distance estimates in §5.6, and summarize the conclusions in §5.7.

Chapter 6 begins with a discussion of the observed dipole in the CMB (§6.1). In §6.2, I analyze the predicted contributions to the motion of the LG. In §6.3, I discuss the necessary steps to reconcile the two values, and summarize the conclusions in §6.4. A portion of the discussion in this chapter has been published in Crook et al. (2009). Finally, we summarize our conclusions in Chapter 7.

Portions of the work presented in this thesis have been published in Crook et al. (2007, 2008), and Crook et al. (2009). All the analyses and discussions presented here have been performed/written by myself, although the analysis makes use of proprietary data which was obtained and reduced through a collaborative effort involving members of the 2MASS Redshift Survey team.

1.3 Gravitational Instability Theory

If one assumes that the mechanism for formation of large-scale structure and peculiar motions in the Universe is the growth of primordial density perturbations (e.g., Peebles, 1980), then one can relate the peculiar velocities observed today to the underlying distribution of mass.

The derivation below is presented by Strauss & Willick (1995). First, we write the first-order equations of mass continuity, force, and Poisson's equation in an expanding Universe, neglecting terms associated with pressure and ignoring relativistic effects:

$$\frac{\partial \delta(\mathbf{x},t)}{\partial t} + \frac{1}{a(t)}\nabla.\mathbf{v} = 0 \tag{1.1a}$$

$$\frac{\partial \mathbf{v}(\mathbf{x},t)}{\partial t} + \frac{\dot{a}(t)}{a(t)}\mathbf{v}(\mathbf{x},t) + \frac{1}{a(t)}\nabla\phi = 0 \tag{1.1b}$$

$$\nabla^2\phi = 4\pi G a^2(t)\rho(\mathbf{x},t) \tag{1.1c}$$

where $\delta(\mathbf{x},t) \equiv [\rho(\mathbf{x},t) - \bar{\rho}(t)]/\bar{\rho}(t)$ is the relative deviation from the background density, $\mathbf{v}(\mathbf{x},t)$ is the velocity relative to the comoving frame, $a(t)$ is the scale factor, t is the cosmic time, ϕ is the gravitational potential, and the spatial derivatives are taken with respect to comoving coordinates, $\mathbf{x}$.

Substituting Eq. (1.1c) and the divergence of Eq. (1.1b) into the time derivative of Eq. (1.1a) yields:

$$\frac{\partial^2\delta}{\partial t^2} + \frac{2\dot{a}}{a}\frac{\partial\delta}{\partial t} = 4\pi G\bar{\rho}\delta \tag{1.2}$$

The solution is separable, and can be written in terms of growing and decaying modes:

$$\delta(\mathbf{x},t) = A(\mathbf{x},t)D_+(t) + B(\mathbf{x},t)D_-(t) \tag{1.3}$$

If we assume the decaying mode can be neglected at late times, then Eq. (1.1a) can be re-written as

$$\nabla.\mathbf{v} = -a\delta\frac{\dot{D}_+}{D_+} = -aH_0 f\delta \tag{1.4}$$

where

$$f \equiv \frac{1}{H_0 D}\frac{\mathrm{d}D_+}{\mathrm{d}t} = \frac{1}{H_0 D}\frac{\mathrm{d}D_+}{\mathrm{d}a}\frac{\mathrm{d}a}{\mathrm{d}t} = \frac{\mathrm{d}\ln D_+}{\mathrm{d}\ln a} \tag{1.5}$$

is the growth factor which depends on the cosmology. It is approximately given by $f(\Omega_m) \approx \Omega_m^{6/11}$ in a ΛCDM Universe (Wang & Steinhardt, 1998). Inverting Eq. (1.4) and evaluating today ($a(t_0) = 1$), we find

$$\mathbf{v}(\mathbf{r}) = \frac{H_0 f(\Omega_m)}{4\pi}\int \mathrm{d}^3\mathbf{r}'\frac{\mathbf{r}' - \mathbf{r}}{|\mathbf{r}' - \mathbf{r}|^3}\delta(\mathbf{r}') \tag{1.6}$$

In the most commonly used model of linear bias, the relative amplitude of the deviations from a uniform background density ($\bar{\rho}_e$) of the estimators of density (e.g., galaxies, galaxy clusters, galaxy luminosities) are assumed to be proportional to the relative density fluctuations of the gravitating mass, such that $\delta\rho_e/\bar{\rho}_e = b\delta\rho/\bar{\rho}$. Defining

$$\beta \equiv f(\Omega_m)/b \tag{1.7}$$

we can write

$$\mathbf{v}(\mathbf{r}) = \frac{H_0\beta}{4\pi\bar{\rho}_e}\int \mathrm{d}^3\mathbf{r}' \frac{\mathbf{r}'-\mathbf{r}}{|\mathbf{r}'-\mathbf{r}|^3}\rho_e(\mathbf{r}') \tag{1.8}$$

where we make appropriate choices of β (often referred to as the *redshift distortion parameter*) and $\bar{\rho}_e$ upon application of this framework.

1.4 The Data

The Two Micron All-Sky Survey (2MASS, Skrutskie et al., 2006) began in the early 90s with the purpose of mapping the Milky Way and nearby Universe. Previous all-sky surveys suffered from a variety of selection effects. Observations at optical wavelengths suffer from severe extinction at low galactic latitudes, e.g., the Optical Redshift Survey (ORS Santiago et al., 1995) which only sampled down to $|b| = 20°$, and the B–band fluxes are biased toward the detection of star-forming galaxies (e.g., Kennicutt et al., 1994). The large zone of avoidance spanning the galactic plane in optical bands motivated surveys conducted in the infrared. Many *IRAS*-selected galaxy samples have been investigated as tracers of the density field, e.g.,Strauss et al. (1992); Fisher et al. (1995), based on the 1.9 Jy and 1.2 Jy samples, respectively, and Branchini et al. (1999) based on the PSC*z* catalog (Saunders et al., 2000). However, these samples are based on fluxes in the far-infrared and miss many early-type galaxies, thus underestimate the total galaxy number density and are expected to underestimate the masses of rich clusters (e.g Branchini et al., 1999; Bell & de Jong, 2001). Even though the *IRAS*-selected samples are not biased by extinction, they still suffer from confusion in high-density regions. Furthermore, the sampling is not consistent above and below the galactic plane due to hysteresis in the detectors (see Strauss et al., 1990).

2MASS uniformly mapped the entire sky in the J (1.25 μm), H (1.65 μm), and K_s (2.16 μm) bands. By observing in the near-infrared, 2MASS is less susceptible to the severe extinction at low galactic latitudes from which observations at optical wavelengths suffer. Since galaxy spectra peak at $\sim$ 1.6μm, 2MASS maximizes the number of galaxies detected at a specified flux limit, resulting in the most complete all-sky survey performed to date.

Two catalogs, complete to $K_s \sim 13.5$ mag, were released in early 2003 (see the 2MASS explanatory supplement Cutri et al. 2003, and Jarrett et al. 2000): a point-source catalog with 470,992,970 entries and an extended source catalog (XSC) with 1,647,559 extended sources, most of which are galaxies. Although designed for completeness down to low galactic latitudes, the 2MASS XSC still suffers from confusion near the galactic plane. The 2MASS Redshift Survey (2MRS, Huchra et al., 2009) uses the XSC as its input master list and aims to produce an all-sky, (extinction-corrected) flux-limited redshift catalog that will eventually be complete to $K_s < 12.5$ mag above $|b| = 5°$. Above galactic latitudes of 10°, 2MRS is currently 99.9% complete to $K_s < 11.25$, and 94% complete to $K_s < 11.75$. 2MASS contains a high proportion of early-type galaxies, which are most commonly found in high-density regions (e.g., Bell & de Jong, 2001; Norberg et al., 2001; Zehavi et al., 2002), and therefore we expect a density-field derived from 2MASS to trace the mass more accurately than a model constructed from *IRAS*-selected samples.

The first available sample of the 2MRS galaxy catalog contains positions, redshifts and magnitudes for 23090 galaxies selected from the XSC. The targets were by selected by introducing a cut on the corrected magnitudes of objects in the XSC of $K_s < 11.25$ (the apparent magnitudes had previously been corrected for extinction using the dust maps of Schlegel et al. 1998). This catalog is complete, bar 40 galaxies, for galactic latitudes $|b| > 10°$ between galactic longitudes 330° and 30°, and $|b| > 5°$ for other longitudes. This sample is utilized in the analysis of Chapter 2 due to the fact that it was the deepest complete sample available at the time of the publication of the contents of the chapter.

For the construction of the flow-field model and subsequent analysis (Chapters 3, 5 and 6), it is desirable to use the deepest available magnitude-limited sample, thus the $K_s < 11.75$ sample is considered in these analyses. This sample is 94% complete above $|b| > 10°$, and contains 41,122 redshifts.

Chapter 2

Groups of Galaxies

In this chapter, we create a redshift-limited catalog of groups, uniformly sampled from the entire sky. By assuming the identified groups are virialized systems, we are able to provide estimates of the group masses, avoiding the necessity to assume an intrinsic mass-to-light ratio. The local Universe is sufficiently inhomogeneous at the scales in question that the dynamics due to our interactions with nearby groups are non-negligible. Due to the nature of the all-sky group catalog presented here, we will now be able to estimate the local density field due to baryonic matter in the local Universe. A flow-field model produced from this catalog can be used in conjunction with observations in order to answer the question of whether baryonic matter is a genuine tracer of dark matter.

The creation of group catalogs is not a new concept, however the methods employed in developing these catalogs have evolved with the enhancements in instrumentation. Early group catalogs were based on limited or subjective data (e.g De Vaucouleurs, 1975), associating members based on similarity in apparent magnitude, positional coincidence and (if available) redshift. Turner & Gott (1976) proposed a method that identifies regions in which the surface number density on the sky is enhanced, creating group catalogs from two-dimensional data. This technique suffers because the typical angular separation of galaxies in a group will vary with distance, thus nearby groups with large angular radii will not be identified. Furthermore, when applied to flux-limited surveys, this method will identify different groups for different limiting fluxes.

More recently, the use of objective algorithms to identify groups based on both their position on the sky and in redshift space has become widely accepted (e.g., Huchra & Geller, 1982; Geller & Huchra, 1983; Ramella et al., 1997; Diaferio et al., 1999; Giuricin et al., 2000; Ramella et al., 2002), using methods designed to find the same groups regardless of the limiting magnitude of the sample. The applicability of a particular group-finding algorithm depends on the properties of the sample in question. For example, Marinoni et al. (2002) show that the Voronoi-Delaunay method successfully reproduces the distribution of groups in velocity dispersion in a mock sample based on the Deep Extragalactic Evolutionary Probe (DEEP2) Redshift Survey (Davis et al., 2003); this method is adapted by Gerke et al. (2005) for application to the DEEP2 sample. The SDSS team developed an algorithm (C4, Miller et al.,

2005) that searches for groups in three space-dimensions as well as four photometric colors. Kochanek et al. (2003) used a matched filter algorithm to study clusters in 2MRS at the 89% completeness level. Yang et al. (2005) have developed a halo-based group-finder and successfully applied it to the 2dFGRS sample (Merchán & Zandivarez, 2002; Eke et al., 2004). The same technique has been applied to the SDSS by Weinmann et al. (2006).

In this chapter, we apply a variable linking-length percolation (also commonly referred to as a *friends-of-friends*) algorithm (Huchra & Geller, 1982, hereafter HG82) to determine the groups present in 2MRS. The velocity dispersion within the groups will allow estimates of the virial masses of the groups, thus providing a method to trace the density field associated with luminous matter in the local Universe.

We begin with an outline of the group-identification algorithm in §2.1 below. We discuss the modifications made to the data sample prior to the application of the algorithm in §2.2. §2.3 presents a discussion on the choice of parameters used in the group-identification algorithm. The group catalogs and their properties are discussed in §2.4, and we summarize our conclusions and discuss the potential applications of the catalogs in §2.5.

2.1 Group-identification Algorithm

We use the algorithm described in HG82 to identify groups of galaxies in the $K < 11.25$ mag version of the 2MRS catalog. The procedure is outlined briefly below.

We compare each galaxy in the catalog with its neighboring galaxies; for each pair of galaxies a linking length $D_L(V_{\mathrm{avg}})$ is computed that depends on the average redshift of the galaxies, V_{avg}. Given two galaxies with an angular separation, θ, we ask whether their projected separation, $D_{12} = \sin(\theta/2)V_{\mathrm{avg}}/H_0$, is less than $D_L(V_{\mathrm{avg}})$. If this is true, and the difference in redshift, $V_{12} = |V_1 - V_2|$, is less than some linking velocity, V_L, then we identify both galaxies with the same group. D_L is defined through equation (2.1) below.

$$D_L = D_0 \left[\frac{\int_{-\infty}^{M_{12}(V_{\mathrm{avg}})} \Phi(M) \mathrm{d}M}{\int_{-\infty}^{M_{\mathrm{lim}}} \Phi(M) \mathrm{d}M} \right]^{-1/3} \tag{2.1}$$

where

$$M_{12}(V_{\mathrm{avg}}) = m_{\mathrm{lim}} - 25 - 5\log(V_{\mathrm{avg}}/H_0)$$

Here, $\Phi(M)$ represents the differential galaxy luminosity function for the sample and D_0 the projected separation (in Mpc) at some chosen fiducial redshift V_F. $M_{\mathrm{lim}} = M_{12}(V_F)$ is a constant for a given V_F, and m_{lim} is the apparent-magnitude limit of the sample.

This scaling of the linking length compensates for the bias that would otherwise be introduced due to the variation in sampling of the luminosity function with redshift. There is much debate on how and whether or not to scale V_L (e.g., HG82, Nolthenius & White, 1987; Frederic, 1995b,a). If one assumes uniform density, simple scaling arguments show that the velocity is simply proportional to the radius, suggesting that V_L should be scaled in the same manner as D_L. Such a scaling would include unwanted interlopers at large values of V_L and thus introduce an unwanted correlation between velocity dispersion and redshift. The density profiles of galaxy clusters, however, are usually better described by the isothermal-sphere approximation; in this case the velocity dispersion is independent of the size of the cluster. It follows therefore that by setting V_L to a reasonable fixed value, we will minimize the number of interlopers, but not bias the algorithm against finding distant groups. Hereafter we set

$$V_L = V_0 \tag{2.2}$$

The choice of D_0 determines the minimum density contrast of identified groups, which can be estimated using equation (2.3) below (HG82).

$$\frac{\delta\rho}{\rho} = \frac{3}{4\pi D_0^3}\left[\int_{-\infty}^{M_{\rm lim}} \Phi(M)\mathrm{d}M\right]^{-1} - 1 \tag{2.3}$$

2.2 Sample

For the purposes of this study, we utilize the $K_s < 11.25$ 2MRS galaxy sample as a source catalog (see §1.4) from which to identify groups of galaxies. Before proceeding, however, we explain the modifications that we apply to this data set. We discuss a simple flow-field model applied to provide improved estimates of the distances to the galaxies (see §2.2.1). In §2.2.2 we discuss the method used to populate the galactic plane with random galaxies to prevent any artefacts arising from the significantly reduced observed number density of galaxies behind the plane. We briefly discuss the assumed form of the luminosity function of the sample in §2.2.3 and, in §2.2.4, consider the completeness of the sample in redshift-space.

2.2.1 Distance Estimates

Locally redshifts do not provide a reliable indication of distance because of distortions to the local velocity field due to infall onto concentrations of mass. Although the clustering algorithm is independent of the observer's frame of reference, it is essential to have reasonable estimates of the distances to the galaxies in order to compute the linking parameters, D_{12} and D_L, as well to accurately estimate the luminosities of the galaxies.

We apply the basic flow-field model described in Mould et al. (2000) to account for the local distortions to the velocity field. This prescription first corrects the reference frame to the LG frame (Yahil, Tammann, & Sandage 1977, corroborated by the more recent work of Courteau & van den Bergh 1999), then adjusts the redshift-inferred distances of galaxies near Virgo, Shapley and the GA region as follows: All galaxies within 12° of the center of Virgo with heliocentric redshifts less than 2500 km s^{-1} are placed at the redshift of Virgo (plus a random velocity, drawn from a gaussian distribution with a standard deviation of 20 km s^{-1}, to avoid artefacts in the group properties occurring from galaxies with identical redshifts). All galaxies within 10° and 2000 km s^{-1} of the GA are placed at the redshift of the GA (plus scatter) and all galaxies within 12° and 3000 km s^{-1} of Shapley are placed at the redshift of Shapley (plus scatter). The corrected velocities are then used in place of the heliocentric velocities when computing distances only. To infer the distances we assume Hubble's law is valid to the completeness limit of the 2MRS catalog,[1] using a Hubble constant $H_0 = 100h$ km s^{-1}Mpc^{-1}, where we assume $h = 0.73$ when a specific value is required. This value is chosen based on the three-year WMAP results (Spergel et al., 2007), $h = 0.73 \pm 0.03$. In the very local universe (i.e. where corrected distances are less than $3h^{-1}$ Mpc) we give galaxies an indicative distance of $3h^{-1}$ Mpc. The velocities used in computation of V_{12}, etc. are the heliocentric velocities reported in the 2MRS catalog.

2.2.2 Filling in the Galactic Plane

The 2MRS catalog is currently incomplete near the galactic plane ($|b| < 10°$ between galactic longitudes 330° and 30°, and $|b| < 5°$ for other longitudes). With a significantly reduced number density of galaxies observed behind the galactic plane, a structure that spans the plane will not be identified by the clustering algorithm. Similarly, structures that are visible in part above or below the plane may not be identified as groups, and, even if they are, a bias will be introduced in the number density of groups with centers just above or below the plane. Any flow-field model derived from such a group catalog will suffer from these biasing effects; we therefore attempt to minimize these effects by randomly populating the sample to enhance the galaxy number density behind the galactic plane to reflect that observed above and below it.

We follow a method similar to that of Yahil et al. (1991); this method produces similar results to the more involved Wiener reconstruction [2] discussed in Lahav et al. (1994). We first divide the catalog into bins spanning 10° in galactic longitude and $10h^{-1}$ Mpc in distance. For galactic longitudes ranging from 330° to 30° (masking the bulge) we now consider bins further bound by the lines $|b| = 10°$. Sampling from the adjacent bins ($10° < |b| < 20°$), we populate the bulge with N galaxies drawn at random from the galaxies in adjacent bins; these galaxies are placed at random latitudes and a normal scatter of 20 km s^{-1} is introduced in the velocity to prevent artefacts in the group properties arising due to galaxies at identical redshifts. N is calculated by drawing a random normal deviate from a distribution with a mean equal to the number of galaxies in the two adjacent bins (above and below the plane), then subtracting the number of galaxies already present within the bin. For other galactic longitudes, the latitudes $5° < |b| < 15°$ are used to populate the bins with $|b| < 5°$.[3] The catalog, before and after population of the galactic plane, is shown in Figure 2.1.

---

[1] At the limiting redshifts of the galaxies analyzed, the difference between distances computed using a ΛCDM cosmology and simply assuming Hubble's law is less than 5%.

[2] See Erdoğdu et al. (2006a) for discussions on the Wiener reconstruction of the 2MRS sample.

[3] In this case, we set the mean of the normal distribution from which N is drawn to half the number of galaxies in the adjacent bins.

The population of the plane generated an additional 2076 galaxies.

2.2.3 Luminosity Function

The K-band luminosity function utilized in algorithm is parameterized in terms of a function of the form Schechter (1976),

$$\begin{aligned}\Phi(M) = \quad & 0.4 \ln(10) \Phi^{\star} 10^{0.4(\alpha+1)(M^{\star}-M)} \\ & \times \exp\left[-10^{0.4(M^{\star}-M)}\right]\end{aligned}$$

We use the values reported in Huchra et al. (2005),

$$\begin{aligned}\alpha &= -1.02 \\ M^{\star} &= -24.2 \\ \Phi^{\star} &= 1.08 \times 10^{-2}\, h^{3}\ \mathrm{Mpc}^{-3}\end{aligned} \tag{2.4}$$

which have been computed using the galaxies in the 2MRS catalog with galactic latitudes, $|b| > 10^{\circ}$.

2.2.4 Completeness in Redshift-space

Due to the nature of flux limited surveys, the number density of galaxies observed at sufficiently high redshifts will tend toward zero. At these highest redshifts, the linking lengths used in the algorithm become so large that the majority of identified groups will likely be spurious. For the purposes of building a flow-field model, the groups at the highest redshifts will have the smallest affect on local dynamics, thus we choose to limit the group catalog to a redshift inside which the catalog is reasonably complete. Figure 2.2 shows the cumulative number of galaxies, $N(<D)$, as a function of (estimated) distance, D. The points have been fitted with a curve of the form

$$N(<D) = N_0 \left(\frac{\beta D}{[(\beta D)^{b} + S^{b}]^{1/b}} \right)^{a} \tag{2.5}$$

where the best fit parameters are $N_0 = 2.56 \times 10^{4}$, $a = 2.10$, $S = 106$ Mpc, $\beta = 0.880$, $b = 3.94$. The derivative of equation (2.5) represents the selection function of the survey, $N(D)$, where the number of galaxies observed with estimated distances between D and $D + \mathrm{d}D$ is given by $N(D)\mathrm{d}D$. We choose to cut the group catalog at the distance where the selection function falls to half its maximum, $D_{\mathrm{cut}} = 140$ Mpc, illustrated in Figure 2.2. The entire 2MRS $K < 11.25$ dataset plus the galaxies generated in the population of the galactic plane will be used to create the group catalog, but the catalog will then be truncated, excluding groups with mean estimated distances greater than D_{cut}.

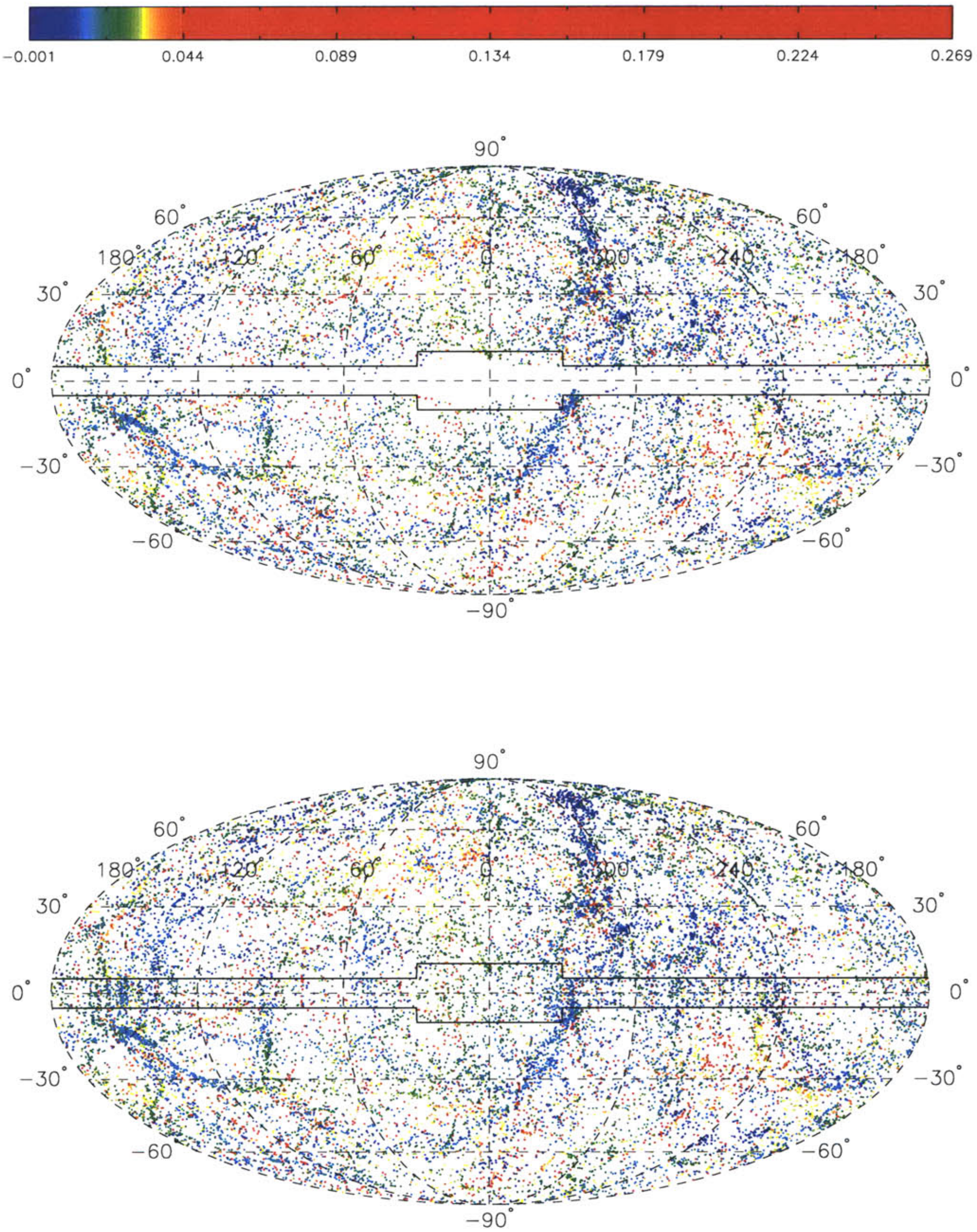

Figure 2.1 Galaxies in 2MRS catalog shown in a Mollweide projection in galactic coordinates. The top panel shows the catalog before the plane was populated. The bottom panel shows the catalog including the addition of the randomly-generated galaxies. The solid line indicates the region that was populated. The color indicates the measured redshift of the galaxy.

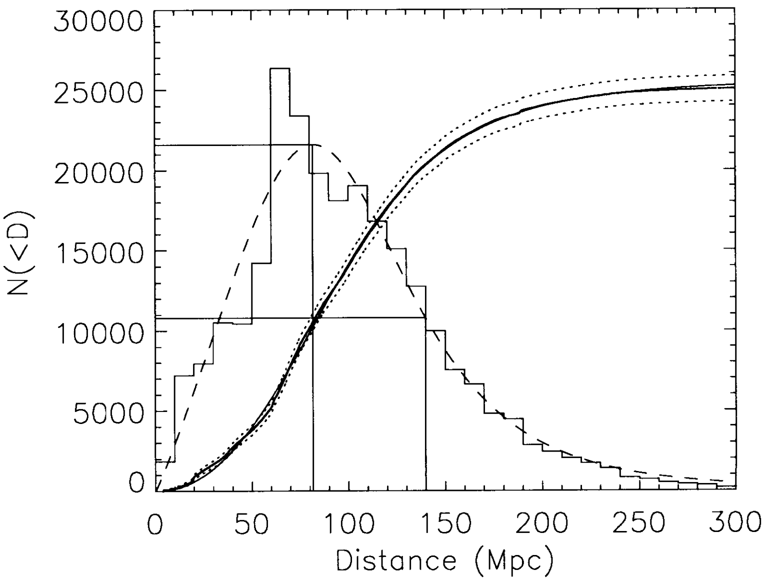

Figure 2.2 Selection function of the 2MRS survey. The data points (shown as small dots) represent the cumulative number of galaxies as a function of (estimated) distance. The data are fit with a curve of the form of equation (2.5) using a least-squares fit (solid line). The dotted lines show the 5σ-errors from Poisson statistics. The data departs from the fit at both the smallest and largest distances shown on the plot. The dashed line shows the derivative of this curve (the selection function) in arbitrary units. The histogram contains the binned data shown in the same arbitrary units as the selection function for purposes of comparison only. The maximum and half-maximum values of the selection function are indicated.

2.3 Parameter Choices

In this section we justify the choice of linking parameters used in the construction of our group catalog. Any group catalog produced from the remaining data sample will contain minimal biasing effects at the highest and lowest redshifts as well as minimal edge effects across the galactic plane. There remains, however, a choice of the parameters that specify the minimum density contrast of detected groups. These parameters, D_0 and V_0 from equations (2.1) and (2.2) above, must be chosen in a somewhat arbitrary fashion.

There is no perfect choice of these parameters that will allow us to identify only groups which are gravitationally bound. In any choice we make, some bound systems may be divided and unbound galaxies will be present in some groups. For very large values of both D_0 and V_0, the algorithm will associate all of the galaxies into a single group. Conversely, if we choose sufficiently small D_0 or V_0, the algorithm will divide substructures within real clusters into multiple systems (Ramella, Pisani, & Geller, 1997), eventually separating each galaxy into its own group. It is clear, therefore, that a suitable parameter choice will lie between these extreme cases. The method of choosing the specific values of the parameters must still remain arbitrary; in order to be able to infer properties of the Universe (e.g., the matter density parameter) from the catalog it is unwise to calibrate the algorithm using simulations based on a set of defined initial assumptions as this would bias our results towards recovering these initial values. It is obvious that there will be a choice of parameters that lie between these extreme values which maximizes the *number* of groups produced. It is therefore reasonable to use a method of maximization to determine the choice of linking parameters, with no alternative method available that does not have similar shortcomings.

At this point, we must consider the size of the group we choose to maximize. We choose to ignore binaries in our definition of groups as previous work has shown such systems identified using percolation algorithms to be unbound in the majority of cases (e.g Diaferio et al., 1999). We consider the parameters obtained when maximizing the number of groups of G or more members for $3 \leq G \leq 20$ as described below. We choose to set $V_F = 1000$ km s^{-1} following HG82. Figure 2.3 shows the number of groups containing 3 or more members in D_0–V_0 space. In Figure 2.3 we explore the parameter space on the intervals $D_0 = [0, 10]$ Mpc, $V_0 = [0, 2000]$ km s^{-1}. We then attempt to maximize the number of groups obtained by the following method: we divide the region spanning $0 \rightarrow 10$ Mpc in D_0 and $0 \rightarrow 2000$ km s^{-1} in V_0 into a 5×5 grid and search for the combination of parameters that produces the largest number of groups. We then change the range of the D_0 and V_0 parameters spanned to coincide with a 3×3 grid (as far as possible) centered on the values of D_0 and V_0 that produced the largest number of groups (or if there are multiple values that produce a number of groups within 5 of the maximum, we ensure that the new range spans all maxima). We divide this region into a 5×5 grid and iteratively repeat the procedure until the desired accuracy of the parameters is reached. This procedure is illustrated in the right panel of Figure 2.3. We repeat this maximization procedure for all values of G between 3 and 20. The obtained value of D_0 rises gently with G, while the

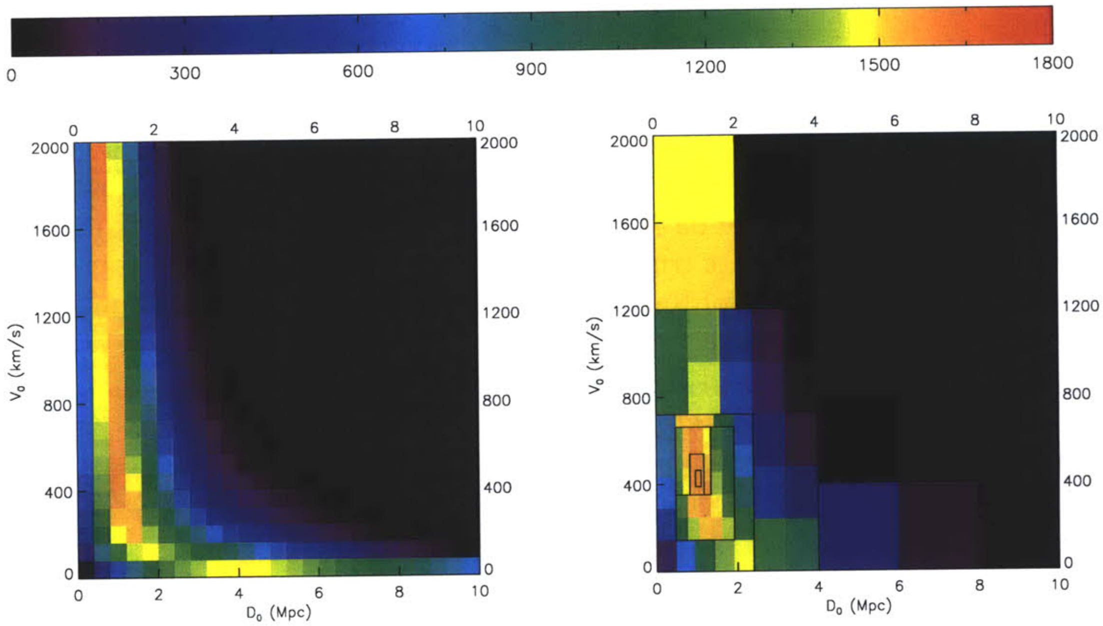

Figure 2.3 The number of groups of 3 or more galaxies obtained as a function of the parameters D_0 and V_0. In the left panel, the clustering algorithm has been executed for each pair of parameters on a 25×25 grid. The right panel contains a graphical representation of the execution of the maximization routine discussed in the §2.3 of the text.

scatter in obtained values of V_0 increases rapidly with G. As observed in Figure 2.3, the number of groups depends highly on D_0, but is comparatively insensitive to V_0. Since the velocity dispersion of a cluster is not expected to depend on the size of the cluster (see the discussion in §2.1 above) it is not sensible to consider large values of V_0 (i.e. > 1000 km s^{-1}) as this will introduce members that are not gravitationally bound and thus propagate errors into the mass estimates. The fraction of interlopers present in a group will also increase with both D_0 and V_0, thus the most sensible choice of parameters to minimize interlopers and reduce the scatter in V_0 corresponds to $G = 3$.

The maximum number of groups of 3 or more members (1587) is obtained for the values (D_0, V_0) = (1.04 ± 0.03 Mpc, 399 ± 15 km s^{-1}), corresponding to the density contrast $\delta\rho/\rho = 12$.

In an analysis of the northern CfA redshift survey[4] (hereafter CfAN), Ramella et al. (1997) show that the group properties are statistically stable for values of density contrasts $\delta\rho/\rho \geq 80$, where they scale V_L in a similar manner to D_L and choose $V_0 = 350$ km s^{-1}. Diaferio et al. (1999) apply a similar choice of parameters to mock CfA surveys based on N-body simulations and conclude that 80% of groups with 4 or more members are true virialized systems, whereas 40% of triplets are not, confirming the hypothesis of Ramella, Geller, & Huchra (1989). As Figure 2.3 shows minimal variation in the number of groups produced with changing V_0 compared to changing D_0, the findings of Ramella et al. (1997) are applicable to this study. We will proceed to analyze the groups produced at both the values of D_0 and V_0 that maximize the number of groups of 3 or more members, as well as the values suggested by Ramella et al. (1997) (i.e. $D_0 = 0.56$ Mpc, which corresponds to $\delta\rho/\rho = 80$,[5] and $V_0 = 350$ km s^{-1}).

2.4 Groups

We present the results of applying the group-finding algorithm (§2.1) to the 2MRS catalog subset (§2.2) using both pairs of parameters discussed in §2.3 above. The group catalogs are presented in Tables A.1–A.6 in the appendix. We provide an overview of the catalogs in §2.4.1 below, then discuss the identified groups and contrast the two catalogs in §2.4.2. We present the properties of the obtained groups (§2.4.3) and discuss the reliability of the clustering algorithm (§2.4.4).

2.4.1 Overview

The catalog produced using the parameters (D_0, V_0) = (1.04 Mpc, 399 km s^{-1}) is presented in Table A.1. These parameters produced the maximum number of groups of 3 or more galaxies and correspond to a density contrast $\delta\rho/\rho = 12$; this catalog

---

[4] This is a subset of the extended CfA redshift survey (de Lapparent et al., 1991; Geller & Huchra, 1989; Huchra et al., 1990, 1995).

[5] The smallest allowed density contrast is chosen to minimize the probability of splitting the richest systems.

will hereafter be referred to as the low-density-contrast (LDC) catalog. The catalog produced using the parameters (D_0, V_0) = (0.56 Mpc, 350 km s^{-1}) is presented in Table A.2. These parameters correspond to the density contrast $\delta\rho/\rho = 80$; this catalog will hereafter be referred to as the high-density-contrast (HDC) catalog.

Figure 2.4 shows the positions and sizes of all groups in the two catalogs. Figures 2.4(a) and 2.4(b) show the groups in equatorial coordinates; Figures 2.4(c) and 2.4(d) show the groups in galactic coordinates. The maps are shown in Mollweide projection, which preserves the area of the structures on the surface of a sphere but distorts their shape, especially close to the poles. The plots show ellipses that have the properties of the groups discussed in §2.4.3 below and are only representative of the shape and size of the group. The Local SuperCluster (LSC) has been clearly identified in Figure 2.4(a) as the large structure in the center of the figure. When applying the algorithm with the higher minimum density contrast, this structure is split into several constituents as shown in Figure 2.4(b). (The same result is evident in Figures 2.4(c) and 2.4(d), however the LSC lies near the pole of the coordinate system in this case. The distortions due to the map projection are therefore enhanced in these plots and the shape is less representative of the true shape of the LSC. The area occupied by the LSC in Figure 2.4(c) is the same as that in Figure 2.4(d). The constituents that have been merged to form the LSC are clearly visible in Figure 2.4(d).)

There is an apparent enhancement in the number of groups with large angular sizes near the galactic plane (see Figures 2.4(b) and 2.4(d)). There are 5 groups shown as ellipses with major axes greater than 5° and with centers inside $|b| < 10°$. Of these, 2 have only 3 members (of which 2 are genuine galaxies from 2MASS XSC) and only 1 out of the remaining 3 groups has more than 10% of its members randomly generated in the population of the plane; the remaining 2 are the only groups with more than 5 members, thus the large apparent sizes of all 5 groups in the figure are due to their proximity. We conclude that the observed enhancement is therefore not an artifact of the population of the plane.

Figure 2.5 shows the same groups as Figure 2.4, however the area of each ellipse is proportional to the number of members in the group, rather than the square of the group's angular size. The areas are normalized such that the major-axis (see §2.4.3) of the largest group appears as its true angular size. These figures are no longer dominated by the foreground groups that have the largest angular sizes, but show how the groups are distributed across the sky out to the redshift limit of the sample.

2.4.2 Identification and Overlap

Due to the nature of the group finding algorithm, we expect to find that all of the galaxies assigned to groups in the HDC catalog will also be assigned to groups in the LDC catalog, however the converse is not necessarily true. We consider all the galaxies assigned to groups in the HDC catalog and determine the correspondence between groups in the two catalogs. The six largest groups in the LDC catalog are plotted in Figure 2.6; the corresponding groups in the HDC catalog are also shown.

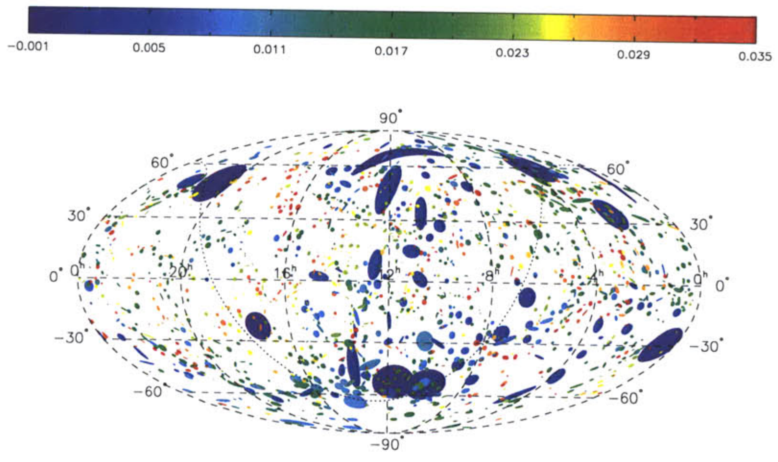

(a) LDC Catalog (Equatorial)

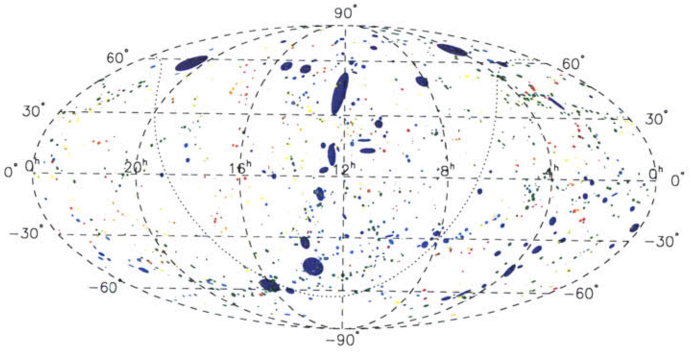

(b) HDC Catalog (Equatorial)

Figure 2.4 Groups (scaled by angular size) identified by clustering algorithm in 2MRS catalog. Figures (a) and (b) are shown using a Mollweide projection in equatorial coordinates, centered at 12^h00^m. Figures (c) and (d) are shown using a Mollweide projection in galactic coordinates. Each group is plotted as an ellipse with the major axis, position angle and axis-ratio of the group. The ellipses are transformed from the x-y coordinate system discussed in §2.4.3 to the appropriate map projection. The color of the ellipse represents the group's mean redshift. The galactic plane is shown by the dotted line in Figures (a) and (b). Figures (a) and (c) show the groups in the LDC catalog ($\delta\rho/\rho = 12$); the LSC has been clearly identified as the central structure. Figures (b) and (d) show the groups in the HDC catalog ($\delta\rho/\rho = 80$); we observe the effect of increasing the minimum density contrast required to identify groups: the LSC has been broken into several constituents. The distortions created by the map projection are maximized near the poles, and enhanced for larger structures. The seemingly strange shape of the LSC in Figure (c) is the result of mapping an ellipse in the x-y coordinate system onto this projection, and is only partly representative of the true shape of the structure.

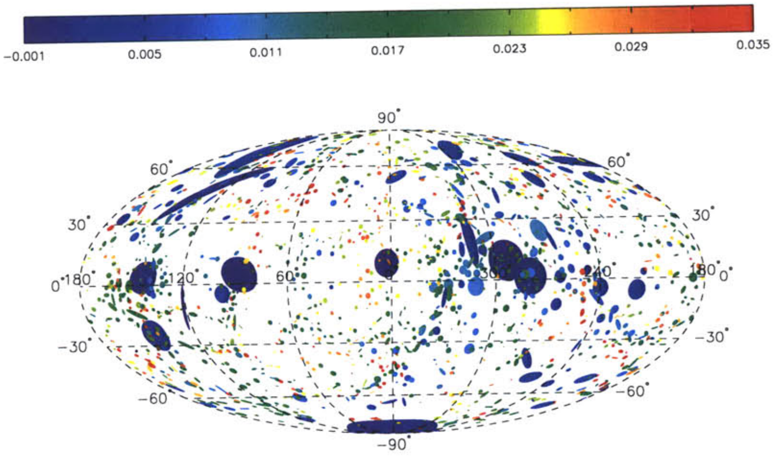

(c) LDC Catalog (Galactic)

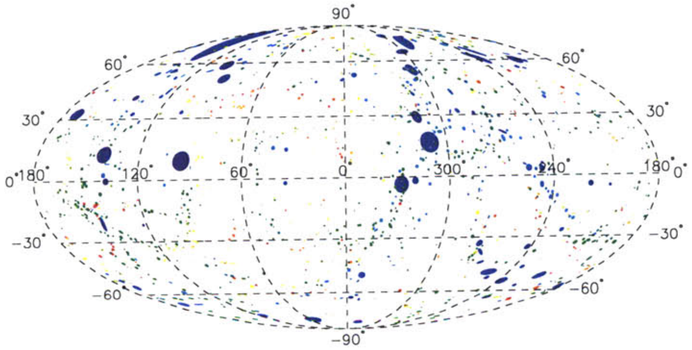

(d) HDC Catalog (Galactic)

Figure 2.4 — *continued...*

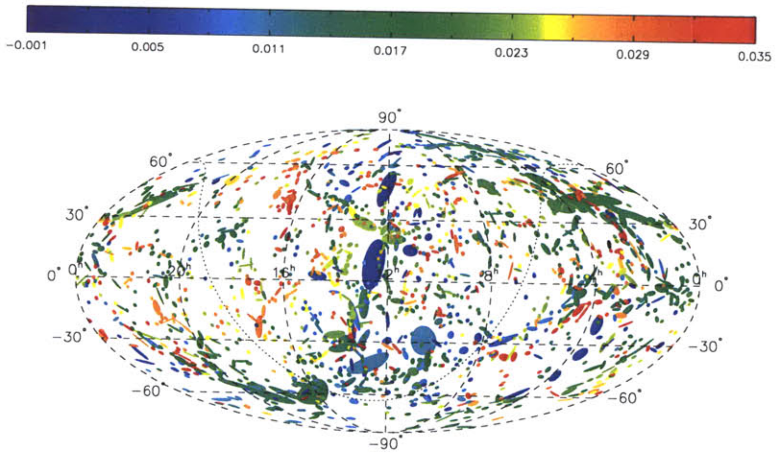

(a) LDC Catalog (Equatorial)

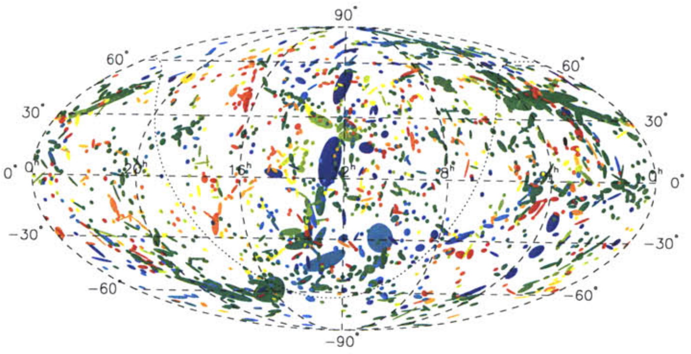

(b) HDC Catalog (Equatorial)

Figure 2.5 Groups (scaled by number of members) identified by clustering algorithm in 2MRS catalog shown in equatorial coordinates. Figures (a) and (b) are shown using a Mollweide projection in equatorial coordinates, centered at 12^h00^m. Figures (c) and (d) are shown using a Mollweide projection in galactic coordinates. Figures (a) and (c) show the groups in the LDC catalog ($\delta\rho/\rho = 12$). Figures (b) and (d) show the groups in the HDC catalog ($\delta\rho/\rho = 80$). Each group is plotted as an ellipse with the position angle and axis-ratio of the group. The areas of the ellipses are proportional to the number of members in the group, scaled such that the major-axis of the largest group is 75% of its true size. The ellipses are transformed from the x-y coordinate system discussed in §2.4.3 to the appropriate map projection. The color of the ellipse represents the group's mean redshift. The galactic plane is shown by the dotted line in Figures (a) and (b).

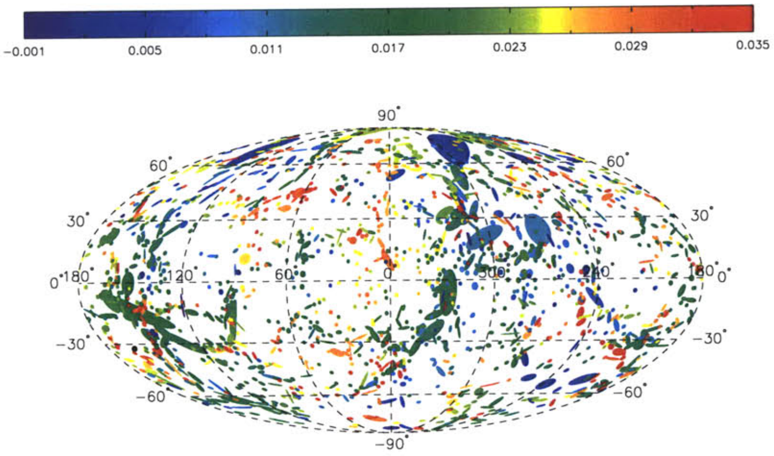

(c) LDC Catalog (Equatorial)

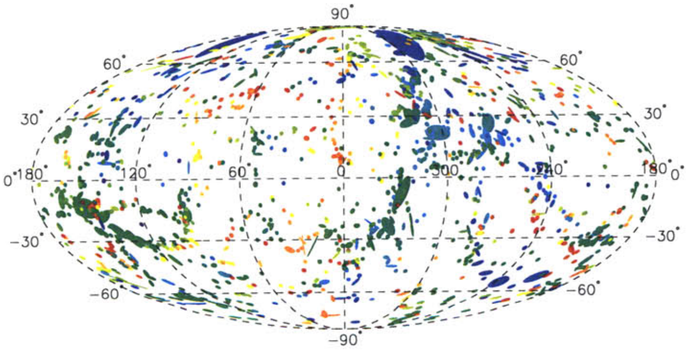

(d) HDC Catalog (Equatorial)

Figure 2.5 — *continued...*

The largest group in the LDC catalog contains 309 members, and has been identified with A426 and A347 of the Perseus-Pisces supercluster. In the HDC catalog, both of these Abell clusters are identified as independent groups; these groups, along with several others, are merged in the LDC due to the larger linking length. The Virgo cluster forms the second largest group in the LDC catalog (301 members), which is also identified in the HDC catalog with 207 members. Norma (A3627, the GA) is identified as the third largest group in the LDC catalog with 220 members (41 of which were randomly generated in the population of the galactic plane); Hydra (A1060), Centaurus (A3526), and Ursa Major S follow with 210, 183, and 138 members, respectively. This exercise demonstrates that the correct choice of parameters used in the group algorithm is entirely dependent on the size of the structures that are desired.

The remaining identifications and correspondence between the catalogs are shown in the appendix (Tables A.3 and A.4), where we consider only groups containing 25 or more members in the HDC catalog. Tables A.5 and A.6 contrast the group assignments of individual galaxies between the two catalogs. It may be surprising that the parameters chosen to maximize the total number of groups actually merge several of the large groups, hence apparently reducing the total number of groups. Although not obvious, this result is not unexpected because the larger linking length will allow many smaller groups to be identified that do not exist in the HDC catalog. The latter association is generating more groups than are removed by the merging of largest groups. It is likely that the groups in the LDC catalog contain a higher fraction of interlopers than the groups in the HDC catalog, however it is evident that the LDC catalog identifies the largest structures on the sky. Since mass estimates are highly sensitive to interloper contamination, this suggests that the HDC catalog would be more suited for the basis of a model of the flow-field (see Chapter 3 for further discussion).

2.4.3 Group Properties

In this section, we discuss the properties of the LDC and HDC catalogs. We begin with a discussion of estimates of the velocity dispersion, size, mass and luminosity, then continue to obtain estimates of the axis-ratio and position angle of the groups.

Basic Properties

The properties of the LDC and HDC catalogs are summarized in Table 2.1. In further analysis, we only consider groups with 5 or more members that are also present in the 2MRS catalog (referred to as *genuine* hereafter), as opposed to those generated in the population of the galactic plane. We do this in an attempt to exclude groups with a high fraction of interlopers in our analysis. We provide two estimates of the mass of the groups. We first compute the virial mass of the group, M_V,

$$M_V = \frac{3\pi}{2}\frac{\sigma_P^2 R_P}{G} \tag{2.6}$$

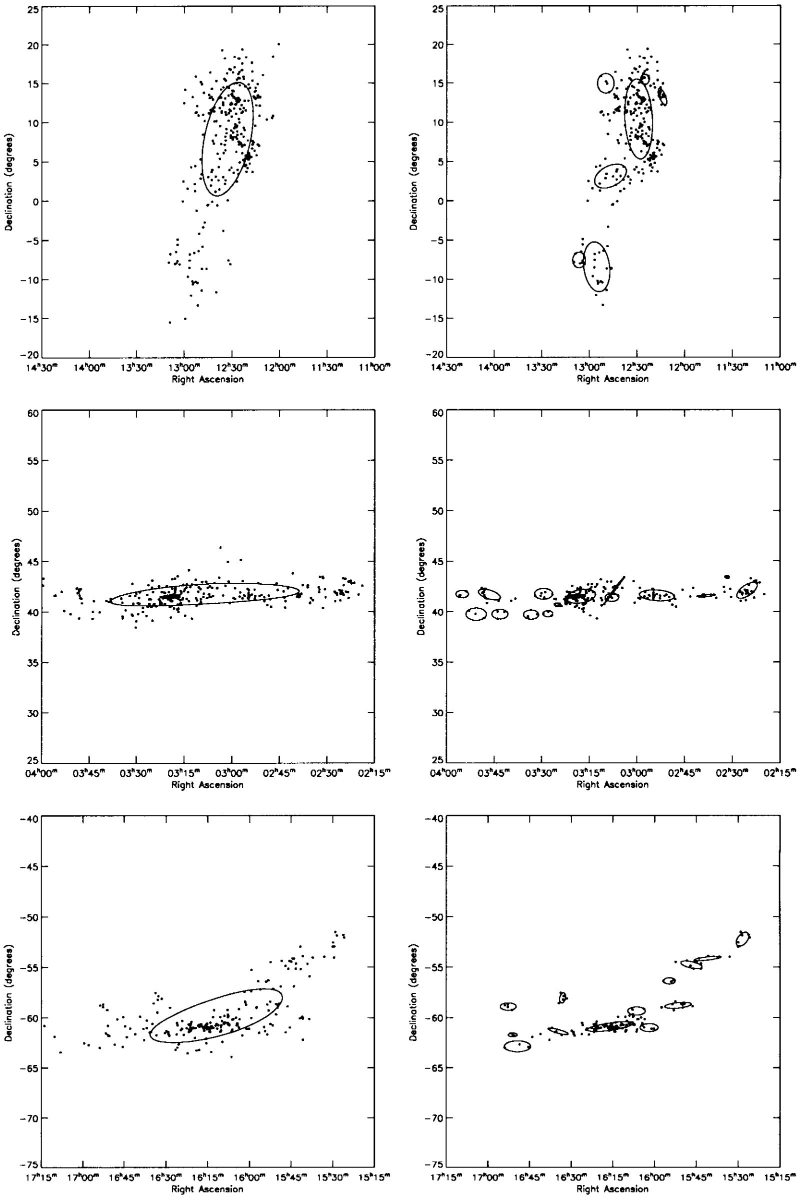

Figure 2.6 Six largest groups in the LDC catalog ($\delta\rho/\rho = 12$). The galaxies in these groups are shown on the plots on the left hand side. The groups identified in the HDC catalog ($\delta\rho/\rho = 80$) in the same region of the sky are shown on the right hand side. The ellipses shown have been computed in the x–y coordinate space discussed in §2.4.3 and mapped onto the equatorial coordinates used in the figure. From top to bottom, the identification of groups with known clusters and superclusters is as follows — 1st page: Top: Virgo (LDC Group #904). Middle: Perseus-Pisces (A426, A347) (LDC Group #224). Bottom: Norma (A3627, the GA) (LDC Group #1172). 2nd page: Top: Hydra (A1060) (LDC Group #729). Middle: Centaurus (A3526) (LDC Group #916). Bottom: Ursa Major S (LDC Group #867).

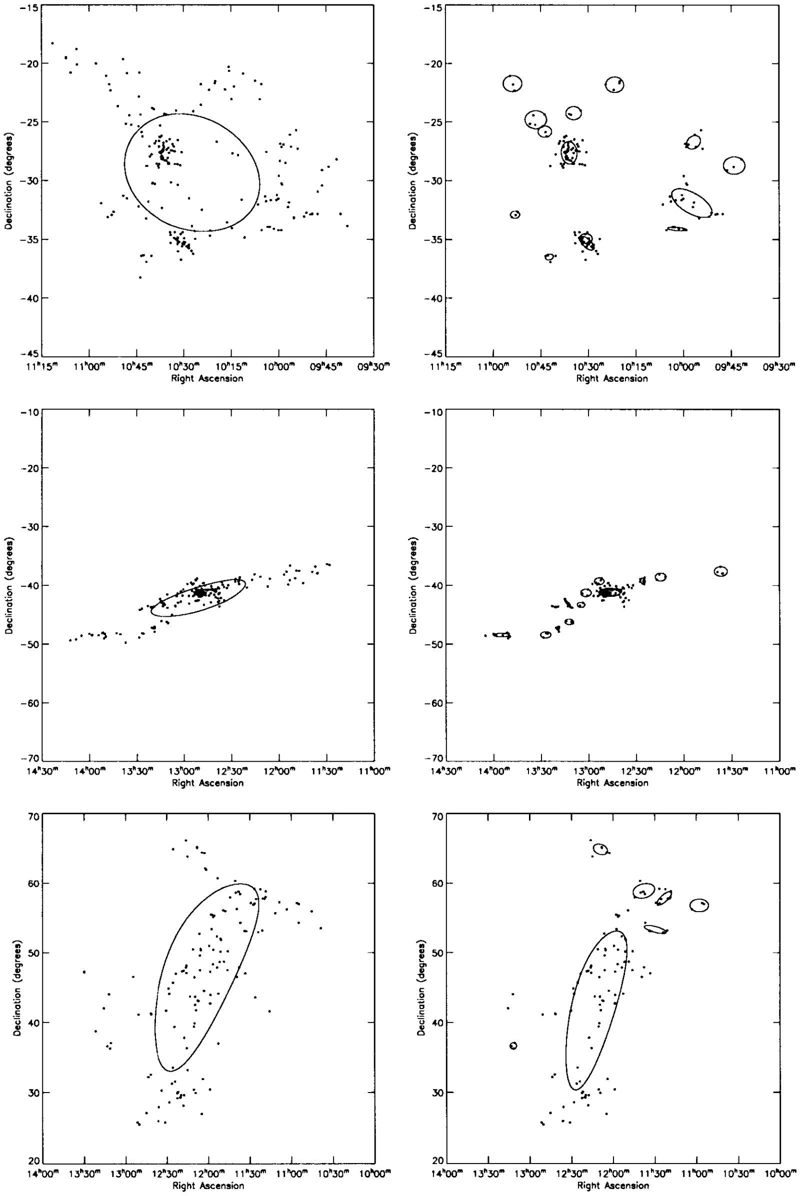

Figure 2.6 — *continued...*

Table 2.1 General properties of the group catalogs

Property	LDC Catalog	HDC Catalog
$\delta\rho/\rho$	12	80
D0 (Mpc)	1.04	0.56
V0 (km s^{-1})	399	350
No. of Singles	5539 (27.5%)	9831 (48.9%)
No. of Binaries	1463 (14.5%)	1743 (17.3%)
No. of Groups of 3+	1587 (58.0%)	1244 (33.8%)
No. of Groups of 10+	215 (28.2%)	97 (10.8%)
No. of Groups of 50+	16 (10.4%)	6 (3.2%)
Mean no. per group	7.36	5.47
Standard Deviation	15.95	8.91
Min/Max per group	3 / 298	3 / 203

Note: The values in parentheses represent the percentages of galaxies that fall into this category.

where G is Newton's constant, σ_P is the projected velocity dispersion,

$$\sigma_P^2 = \frac{\sum_i (V_i - V_G)^2}{N-1} \tag{2.7}$$

and R_P is the projected virial radius,

$$R_P = \frac{N(N-1)}{\sum_{i>j} R_{ij}^{-1}} \tag{2.8}$$

V_G is the mean group velocity and V_i is the line-of-sight velocity of the i^{th} member. N is the total number of galaxies in the group and R_{ij} is the projected separation between two galaxies, defined in terms of their angular separation, θ_{ij}, through

$$R_{ij} = \frac{2V_G}{H_0} \tan\left(\frac{\theta_{ij}}{2}\right)$$

The virial mass estimator is derived from energy considerations of the bound system. After accounting for projection effects, the energy in the system is estimated by considering *projected* inter-particle separations. If two galaxies in the system are observed with a very small projected separation, the potential energy in the galaxy pair is significantly overestimated and will bias the derived mass. To reduce our susceptibility to these biases, we will also calculate the projected mass estimator, M_P (Bahcall & Tremaine, 1981; Heisler et al., 1985),

$$M_P = \frac{f_\mathrm{PM}}{\pi G(N-\gamma)} \sum_i s_i (V_i - V_G)^2 \tag{2.9}$$

where s_i is the offset of the i^{th} member (in physical units) from the center of the group. Following Heisler et al. (1985), we set $\gamma = 1.5$ and $f_{\text{PM}} = 10.2$. The total estimated mass therefore depends on a combination of the observed size and the velocity dispersion, such that the estimate is stable against the biases mentioned above.

We estimate the total isophotal K-band luminosity, L_K of each cluster from the observed luminosity using equation (2.10) below.

$$L_K = \left[1 - \frac{\gamma(\alpha+2, L_{\text{lim}}/L^\star)}{\Gamma(\alpha+2)}\right]^{-1} L_{\text{obs}} \tag{2.10}$$

where L_{obs} is the total isophotal observed K-band luminosity and L_{lim} is the limiting observable luminosity at the distance of the cluster, d_{c},

$$L_{\text{lim}} = 10^{0.4(M_{\odot,K} - m_{\text{lim}} + 25 + 5\log(d_{\text{c}}/\text{Mpc}))} L_\odot \tag{2.11}$$

α and $L^\star$ take the values used quoted in equation (2.4) above, given

$$L^\star = 10^{0.4(M_{\odot,K} - M^\star)} L_\odot$$

and $\gamma(m, x)$ is the lower incomplete gamma function,

$$\gamma(m, x) = \int_0^x t^{m-1} e^{-t} \mathrm{d}t$$

and

$$\Gamma(m) = \gamma(m, \infty)$$

Using the values of M_V, $V - K$ and $K - K_s$ obtained from Cox (2000), we set the K_s-band magnitude zero point, $M_{\odot,\text{K}} = 3.29$. Note that we have not applied an isophotal correction to the luminosities, thus the luminosities presented in this work are lower than the total K-band luminosities.

Table 2.2 contains the median properties of the groups in the catalog that have at least 5 genuine members.

Figure 2.7 shows the fraction of groups, containing at least 5 genuine members, as a function of velocity dispersion, projected virial radius, mass and mass-to-light ratio (using both virial and projected mass estimates). As expected, the distribution of virial radii widens and increases with the larger choice of D_0. Similarly, the velocity dispersions increase with the larger choice of D_0 and V_0 due principally to the change in V_0; re-calculating the groups for various values of D_0 while keeping V_0 constant has little impact on the distribution of velocity dispersions. The net effect is expected to increase the estimated virial mass of the groups, as observed.

We use the median mass-to-light ratio to obtain a value of Ω_m, the ratio of the matter-density, ρ_m (assuming all the mass is contained within galaxy clusters), to the critical density, ρ_c,

$$\rho_c = \frac{3H_0^2}{8\pi G}$$

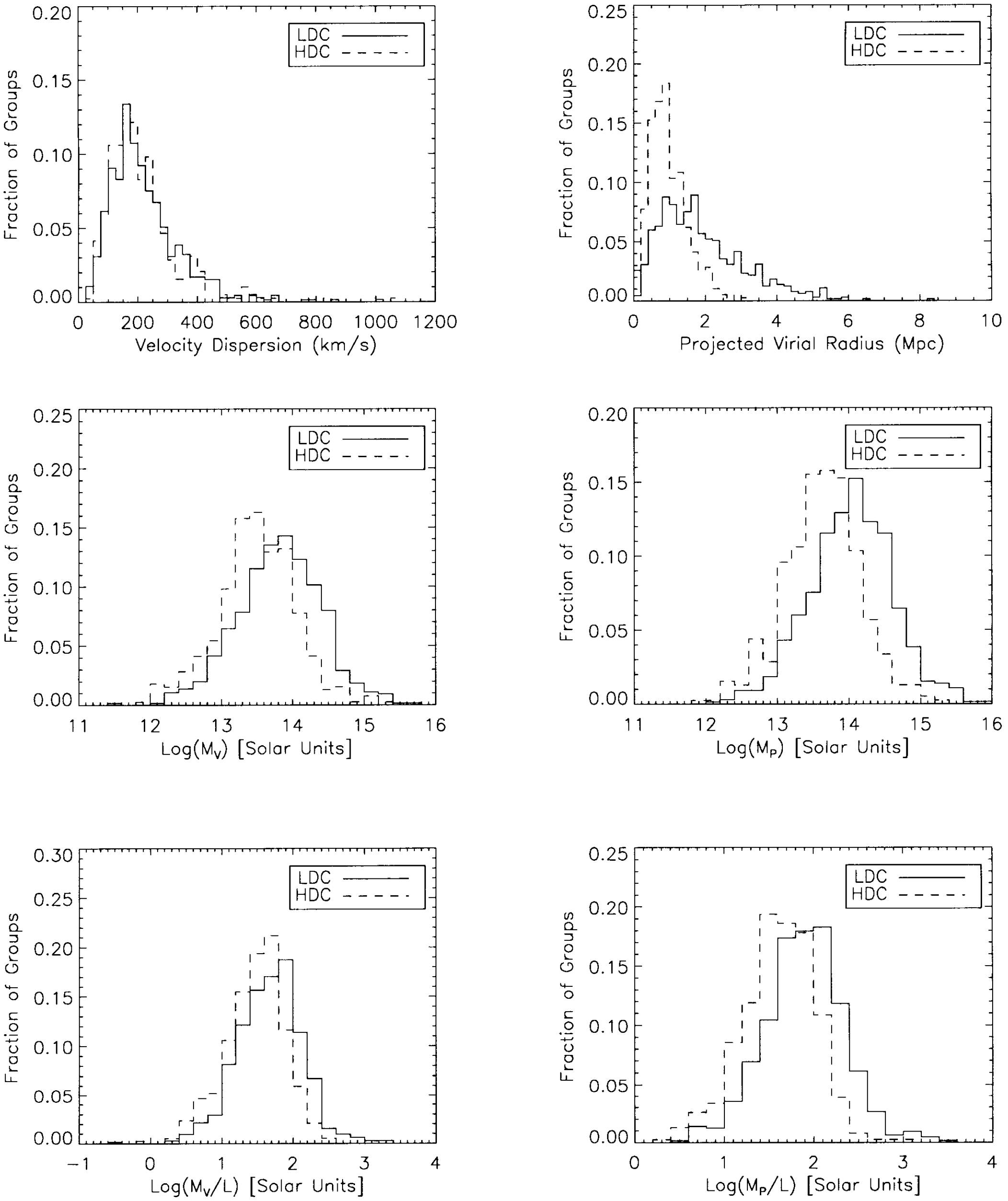

Figure 2.7 Properties of groups with at least 5 genuine members. We contrast the properties of the groups in the LDC catalog (solid line) with those in the HDC catalog (dashed line). Top left: variation in line-of-sight velocity dispersion across the groups. Top right: shows the projected virial radius of each of the groups. Middle: Virial (left) and projected (right) mass estimates of the groups. Bottom: Mass-to-light ratios of the groups using the virial (left) and projected (right) mass estimators. We assume $h = 0.73$.

Table 2.2 Median properties of groups with 5 or more genuine members

Property	LDC Catalog	HDC Catalog
$\sigma_{\rm P}$ (km s^{-1})	196 (184, 205)	187 (175, 202)
$R_{\rm PV}$ (Mpc)	1.67 (1.56, 1.79)	0.89 (0.81, 0.96)
$\log[M_V/M_\odot]$	13.82 (13.74, 13.90)	13.49 (13.42, 13.58)
$\log[M_P/M_\odot]$	14.05 (13.98, 14.11)	13.63 (13.57, 13.71)
$\log[(M_V/L_K)/(M_\odot/L_\odot)]$	1.70 (1.64, 1.75)	1.52 (1.45, 1.58)
$\log[(M_P/L_K)/(M_\odot/L_\odot)]$	1.90 (1.83, 1.95)	1.64 (1.57, 1.70)
$\Omega_{M,V}$	0.14 (0.12, 0.16)	0.09 (0.08, 0.11)
$\Omega_{M,P}$	0.22(0.19 0.25)	0.13 (0.11, 0.14)

The median values are shown, with 99% confidence levels in parentheses. We compute the confidence levels by drawing an equally-sized sample from the observed distributions and computing the median values 5,000 times.

We use the K-band luminosity density, $\mathcal{L}_K$,

$$\mathcal{L}_K = \Phi^\star L^\star \Gamma(\alpha + 2) \tag{2.12}$$

where α, $L^\star$ and $\Phi^\star$ take the values given in equation (2.4), in conjunction with the median mass-to-light ratios to estimate ρ_m,

$$\rho_{m,E} = \langle \frac{M_E}{L_K} \rangle \cdot \mathcal{L}_K \tag{2.13}$$

where E refers to the method of mass estimation (i.e. **V**irial or **P**rojected). For the luminosity function and magnitude zero point used in this work, the critical density corresponds to $\langle M_E/L_K \rangle = 353\ M_\odot/L_\odot$. Similar results were found by Kochanek et al. (2001) and Bell et al. (2003), adjusting for the authors' isophotal corrections and magnitude zero points where appropriate.

The obtained values are given in Table 2.2. Spergel et al. (2007) obtain $\Omega_m = 0.238^{+0.013}_{-0.024}$ assuming $h = 0.73$; this value only agrees, at the 1σ-level, with the value we obtained using the projected mass estimator in the LDC catalog ($\Omega_m = 0.229^{+0.016}_{-0.012}$, 1σ errors). The virial mass estimates predict Ω_m to be too small. For this reason, we will use the projected mass estimator as opposed to the virial mass estimator in further analysis. The fact that the HDC catalog predicts a value of Ω_m significantly smaller than that obtained using WMAP suggests that we are missing a significant fraction of the mass of the cluster in our estimate; selecting groups based on the density contrast $\delta\rho/\rho = 80$ is causing us to underestimate the median mass-to-light ratio. This suggests that the dark matter halos cluster on scales much larger than set by $\delta\rho/\rho = 80$.

Orientation and Ellipticity

We include in the catalog a measure of the axis-ratio, position angle and semi-major axis of the groups containing 5 or more genuine members, calculated using the following method: We rotate the coordinates such that center of the group[6] lies along the z-axis. We measure the angle of each galaxy from the z-axis, Θ, as well as its azimuthal angle ψ, then define

$$x = \Theta\cos(\psi) \quad (2.14)$$

$$y = \Theta\sin(\psi) \quad (2.15)$$

such that the positive y-axis points north and the positive x-axis points east.[7] This definition is chosen such that the shape of the group is not distorted under the projection onto a plane.

We rotate the axes to some angle, ϕ, and define the coordinates of the galaxies in the rotated frame as $(\tilde{x}_i, \tilde{y}_i)$. We choose the value of ϕ that minimizes $\Sigma_i \tilde{y}_i^2$. We compute the 75$^{\text{th}}$–percentile values of $|\tilde{x}|$ and $|\tilde{y}|$ ($\tilde{x}_{75}$ and $\tilde{y}_{75}$) and record their ratio, η, $(0 < \eta < 1)$ as a measure of the axis-ratio of the group. We also record the larger of $\tilde{x}_{75}$ and $\tilde{y}_{75}$ as a measure of the semi-major axis of the cluster, a, as well as the angle of rotation of the semi-major axis from north toward east (the position angle of the group, ϕ). We verify that these angles are approximately uniformly distributed by showing the number of galaxies as a function of position angle in Figure 2.8.

The above properties of the groups are illustrated graphically, by using ellipses with the same semi-major axes, axis-ratios and position angles in Figure 2.4 and with the same axis-ratios and position angles in Figure 2.5. For groups with 3–4 members, a circle is drawn with an angular radius equal to the 75$^{\text{th}}$–percentile mean offset.[8]

In Figure 2.6, we show the galaxies that are associated by the clustering algorithm to form the six largest groups in the LDC catalog. The corresponding ellipses have been overlayed on this plot.[9] The figure also shows the corresponding groups identified in the HDC catalog. It is evident that the higher density contrast used in the latter choice of parameters splits the large structures identified when choosing a lower-density contrast.

2.4.4 Reliability of the Algorithm

In this section we discuss the verifications performed to ensure that the groups obtained are consistent with both expectation and the literature. We first examine the distance-dependence of the velocity dispersions and mass-to-light ratios of the groups. We compute the mass functions of the group catalogs and compare them with expectation. Finally, we compare the 2MRS group catalogs directly with the UZC-SSRS2

---

[6] We define the center as the mean position of the galaxies in cartesian coordinates, assuming the galaxies lie on the surface of a unit sphere.

[7] Note that the mean values of x and y are not strictly zero but, in the analyzed data, are sufficiently small that an iterative centering procedure is not required.

[8] This value is also reported under the column titled a in Tables A.1 and A.2.

[9] Note that the shapes of the ellipses have been distorted due to the choice of coordinate system.

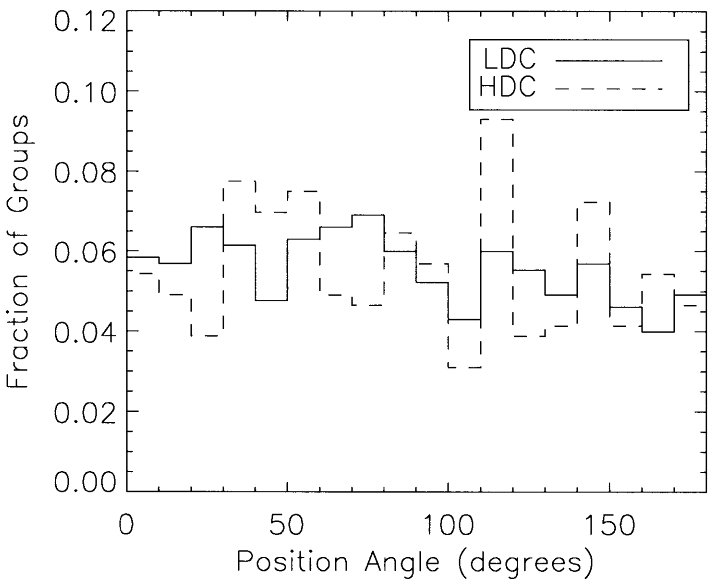

Figure 2.8 Position angles of groups with 5 or more genuine members. The figure shows the fraction of groups with position angles in the specified intervals (binned by 10°). The groups in the LDC (HDC) catalog are represented by the solid (dashed) line.

and CfAN group catalogs.

Variation with Distance

Figure 2.9 shows the velocity dispersion, σ_P, of the groups as a function of distance. We fit a curve of the form

$$\sigma_P = 10^{(\alpha D+\beta)} \text{ km s}^{-1} \tag{2.16}$$

to the data, where the best-fit parameters are given in Table 2.3. The large scatter and very small correlation observed in Figure 2.9 (the mean velocity dispersion changes by a factor of $0.56\bar{\sigma}$ between [20, 40] Mpc and [120, 140] Mpc in the HDC catalog, and $0.35\bar{\sigma}$ in the LDC catalog[10]) demonstrates that there is minimal bias introduced in the velocity dispersion of groups with distance; this was desired in the construction of the algorithm (see §2.1). Had we chosen to scale V_0 with distance, we would expect the velocity dispersions of the most distant groups to be larger than observed in this figure. Since the correlation is already slightly positive, scaling V_0 would have introduced a more significant bias with distance.

Figure 2.10 shows the mass-to-light ratios (computed using the projected mass estimators) as a function of distance for both pairs of parameters. We fit a curve of

---

[10] $\bar{\sigma}$ represents the average standard deviation, weighting the standard deviation of the velocity dispersions in each interval equally.

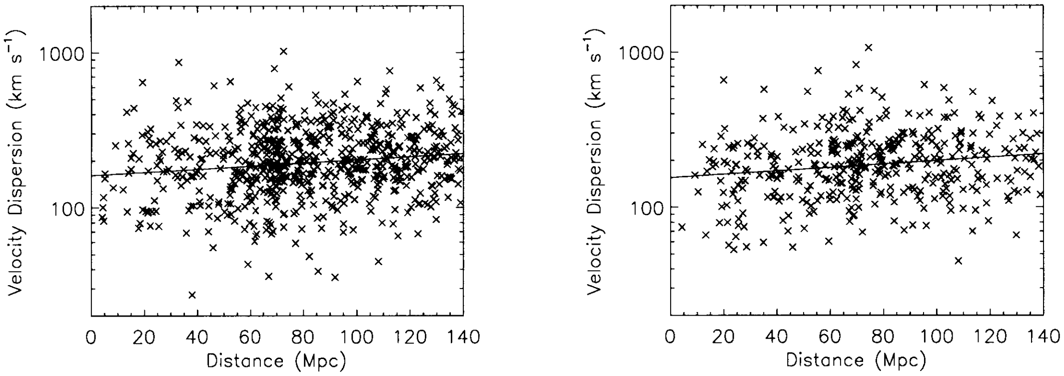

Figure 2.9 Velocity dispersion of groups as a function of distance. The left panel shows the groups in the LDC catalog ($\delta\rho/\rho = 12$). The right panel shows the groups in the HDC catalog ($\delta\rho/\rho = 80$). Only groups with 5 or more genuine members are included. The solid line shows a linear fit to the data as described in the text.

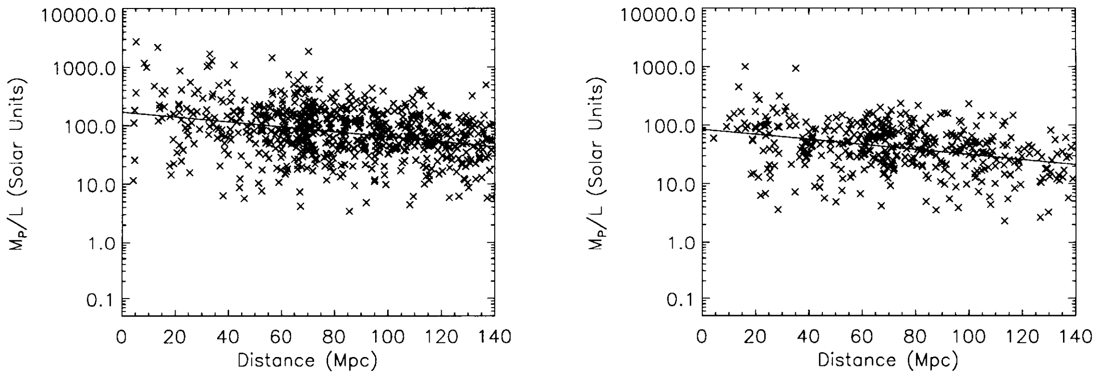

Figure 2.10 Mass-to-light ratio of groups as a function of distance. The plots show the ratio of the projected mass estimate to the corrected K-band luminosity of the cluster. The left panel shows the groups in the LDC catalog ($\delta\rho/\rho = 12$). The right panel shows the groups in the HDC catalog ($\delta\rho/\rho = 80$). Only groups with 5 or more genuine members are included. The solid line shows a linear fit to the data as described in the text.

Table 2.3 Velocity-dispersion– and M/L–distance relations

Parameter	LDC Catalog	HDC Catalog
α (10^{-3} Mpc^{-1})	1.0 ± 0.3	1.1 ± 0.3
β	2.21 ± 0.02	2.19 ± 0.03
p (10^{-3} Mpc^{-1})	-4.3 ± 0.5	-4.3 ± 0.6
q	2.23 ± 0.04	1.93 ± 0.05

Values correspond to the parameters in equations (2.16) and (2.17) that minimize their respective χ^2–statistic.

the form

$$\frac{M_P}{L_K} = 10^{(pD+q)}\ \frac{M_\odot}{L_\odot} \tag{2.17}$$

to the data, where the best-fit parameters are given in Table 2.3. The lower limit to the mass-to-light ratios computed as a function of distance remains approximately constant, while the upper limit decreases with distance, giving rise to the negative slope. Due to the nature of the flux-limited sample, at the largest distances we are not sensitive to (intrinsically) faint objects, therefore we are preferentially selecting the brightest groups. The scaling of the linking length, D_L, is designed to produce groups with a similar number of members at all distances. Since we are further correcting the luminosity of the groups to account for those galaxies to which the survey was not sensitive, we expect the mean luminosity of groups to increase with distance. As we have already shown that the velocity dispersions of the groups we find (and hence the estimated masses) are comparatively uncorrelated with distance, we would expect that we should miss those groups with high mass-to-light ratios at the largest distances, as indeed we observe in Figure 2.10. To correct for this effect, one may introduce a scaling in the linking length in velocity space, V_L, with distance. This would increase the estimated group mass with distance, however such mass estimates would be based on groups containing many interlopers and thus not accurately represent the mass of the group.

Mass Functions

The large number of groups in the sample allows us to obtain an accurate estimate of the mass function for groups in the LDC and HDC catalogs. In this section we only consider groups with at least 5 genuine members at a distance of $10/h$ Mpc or greater. We compute the mass function using the $1/V_{\rm max}$ procedure (e.g., Martínez et al., 2002), whereby each group is weighted by the inverse of the maximum comoving volume, $V_{\rm max}(L_i)$, in which the group remains observable given the flux limit of the survey. L_i is the luminosity of the fifth brightest member of the group. The differential

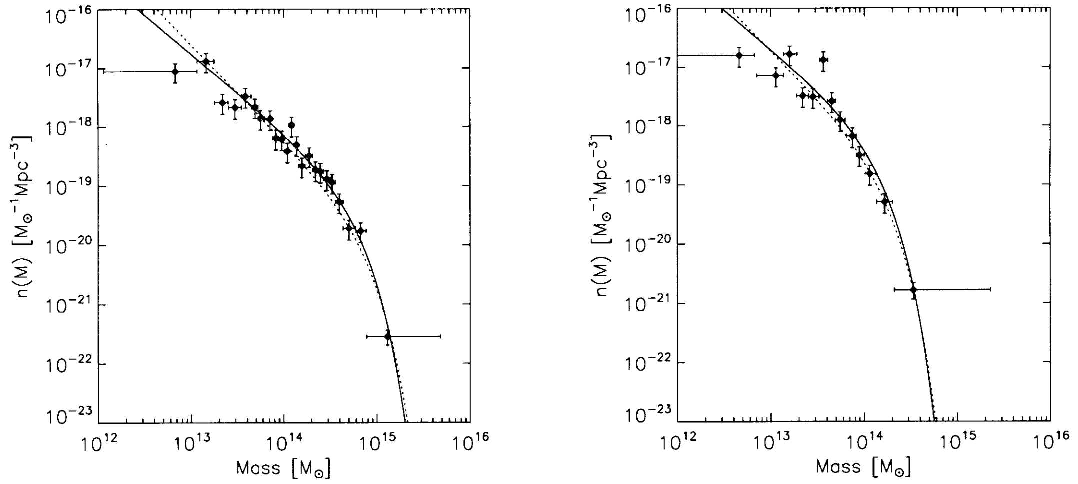

Figure 2.11 Mass functions of the groups. The left panel shows the differential mass function of the groups in the LDC catalog ($\delta\rho/\rho = 12$); the right panel shows that of the groups in the HDC catalog ($\delta\rho/\rho = 80$). The masses are estimated using the projected mass estimator. 2σ error-bars are shown on the plots. Only groups at a distance of at least 10 Mpc containing at least 5 genuine members are included. The points have been fitted with a Press-Schechter (PS74) mass function (solid line) and a Sheth-Tormen (ST99) mass function (dotted line). The former fit produces the smaller χ^2–statistic in both cases. We assume $h = 0.73$.

mass function can be then computed as

$$n(M) = \sum_{|M_i - M| \leq \Delta M} [V_{\max}(L_i)]^{-1} \tag{2.18}$$

where M_i are the group masses and ΔM is the (variable) bin width. The results are shown in Figure 2.11.

We consider analytical differential mass functions of the form suggested by Sheth & Tormen (1999) (also see Jenkins et al., 2001),

$$n(M) = A\frac{\gamma\bar{\rho}}{M^2}\sqrt{\frac{a}{\pi}}\left(\frac{M}{M_0}\right)^{\gamma/2}\left[1 + \frac{1}{(2a)^p}\left(\frac{M}{M_0}\right)^{-\gamma p}\right]\exp\left[-\left(\frac{M}{M_0}\right)^{\gamma}\right] \tag{2.19}$$

where $\gamma = 1 + (\tilde{n}/3)$ and we set $\tilde{n} = 1$. The choice of parameters $a = 1$, $p = 0$, $A = 0.5$ corresponds to the analytical prediction of Press & Schechter (1974) (hereafter, PS74). Sheth & Tormen (1999) suggest the alternative choice parameters $A = 0.3222$, $a = 0.707$, $p = 0.3$ (hereafter, ST99), which provide good agreement with a subset of N-body simulations analyzed by Jenkins et al. (2001).

We fit functions of the form of equation (2.19) to groups in the LDC and HDC catalogs using the parameter choices of both PS74 and ST99 (see Figure 2.11 and

Table 2.4 Best-fit values for Press-Schechter and Sheth-Tormen mass functions

Parameter	LDC Catalog	HDC Catalog
PS74 form[a]		
$\bar{\rho}$ (10^{10} $M_\odot$ Mpc^{-3})	2.6 ± 1.3	1.1 ± 0.7
$\log(M_0/M_\odot)$	14.65 ± 0.18	14.03 ± 0.17
ST99 form[b]		
$\bar{\rho}$ (10^{10} $M_\odot$ Mpc^{-3})	3.2 ± 1.5	1.4 ± 1.0
$\log(M_0/M_\odot)$	14.61 ± 0.23	13.97 ± 0.20

Values correspond to the parameters in equation (2.19) that minimize the χ^2–statistic. [a]Press & Schechter (1974). [b]Sheth & Tormen (1999).

Table 2.4). The analytical descriptions are both good approximations to the data; similar conclusions were also drawn by Martínez et al. (2002), however we find the fit to the PS74 form produces a slightly smaller χ^2–statistic in both cases.

We compare the ratio of the best-fit values for M_0 in the PS74 form of the mass function to the value predicted using the simple arguments of PS74. M_0 scales with the minimum density contrast according to

$$M_0 \propto \left(\frac{\delta\rho}{\rho}\right)^{-2/\gamma} \tag{2.20}$$

and thus we expect the ratio of the determined values of M_0 to be given by

$$\begin{aligned}\log\frac{M_0^{(\mathrm{LDC})}}{M_0^{(\mathrm{HDC})}} &= \log\left[\frac{(\delta\rho/\rho)_{\mathrm{LDC}}}{(\delta\rho/\rho)_{\mathrm{HDC}}}\right]^{-2/\gamma} \\ &= -\tfrac{2}{\gamma}\log\left(\tfrac{12}{80}\right) = 1.24\end{aligned}$$

The obtained values of M_0 give log-ratio of 0.79 ± 0.25, providing agreement only at the 2σ-level with Press-Schechter theory. The two methods cannot be expected to be within perfect agreement as the group-identification algorithm will find different groups as V_0 is varied but D_0 is held constant. The computed estimates of the group masses will therefore vary, while the ratio predicted by the Press-Schechter treatment (which is sensitive only to the change in density contrast, thus D_0) does not.

Comparison with other Group Catalogs

To verify the validity of the produced group catalogs, we compare the 2MASS group catalogs with the UZC-SSRS2 group catalog (Ramella et al., 2002) and the CfAN group catalog (Ramella et al., 1997). The former is constructed from partial versions of the Updated Zwicky Catalog (UZC; Falco et al., 1999) and the Southern Sky Redshift Survey (SSRS2; da Costa et al., 1998) and covers 37% of the sky; the latter covers 10%. The selection criteria for the three catalogs result in completeness

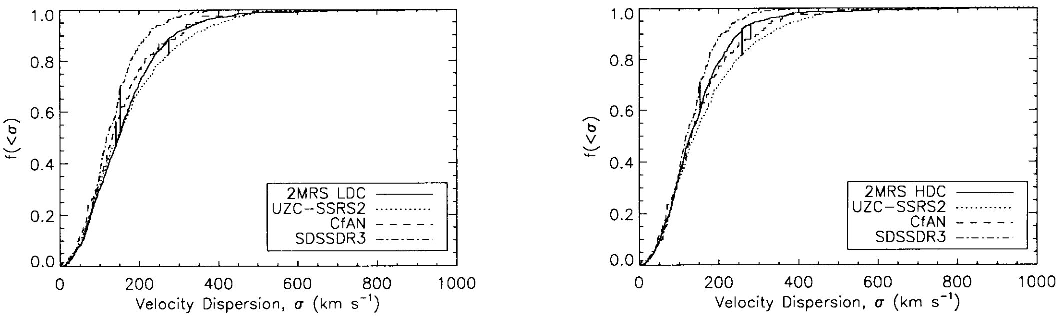

Figure 2.12 Cumulative fraction of velocity dispersions of groups. The velocity dispersions in the UZC-SSRS2, CfAN and SDSSDR3 group catalogs catalogs are compared with the 2MRS LDC catalog (left panel) and the 2MRS HDC catalog (right panel). The vertical lines indicate the corresponding D-statistic used in the K-S test.

limits at different velocities. To compute the completeness in redshift-space, we use the same technique as §2.2.4 above, however in this case, we determine the velocity corresponding to the peak in the derivative of equation (2.5). When comparing the 2MASS group catalog with the other two, we cut both catalogs at the smallest of the two corresponding velocity limits (2MRS at 5795 km s^{-1} in the LDC catalog and 5501 km s^{-1} in the HDC catalog, UZC-SSRS2 at 7115 km s^{-1}, CfAN at 9390 km s^{-1}).

For each of the groups present in the UZC-SSRS2 and CfAN catalogs, we search the 2MRS group catalogs for a group within a radius set by twice the sum of the virial radii of the group in 2MRS and the group in the comparison catalog, with mean velocities that differ by less than 30%. We find that 92% of the groups in UZC-SSRS2 and 84% of the groups in CfAN are present in the 2MRS LDC group catalog, whereas 78% of the groups in UZC-SSRS2 and 59% of the groups in CfAN are present in the 2MRS HDC group catalog. There is reasonable agreement in both cases given the differing selection criteria employed in the three samples.

We also compare the distributions of velocity dispersion using the two-sided Kolmogorov-Smirnov (K-S) test (Chakravarti et al., 1967). The cumulative fractions of the LDC and HDC catalogs are compared with the cumulative fractions of the UZC-SSRS2 and CfAN catalogs (see Figure 2.12). For comparison, we also show the velocity dispersions of groups in Sloan Digital Sky Survey Data Release 3 (SDSSDR3, Merchán & Zandivarez, 2005). The results of the test are shown in Table 2.5. The velocity dispersions in both the LDC and HDC catalogs are consistent with the CfAN sample. However only the LDC catalog produces groups with velocity dispersions consistent with those in the UZC-SSRS2 catalog, although the discrepancy with the HDC catalog is small. Any discrepancy with the CfAN catalog is not appreciable due to the smaller number of groups in the compared sample of CfAN galaxies.[11] Neither the LDC nor HDC catalogs are consistent with the SDSSDR3 group catalog. The discrepancy is expected due to the difference in the algorithms used to identify

---

[11] This is accounted for in the Kolmogorov-Smirnov test.

Table 2.5 Comparison between 2MRS, UZC-SSRS2, CfAN and SDSSDR3 groups

Property	LDC Catalog	HDC Catalog
No. of 2MRS Groups	792	630
Comparison with UZC-SSRS2		
No. of UZC-SSRS2 Groups	459	425
D-statistic[a]	0.062	0.106
P-value[b]	0.208	0.006
Comparison with CfAN		
No. of CfAN Groups	121	115
D-statistic[a]	0.095	0.060
P-value[b]	0.288	0.867
Comparison with SDSSDR3		
No. of SDSSDR3 Groups	209	191
D-statistic[a]	0.186	0.118
P-value[b]	10^{-5}	0.030

The table presents the results of two-sided Kolmogorov-Smirnov test on the comparison between the distributions of velocity dispersions of the groups in 2MRS catalog with the UZC-SSRS2, CfAN and SDSSDR3 catalogs. [a] D-statistic used in computation of P-value in Kolmogorov-Smirnov test. [b] P-value represents the probability that such a difference would be observed under the assumption that the two samples were drawn from the same parent distribution. We consider values of $P < 0.05$ to indicate that the two samples were drawn from significantly-different parent distributions.

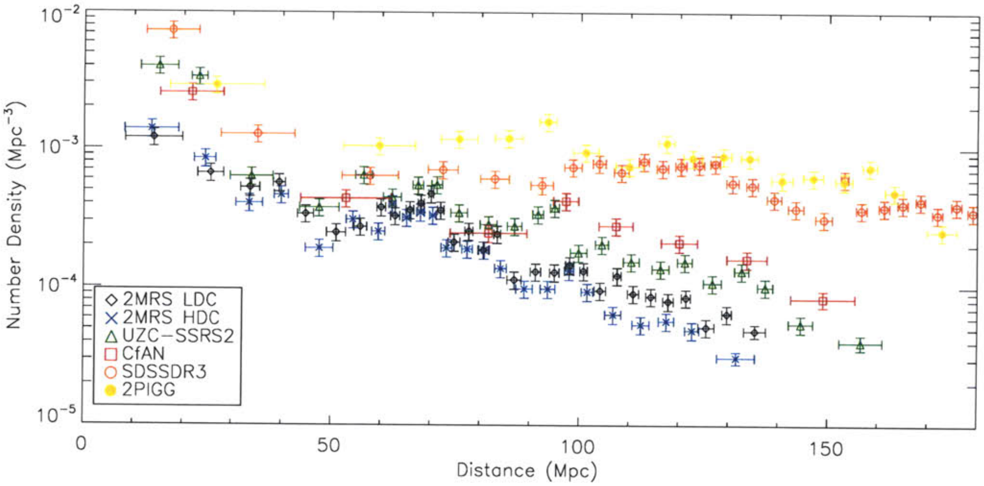

Figure 2.13 Number density of groups as a function of distance. We show the number density for the LDC (diamond) and HDC (cross) catalogs, as well as the UZC-SSRS2 (triangle), CfAN (square), SDSSDR3 (open circle) and 2PIGG (filled circle) catalogs. (The symbols are colored black, blue, green, red, orange and yellow, respectively.) We assume $h = 0.73$.

groups.

The difference in the distributions of velocity dispersion is due in part to the different scalings of the velocity-linking parameter. When scaling the linking length, the more distant groups are likely to have higher velocity dispersion. These groups may not be present in a group catalog derived by setting the parameter to a constant. The velocity dispersions of groups in the USZ-SSRS2 and CfAN catalogs tail off at ~400 km s^{-1}. The LDC catalog is in reasonable agreement with this since the velocity linking parameter is ~400 km s^{-1}. The HDC catalog, however, contains a smaller fraction of groups with velocity dispersions between 350–400 km s^{-1} than are present in the other catalogs. This is consistent with the above hypothesis since, in this case, the velocity linking parameter is set to 350 km s^{-1}. Without knowledge of the complete phase-space positions of the galaxies, we cannot determine whether the majority of groups with velocity dispersions greater than 350 km s^{-1} in the LDC, UZC-SSRS2 and CfAN catalogs are bound or not.

We further examine the number density of groups as a function of redshift (see Figure 2.13). For comparison, we include the number density of groups in SDSSDR3 and the 2dFGRS Percolation-Inferred Galaxy Group (2PIGG) catalog (Eke et al., 2004), although these surveys have very different selection biases and fainter flux limits, which result in a higher number density of groups than that detected in 2MRS. The 2MRS group catalogs contain an approximately constant number density of groups to ~80 Mpc, before following a power-law decay. The LDC catalog has slightly more uniform coverage out to this distance than the HDC catalog. The observed shape of the function is consistent between the LDC, HDC, UZC-SSRS2 and CfAN catalogs, and the values only diverge at ~90 Mpc where the linking length becomes large enough that the selection biases of the parent surveys will have a significant effect on the identified groups. The number density of groups in the SDSSDR3 and 2PIGG catalogs is approximately constant over the entire range of distances considered due to the lower flux limits of the surveys. We note that the HDC catalog contains fewer groups than the LDC catalog beyond ~30 Mpc, as expected. The observed peak at ~70 Mpc corresponds to the location of the great attractor, and is enhanced by the distance corrections discussed in §2.2.1.

2.5 Summary

We have presented two catalogs of groups in the 2MASS Redshift Survey, identified using a variable-linking-length percolation algorithm (HG82). We discussed the effect of the variation of the input parameters, D_0 and V_0, on the number of groups obtained. As demonstrated in §2.4.4 above, we see that the correct choice of parameters depends on the purpose of the catalog, and full phase-space information of each galaxy is required to understand the most suitable choice of parameters to find virialized groups.

We justify the choice of two pairs of parameters: $(D_0, V_0) = (1.04\,\mathrm{Mpc}, 399\,\mathrm{km\ s^{-1}})$, corresponding to a density contrast $\delta\rho/\rho = 12$ (LDC catalog), and $(D_0, V_0) = (0.56\ \mathrm{Mpc}, 350\ \mathrm{km\ s^{-1}})$, corresponding to a density constrast $\delta\rho/\rho = 80$ (HDC catalog). We show that the latter choice of parameters identifies the largest nearby clusters individually, while many of these groups are merged with the former parameter choice.

We compute virial and projected mass estimates for the clusters under the assumptions that the identified groups have spherical symmetry and that the light traces the distribution of the mass. We find that the projected mass estimates give mass functions in agreement at the 2σ-level with Press-Schechter theory, although given the dependence of the algorithm on V_0, 1σ-agreement is not expected.

We calculate corrected K-band luminosities for each cluster and use these to estimate the mass-to-light ratios and corresponding values of Ω_m. The values predicted using the virial mass estimator in both the LDC and HDC catalogs are significantly smaller than the 3-year WMAP result (Spergel et al., 2007) of $\Omega_m = 0.238^{+0.013}_{-0.024}$ motivating the use of the projected mass estimator over the virial mass estimator in subsequent analysis. The projected mass estimates of groups in the LDC catalog produce a value of $\Omega_m = 0.23 \pm 0.03$, which agrees with the WMAP result at the 1σ-level. The HDC catalog significantly under-predicts the WMAP value, suggesting dark matter clusters on scales much larger than defined by $\delta\rho/\rho = 80$.

The distribution of velocity dispersions of groups in the 2MRS LDC catalog is in agreement with the groups in the UZC-SSRS2 catalog (Ramella et al., 2002) as well as CfAN group catalog. The 2MRS HDC catalog velocity dispersions are in agreement with the groups of the CfAN catalog, however we find that there is a statistically significant difference between the distributions of velocity dispersions in the 2MRS HDC and UZC-SSRS2 catalogs.

The group catalogs presented in this chapter provide an estimate of cluster locations and masses without the necessity to assume an intrinsic mass-to-light ratio. These group catalogs form the basis for a map of baryonic density enhancements in the nearby Universe.

Chapter 3

Modeling the Flow-field with Groups of Galaxies

The previous chapters have provided us with the constructs required to develop a model of the flow-field using groups of galaxies. In §1.3, we introduced the framework of gravitational instability theory (Peebles, 1980). In Chapter 2, we discussed a method for constructing a catalog of groups from a magnitude-limited redshift survey and presented two catalogs constructed at different density-contrast thresholds. In this chapter, we will apply the constructs discussed thus far to gain an understanding of the dynamics of galaxies in the nearby Universe using data from the 2MASS Redshift Survey (see §1.4).

We begin with a brief discussion of the catalog of groups and explain modifications that we apply (§3.1). We then describe the method we use to construct a flow-field from the identified groups in §3.2 below and present the results of the construction in §3.3. Finally, we compare the constructed flow-field with existing models in §3.4 and summarize the main points from this chapter in §3.5.

Throughout this and future chapters, when a value of the Hubble constant is required, we assume $H_0 = 100h = 74.2$ km s^{-1} Mpc^{-1} (Riess et al., 2009).

3.1 Catalog of Galaxy Groups

In Chapter 2, we presented two catalogs of groups constructed from the $K_s < 11.25$ 2MRS source catalog. Here, we utilize the $K_s < 11.75$ source catalog (see §1.4) in order to maximize the range over which the flow-field is informative. As discussed in §2.4.2, many known structures identified in the HDC catalog (constructed with a minimum density contrast of $\delta\rho/\rho = 80$) were found to be merged in the LDC catalog (constructed at the lower minimum density contrast, $\delta\rho/\rho = 12$). Since the mass estimates are obtained dynamically, these are only valid when applied to relaxed systems; masses constructed from merged relaxed systems will tend to overestimate the combined mass of the clusters. For this reason, we choose to proceed with a group catalog, constructed using the same method, minimum density contrast, and velocity linking-length as the HDC catalog.

Table 3.1 Properties of groups used to model the flow-field

Property	Value
Total no. of Galaxies inside $120/h$ Mpc	35130
No. of Groups of 5+[a]	674 (19.0%)
No. of Groups of 10+[a]	160 (10.0%)
No. of Groups of 20+[a]	38 (5.3%)
Mean no. per Group[b]	9.68
Standard Deviation[b]	13.02

[a] The values in parentheses represent the percentages of galaxies that fall into this category. [b] The values are computed using only the groups with 5 or more members (i.e. those groups used to construct the flow-field model).

We follow the prescription of Chapter 2 to identify groups, first populating the galactic plane using a random-sampling technique to ensure the galaxy-density within the plane is representative of that above and below (see §2.2.2), then implementing the percolation algorithm of Huchra & Geller (1982), as adapted in §2.1. While populating the galactic plane prevents edge effects disrupting the percolation algorithm, we do not intend for simulated data to alter the results presented here. Therefore, any properties of groups are calculated using only 2MASS observed galaxies, and groups containing only simulated galaxies are removed. See Table 3.1 for a summary of the properties of the catalog.

In the remainder of this section, we discuss several modifications that have been applied to the sample before using it to construct a model of the flow-field.

3.1.1 Identification of the Virgo Cluster

The Virgo cluster is the largest group (by number of members) identified in both the $K_s < 11.25$ and $K_s < 11.75$ catalogs. A background group, which lies ~ 8 degrees from the center of the Virgo cluster and has a heliocentric redshift of ~ 2200 km s^{-1}, has been associated with the Virgo group through the application of the friends-of-friends algorithm. A plot of the angular positions of the identified members of Virgo is shown in Figure 3.1 along with the distribution of galaxy velocities. It is evident from Figure 3.1 that this group is a dynamically separated system to the Virgo Cluster. In order to reduce distortions in the position and velocity of the identified groups, we assign any galaxy inside the indicated ellipse with redshifts greater than 1850 km s^{-1} to a separate group before computing any of the groups' properties. Since the Virgo Cluster is the closest large attractor to the LG, it will play a significant role in the predicted peculiar velocity of the LG. To further reduce uncertainties in the model, we assign a distance to the Virgo cluster of 16.8 Mpc (Tully et al., 2008), and a mass such that the mean overdensity within our radius is in agreement with the value of Tonry et al. (2000), $\delta = 1.0 \pm 0.07$.

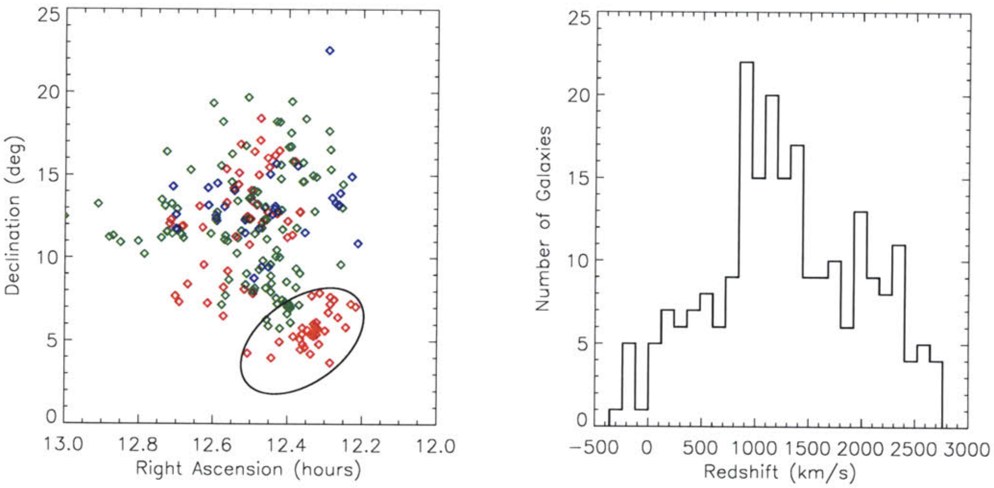

(a) Locations of Member Galaxies

(b) Redshifts of Member Galaxies

Figure 3.1 Galaxies associated with the Virgo group. Panel (a) shows the positions on the sky of galaxies associated with the Virgo group through the application of the group-finding algorithm. The colors indicate the heliocentric redshift (Blue: $cz < 500$ km s^{-1}, Green: $500 < cz < 1500$ km s^{-1}, Red: $cz > 1500$ km s^{-1}). The ellipse shows the region inside which member galaxies with $cz > 1850$ km s^{-1} are assigned to a distinct group. Panel (b) shows the distribution of redshifts for galaxies associated with the Virgo group. The second peak (at $\sim$ 2200 km s^{-1}) represents the background group that has been merged with the Virgo Cluster by the group-identification algorithm.

3.1.2 Local Velocity Distortions

Reliable measurements of the recession velocity of a galaxy are available with respect to the heliocentric reference frame. Since we are assuming the linear regime, we must first remove any non-linearities in the peculiar motion of the Sun with respect to the observing target — these consist of the motion of the Sun about the center of the Milky Way and the motion of the Milky way about the LG barycenter. The recent work of Tully et al. (2008) argue in favour of a reference frame they name the *Local Sheet* (LS). Inside $\sim$ 7 Mpc, galaxies are essentially at rest with respect to the local Hubble flow. This reference frame is defined with respect to the motions of these galaxies, and therefore represents a volume sufficiently large that we expect the net motion of groups within (relative to galaxies beyond 7 Mpc) to be well explained using the linear approximation of §1.3. The authors argue that this frame is more reliable as a local rest frame, in which the LG has a motion of 66 ± 24 km s^{-1} toward ($SGL = 150° \pm 37°$, $SGB = +53° \pm 20°$) (see §3.2.1).

Since the peculiar motions of groups within the Local Supercluster (see §3.2.1 below) are dominated by the presence of the Virgo cluster, which has a mass nearly three orders of magnitude larger than the LG or M81 group, we choose to remove all groups (see §3.1.3 below) identified inside a sphere of radius 7 Mpc, centered on the Milky Way, from the catalog. We then correct the velocities of more distant groups to the LS reference frame.[1] This will improve the accuracy of the reconstructed LG velocity, which is essential when calculating velocities *relative* to our own motion. The correction from a velocity referenced with respect to the heliocentric frame ($V_{\rm hel}$) to the LS frame, for an object at galactic coordinates (l, b), is shown below:

$$V_{\rm LS} = V_{\rm hel} + V_{\rm LS}^{\odot}(\cos b \cos b_{\rm LS}^{\odot}[\cos l \cos l_{\rm LS}^{\odot} + \sin l \sin l_{\rm LS}^{\odot}] + \sin b \sin b_{\rm LS}^{\odot}) \tag{3.1}$$

where $V_{\rm LS}^{\odot} = 318 \pm 20$ km s^{-1}, $l_{\rm LS}^{\odot} = 96° \pm 4°$ and $b_{\rm LS}^{\odot} = -1° \pm 4°$.

3.1.3 Group Properties

To prevent the mis-identification of nearby groups, we cross-correlate the distance catalogs of Tully et al. (2008) and Springob et al. (2007) with galaxies in the 2MRS sample, obtaining a distance estimate to a total of 2864 galaxies (these catalogs are described in more detail in §5.4 and §5.6).

We compute the mean LS-centric redshift for each group by averaging the values of the member galaxies. For groups with mean redshifts less than 2500 km s^{-1}, we find those groups that contain one or more galaxies with a redshift-independent distance estimate. For these groups with fewer than 15 members, we assume the distance to the group is given by the mean of the distance estimates to the afore-mentioned galaxies, but for larger groups, we require at least 5 members to have distance measurements before executing the same procedure. This selection process ensures that small nearby groups are not incorrectly placed, while preventing an interloper with a distance

---

[1] Due to the dominance of the Virgo cluster in the Local Supercluster, the removal of very nearby groups has little effect of the dynamics of other groups outside the 7 Mpc sphere.

estimate from inadvertantly modifying the location of larger groups. For groups beyond 2500 km s^{-1}, or when a group does not contain any galaxies with redshift-independent distance estimates, we initially assign a distance to the group given by the mean redshift of the member-galaxies, with respect to the reference frame of the LS.

The group masses are estimated using the projected mass estimator, M_P (Bahcall & Tremaine, 1981), as in 2.4.3, which we write, for convenience, in velocity units:

$$M_P H_0 = \frac{f_{\mathrm{PM}} v_H}{\pi G(N-\gamma)} \sum_i \tan(\theta_i)(u_i - v_m)^2 \tag{3.2}$$

where θ_i is the angular offset from the center and u_i is the heliocentric velocity of the i^{th} member of the group. N is the number of members in the group and v_m corresponds to the mean heliocentric velocity of the group members. v_H is the distance to the group. The values of the remaining parameters correspond to those suggested by Heisler et al. (1985), $\gamma = 1.5$ and $f_{\mathrm{PM}} = 10.2$.

From this point forward, we consider only groups with at least 5 members to act as tracers of the mass. We will see in §4.4.1 that using groups with fewer to contribute to the density field introduces a significant error in the dynamically-estimated masses for simulated groups; while there are caveats in extending the results of the simulation analysis (see §4.2.1), the motivation for avoiding small sample sizes is clear. Even with 5 member-groups, we need to be careful with estimates of of the uncertainties. In the ideal scenario, the dynamical mass estimate is limited only by the finite number of tracers. However in practicality the problem of interlopers is likely to be more severe. If an interloper is assigned to a group, it will generally act to increase the calculated velocity dispersion, resulting in an overestimate of the mass. We expect this problem to be more significant in smaller groups, since a single interloper will contribute a larger weight to the velocity dispersion compared with groups that have a large number of members.

In an effort to model this error, we examine the mass-to-light ratio of groups as a function of the number of member galaxies. While we do not wish to introduce restrictions on the mass-to-light ratio of individual galaxies in this model, one would expect that the mass-to-light ratio for clusters should not vary significantly between clusters of similar sizes. Group luminosities are computed as described in §2.4.3, correcting for the magnitude-limit of the survey by assuming a universal luminosity function (Eq. 2.10). Figure 3.2 shows the difference between the 68th and 32nd percentile values, divided by the median value of the mass-to-light ratio of groups inside a bin containing at least 20 groups. As anticipated, we find groups with fewer members have a larger relative scatter in their mass-to-light ratio. We note that the data can be described approximately by a function of the form

$$\Delta_{M/L}(N) = q + p/N \tag{3.3}$$

where N is the number of members in the group, and $\{q = 0.25,\ p = 0.99\}$ are obtained using a least-squares fit. We will use this observation to assist in modeling

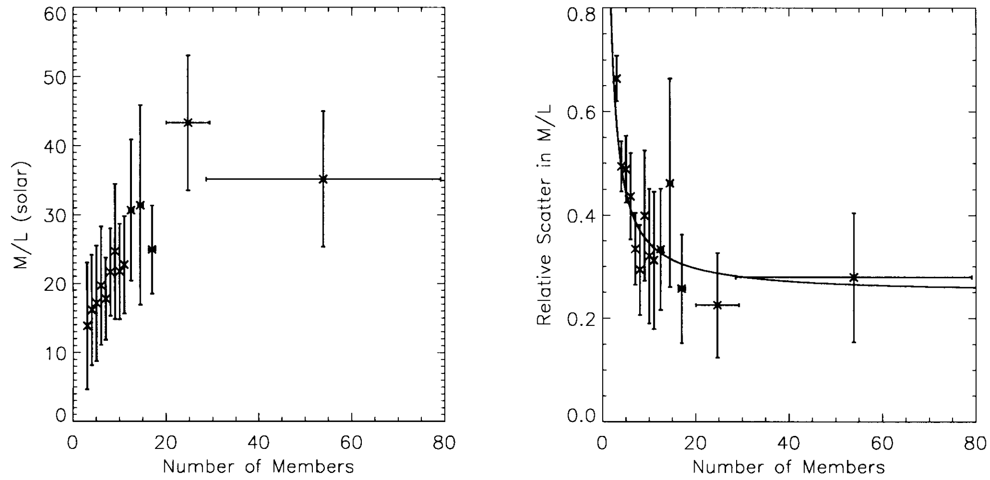

(a) Mass-to-light ratio of Groups

(b) Scatter on M/L

Figure 3.2 Dependence of mass-to-light ratio and associated scatter on the number of group members. (a) shows the mass-to-light ratio of groups as a function of the group size. Groups with more observed members (which generally correspond to the more massive groups) have larger mass-to-light ratios than groups with few members. While the absolute error remains approximately constant, the relative error decreases with group size. (b) shows the difference between the 68^{th} and 32^{nd} percentile values, scaled by the median, of the mass-to-light ratio of groups with N members as a function of N. The bins are chosen such that each bin contains at least 20 groups, where groups with N members are all assigned to the same bin. The scatter is larger for smaller group sizes due to the high proportion of interlopers in the group. The curve shows a least-squares fit to a function of the form (3.3).

the errors in mass estimates in §5.4.1. In order to prevent errors in the estimated masses of groups significantly influencing the flow, for groups with fewer than 15 members whose masses exceed

$$M_{\mathrm{max}}(L_{\mathrm{group}}) = \langle M/L\rangle_{+1\sigma} L_{\mathrm{group}} \tag{3.4}$$

(where L_{group} is the luminosity of the group, and $< M/L >_{+1\sigma}$ is the mass-to-light ratio 1σ above the median ratio for all groups with at least 5 members with LS redshifts below 12,000 km s^{-1}) we replace the group mass with $M_{\mathrm{max}}(L_{\mathrm{group}})$. We will return to the discussion of the relative influence of small and large groups on the velocity of the LG in Chapter 6, but presently move on to discuss the construction of the flow-field from this modified catalog of groups.

3.2 Modeling the Flow-field

In §1.3, we demonstrated that the expected deviation from the Hubble flow at any point in space can be estimated given knowledge of the (three-dimensional) spatial locations and masses of the objects driving the flow. For the reconstruction presented here, we assume that the flow is driven by the presence of dark matter, and that the overdensity of dark matter at any location is simply proportional to the overdensity inferred from the dynamical mass estimate of the galaxy clusters and groups identified in 2MRS. While we have obtained estimates of the masses of the groups, the groups themselves are expected to be moving with non-zero peculiar velocities relative to the Hubble expansion. Six phase-space coordinates are required to uniquely identify a galaxy group's location and velocity; we only have three measurements available from 2MRS, namely the right ascension and declination (giving the angular position on the sky), and the redshift, which is a linear combination of the distance (from Hubble's law) and line-of-sight component of the peculiar velocity (relative to the LG).

In order to model the flow-field accurately, we need to be able to separate the component of the redshift due to the Hubble expansion from the contribution due to the peculiar velocities of the LG and the group in question. We discuss the technique we apply for this purpose at the end of this section. However, first we digress to a brief discussion of coordinate systems (§3.2.1), reference frames (§3.2.2) and models of galaxy clusters (§3.2.3). We then describe the procedure used to estimate peculiar velocities at any point in real-space (§3.2.4) and discuss the effect of selection bias in §3.2.5, before returning to the discussion of distance estimates (§3.2.6).

3.2.1 Supergalactic Coordinates

In Chapter 2, we used the familiar equatorial and galactic coordinate systems. While the former makes sense from an observational point of view, the latter is advantageous since the region masked by the galactic plane has a significantly reduced number of measured galaxy redshifts. It is useful to understand the proximity of structures to the plane of the galaxy so we might gain insight into the likelihood of missing significant groups due to our phase of rotation about the galactic center at this epoch.

In this chapter, we introduce yet another coordinate system which has particular relevance for modeling the flows around nearby galaxy groups. De Vaucouleurs (1953) first described the presence of an overdensity of galaxies in the local Universe as a *Super-galaxy*, or *Local Supercluster of galaxies* (De Vaucouleurs, 1958). He noticed that the galaxies appeared to be approximately located in a plane, and defined the Supergalactic Plane, which has since been precisely defined such that the north pole ($SGB = 90°$) lies at galactic coordinates ($l = 47.37°$, $b = +6.32°$) and the zero point ($SGB = 0°$, $SGL = 0°$) lies at at the intersection of the supergalactic plane with the galactic plane ($l = 137.37°$, b $= 0°$). In addition to Perseus-Pisces, the Virgo Cluster and Centaurus, the largest more distant groups (e.g., the Coma Cluster and the Shapley concentration) also lie very close to this plane. By proceeding with this coordinate system, we can characterize the most significant flows by examining the slice through the supergalactic plane.

3.2.2 Reference Frames

While the physics cannot depend on the choice of reference frame in which a calculation is performed, there are certain advantages to performing our analysis in a given reference frame. There are two reference frames commonly used in the literature:

1. The LG frame — a comoving frame in which an observer measures the peculiar velocity of the LG to be zero.
2. The CMB frame — a comoving frame in which an observer has no net velocity with respect to the Cosmic Microwave Background radiation.

While we have chosen to use the LS frame (§3.1.2) in favor of the LG frame, the advantages are similar. After correcting for the motion of the Sun around the galactic center, in addition to the motion of the Milky Way relative to the barycenter of the LG (and in the case of the LS frame, the motion of the LG relative to the galaxies inside 7 Mpc), the redshift of a nearby group of galaxies is approximately proportional to its distance. The CMB frame, on the other hand, is useful since at sufficiently large scales, we expect this to correspond to the rest frame of the Hubble expansion.

In this work, we will calculate the peculiar velocities in a self-consistent manner. There exists a reference frame in which the motion of the LG can be explained using gravitational instability theory applied to all groups of galaxies inside the sampled volume. In this reference frame, we expect the LG peculiar velocity to be non-zero, and the motions of groups near the LG to have similar peculiar velocities to the LG itself. Far from the LG, we expect the averaged motion of groups to be at rest with respect to this reference frame. For cosmological arguments (e.g., Watkins et al., 2009), if the volume is large enough and the LG motion computed accurately, this frame would be equivalent to the CMB frame, however sufficient evidence has been presented to warrant this assumption unjustified (see §1.1). We proceed, therefore, to construct the peculiar velocities relative to this reference frame, which we will refer to as the "Local Rest" (LR) frame. Discussion of the difference between the LR frame and the CMB frame is postponed until §6.3.[2]

3.2.3 Modeling Galaxy Clusters

Numerous models for galaxy cluster density profiles have been used in the literature. NFW profiles (Navarro et al., 1997) have been shown to provide a good description of clusters in N–body simulations, however there remains skepticism as to whether they offer improvement observationally over isothermal models (e.g., Shu et al., 2008). The most commonly used density profiles to model infall far from the cluster core follow $\rho(r) \propto r^{-\gamma}$, where r is the distance from the cluster, with the proposed $\gamma = 2$ (e.g., Peebles, 1976b), although often γ is chosen to best fit the observed data. The assumption of spherical symmetry may not be well justified (e.g., Schipper & King, 1978). However, we choose to retain the simplicity of the spherically-symmetric model, and utilize the profile defined below:

$$\begin{aligned} \rho(r) &= \rho_0 & r &< r_{100} \\ \rho(r) &= \rho_0 \left(\frac{r_{100}}{r}\right)^2 & r_{100} \leq r &< r_{10} \\ \rho(r) &= 0 & r &\geq r_{10} \end{aligned} \tag{3.5a}$$

where ρ_0 is chosen such that the total mass of the cluster is equal to M^{eff} (we will define this shortly in §3.2.5, Eq. 3.18, below) and r_{100} (r_{10}) is defined such that the average interior overdensity would be 100 (10) if the entire mass was placed at the center of the group. The choice of the uniformly-dense spherical interior was made to avoid encountering artificially high velocities. Close to cluster cores, the linear approximation breaks down and cannot be used to predict peculiar velocities over this scale. Therefore the actual value of the inner cut-off generally does not matter so long as it is sufficiently small that it is not much larger than the radius of the core, yet large enough to avoid non-linear scales. When considering the peculiar velocities of observed galaxies near cluster cores, we will need a different approach, which we discuss in Chapter 5.

3.2.4 Estimating Peculiar Velocities

To estimate the peculiar velocity, given the locations of the groups (see §3.2.6 below), we apply the framework of §1.3 as described below. If the size of the sampled volume is given by $(v_H)_{\mathrm{lim}}$, to calculate the peculiar velocity induced at spatial position $\mathbf{r}$, we

---

[2] While each reference frame has its advantages for performing calculations, the LS, LG, LR (and to an extent, the CMB) frames all stand to change over time as the accuracy of measurements increases. The heliocentric reference frame is known to a fraction of a km s^{-1}, and therefore it is often argued that reported results should be referenced with respect to the heliocentric frame so they stand the test of time.

consider a sphere centered at $\mathbf{r}$ of radius $S(\mathbf{r})$, where

$$S(\mathbf{r}) = \begin{cases} (v_H)_{\rm lim} - |\mathbf{r}|H_0 & \text{if } (v_H)_{\rm lim} \geq |\mathbf{r}|H_0 \\ 0 & \text{otherwise} \end{cases} \tag{3.6}$$

We choose $(v_H)_{\rm lim} = 12{,}000$ km s^{-1} for reasons discussed in §3.2.5 below.

For all identified groups j whose center lies within this sphere, we sum their contributions toward the peculiar velocity at $\mathbf{r}$, given by Eq. (1.8),

$$\mathbf{v}(\mathbf{r}) = \frac{H_0\beta}{4\pi\bar{\rho}_g}\sum_j{}' \int \mathrm{d}^3\mathbf{r}' \frac{\mathbf{r}' - \mathbf{r}}{|\mathbf{r}' - \mathbf{r}|^3}\rho_j(|\mathbf{r}' - \mathbf{r}_j|) \tag{3.7}$$

where $\bar{\rho}_g$ is the average density in groups and $\rho_j(r)$ is given by Eq. (3.5) for each group. The sum is restricted to groups with $|\mathbf{r_j} - \mathbf{r}| \leq S_i$.

Defining

$$\tilde{\mathbf{g}}_j(\mathbf{r}) = \int \mathrm{d}^3\mathbf{r}' \frac{\mathbf{r}' - \mathbf{r}}{|\mathbf{r}' - \mathbf{r}|^3}\rho_j(|\mathbf{r}' - \mathbf{r}_j|) \tag{3.8}$$

we take the divergence of Eq. (3.8), and noting that

$$\nabla.\left(\frac{\mathbf{x}}{|\mathbf{x}|^3}\right) = 4\pi\delta_D(\mathbf{x}) \tag{3.9}$$

where $\delta_D(\mathbf{x})$ is the Dirac delta function, we obtain

$$\nabla.\tilde{\mathbf{g}}_j(\mathbf{r}) = 4\pi \int \mathrm{d}^3\mathbf{r}'\delta_D(\mathbf{r}' - \mathbf{r})\rho_j(|\mathbf{r}' - \mathbf{r}_j|) = 4\pi\rho_j(|\mathbf{r} - \mathbf{r}_j|) \tag{3.10}$$

Defining $\mathbf{s}_j = \mathbf{r}_j - \mathbf{r}$ and $s_j = |\mathbf{s}_j|$, since $\rho_j(s_j)$ is spherically symmetric about $s_j = 0$, we can integrate over a spherical volume centered at $\mathbf{r}_j$, and apply the divergence theorem, to find

$$\tilde{\mathbf{g}}_j(\mathbf{r}) = \frac{\mathbf{s_j}}{s_j^3}\int_0^{s_j} 4\pi\rho_j(s')s'^2\mathrm{d}s' \tag{3.11}$$

Equating with Eq. (3.8) and substituting back into Eq. (3.7), we obtain

$$\mathbf{v}(\mathbf{r}) = \frac{H_0\beta}{4\pi\bar{\rho}_g}\sum_j{}' \left(\frac{\mathbf{r}_j - \mathbf{r}}{|\mathbf{r}_j - \mathbf{r}|^3}\right)\int_0^{|\mathbf{r}-\mathbf{r}_j|} 4\pi\rho_j(s')s'^2\mathrm{d}s' \tag{3.12}$$

which we can use to compute the peculiar velocity.

To reduce any adverse effects from peculiar velocities calculated in the non-linear regime, we choose to cap the magnitude of computed peculiar velocities at 2000 km s^{-1}. Note that the computed velocity depends on the chosen value for β.

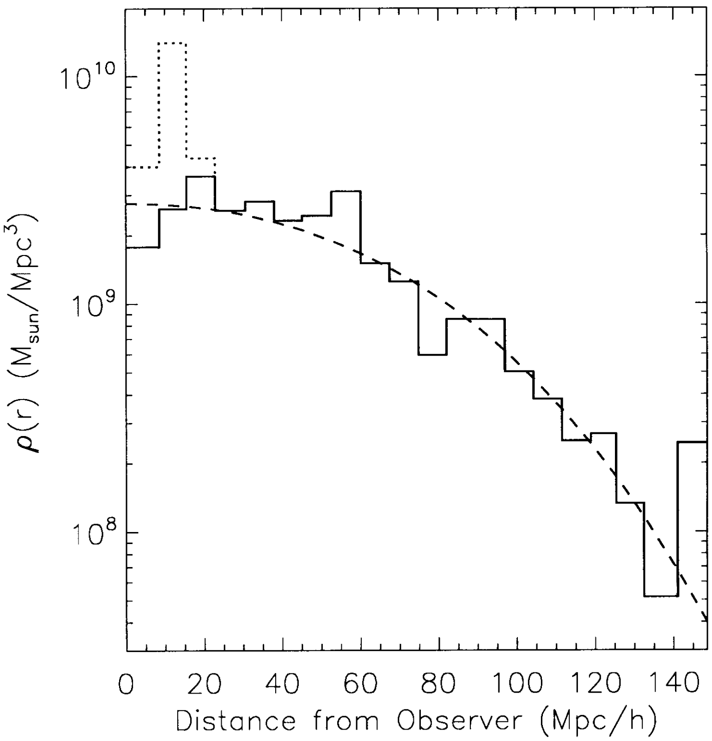

Figure 3.3 Observed mass density in groups. The graphs show the mass density as a function of distance from the Local Group. The dotted line involves all groups in the sample; the solid line is the result of first removing the Local Supercluster (see §3.2.5 for details). The dashed line shows a least-squares fit to the data (with the Local Supercluster removed) using an equation of the form (3.13).

3.2.5 Selection Bias

Due to the sampling-bias in a magnitude-limited survey, the observable mass-density decreases with distance from the observer. While the group-identification algorithm (§2.1) attempts to compensate for this by increasing the linking length at larger distances, the effect is only reduced. If uncorrected, computed peculiar velocities of groups other than the LG will be biased preferentially toward the observer. The effect will be most significant for those groups at a distance equal to approximately one third of the sample limit ($\sim$ 4000 km s^{-1}). To correct for this bias, we need to understand how the average density varies with distance. In Figure 3.3, we plot the mass density in groups, identified with 5 or more members, as a function of distance from the observer (indicated by the dotted line). Since the LG is located in the Local Supercluster (see §3.2.1 above), we are necessarily in an overdense region in the Universe. Any attempt to compute the background density using nearby masses must take care to account for this. We remove groups with estimated distances less than $20/h$ Mpc that lie within 20° of the supergalactic plane, and recompute the density as a function of distance (accounting for the reduced volume of the sample inside $20/h$ Mpc); the result is shown by the solid line in Figure 3.3.

We find that the density is well described by a function of the form

$$\rho_{\rm obs}(r) = \bar{\rho}_g \exp\left(\lambda\left[1 + \frac{r}{r_0} - e^{r/r_0}\right]\right) \tag{3.13}$$

which satisfies the properties that the $\mathrm{d}\rho/\mathrm{d}r \rightarrow 0$ for $r = 0$ and $r \rightarrow \infty$, and $\rho(r \rightarrow \infty) = 0$. We use a least-squares fit to obtain values for the parameters: $\rho_0 = 2.76 \times 10^9\ M_\odot\ \mathrm{Mpc}^{-3}$, $\lambda = 10.9$, $r_0 = 261$ Mpc, the curve for which is shown by the dashed line in Figure 3.3. We also compute the standard error of the mean on the differences between the observed density and the average density obtained from the fit; we obtain $\sigma_\rho = 1.1 \times 10^8$. We then define the radial selection function,

$$\phi(r) = \frac{\rho_{\rm obs}(r)}{\bar{\rho}_g} \tag{3.14}$$

The selection function $\phi(r)$ drops to 0.05 at a distance of $128/h$ Mpc; we therefore choose to limit further analysis to groups inside 12,000 km s^{-1} in order to prevent the bias correction introducing significant artefacts in the analysis.

With an understanding of how the observed mass density varies with distance from the observer, we can estimate effect of the biased sampling on the resulting peculiar velocities. Considering a spherically symmetric distribution of mass centered on the LG with a radial density profile described by Eq. (3.13), we calculate the expected peculiar velocity of a test particle as a function of the distance from the origin using the procedure described in §3.2.4 above. For the case $\beta = 0.19$, the result is shown in Figure 3.4. Note that the largest magnitude of the correction is comparable to the r.m.s. uncertainty in the modeled peculiar velocities (see §5.4.1).

To ensure that the computed peculiar velocities are not systematically biased toward the observer, it is important to correct for this bias. The appropriate correction is equivalent to introducing the unobserved mass back into the sampled volume, such that the density remains invariant with distance from the observer. It is unclear, however, as to how the unobserved mass should be distributed. There are two extreme cases:

1. **Isotropic Distribution.**
   The unobserved mass is assumed to be distributed isotropically; this is equivalent to adding a velocity along the line-of-sight direction (away from the observer) to the peculiar velocity of a test particle estimated from the observed mass distribution. The magnitude of this velocity correction is given by

$$v_{\rm bias}(\mathbf{r}) = \frac{H_0\beta}{4\pi\bar{\rho}_g}\int_0^{S(r)} r'^2\mathrm{d}r' \int_0^{\pi} 2\pi\sin\theta\mathrm{d}\theta \frac{\rho_{\rm obs}(|\mathbf{r}+\mathbf{r}'|)\cos\theta}{r'^2} \tag{3.15}$$

   where $S(r)$ is defined by Eq. (3.6), such that the integral is performed over a sphere centered at $\mathbf{r}$. The result is shown in Figure 3.4.

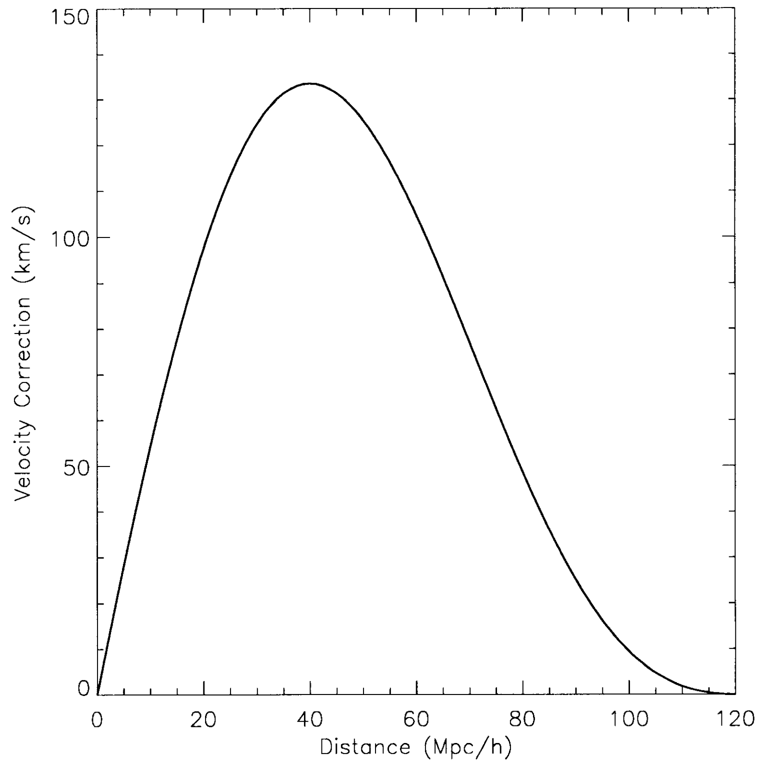

Figure 3.4 Velocity bias from radial selection function. The graph shows the estimated peculiar velocity of a test particle as a function of the distance from the observer for a spherically-symmetric mass distribution defined by Eq. (3.13) with $\beta = 0.19$. The velocity is directed along the line-of-sight toward the observer. It drops to zero at the edge of the sample since the volume used to estimate the peculiar velocity decreases. It is zero at the origin since the mass distribution is spherically symmetric about the observer.

2. **Group Distribution.**
   The distribution of the unobserved mass is assumed to follow the distribution of the observed mass. This is equivalent to modifying the mass of the observed groups according to the selection function (Eq. 3.14), such that

$$\tilde{M}_i^{\text{eff}} = \frac{M_i}{\phi(r_i)} \tag{3.16}$$

   where this effective mass then characterizes the density profile in §3.2.3.

In reality, the distribution most representative of the real Universe is likely to lie somewhere between these two extremes. Assuming that a fraction f_I of the unobserved mass is distributed isotropically, and the remaining fraction $(1 - f_I)$ is correlated with the observed groups, the resulting peculiar velocity at location $\mathbf{r}$ can be estimated using

$$\mathbf{v}(\mathbf{r}) = \frac{H_0 \beta}{4\pi \bar{\rho}_g} \sum_j{}' \left(\frac{\mathbf{r}_j - \mathbf{r}}{|\mathbf{r}_j - \mathbf{r}|^3} \right) \int_0^{|\mathbf{r}-\mathbf{r}_j|} 4\pi \rho_j(s') s'^2 \mathrm{d}s' + f_I v_{\text{bias}}(\mathbf{r}) \hat{\mathbf{r}} \tag{3.17}$$

where we define the effective group mass

$$M_i^{\text{eff}}(f_I) = \frac{M_i}{1 - (1 - f_I)[1 - \phi(r_i)]} \tag{3.18}$$

and, for each group j, the normalization of the density profile ρ_0 (Eq. 3.5) is defined by requiring

$$M_i^{\text{eff}}(f_I) \equiv \int_0^{\infty} 4\pi \rho_j(s') s'^2 \mathrm{d}s' \tag{3.19}$$

In the remainder of this chapter, as well as Chapters 5 and 6, we will consider the resulting flow-field for both of the extreme cases: $f_I = 0$, which we will refer to as *Coherent Mass Correction* (CMC), and $f_I = 1$, which we will refer to as *Incoherent Mass Correction* (IMC).

3.2.6 Distances and Peculiar Velocities

The measured redshift[3] of a galaxy (or group of galaxies), z, can be broken down into three components:

$$cz = v_H + \mathbf{v}_{\text{pec}} \cdot \hat{\mathbf{r}} - \mathbf{u}_{\text{pec}} \cdot \hat{\mathbf{r}} \tag{3.20}$$

v_H is the velocity due to the Hubble expansion ($v_H = H_0 D$, where D is the distance to the object), $\mathbf{v}_{\text{pec}}$ is the peculiar velocity of the galaxy/group with respect to some comoving reference frame and $\mathbf{u}_{\text{pec}}$ is the velocity of the observer with respect to the same reference frame. $\hat{\mathbf{r}}$ is the unit vector in the direction of the observed galaxy/group, and c is the speed of light.

---

[3] In order to avoid confusion, we will use cz to refer to the measured redshift (generally reported in km s^{-1}), and the letters u and v (with various subscripts) to refer to components of the velocity that have been computed.

While we only measure z, it is possible to use our knowledge of the locations of other galaxies/groups, in conjunction with some assumptions about the physics (§1.3) in order to estimate the three separate contributions to the redshift. Since the flow-field that we are computing will predict the peculiar velocities of the groups, *if* we have an initial estimate for the distance, we can use an iterative approach to construct a flow-field model where the distances and predicted velocities are self-consistent. A similar approach has previously been applied by Yahil et al. (1991), Strauss & Davis (1991) and Branchini et al. (1999) using galaxies as mass tracers, but here we present a modified method that accounts for the differences between the application to galaxies and to groups of galaxies.

Initially, we assume the distance to the group is given by the group's redshift in the LS frame, unless a redshift-independent distance estimate is available (see §3.1.3 above). The following sequence of steps are then executed iteratively:

1. We compute the projected masses of the groups, given the distance estimates, using equation (3.2).

2. Analagous to §3.2.4 above, for each group i, we consider a sphere of radius S_i, centered on the group, where

   $$S_i = \begin{cases} (v_H)_{\rm lim} - (v_H)_i & \text{if } (v_H)_i \le (v_H)_{\rm lim} \\ 0 & \text{otherwise} \end{cases} \tag{3.21}$$

   and $(v_H)_{\rm lim}$ is the chosen sample limit.

   For all identified groups j whose center lies within this sphere, we sum their contributions toward the peculiar velocity of group i. Since the contribution from group i is zero due to the choice of the density profile (§3.2.3), Eq. (3.17) becomes

   $$\mathbf{v}_i = \frac{H_0\beta}{4\pi\bar{\rho}_g} \sum_j{}' (\mathbf{r}_j - \mathbf{r}_i) \int_0^{|\mathbf{r}_j - \mathbf{r}_i|} 4\pi\rho_j(s')s'^2 \mathrm{d}s' + f_I v_{\rm Bias}(\mathbf{r})\hat{\mathbf{r}}_i \tag{3.22}$$

   The sum is restricted to the values where $j \neq i$ and $|\mathbf{r_j} - \mathbf{r_i}| \le S_i$.

3. For groups without a redshift-independent distance estimate, we compute a revised estimate for v_H,

   $$(v'_H)_i = (v_H)_i - \alpha[(\mathbf{v}_{\rm pec})_i - \mathbf{u}_{\rm pec}] \cdot \hat{\mathbf{r}}_i \tag{3.23}$$

   where α is a measure of the step size and a prime denotes the subsequent iteration. We choose to set $\alpha = 0.5$, and also limit the maximum change in the Hubble distance (v_H) to 100 km s^{-1} or 50% of the distance from the origin to the group in question (whichever is smaller) in one iteration to dampen any oscillations as the values converge.

4. Using the new value of $(v_H)_i$, we return to step 1 and iterate.

The estimates of v_H converge rapidly, generally requiring fewer than 10 iterations.[4] The group masses and locations that define the self-consistent density-field are presented in Tables B.1 (CMC) and B.2 (IMC) in Appendix B.

3.3 Mapping the Velocity-field

In the previous sections, we discussed the method for refining the locations of groups of galaxies that not only drive the flow, but also respond to it. In this section, we present a model that predicts the velocity of a test mass placed at any location in space, using the framework of §1.3. Our motivations for choosing a particular value of β are discussed in Chapter 5, but for the purposes of this chapter, the chosen values may be considered arbitrary. For the CMC case, we will present the results for $\beta = 0.17$; for the IMC case, we will present the results for $\beta = 0.19$. Since, by construction, the LG peculiar velocity is in the direction predicted by the inhomogeneities in the local density field, the computed peculiar velocities are referenced with repect to the LR frame, by definition (see §3.2.2).

We construct a grid of uniformly-spaced points, choosing to align the grid axes with the cartesian components of supergalactic coordinates, referred to hereafter as (SGX, SGY, SGZ). At each point, we compute the peculiar velocity of a test mass induced by inhomogeneities in the local density field through Eq. (3.12). Finally, we convolve the resulting velocities with a three-dimensional Gaussian with FWHM = 500 km s^{-1} to remove any sharp edge-effects and reduce the effect of non-linearities in the vicinity of cluster cores.

Figures 3.5 and 3.6 show a slice of the velocity-field through the supergalactic plane, for the coherent and incoherent mass corrections, respectively. Figures 3.7 and 3.8 show parallel slices at $SGZ = \pm 3000, \pm 6000$ km s^{-1}. The distribution of the cartesian components of predicted peculiar velocities for grid-points inside 8000 km s^{-1} is shown in Figure 3.9. Note that velocities computed assuming the incoherent mass correction have a narrower distribution than those computed assuming the coherent mass correction. This is expected since, at regions far from the origin, the number density of groups decreases. Since the grid points are distributed uniformly in the volume, there are many sampled locations far from groups where the predicted peculiar velocities will be small, since the surrounding mass is distributed fairly isotropically and does not give rise to a net velocity. The velocity distribution of groups inside 8000 km s^{-1} is shown in Figure 3.10. The r.m.s. of the CMC and

---

[4] It was noted by Kaiser (1987) that when computing the motion of a test mass using redshifts as distance estimators, a distortion will be introduced into the estimated peculiar velocity. The self-consistent nature of this model will remove the uncertainty *if* the model is correct. If the sample is redshift-limited, instead of distance-limited and the LG has a motion relative to nearby groups that cannot be explained by their presence, then we will introduce a bias into the velocity of the LG in the direction of its true motion. Since locally the Universe is relatively quiet (i.e. Hubble's law works well), distortions will only arise from large scales, where the relative error on a redshift-estimated distance is small, and the bias is expected to account for less than 10% of the predicted motion of the LG in the worst case scenario (i.e. we fail to identify any distant groups correctly). Since this is less than the errors associated with uncertainties in the model (see §6.2.2), it can be neglected.

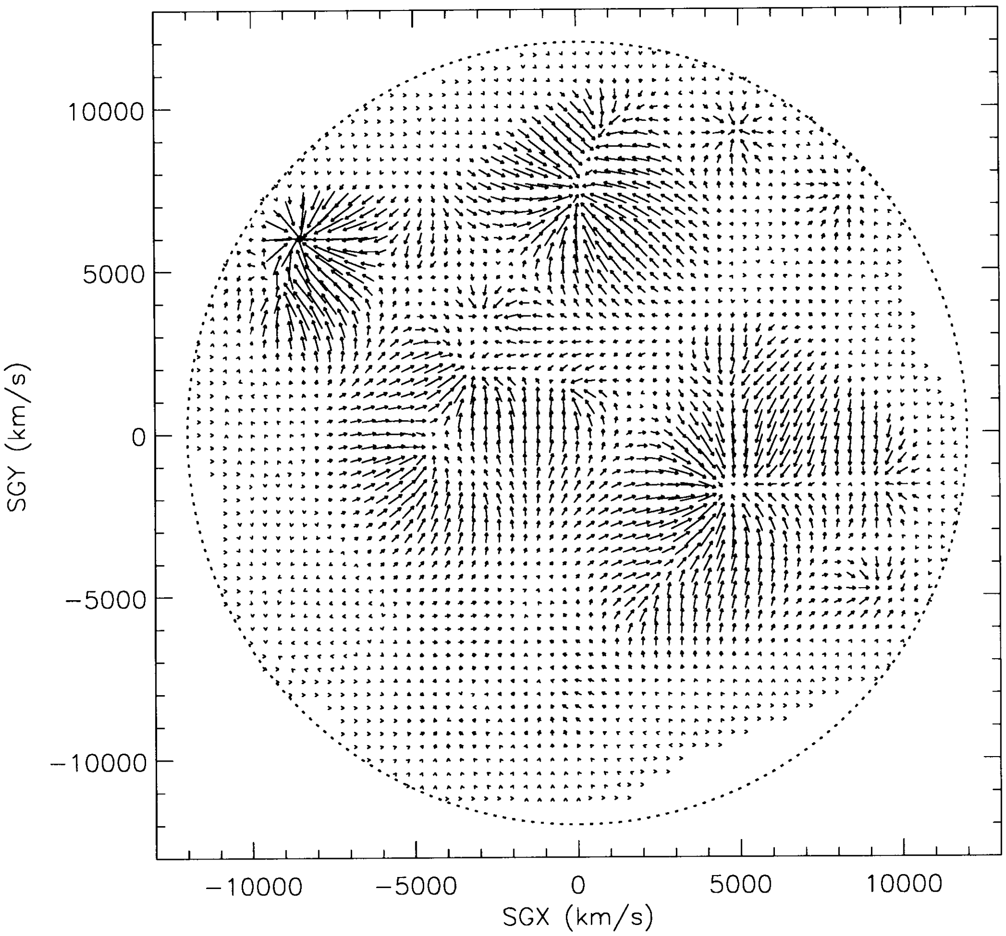

Figure 3.5 Real-space velocity-field in supergalactic plane due to groups of galaxies in 2MRS (CMC). This figure shows the predicted velocity for a test mass placed at the indicated spatial location, assuming the coherent mass correction. The axes are in supergalactic coordinates, and the figure shows a slice through the supergalactic plane. The length of the arrows represent the magnitude of the component of the velocity in the supergalactic x–y plane. The known structures are recognizable – the Virgo Cluster at $(SGX,\ SGY) \sim$ (-250, 1250), Hydra-Centaurus at $(SGX,\ SGY) \sim$ (-3500, 2000), Perseus-Pisces at $(SGX,\ SGY) \sim$ (4500, -2000), the Norma Cluster at $(SGX,\ SGY) \sim$ (-4000, -500), and the Coma cluster at $(SGX,\ SGY) \sim$ (0, 7500). The region of high infall at $(SGX,\ SGY) \sim$ (-8000, 6000) is the front of the Shapley concentration, which has been separated from the main group by the group-identification algorithm. The peculiar velocities in this region are amplified by the corrections to the selection bias introduced so close to the edge of the sample. The lack of points near the edge at some areas of the map are due to insufficient groups inside the sphere defined by Eq. (3.6) to be able to predict peculiar velocities.

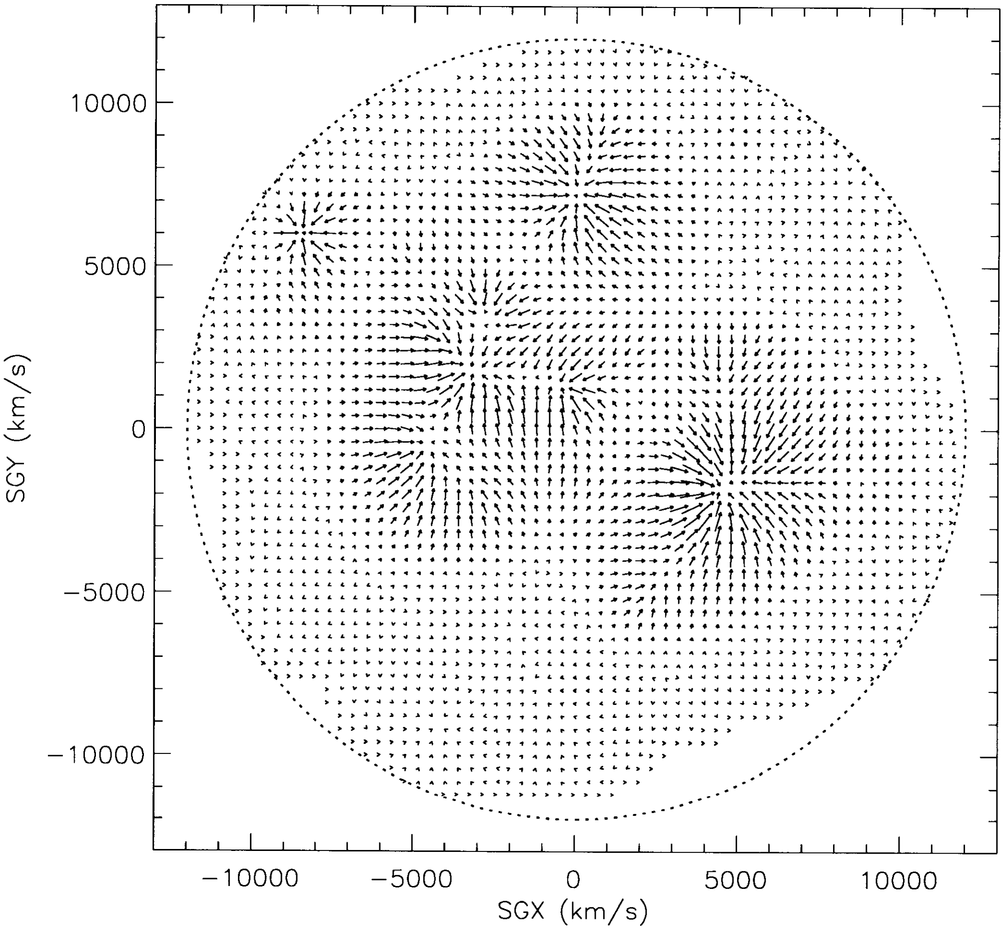

Figure 3.6 Real-space velocity-field in supergalactic plane due to groups of galaxies in 2MRS (IMC). This figure shows the predicted velocity for a test mass placed at the indicated spatial location, assuming the incoherent mass correction. The details of the figure are as Figure 3.5. The same structures are recognizable, although the amplitudes of the velocities near the distant clusters are lower than observed in Figure 3.5

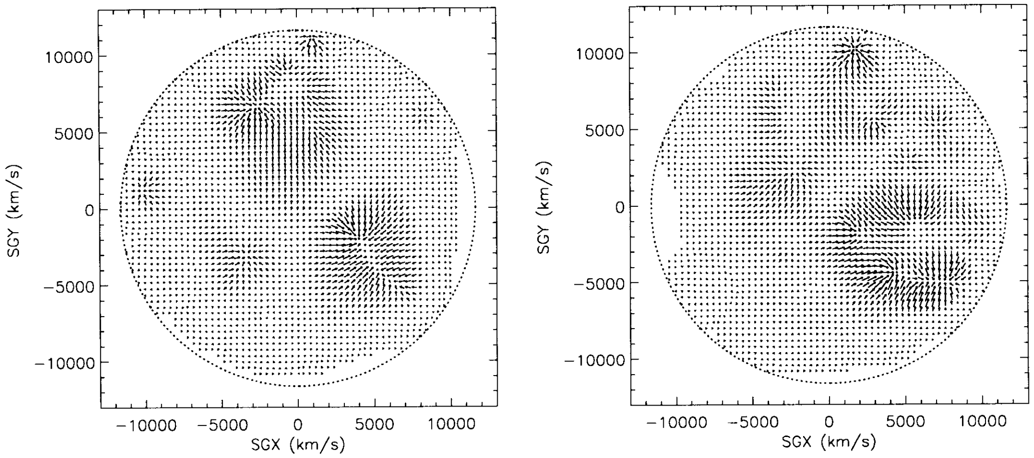

(a) SGZ = +3000 km s^{-1} (b) SGZ = -3000 km s^{-1}

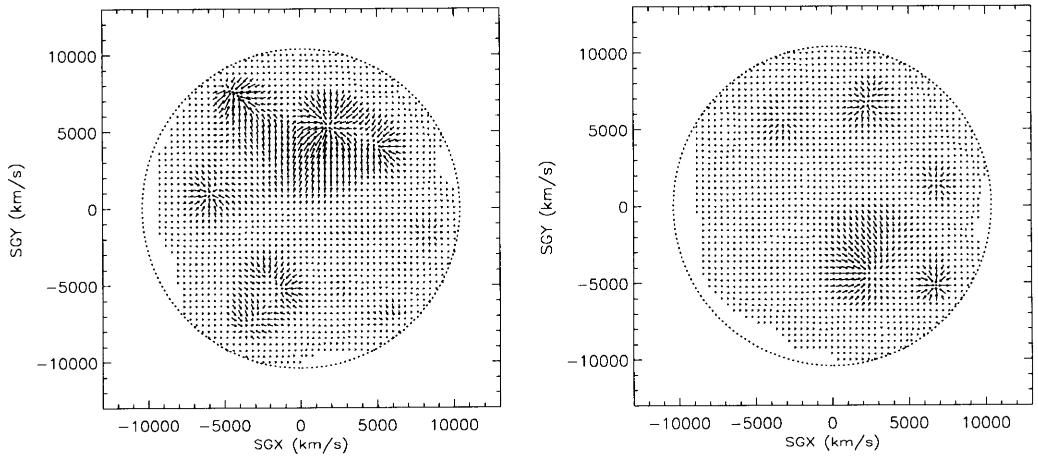

(c) SGZ = +6000 km s^{-1} (d) SGZ = -6000 km s^{-1}

Figure 3.7 Real-space velocity-field due to groups of galaxies in 2MRS above and below the supergalactic plane (CMC). The figures show slices at constant SGZ, parallel to the supergalactic plane. The length of the arrows represent the magnitude of the component of the velocity in the supergalactic x–y plane, assuming the coherent mass correction. The region at SGZ = 3000 km s^{-1} is largely underdense. The Local Void extends above the supergalactic plane, connecting to Tully's void. Velocities in this region are directed prominently in the SGZ–direction and these components are not shown on the map. At SGZ = -3000 km s^{-1}, we observe the downward extension of the Perseus-Pisces supercluster.

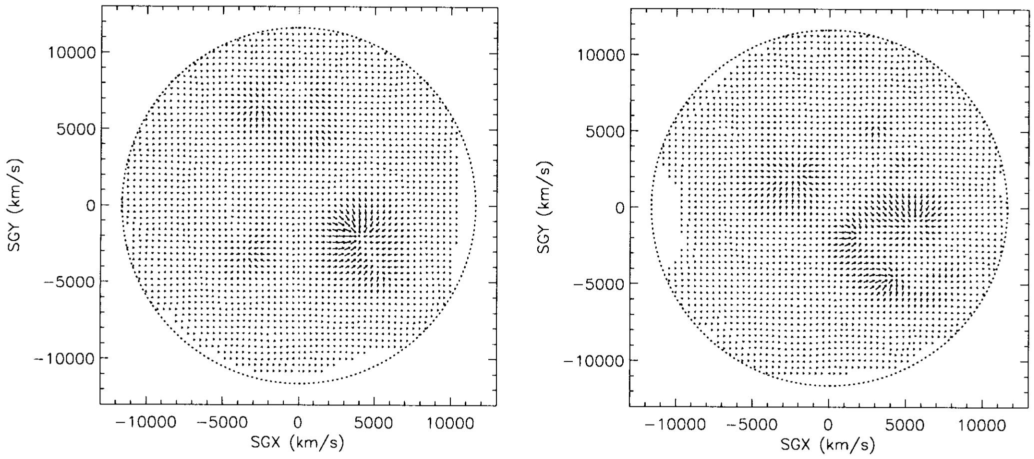

(a) SGZ = +3000 km s^{-1} (b) SGZ = -3000 km s^{-1}

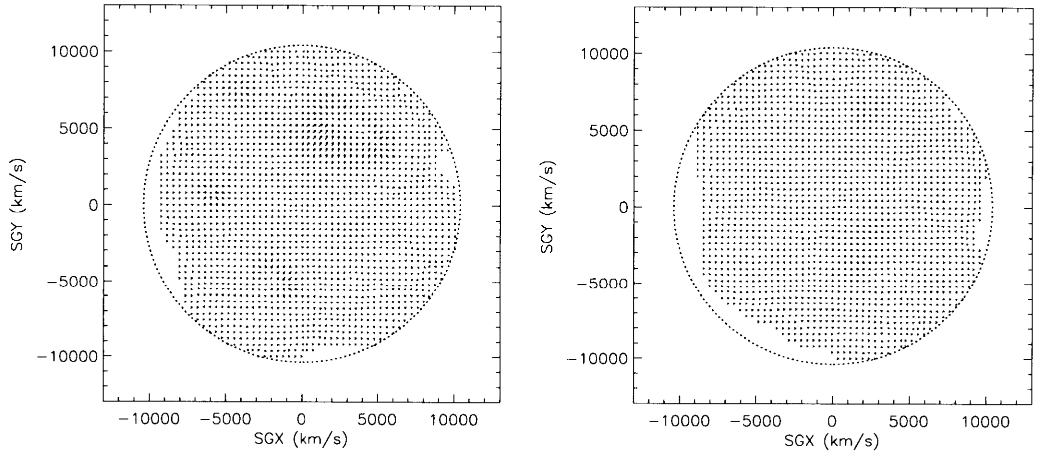

(c) SGZ = +6000 km s^{-1} (d) SGZ = -6000 km s^{-1}

Figure 3.8 Real-space velocity-field due to groups of galaxies in 2MRS above and below the supergalactic plane (IMC). The figures show slices at constant SGZ, parallel to the supergalactic plane. The length of the arrows represent the magnitude of the component of the velocity in the supergalactic x–y plane, assuming the incoherent mass correction. The velocity-fields are considerably quieter than the CMC case since the incoherent mass distribution results in smaller peculiar velocities. Extensions of the Perseus-Pisces region are observed in the slices at $SGZ = \pm 3000$ km s^{-1}.

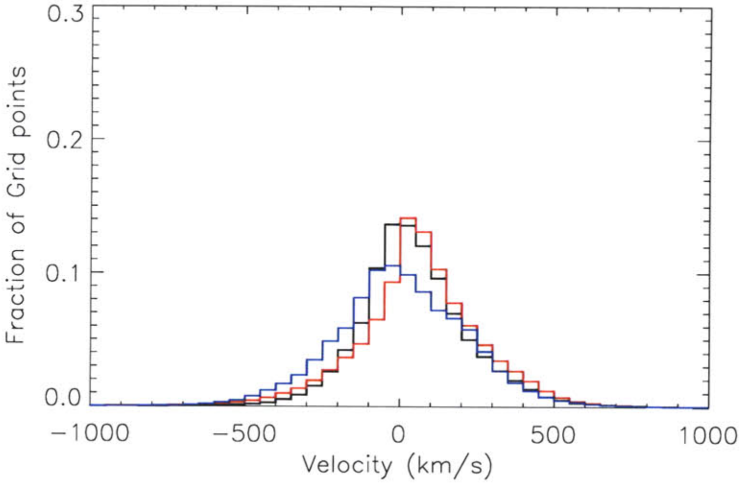

(a) Coherent Mass Correction

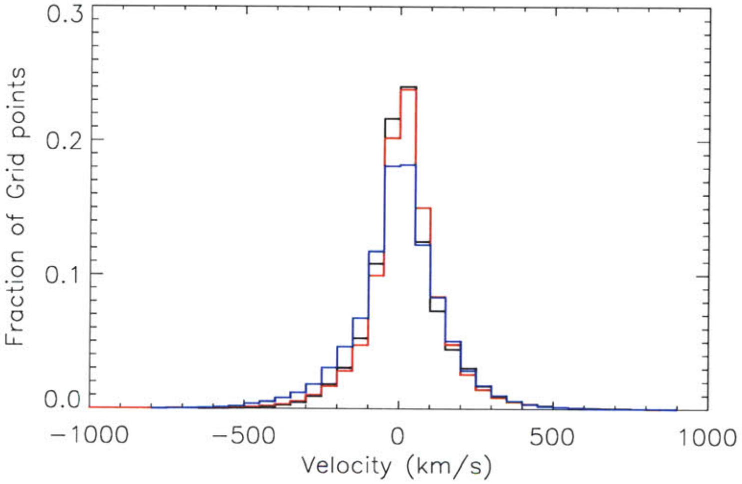

(b) Incoherent Mass Correction

Figure 3.9 Components of predicted peculiar velocities. The figures show the cartesian supergalactic components of the velocities predicted by the flow-field at 267,761 uniformly-spaced grid-points inside a sphere of radius $80/h$ Mpc centered on the LG in the LR frame. The black, red, and blue lines show the SGX, SGY, and SGZ–components, respectively. Panel (a) shows the CMC case for $\beta = 0.17$ and panel (b) shows the IMC case for $\beta = 0.19$. The IMC case peaks sharply for small velocities because the incoherent correction results in large regions of low predicted velocities beyond the distance where the selection function turns over.

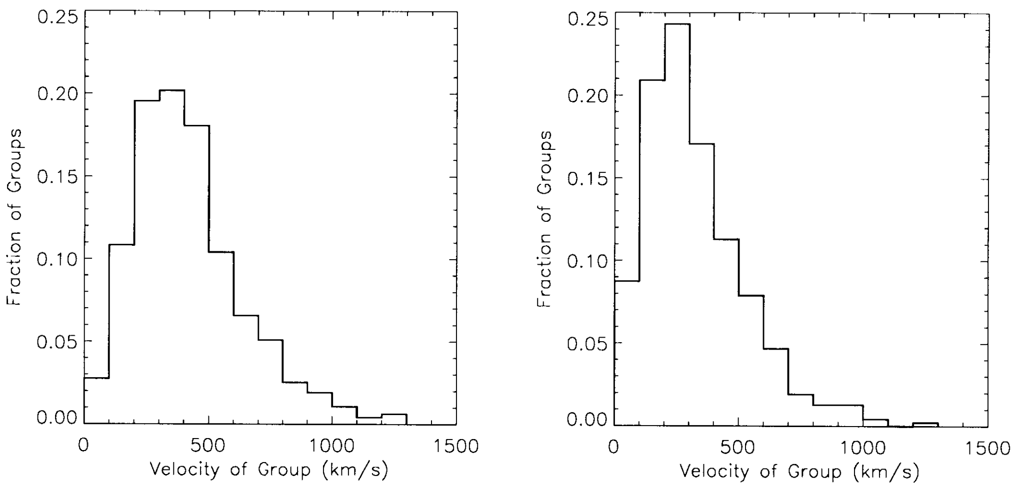

(a) Coherent Mass Correction

(b) Incoherent Mass Correction

Figure 3.10 Predicted group peculiar velocities. The figures show the distribution of magnitudes of the predicted peculiar velocities of groups inside $80/h$ Mpc. Panel (a) is computed assuming the coherent mass correction. The r.m.s. of the distribution is 475 km s^{-1}. Panel (b) is computed assuming the incoherent mass correction. The r.m.s. of the distribution is 382 km s^{-1}.

IMC cases are 475 km s^{-1} and 382 km s^{-1}, respectively. Here, the difference between the values is due to the reduced amplitude of the velocities for groups far from the origin for the IMC case. Note that in the CMC (IMC) case 15% (8%) of groups have predicted peculiar velocities larger than 627 km s^{-1}, which corresponds to the velocity of the LG in the CMB rest frame (e.g., Erdoğdu et al., 2006b). The magnitude of the observed motion of the LG in the CMB rest frame is large compared with the velocities expected to be generated inside a volume limited to 12,000 km s^{-1}, but remains plausible within 95% confidence.

We now examine the slice through the supergalactic plane (Figures 3.5 and 3.6). We note that the most massive structures are instantly identifiable. Nearby, we observe infall into the Virgo Cluster at (SGX, SGY) $\sim$ (-250, 1250). The Hydra-Centaurus supercluster appears at (SGX, SGY) $\sim$ (-3500, 2000) and Perseus-Pisces at (SGX, SGY) $\sim$ (4500, -2000), which appears slightly elongated in the positive x–direction. The Norma Cluster appears at (SGX, SGY) $\sim$ (-4000, -500), and the Coma cluster at (SGX, SGY) $\sim$ (0, 7500). The center of the Shapley concentration is slightly beyond the sample limit. However, the sample contains an overdensity of galaxies at redshifts between 10,000–12,000 km s^{-1}, which are likely falling into Shapley with peculiar velocities of $\sim$ 2000 km s^{-1}. Since only the galaxies at the lower-velocity end of Shapley are mapped by the sample, the group catalog contains a representation of the front of Shapley at a distance of $\sim 11,000$ km s^{-1}. We therefore observe an infall at (SGX, SGY) $\sim$ (-8000, 6000) toward the Shapley concentration, however the back infall is likely to be an artefact of the construction. While the structures are identifiable in both plots, the predicted flow-field differs far from the origin. The coherent mass correction results in larger amplitudes in the predicted velocities compared with the incoherent mass correction. Such a result is expected since an isotropic distribution of mass will not give rise to a net peculiar velocity.

Figures 3.7 and 3.8 show the velocity-field in slices above and below the supergalactic plane, at constant SGZ = [±3000, ±6000]. The cross-section at SGZ = +3000 km s^{-1} is largely underdense. The Local Void extends above the supergalactic plane, connecting to the void identified by Tully (1988). The infall at (SGX, SGY) $\sim$ (5000,-4000) is due to the extended nature of the Perseus-Pisces supercluster; the structure extends down to the SGZ = -3000 km s^{-1} cross-section. In Figure 3.7, we also observe infall toward the Coma cluster at large SGY in the SGZ = +3000 km s^{-1} plot, where the components in the SGX and SGY–directions are small due to their downward SGZ–motion. Little structure is visible in the SGZ = -6000 km s^{-1} cross-section, but large coherent structures, are again visible above the void in the SGZ = +6000 km s^{-1} plane, where we can identify the Hercules Supercluster (Abell 2199) at (SGX, SGY) $\sim$ (2000, 6000). These structures are not visible in Figure 3.8; groups at large distances from the LG are not sampled as well as the nearby groups, and therefore fewer large groups are identified at large distances. In the case of the coherent mass correction, we compensate for this effect by assuming the total expected mass is distributed in the same way as the groups, giving rise to the observable peculiar velocities.

While this examination of the velocity-field is insightful, only the prediction of the line-of-sight components of the peculiar velocities can be tested observationally.

We examine the line-of-sight components of the velocity-field in the LR frame, on successively deeper shells centered on the LG. In Figure 3.11, we show the prediction of the peculiar velocity at our location – a dipole in a direction part way between the Virgo Cluster and Hydra.[5] We will discuss the details of the predicted dipole in detail in Chapter 6, but present this figure here for completeness in the discussion that follows.

In Figures 3.13 and 3.12, we plot the line-of-sight components of the velocity field as a function of angular position on the sky at shells of incremental real-space depths to 10,000 km s^{-1}. At 1000 km s^{-1}, the Virgo Cluster ($SGL \sim 100°$, $SGB \sim 0°$) is the most prominant feature, with higher infall expected closer to the cluster core. The blue region part way between the anticenter of Virgo and Hydra-Centaurus indicates infall toward Hydra and Virgo on the opposite side of the sky. At 2000 km s^{-1}, we begin to notice slight infall into Hydra ($SGL \sim 140°$, $SGB \sim -40°$) and Centaurus ($SGL \sim 150°$, $SGB \sim -10°$) in addition to the Perseus-Pisces region ($SGL \sim 350°$, $SGB \sim -10°$). At 3000 km s^{-1}, we continue to predict infall into Centaurus. While distance estimates to Hydra and Centaurus (Mieske et al., 2005) suggest that Hydra lies 4 Mpc closer than Centaurus, but has an outward peculiar velocity $\sim$ 1000 km s^{-1} larger along the line of sight, our sample of distances did not contain sufficient galaxy distance estimates to allow us to assign a distance to the cluster through the uniformly-applied method. The initial distance estimates were based on the redshifts of the clusters, and the flow-field model did not predict these discussed dynamics. A small group in the foreground of Hydra, however, was identified separately, and appears to be an extension of the Hydra cluster. The attractors are sufficiently close to one another that the impact this has on the overall density-field is unlikely to be significant; however, the predictions of peculiar velocities in the foreground of Hydra may suffer. At 4000 km s^{-1}, therefore, we predict back infall toward Centaurus, as expected, although we still see a prediction for infall toward Hydra, which has been placed just outside this shell. Motion toward the Perseus-Pisces supercluster now dominates the center the map, and we begin to see infall predicted in the direction of the Norma Cluster at ($SGL \sim 190°$, $SGB \sim 5°$).

Up to this point, the models constructed using the CMC and IMC assumptions have provided very similar results. This is expected since the selection function remains relatively flat out to $\sim$ 6000 km s^{-1}. However, once we consider shells near or beyond this limit, the predicted infall is significantly smaller in the case of the incoherent mass distribution since we assume that all the mass correlated with the group location has been observed. The remaining mass (assumed to be distributed isotropically) does not induce any net peculiar velocities, other than removing the bias of infall toward the LG (see §3.2.5). The details that follow can be seen on both sets of figures, but are generally more obvious in Figure 3.12.

At 5000 km s^{-1}, we begin to see infall toward the Coma Cluster ($SGL \sim 90°$, $SGB \sim 10°$); Perseus-Pisces appears mostly green as we approach the core of the cluster. At 6000 km s^{-1}, infall into Coma dominates the map, and predict back infall into Perseus-Pisces as well as the Norma region. At 7000 km s^{-1}, we see further infall

---

[5] Note that the direction is closer to Hydra in the IMC case, and of a slightly smaller magnitude.

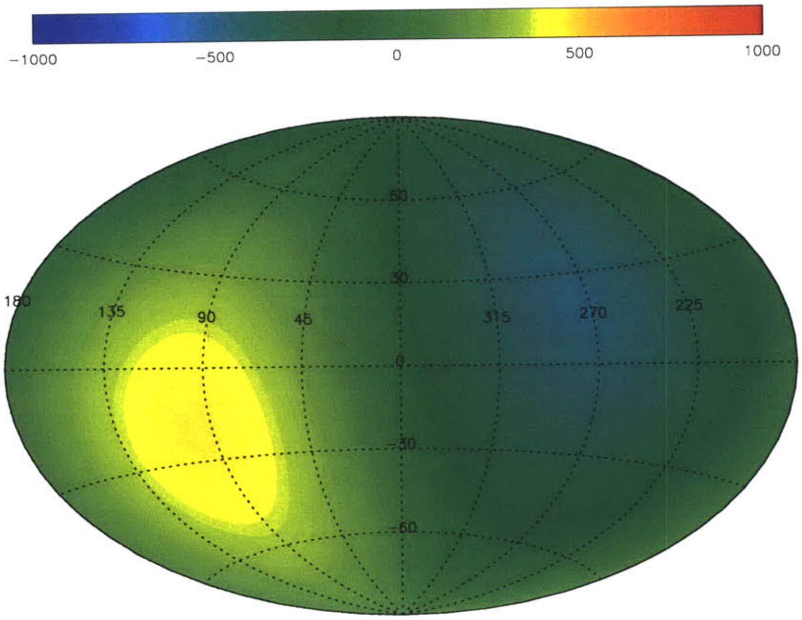

(a) Coherent Mass Correction

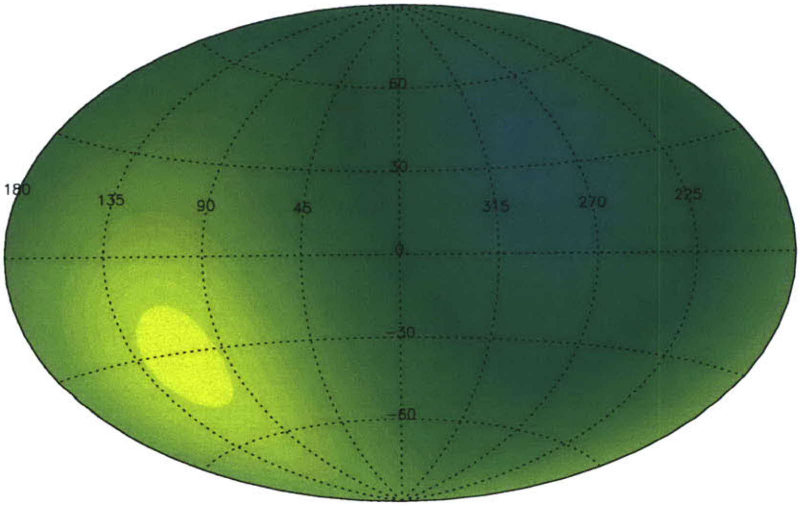

(b) Incoherent Mass Correction

Figure 3.11 Dipole term from LG motion in the LR frame. The motion is directed toward the orange/yellow-shaded region. The color indicates the component of the LG peculiar velocity as a function of angular position on the sky in supergalactic coordinates. The top (bottom) panels shows the results when computed assuming the coherent (incoherent) mass correction.

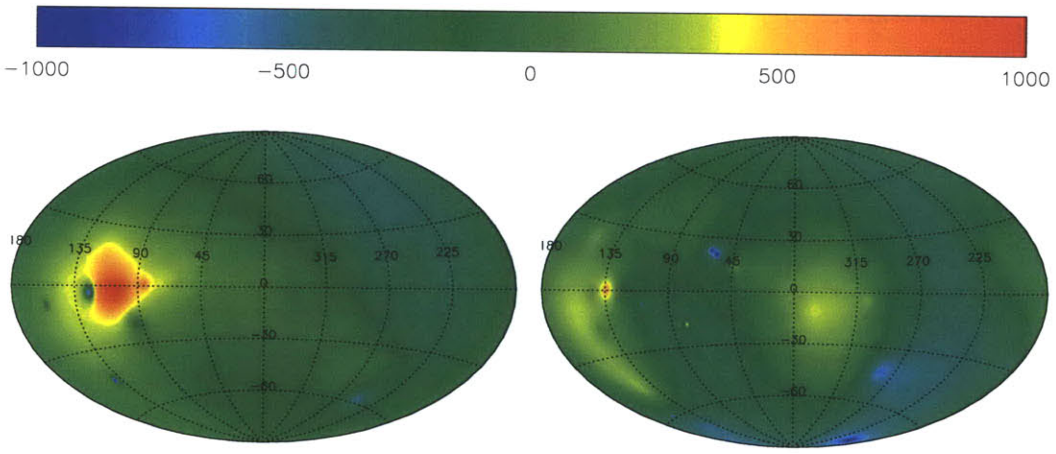

(a) $D = 1000$ km s^{-1}

(b) $D = 2000$ km s^{-1}

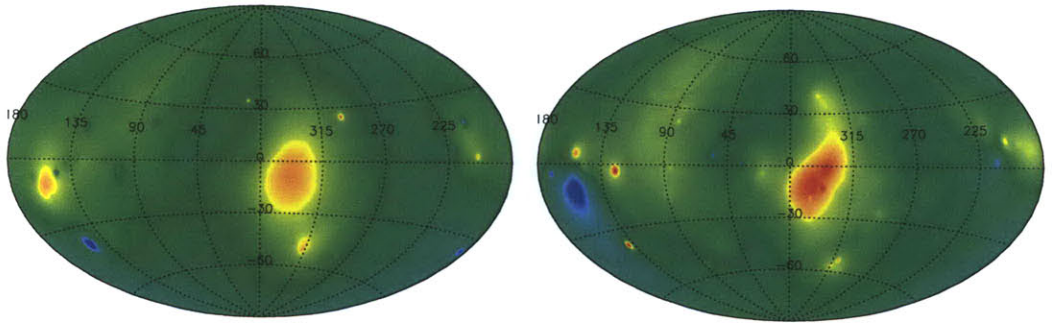

(c) $D = 3000$ km s^{-1}

(d) $D = 4000$ km s^{-1}

Figure 3.12 Line-of-sight components of peculiar velocities in LR frame (CMC). The figures show the peculiar velocities relative to the Hubble flow at specified distances (given in km s^{-1}) from the LG. The velocities have been computed from the flow-field model assuming the coherent mass correction. The maps are shown in supergalactic coordinates in an Aitoff projection. Yellow/red colors indicate a test mass at the specified location is expected to have a peculiar velocity (relative to the LR frame) in an outward direction, and blue colors indicate an inward velocity. Green areas indicate low net line-of-sight motions with respect to the LR frame. The units of the indicated color scale are km s^{-1}. See the text for a description of features in the plot.

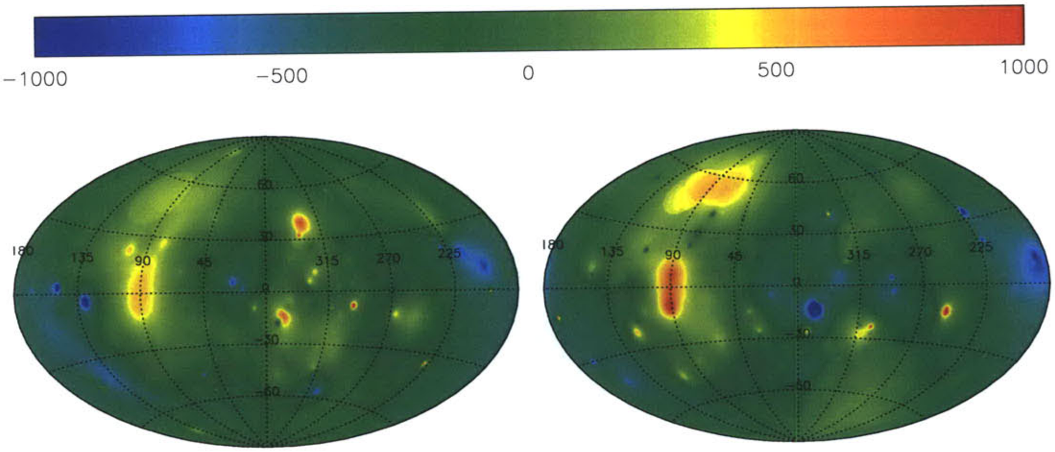

(e) $D = 5000$ km s^{-1}

(f) $D = 6000$ km s^{-1}

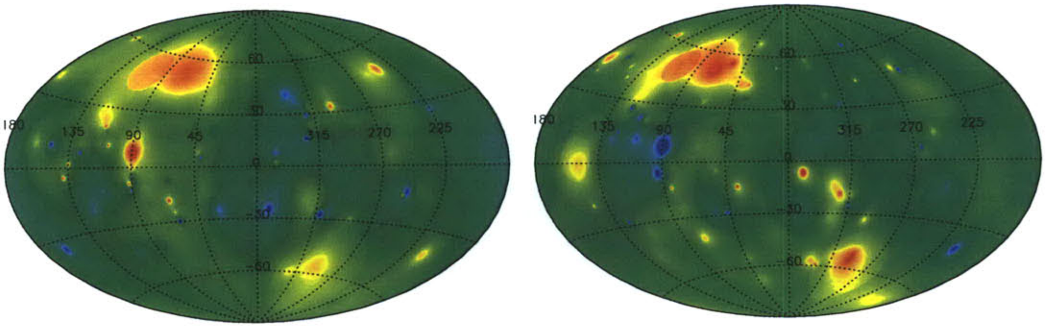

(g) $D = 7000$ km s^{-1}

(h) $D = 8000$ km s^{-1}

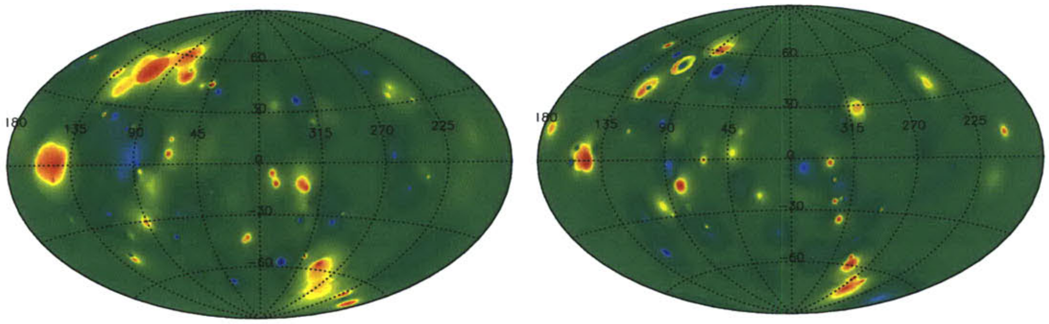

(i) $D = 9000$ km s^{-1}

(j) $D = 10000$ km s^{-1}

Figure 3.12 — *continued...*

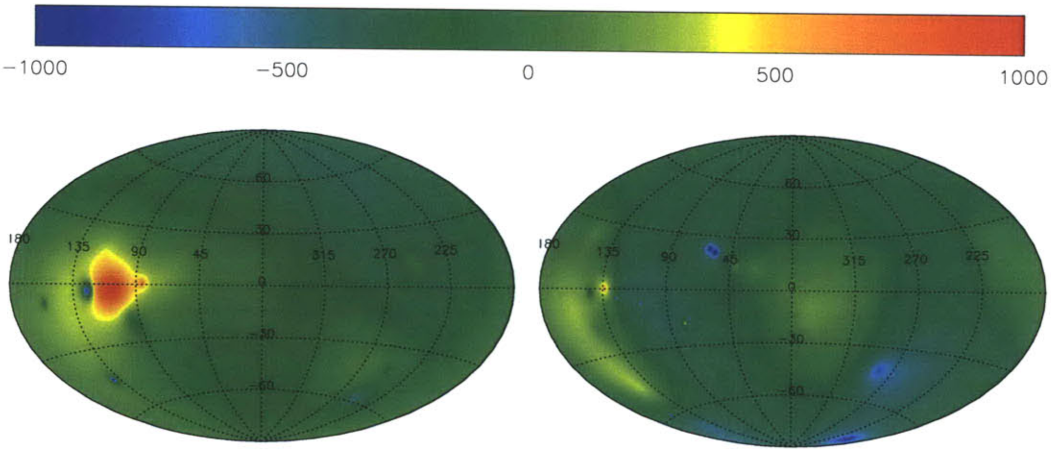

(a) $D = 1000$ km s^{-1}

(b) $D = 2000$ km s^{-1}

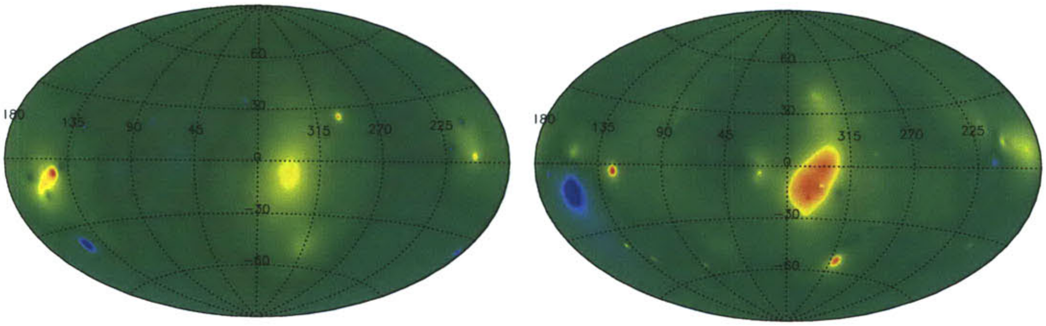

(c) $D = 3000$ km s^{-1}

(d) $D = 4000$ km s^{-1}

Figure 3.13 Line-of-sight components of peculiar velocities in LR frame (IMC). The figures show the peculiar velocities relative to the Hubble flow at specified distances (given in km s^{-1}) from the LG. The velocities have been computed from the flow-field model assuming the incoherent mass correction. The maps are shown in supergalactic coordinates in an Aitoff projection. Yellow/red colors indicate a test mass at the specified location is expected to have a peculiar velocity (relative to the LR frame) in an outward direction, and blue colors indicate an inward velocity. Green areas indicate low net line-of-sight motions with respect to the LR frame. The units of the indicated color scale are km s^{-1}. See the text for a description of features in the plot.

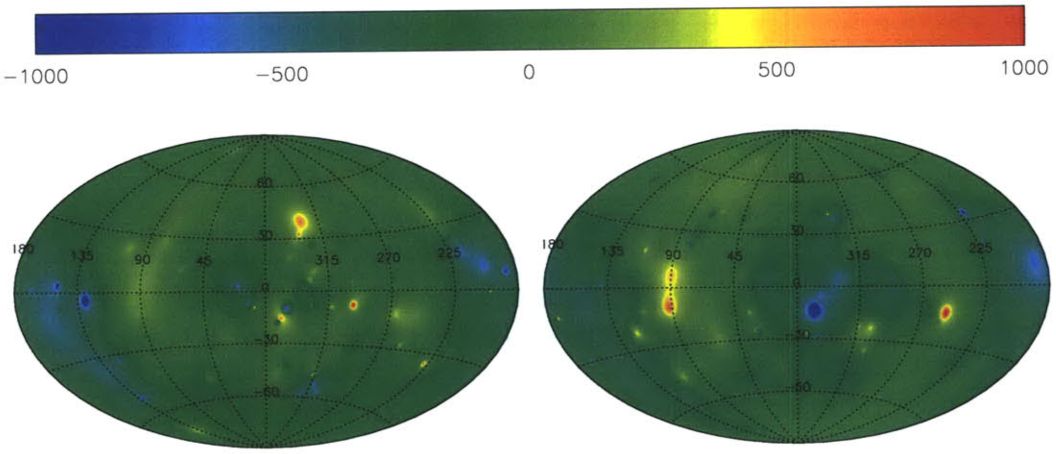

(e) $D = 5000$ km s^{-1}

(f) $D = 6000$ km s^{-1}

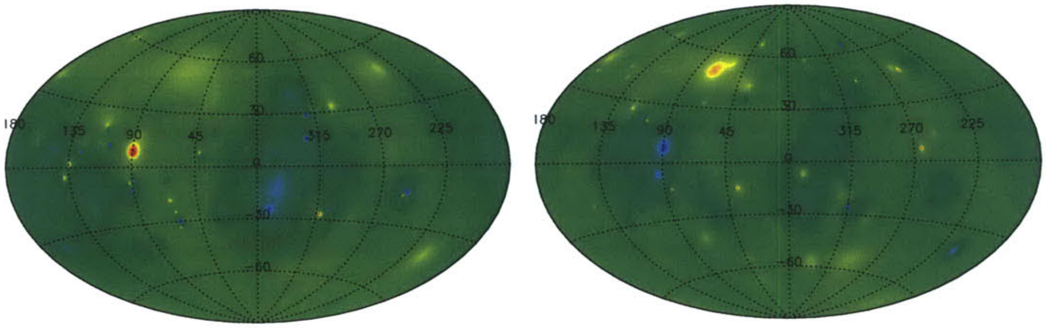

(g) $D = 7000$ km s^{-1}

(h) $D = 8000$ km s^{-1}

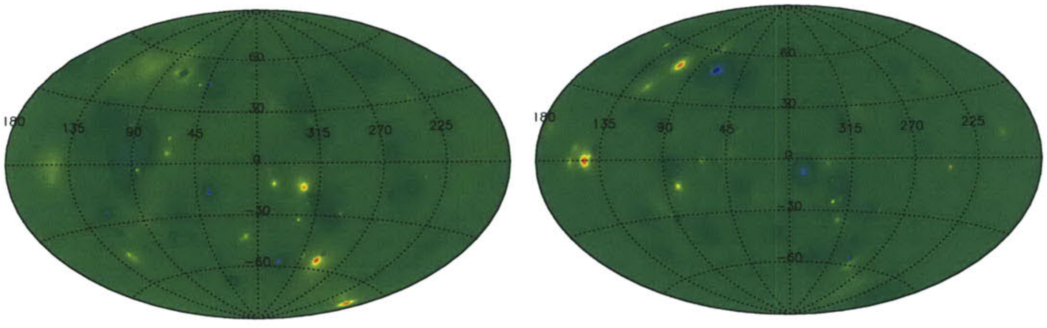

(i) $D = 9000$ km s^{-1}

(j) $D = 10000$ km s^{-1}

Figure 3.13 — *continued...*

predicted into Coma, and significant peculiar motion toward Abell 2199 ($SGL \sim 70°$, $SGB \sim 50°$). Note that as we map to larger distances, we get closer to the limit of the selection function. In Figure 3.12, infall into groups is amplified as a result, especially for the most distance groups (e.g., A2199, which is placed at a redshift of $\sim 9700\,\mathrm{km\ s^{-1}}$). In the case where interlopers have distorted the mass estimate (which is more likely at larger distances), this may be misleading. Efforts have been made to reduce this effect (see §3.1.3), however, and we can still recognize the expected infall toward the Shapley concentration at ($SGL \sim 150°$, $SGB \sim 0°$) as we approach the 10,000 km s^{-1} shell. In Figure 3.13, the maps appear relatively quiet near the limit of the sample. The angular sizes of the observed groups are small due to their distance, and peculiar velocities are only significantly different from zero in close proximity to the groups.

Since the LG (and LS) also has a peculiar velocity with respect to the LR frame (Figure 3.11), any experimentally measured peculiar velocity will be obtained relative to the observer and can be corrected to the LS reference frame using the method presented in §3.1.2. The flow-field model predicts the peculiar velocity relative to the LS frame at our location to be in a direction between Virgo and Hydra. The predicted velocities, corrected to the LS frame, are therefore given by subtracting this dipole from the plots of Figures 3.12 or 3.13, which we show in Figures 3.14 and 3.15, respectively.

Test masses in the vicinity of the LG will have similar peculiar velocities to the LG so there are few residuals from the peculiar motion nearby. A large component of the LS dipole is in the direction of Virgo so, at 1000 km s^{-1}, much of the Virgo infall seen in Figures 3.12(a) and 3.13(a) has been subtracted. This suggests that, nearby, the LS-centric redshift performs well as a predictor of distances with a simple application of Hubble's law. The high density of groups in the supergalactic plane results in a predicted motion below the plane directed back toward the plane. Even at 2000 km s^{-1}, objects in the southern hemisphere falling toward Hydra-Centaurus and Virgo will have negative line-of-sight components to their peculiar velocities (in the LR frame) due to their relative locations, even though Hydra is at a higher redshift as measured by an observer at the LG. This is a prediction of the model, and would not be true if a sufficiently massive attractor in the Shapley concentration increased the streaming motion toward Shapley.

Beyond Virgo, a significant portion of the LG motion has been accounted for, and we therefore see the necessary correction from the LS frame to the LR frame begin to appear in the form of an opposing dipole component. This is enhanced by the predicted streaming toward Perseus-Pisces at 3000 km s^{-1}, which increases the LS-centric redshift in the direction of the supercluster. As we look deeper, beyond Hydra-Centaurus, Perseus-Pisces and Norma, nearly all of the predicted LG motion has been accounted for, so the dipole correction that needs to be applied to the observed peculiar velocities is easily visible in the map, and, by 10,000 km s^{-1}, the inverse of the LG dipole (shown in Figure 3.11) is a prominent feature of the plot. This is expected since the LR frame is defined such that the LG dipole is accounted for at the sample limit. Due to the bias-correction utilized in Figure 3.14, perturbations in the density-field are amplified at larger distances, resulting in the large predicted

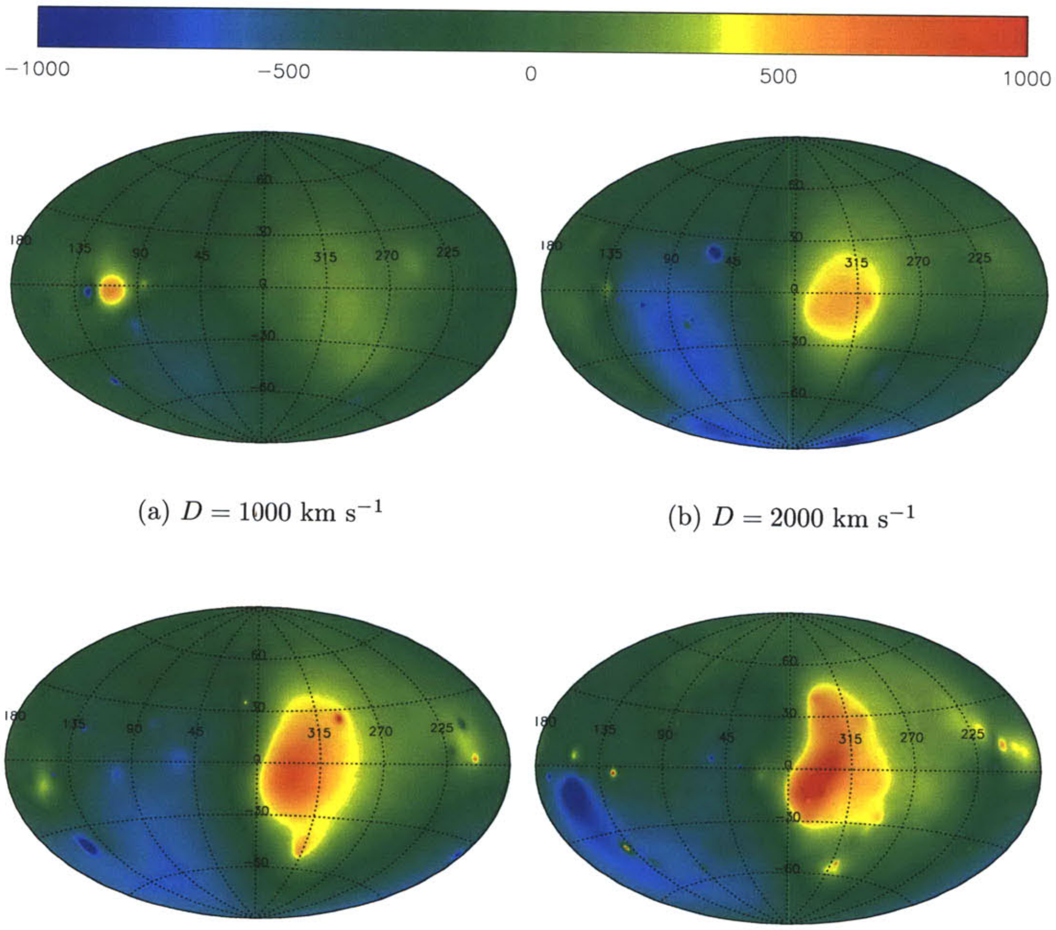

(a) $D = 1000$ km s^{-1}

(b) $D = 2000$ km s^{-1}

(c) $D = 3000$ km s^{-1}

(d) $D = 4000$ km s^{-1}

Figure 3.14 Line-of-sight components of peculiar velocities in LS frame (CMC). The figures show the LR-frame prediction of the line-of-sight component of the peculiar velocity, with the dipole of the LS subtracted, assuming the coherent mass correction. The plots are for slices in real-space, and the colors indicate the magnitude of the peculiar motion. The remaining details are as Figure 3.12.

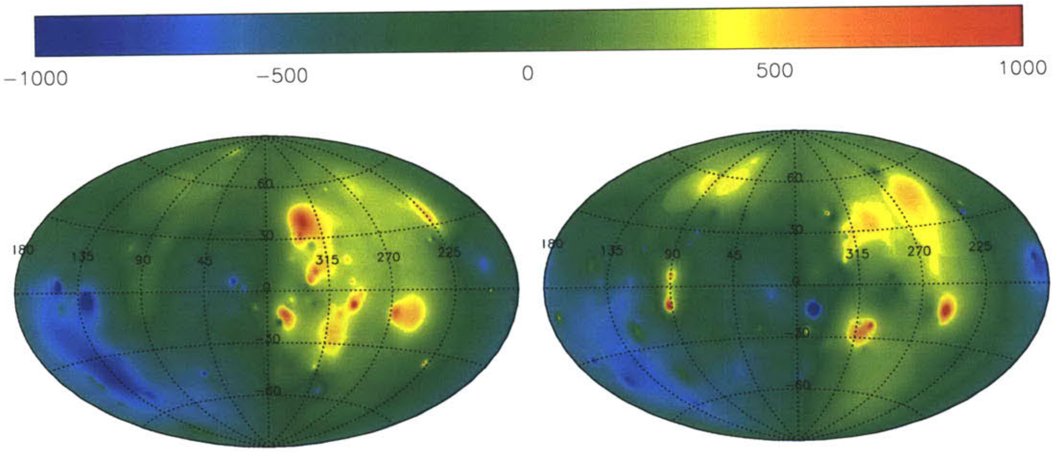

(e) $D = 5000$ km s^{-1} (f) $D = 6000$ km s^{-1}

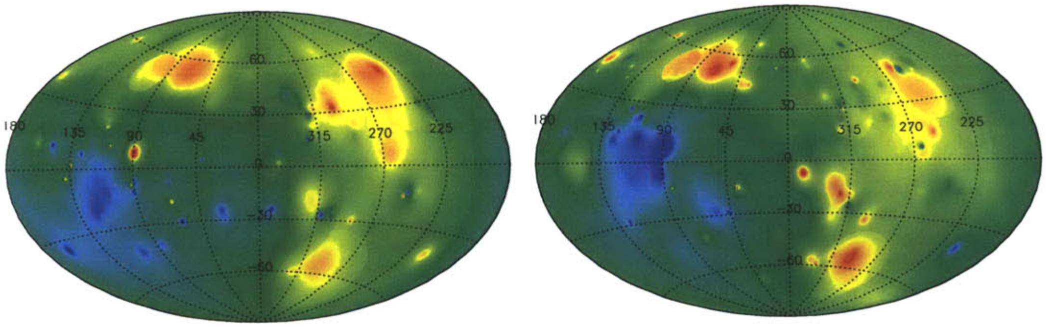

(g) $D = 7000$ km s^{-1} (h) $D = 8000$ km s^{-1}

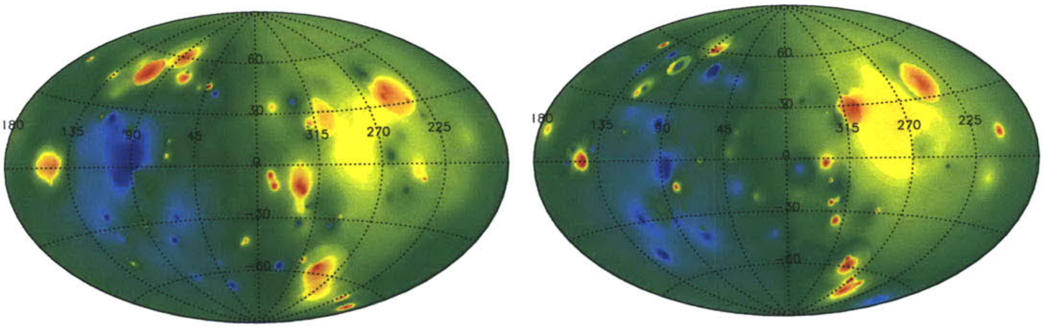

(i) $D = 9000$ km s^{-1} (j) $D = 10000$ km s^{-1}

Figure 3.14 — *continued...*

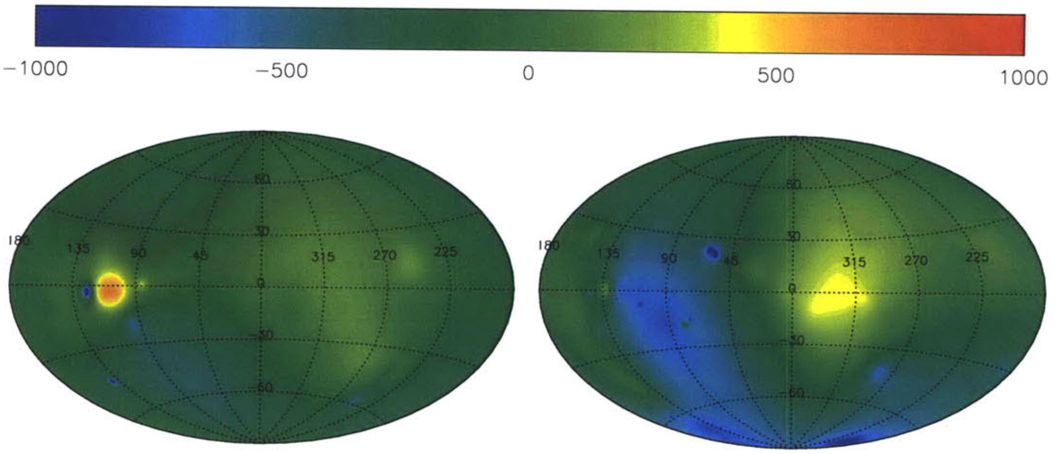

(a) $D = 1000$ km s^{-1}

(b) $D = 2000$ km s^{-1}

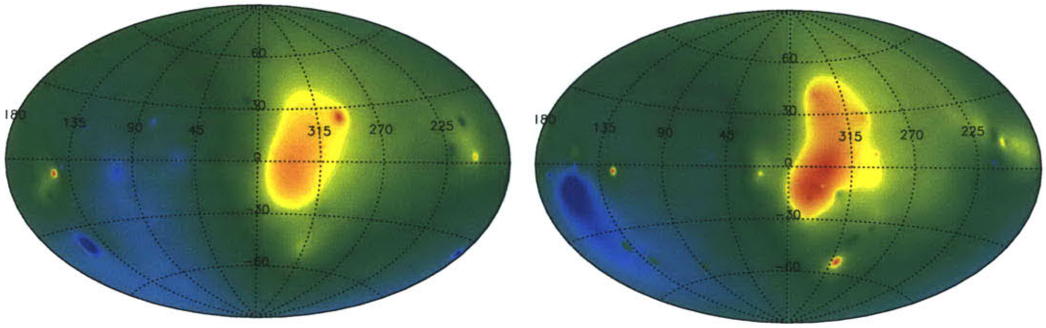

(c) $D = 3000$ km s^{-1}

(d) $D = 4000$ km s^{-1}

Figure 3.15 Line-of-sight components of peculiar velocities in LS frame (IMC). The figures show the LR-frame prediction of the line-of-sight component of the peculiar velocity, with the dipole of the LS subtracted, assuming the incoherent mass correction. The plots are for slices in real-space, and the colors indicate the magnitude of the peculiar motion. The remaining details are as Figure 3.13.

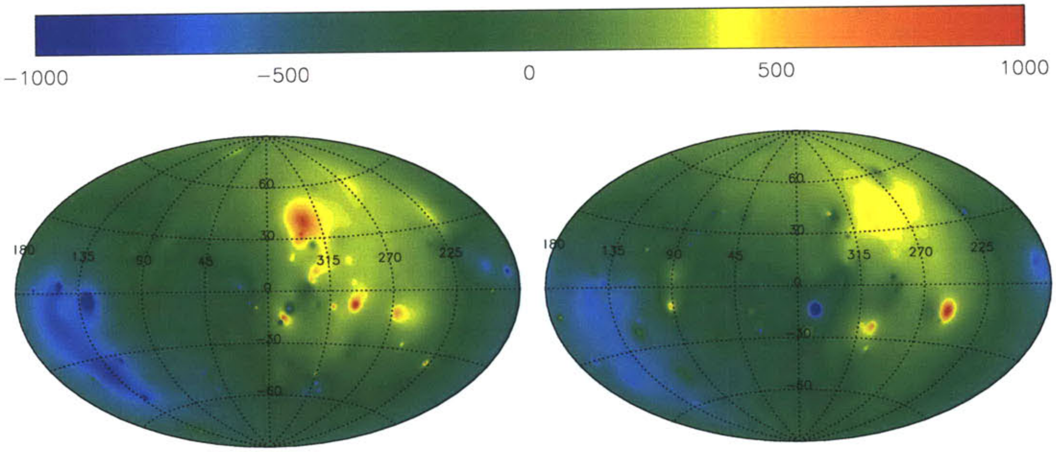

(e) $D = 5000$ km s^{-1} (f) $D = 6000$ km s^{-1}

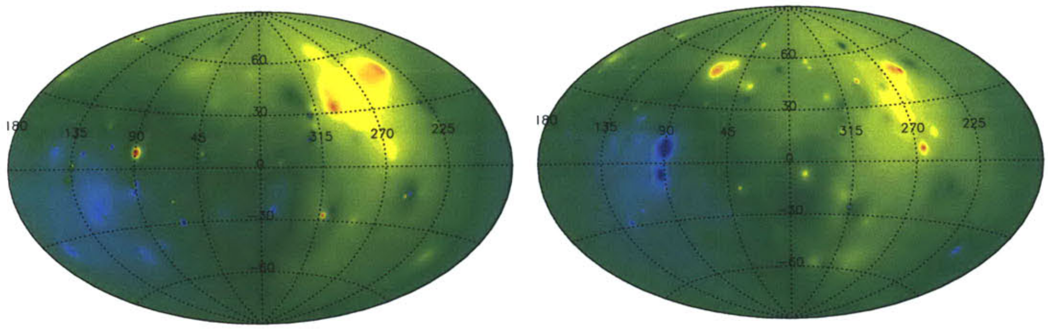

(g) $D = 7000$ km s^{-1} (h) $D = 8000$ km s^{-1}

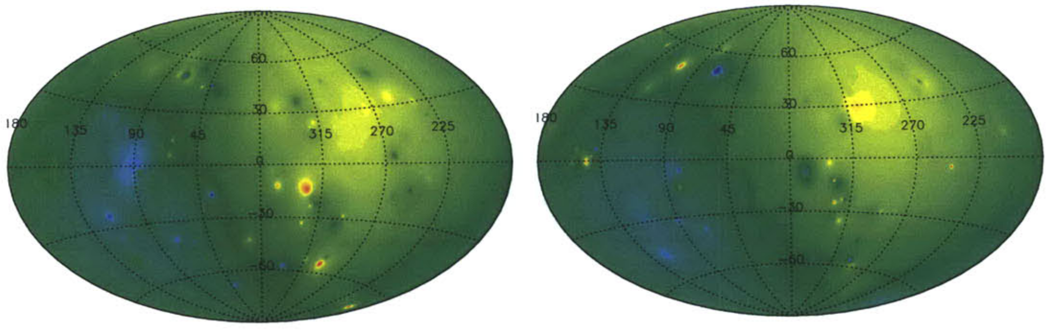

(i) $D = 9000$ km s^{-1} (j) $D = 10000$ km s^{-1}

Figure 3.15 — *continued...*

perturbations in the peculiar velocity-field at 10,000 km s^{-1}.

3.4 Comparison with Existing Models

We compare the velocity-field constructed from groups of galaxies in 2MRS (hereafter, the 2MG velocity-field) with two existing models: Branchini et al. (1999) and Erdoğdu et al. (2006a). The comparisons are presented in subsections §3.4.1 and §3.4.2 below, prefaced with an introduction to the respective models.

3.4.1 PSCz Velocity-field

The velocity-field of Branchini et al. (1999) was constructed from the PSCz redshift catalog (Saunders et al., 2000); the latter contains $\sim 15,000$ *IRAS* PSC galaxies with 60μm flux $f_{60} > 0.6$ Jy, covering $\sim 84\%$ of the sky. The velocity-field was constructed from a subsample of 11,206 galaxies with LG-centric redshifts less than 20,000 km s^{-1}. Since the catalog is based upon sources selected at 60μm, the sampling is biased toward dust-rich star-forming galaxies, under-sampling the massive elliptical galaxies found predominantly in rich clusters. The velocity-field was computed in a similar manner to the 2MG velocity-field, with estimates of the distances derived by requiring self-consistency between the density and velocity fields. The velocity-field has been smoothed with a Gaussian filter with a radius of $3.2/h$ Mpc.

In order to compare the PSCz and 2MG velocity-fields, we construct a grid of $51 \times 51 \times 51$ uniformly-spaced points throughout a cube of side $200/h$ Mpc, centered on the LG. At each point, we interpolate the cartesian components of the predicted velocity. Since the 2MG velocity-field is limited to a spherical volume, we consider only the grid-points inside a sphere of radius $100/h$ Mpc. In both the PSCz catalog and 2MRS, the completeness of the samples fall at low-galactic latitudes due to a combination of confusion with stars in the Milky Way and the difficulty in obtaining (optical) targeted redshifts at very low galactic latitudes. The approach taken to reduce artefacts in the model arising from this incomplete sampling is similiar in both cases, but, in a comparison between the two models, we do not want the effects of the reconstruction of the plane influencing the results. Through the definition of the supergalactic plane (§3.2.1), the SGY–component of the velocity is least affected by the density-field in the galactic plane, and therefore by comparing only this component of the velocity, we reduce our sensitivity to such artefacts.

Due to the nature of the data sets, the bias parameters associated with *IRAS* galaxies and 2MRS groups are incompatible. The absolute difference in magnitudes is not meaningful, therefore we scale the velocities such that the standard deviation of the SGY–component of the velocities inside 6000 km s^{-1} is 200 km s^{-1}. Figures 3.16 and 3.17 show the resulting 2MG velocity-field for the CMC and IMC cases, respectively, and Figure 3.18 shows the derived PSCz velocity-field. To demonstrate the differences between the two models, we plot the SGY–components of the velocity at 1000 randomly chosen grid points within a sphere of radius 6000 km s^{-1} centered on the origin. The results are shown in Figures 3.19(a) and 3.19(c). The velocities have

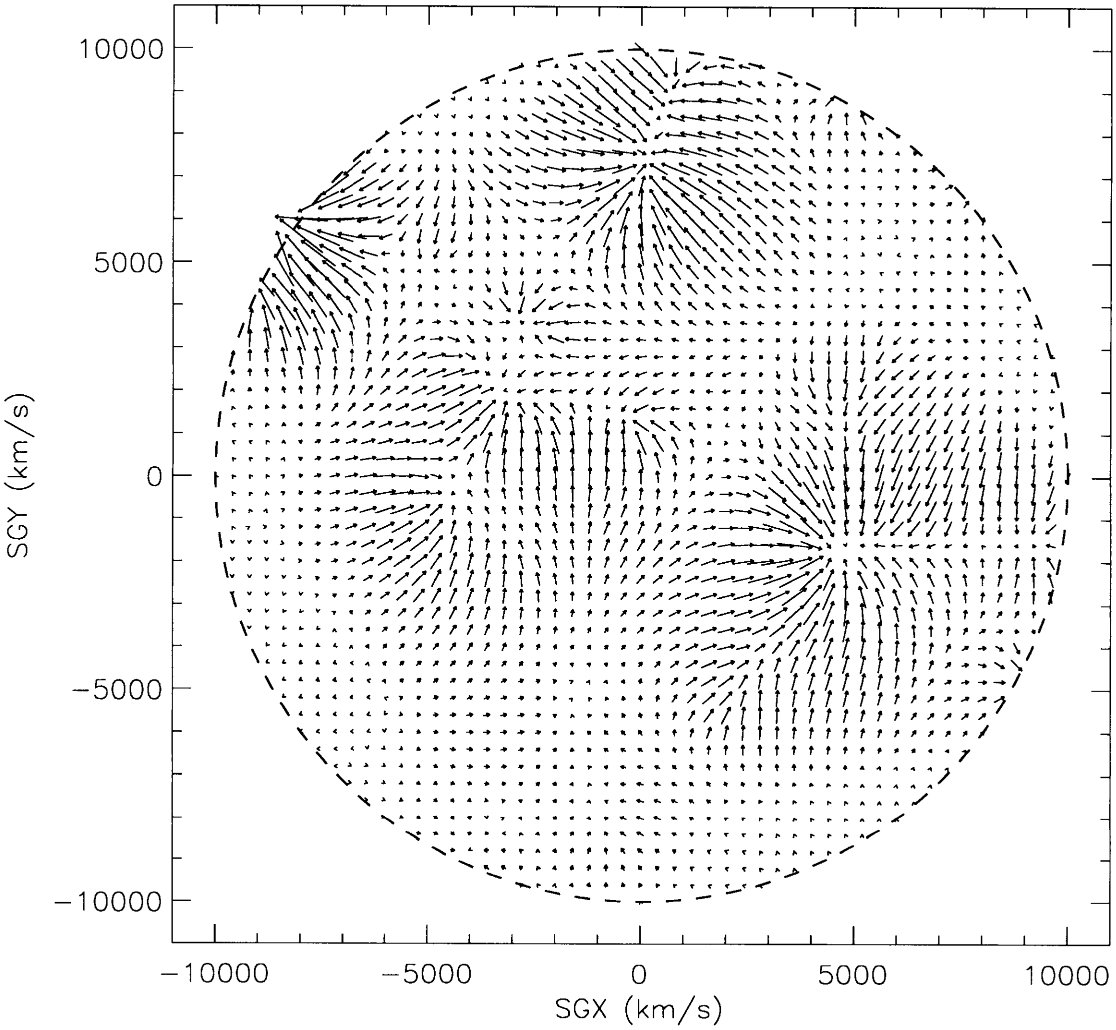

Figure 3.16 2MG velocity-field: A cross-section through the supergalactic plane (CMC). The 2MG velocity-field inside 10,000 km s^{-1} has been constructed assuming the coherent mass correction. The magnitudes of the peculiar velocities have been scaled such that the *SGY*–components of the velocities have a standard deviation of 200 km s^{-1}.

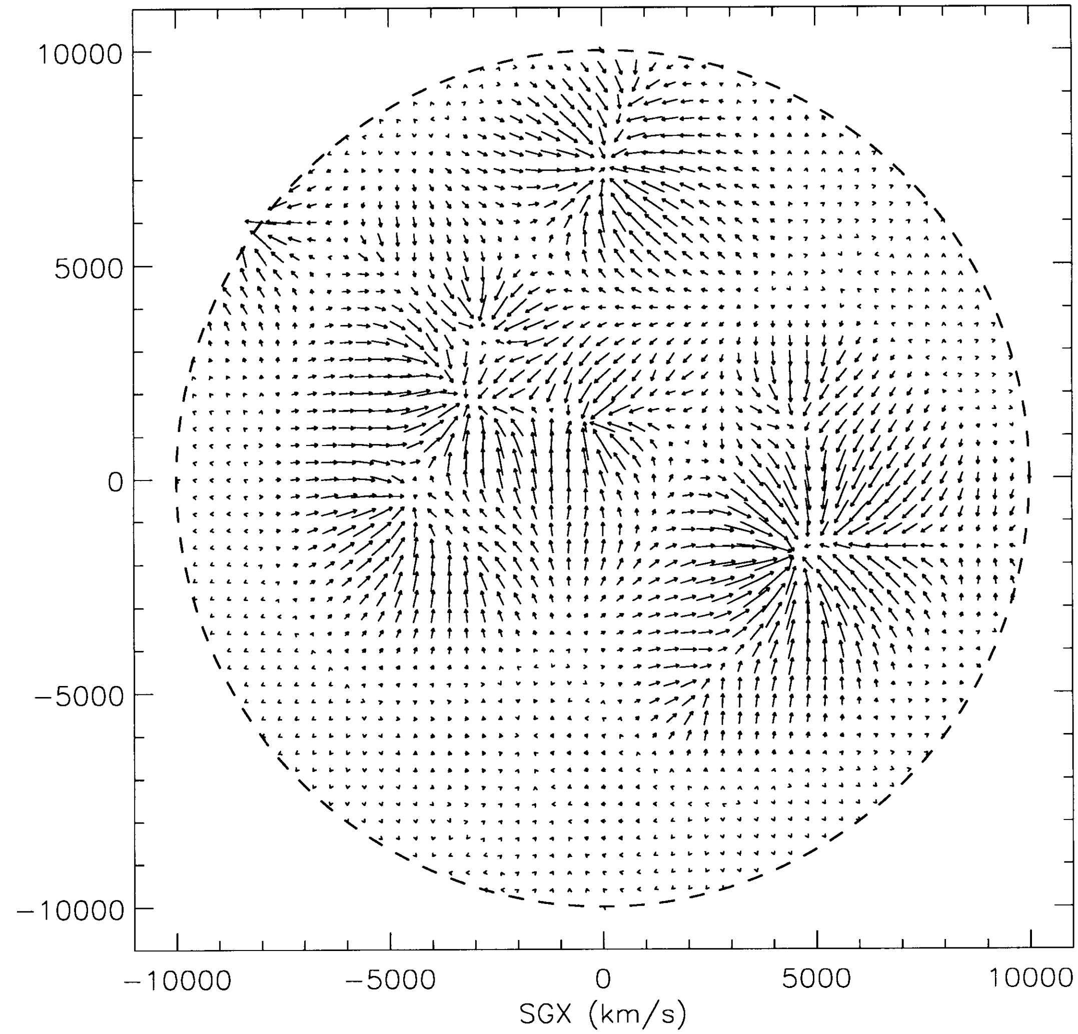

Figure 3.17 2MG velocity-field: A cross-section through the supergalactic plane (IMC). The 2MG velocity-field inside 10,000 km s^{-1} has been constructed assuming the incoherent mass correction. The magnitudes of the peculiar velocities have been scaled such that the *SGY*–components of the velocities have a standard deviation of 200 km s^{-1}.

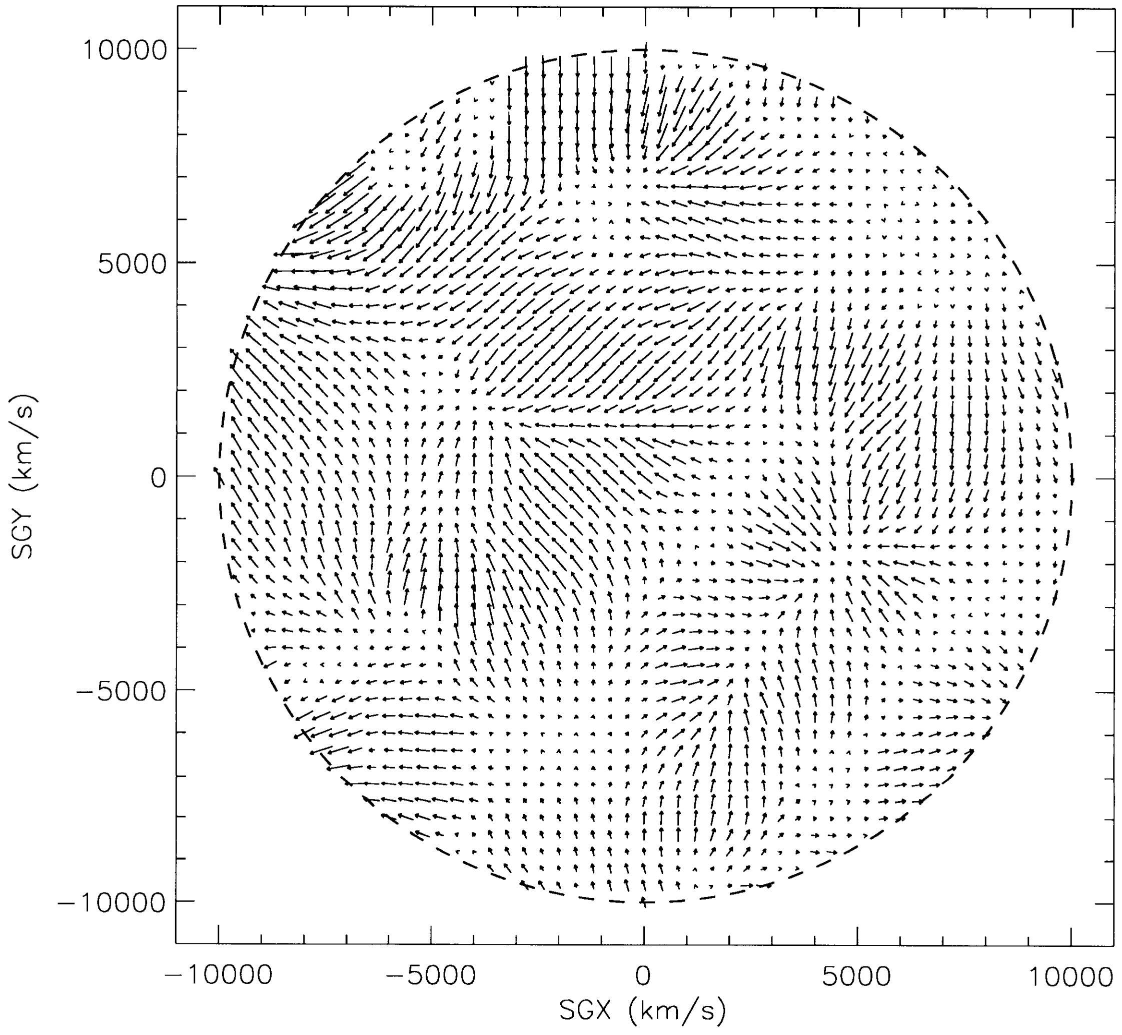

Figure 3.18 PSCz velocity-field: A cross-section through the supergalactic plane. The magnitudes of the peculiar velocities have been scaled such that the SGY–components of the velocities have a standard deviation of 200 km s^{-1}.

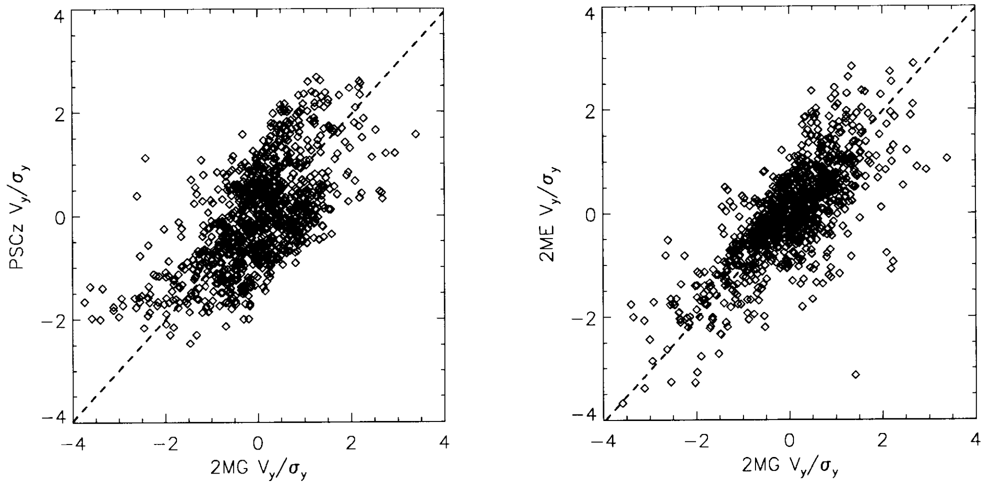

(a) 2MG (CMC) vs. PSC*z*

(b) 2MG (CMC) vs. 2ME

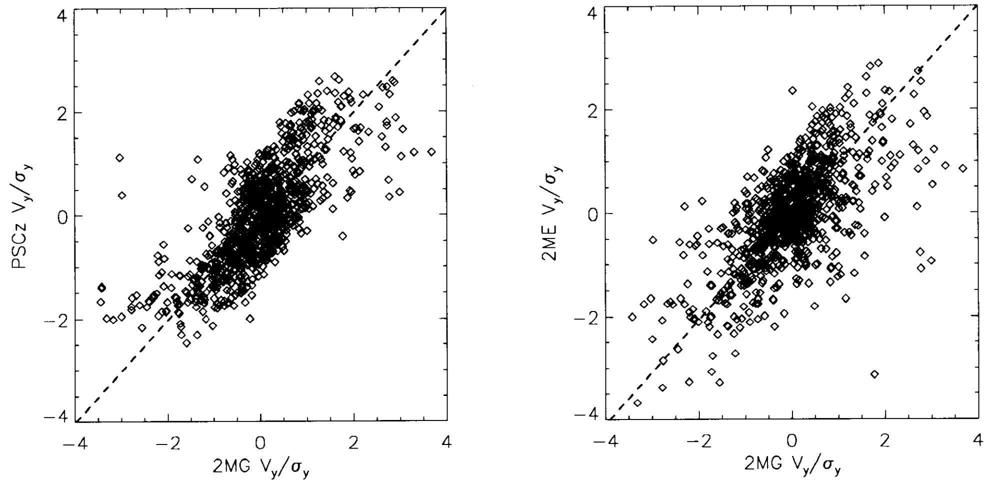

(c) 2MG (IMC) vs. PSC*z*

(d) 2MG (IMC) vs. 2ME

Figure 3.19 *SGY*–components of predicted velocities. The figures show a comparison between the velocities predicted by the 2MG model and PSC*z* and 2ME models. The comparison is performed for the 2MG model computed assuming both the coherent mass correction and incoherent mass correction. A sample of 1000 randomly chosen points inside a sphere centered on the LG of radius 6000 km s^{-1} are plotted. The velocities are scaled such that the mean of each sample is zero, and are normalized by the standard deviation of the sample. The lines represent a linear fit obtained using perpendicular regression.

been adjusted such that the sample means are zero, which ensures we are performing the comparison in the same reference frame. The line is the result of a perpendicular linear regression, and the r.m.s. perpendicular offset ($\epsilon_{\rm rms}$, in units of $\sigma_{\rm V,SGY}$) of the points from the line is a measure of the uncertainty between the models, independent of the gradient, which is determined by β.[6] Note that in §5.4.1, we estimate the error on the line-of-sight components of peculiar velocities evaluated at locations inside 3000 km s^{-1}, and find a r.m.s. model error of 116 km s^{-1}–131 km s^{-1}. On this scaling, it implies that a value of $\epsilon_{\rm rms} \lesssim 0.66$ is within the 1σ uncertainty of the reconstruction method. For this random sample, we find $\epsilon_{\rm rms} = 0.60$ for the CMC case and $\epsilon_{\rm rms} = 0.51$ for the IMC case, both within the errors of the model.

The result is also evident in Figure 3.20, where we show the difference in the SGY–component of the peculiar velocities as a function of position in the supergalactic plane. The white areas indicate regions where the two models are consistent to within $0.5\sigma_{V,SGY}$, where contours were chosen to coincide with the errors on the reconstruction method, estimated to be $0.48\sigma_{V,SGY}$ on this scaling (see §5.4.1). The largest noticeable difference occurs in the void behind the great attractor. The 2MG model predicts infall toward the Norma cluster, then streaming motion toward Hydra-Centaurus, whereas the PSCz model predicts streaming velocities toward Shapley. The dark regions at (SGX, SGY) ~ (-3000, 2000±1000) are due to higher predictions for the infall into Hydra-Centaurus. Similar regions of higher velocities for cluster infall are observed at the locations of Perseus-Pisces and Coma. This is anticipated due to the fact that the *IRAS*–based model under-sampled the number density of galaxies in rich clusters in comparison with 2MRS (e.g., Norberg et al., 2001; Zehavi et al., 2002; Branchini et al., 1999), and therefore we expect a density-field derived from 2MASS to trace the mass more accurately than a model constructed from an *IRAS*-selected sample. Furthermore, the dynamical mass estimates used in the 2MG model are likely to account for the higher density of dark matter expected in clusters. Note, however, that since the 2MG model does not trace individual galaxies, it will be unable to detect smaller peaks in the density field, so the normalization process may overestimate the velocities near clusters to compensate. The 2MG model predicts backside-infall into the Norma cluster, whereas in the PSCz reconstruction, the flow streams directly into the Shapley concentration. The PSCz velocity-field also predicts the flow in front of the Coma cluster directed toward Shapley, whereas the higher density of Coma in the 2MG model predicts infall into the Coma cluster. Comparing both 2MG models (constructed with the coherent and incoherent mass corrections) with the PSCz velocity-field, we note that the discrepancies occur in the same spatial locations. This signifies that the choice of bias correction does not have a significant impact on the conclusions we have drawn in this section.

---

[6] The gradient of the line is approximately unity due to the fact that the velocities were scaled by the standard deviation of their y-component, however, if the values are not normally distributed, then the gradient will deviate from unity, so a statistic that does not depend on the gradient of the line is appropriate in this case.

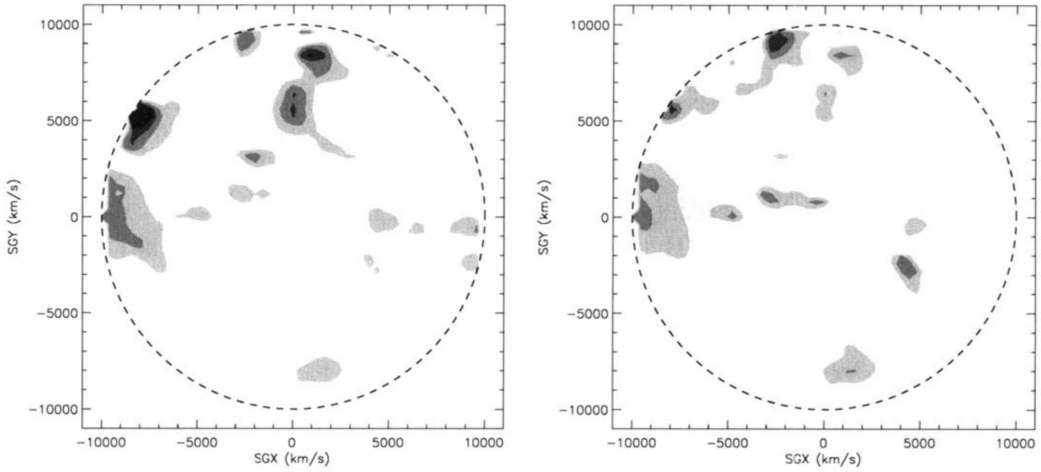

(a) Coherent Mass Correction

(b) Incoherent Mass Correction

Figure 3.20 Comparison between 2MG and PSCz velocity-fields. In the left (right) panel, the 2MG model is computed assuming the coherent (incoherent) mass correction. The contours represent 0.5σ (i.e. 100 km s^{-1} on the chosen scaling) differences between the SGY–component of the peculiar velocities predicted at any point. White regions indicate agreement within $0.5\sigma_{P,SGY}$ (which is approximately equal to the uncertainty in the model; see §5.4.1). The 2MG model predicts significantly larger peculiar velocities in the vicinity of massive clusters, and the large difference indicated on the left of the map is due to the 2MG prediction of backside-infall into the Hydra-Centaurus-Norma supercluster, whereas the PSCz model predicts continuous streaming motion into the Shapley concentration. The difference maps produced with the CMC and IMC models are remarkably similar, demonstrating that these discrepancies are not due to the choice of bias correction.

3.4.2 2MRS Galaxy Velocity-field

The velocity-field of Erdoğdu et al. (2006a) (hereafter, 2ME) was constructed from the $K_s < 11.25$ 2MRS galaxy sample (see §1.4). The method for reconstruction is based on linear theory, but the authors approach the problem by first decomposing the density field in redshift-space into spherical harmonics and Bessel functions, then reconstruct the real-space velocity-field using a Wiener filter to reduce the noise in the reconstruction. The density-field is constructed using galaxies as point tracers of the mass, weighted by the inverse of the selection function. This method inherently assumes that the instrinsic mass density is proportional to the number density, which is the crucial difference between the 2MG reconstruction and the 2ME velocity-field.

For comparison, the velocity-field is sampled on grid of $51 \times 51 \times 51$ uniformly-spaced points throughout a cube of side $200/h$ Mpc, centered on the LG. As in §3.4.1, the magnitude of the velocities are scaled such that the standard deviation of the SGY–component of predicted velocities inside 6000 km s^{-1} is 200 km s^{-1}. We plot the SGY–components of the velocities for a random sample of 1000 points within this region, and compare the predictions of the 2MG and 2ME models (see Figure 3.22). We find $\epsilon_{\rm rms} = 0.49$ (CMC case) and $\epsilon_{\rm rms} = 0.57$ (IMC case), suggesting good agreement with the 2MG model. The value for the IMC case is notably larger, however, because the velocity distribution is narrower (see Figure 3.9). Far from the origin, the predicted velocities are small due to the fact that the distribution is highly isotropic by construction. Since we scale the velocities by their standard deviation, the predicted velocities for nearby grid points are much larger relative to the standard deviation than the equivalent 2MG grid points, and so the scatter observed in Figure 3.19(d) is large.

A cross-section of the velocity-field through the supergalactic plane is shown in Figure 3.21, and Figure 3.22 shows the difference in the SGY–components of the 2MG and 2ME models as a function of position in the supergalactic plane. The qualitative features described in §3.3 above are common to both velocity-fields; this is expected since the 2MRS galaxy model is based on a subset of the source data of the 2MG model. Notably, both predict backside-infall into the Norma region which is not predicted by the PSCz model. In fact, the 2ME model predicts higher backside-infall into Norma, which is indicated by the dark region at (SGX, SGY) 4$\sim$ (-5000, -2000). While this may be surprising at first, the location of the Norma cluster is very close to the galactic plane. The incomplete sampling at low galactic latitudes has a more significant impact on the group catalog than the source catalog, and so it is plausible that the mass of the Norma cluster has been underestimated in the 2MG model. The models are in reasonable agreement around the Hydra-Centaurus region, although the local Virgo infall predicted in the 2MG model has been smoothed over in the 2ME velocity-field. The 2MG model predicts higher infall velocities around the Perseus-Pisces region than the 2ME model. The use of a larger smoothing radius reduces the majority of the discrepancies between the two velocity-fields. The difference at Coma persists, however, due to the fact that the distance estimates used in the reconstruction of Erdoğdu et al. (2006a) are inferred from the LG-centric redshifts. In the 2MG model (and PSCz model), the distance estimates

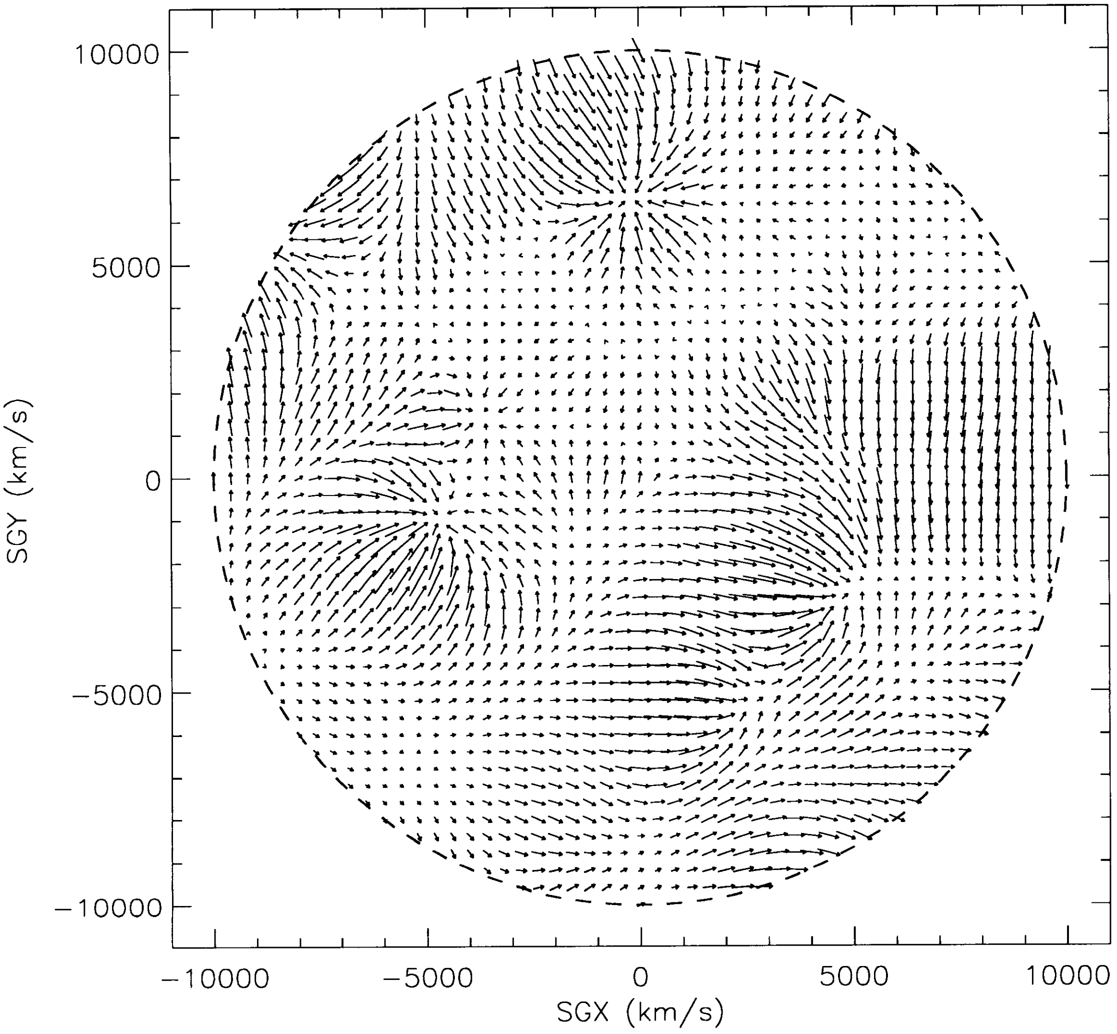

Figure 3.21 2MRS-galaxy (2ME) velocity-field: A cross-section through the supergalactic plane. The magnitude of the peculiar velocities have been scaled such that the *SGY*–components of the velocities have a standard deviation of 200 km s^{-1}.

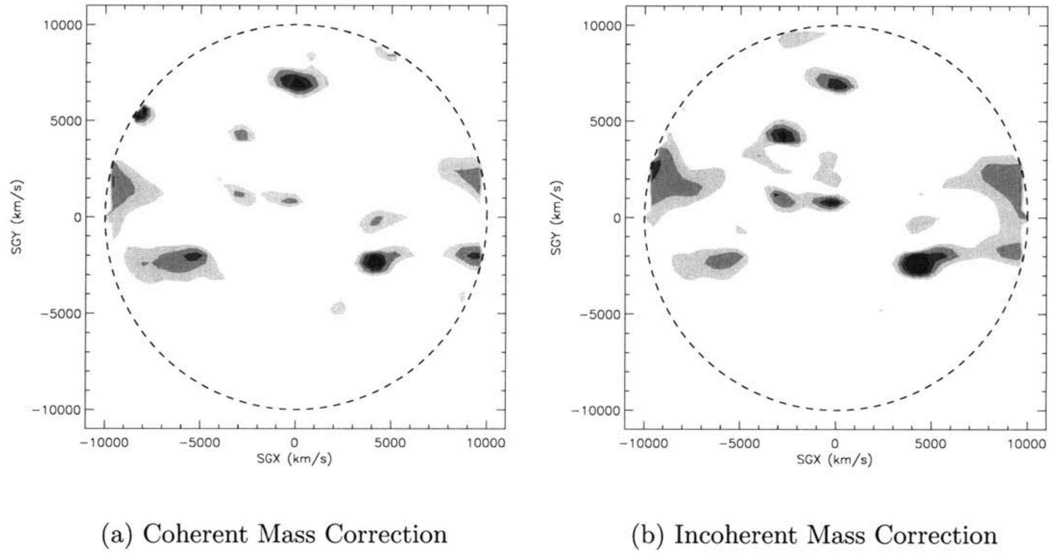

(a) Coherent Mass Correction

(b) Incoherent Mass Correction

Figure 3.22 Comparison between 2MG and 2ME velocity-fields. In the left (right) panel, the 2MG model is computed assuming the coherent (incoherent) mass correction. The contours represent 0.5σ (i.e. 100 km s^{-1} on the chosen scaling) differences between the SGY–components of the predicted peculiar velocities. White regions indicate agreement within 0.5σ. As in Figure 3.20, the difference maps produced with the CMC and IMC models are remarkably similar, demonstrating that these discrepancies are not due to the choice of bias correction.

are revised to obtain self-consistent density and velocity fields. Using a LG-centric redshift to infer the distance to the Coma Cluster would result in an underestimate of its Hubble distance, since the LG peculiar velocity has a positive component in the direction of Coma. The discrepancy in these distances results in different spatial velocity-fields in close proximity of the Coma Cluster. As noted in §3.4.1 above, the similarity between Figures 3.22(a) and 3.22(b) signifies that the choice of bias correction does not have a significant impact on the conclusions we have drawn in this section.

3.5 Summary

In this chapter we have presented a model of the flow-field constructed from groups of galaxies identified in the 2MASS Redshift Survey (2MRS). Using dynamical mass estimates and allowing for a linear bias between the inferred cluster masses and underlying dark matter distribution, we presented a method to estimate distances to groups such that the density and velocity fields are self-consistent. On application to 2MRS, we predict significant infall in the vicinity of Virgo, Perseus-Pisces, Hydra-Centaurus, Coma, Norma and Hercules. Evidence suggests that the Shapley concentration, which lies just outside the modeled volume, distorts the flow toward the limit of the sample. We note that at least 8% of groups are predicted to have peculiar velocities larger than the 627 km s^{-1} that the Local Group (LG) is observed to have in the rest frame of the Cosmic Microwave Background (CMB) (this number rises to 15% when assuming the coherent mass correction), suggesting that, while this magnitude is large, it is not unreasonable.

We define a reference frame — the Local Rest (LR) frame — in which the motion of the Local Sheet (LS) and galaxies/groups within can be completely accounted for by the sampled groups of galaxies in 2MRS inside 12,000 km s^{-1}; we find that the motion of groups inside the LS is directed toward a region between Virgo and Hydra with respect to the LR frame. We use this prediction, in conjunction with the modeled flows, to estimate line-of-sight peculiar velocities relative to the Local Sheet as a function of spatial position.

We compared the 2MRS Groups (2MG) velocity-field with the PSCz velocity-field of Branchini et al. (1999), and find that the 2MG field consistently predicts higher infall into the known rich clusters — an expected result since the *IRAS*-selected samples are biased toward the detection of star-forming galaxies and therefore underestimate the mass of rich clusters. We also predict backside-infall into the Norma region, a feature that is absent from the PSCz model. Comparing the 2MG field with a reconstruction from a 2MRS galaxy-based sample (Erdoğdu et al., 2006a, 2ME), we reproduce the same qualitative features, and note that both models constructed from 2MRS predict backside-infall into the Norma region.

Chapter 4

Reconstructing Peculiar Velocities in the Hubble Volume Simulation

In this chapter, we test the principles of the method employed in Chapter 3 to reconstruct the flow-field from galaxy groups. Whilst gravitational instability theory has been applied successfully in the past to model the dynamics of infall into clusters (e.g., Peebles, 1976b; Yahil et al., 1980; Tonry et al., 2000, to mention but a few), its application to construct a model of the flow-field from galaxy groups has not previously been tested.

The purpose of this chapter is not to provide a rigorous test of the model and its associated errors, but to demonstrate that the method can, in principle, be effectively employed to reliably predict the motions of galaxy groups. We will test the model on observational data in Chapter 5. However, uncertainties in redshift-independent distance estimates, in addition to biases associated with the target selection, mean that the results of a comparison with observation are only valid over a small range of distances and are subject to interpretation.

N–body simulations provide a means to accomplish this goal. A snapshot of the evolved sample of mass particles can be considered as a mock data set with estimates of distances and velocities that are limited only by the precision of the simulation. Such a data set will provide the means to assess the limits to which peculiar velocities of groups of particles can be reconstructed using gravitational instability theory, in the context of our model.

We begin with an overview of the chosen simulation snapshot and discuss its relevance to our data (§4.1). In §4.2, we discuss the choice of an optimal set of groups for the purpose of our analysis. Due to differences between the content of the chosen simulation and 2MRS galaxies, the analysis is relevant, but not equivalent to choices we can make with observational data; we discuss the results of the analysis and its relevance to our method. In §4.3, we estimate the uncertainties in reconstructed peculiar velocities of simulated groups of particles, in an effort to understand the errors associated with a reconstruction of the LG dipole. In §4.4, we discuss the effect of dynamical mass estimates and absence of redshift-independent distance estimates on the results, and, finally, summarize our conclusions in §4.5.

4.1 Simulation Data

For the purposes of our analysis, we will consider the results of the Hubble Volume simulations (Colberg et al., 2000; Jenkins et al., 2001). The simulations evolved 10^9 particles of mass $2.2\times10^{12}h^{-1}M_\odot$, in various specified cosmologies. In our analysis, we will consider the $z = 0$ snapshot of the ΛCDM Hubble Volume simulation with cosmological parameters $\Omega_m = 0.3$, $\Omega_\Lambda = 0.7$, $\sigma_8 = 0.9$, and $H_0 = 100h = 70$ km s^{-1}Mpc^{-1}. The evolved volume was a cube of comoving side length $3000/h$ Mpc; the simulation began at $z = 35$ with a power spectrum computed using CMBFAST (Seljak & Zaldarriaga, 1996; Zaldarriaga et al., 1998; Zaldarriaga & Seljak, 2000). For all computations below, we will consider only a subsample of the simulation: a sphere of radius $375/h$ Mpc, since this is still well beyond the completeness limit of the 2MRS data. The simulation was designed to resolve a structure equal to the mass of the Coma cluster at the level of 500 mass elements. The Hubble Volume Simulation was selected as a reasonable test set that would allow identification of relaxed multi-particle systems of similar sizes (by particle number) to those observed. While the more recent Millennium simulation (e.g., Springel et al., 2005) maps the structure with higher resolution, the choice was the result of a balance between the required computational intensity and the value of the study.

The analysis, however, will be limited by the resolution of the simulation. A single mass element is equivalent to $3.1 \times 10^{12}M_\odot$, which is larger than the estimated mass of the LG ($1.9 \times 10^{12}M_\odot$, Karachentsev et al., 2009). Furthermore, using the median mass-to-light ratio for the HDC catalog presented in §2.4.3, the mass of an $L_\star$ galaxy is $\approx 3.3\times10^{12}M_\odot$, implying that half of the luminosity comes from galaxies below the mass resolution (which make up the majority, by number, of galaxies in the Universe). It is therefore important to be aware that small groups identified by grouping particles in the simulation are significantly more massive than equivalently-sized groups in the real Universe. The principle of the reconstruction method, however, can still be tested, as we describe below, and the results will act as useful guidance in our understanding of the model of the flow-field. Due to the significant difference between groups in the simulation and the real Universe, we limit our discussion to the crucial points of interest.

4.2 Reconstructed Peculiar Velocities

The gravitational instability framework described in §1.3 provides a method that can be used to estimate the peculiar velocities of galaxies or galaxy groups from inhomogeneities in the underlying density-field. If we assume the groups themselves are tracers of the density field, we can use this technique to estimate the peculiar velocities of the same galaxies or galaxy groups. We note that the peculiar velocity (given by Eq. 1.8) has only a weak dependence on the cosmology. The growth factor, $f(\Omega_m) \approx \Omega_m^{6/11}$ in a ΛCDM Universe, is better approximated by $\Omega_M^{4/7}$ for an OCDM Universe (e.g. Wang & Steinhardt, 1998); the small difference between the values of $f(\Omega)$ for $\Omega_m = 0.3$ has little effect on the peculiar velocities over linear scales, and the dependence on the cosmology can be absorbed into a proportionality constant (β), which can be chosen to best fit the "observed" data (in either the case of simulated particles, or the real Universe). The analysis presented below is therefore applicable to various reasonable choices of cosmological parameters.

The selection processes employed to identify groups in the Hubble Volume Simulation are discussed in §4.2.2–§4.2.3 below. However, we begin by describing the method used to assess the performance of the reconstructed flow-field.

4.2.1 Assessment

The peculiar velocity of a galaxy or galaxy group can be estimated using Eq. (3.22). The magnitude depends on a constant of proportionality, β, which, in turn, depends on the cosmology and the bias parameter b of the objects (galaxies or galaxy groups) being used to trace the density-field. For the purposes of this chapter, where we will only evaluate the flow-field at the locations of the centers of groups, we assume the groups can be treated as point masses. With the assumption of spherical symmetry already present in Eq. (3.22), the extension to treat groups as point masses is justified, since if two groups were sufficiently close together to need to account for the form of the density profile, then, for reasonable choices of linking parameters, we expect that they would have been merged into the same group[1] (see §4.2.2).

Our objective here is to test the limitations of the reconstruction method. Since the relationship between the simulation data and the real Universe is not clearly understood, we will attempt only to determine the limits to which linear theory can usefully be applied in the context of a flow-field, under *idealized* conditions, which we explain below.

1. Group Membership. The determination of membership to a group is assessed in real-space instead of redshift space. Although we can still construct groups that are not virialized systems, the likelihood of inclusion of interlopers is reduced in comparison with group-identification algorithms such as those employed in Chapters 2 and 3.

2. Location. The position of the center of the group is determined by computing the mean location of members in real space, not in redshift space. Note that we still consider the effect of a group's peculiar velocity modifying the observed redshift (see §4.4 below).

3. Luminosities. All the particles evolved in the simulation are equal in mass (see the caveat discussed in §4.1). Assignment of luminosities randomly drawn from the 2MRS selection function is an option, however, since a relationship between the mass and luminosity of galaxies has been observed in the real Universe (e.g., Faber & Gallagher, 1979), this approach is not physical. Through the mechanism of the formation of clusters in the simulation, the most massive (and

---

[1] This actually depends on the choice of the linking length, but generally holds true for the values used in the remainder of this chapter.

generally most luminous) galaxies would sink to the bottom of the potential well, and therefore the assigned luminosity should depend on the location of the observed particle. Since the simulation is not sufficiently high in resolution to allow for variation in the particle mass, we do not address the limitations of the reconstruction that are tied directly to the luminosity here, but discuss errors that arise from this in more detail with respect to 2MRS data in Chapter 5.

4. Group Mass. Given the assumption of membership in a group, the mass of groups in the simulation can be either estimated dynamically, or calculated summing the masses of the particles. We will consider both options, beginning with the former in this section.

While the sphere inside which we have tracers of the density field measures $375/h$ Mpc in radius, for the purposes of the tests below we will assess the estimated peculiar velocities of a set of *test groups*, which we define as those groups with at least 5 members[2] inside a smaller sphere of radius $75/h$ Mpc, chosen such that we have a large sample of groups for which we can evaluate the contributions to the peculiar velocities from distances well beyond the 2MRS survey depth. We consider each cartesian component of the predicted and simulated peculiar velocity as a separate point of comparison, and minimize the quantity

$$\Delta^2 = \sum_i \sum_{k=1}^{3} [(\mathbf{v}_{\rm sim})_i^k - (\mathbf{v}_{\rm rec}[\beta])_i^k]^2 \tag{4.1}$$

where $(\mathbf{v}_{\rm sim})_i^k$ represents the $k^{\rm th}$ cartesian component of the "observed" (i.e. evaluated in the simulation) peculiar velocity for the $i^{\rm th}$ group, and $(\mathbf{v}_{\rm rec}[\beta])_i^k$ represents the corresponding reconstructed component of the velocity.

For a given construction (i.e. specified choice of minimum group size and linking length), we can therefore choose β to minimize Δ^2. Comparing values of Δ^2 will then allow us to assess the performance of various constructions.

4.2.2 Identifying Groups

We identify groups in the simulation through the application of a friends-of-friends algorithm with a fixed linking-length. In this section, we consider the case where the mean locations and total masses are extracted directly from the simulation. In Figure 4.1 (solid line), we show the effect of varying the linking length, l, on the quantity Δ (Eq. 4.1). We see that if the linking length is too small, the groups selected by the friends-of-friends algorithm are parts of larger relaxed structures, and the peculiar velocities of the identified groups do not behave as predicted by linear perturbation theory (Eq. 1.8). If the chosen linking length is too large, multiple structures become linked and the assumption of treating the tracers of the density field as a set of discrete masses breaks down due to their extended nature. There is an optimal linking length,

---

[2] This choice will be justified in §4.4 below.

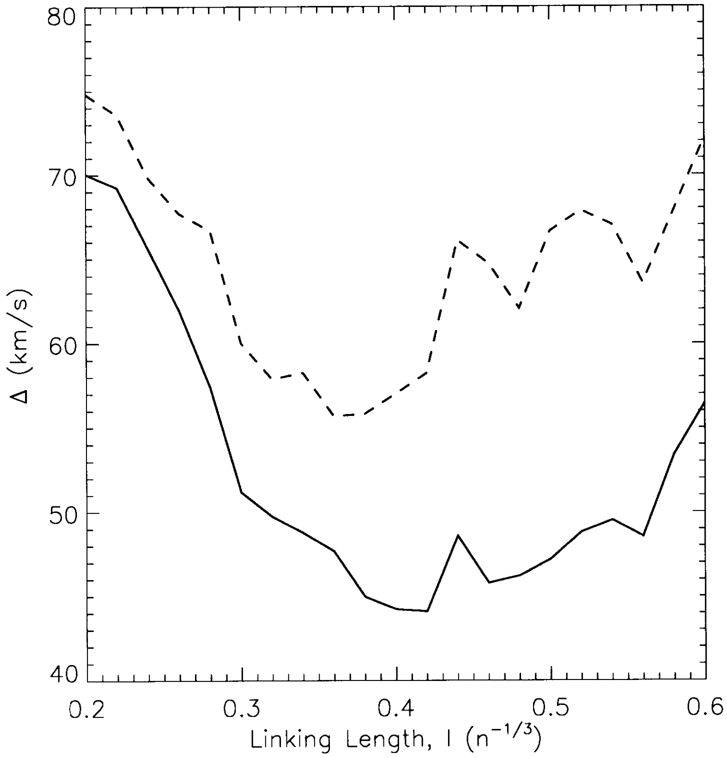

Figure 4.1 Optimal linking length for peculiar velocity recovery. Identifying groups of galaxies with a fixed linking length, l (shown on the horizontal axis), the peculiar velocities of groups with 5 or more members are reconstructed using all groups of 5 or more members as tracers of the density field. Δ (Eq. 4.1) is plotted as a function of l. When inferring the masses from the simulation particles (solid line), the optimal linking length is found to be $l = 0.42\bar{n}^{-1/3}(\Delta_{\rm min} = 44$ km s^{-1}). When inferring mass estimates through the projected mass estimator (dashed line), the optimal linking length is found to be $l = 0.36\bar{n}^{-1/3}(\Delta_{\rm min} = 56$ km s^{-1}). The linking length is in units of the mean inter-particle separation, $\bar{n}^{-1/3} = 3/h$ Mpc.

$l = 0.42\bar{n}^{-1/3}$ (where $\bar{n}$ is the average number density of particles in the simulation) that allows the recovery of the velocity-field with the smallest value of Δ; thus we proceed with groups constructed using this linking length for the remainder of section §4.2.

4.2.3 Group Sizes

When using groups of galaxies to construct the velocity field, it is unclear what limit, if any, should be placed on the minimum group size utilized. Whilst it is difficult to address this question directly in the simulation (since the simulated mass in small groups is significantly larger than the observed dynamical mass estimates), we can gain some insight by studying the effect on the reconstructed velocities of varying the minimum number of mass particles in a group. We consider the estimated peculiar velocities of the test groups (defined according to §4.2.1) in response to a density-field traced by groups with at least N_G members.[3] We compute Δ as a function of N_G for the case where the mass is extracted directly from the simulation, as shown in Figure 4.2 (solid line). It is evident that, providing we know the masses of the groups precisely, including even the smallest groups will improve the reconstruction of the velocity-field. The assumption that we can accurately estimate the mass of small groups is investigated in §4.4 below. It is also evident that to trace larger structures (e.g., groups of size 10–20 members), we only need consider groups of the same approximate mass. For example, the peculiar velocities of groups of 20 or more members can be ascertained by modeling their response to the density-field traced by groups of 20 or more members to an uncertainty $\Delta \sim 50$ km s^{-1}. Similarly, the peculiar velocities of groups of 10 or more members can be ascertained by modeling their response to the density-field traced by groups of 10 or more members to the same uncertainty.

4.2.4 Non-linear Motions of Galaxies

We consider the application of gravitational instability theory to particles without any account for group membership. This is equivalent to selecting a linking parameter l so small that no groups of 2 or more members are identified. We expect that galaxies sufficiently clustered will exhibit non-linear motions that cannot be predicted using Eq. (1.8). This effect is evident in the simulation data — in Figure 4.3(a), we show the prediction of the galaxies' peculiar velocities estimated using Eq. (3.22) plotted against the values of their velocities extracted from the simulation. Figure 4.3(b) shows the same reconstruction for groups of particles (including groups of one) identified using the friends-of-friends algorithm with $l = 0.42\bar{n}^{-1/3}$. Whilst this result is expected, it suggests that linear theory cannot be used to estimate the peculiar velocities of individual galaxies without consideration of group membership. We will discuss this limitation in more depth in Chapter 5.

---

[3] For $N_G > 5$, the test groups with insufficient members are excluded from the analysis.

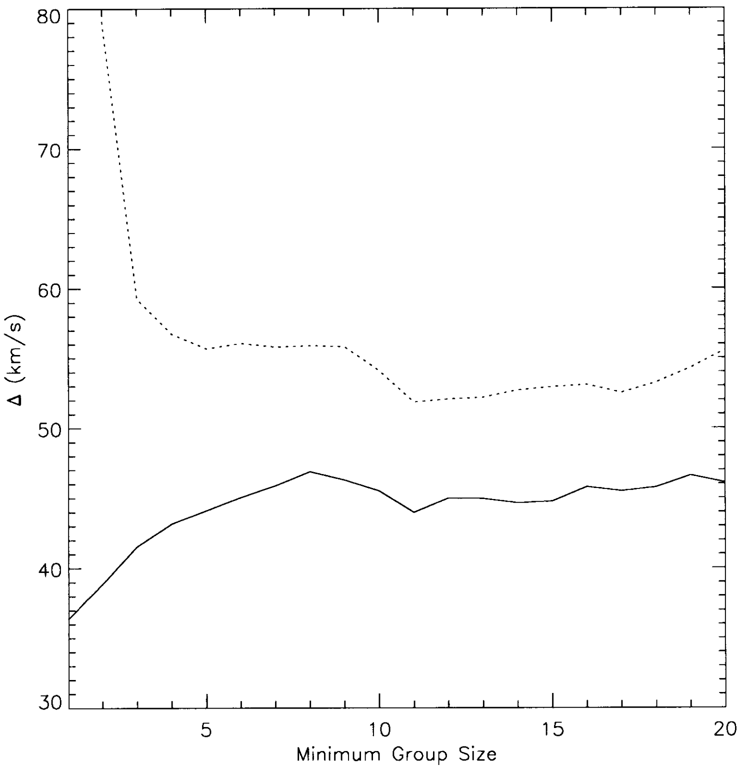

Figure 4.2 Effect of minimum group size on velocity-field recovery. As a function of the minimum group size used to compute the flow-field, the figure shows the quantity Δ (Eq. 4.1), for the following two cases: (i) *[solid line]* Masses calculated by summing mass of simulated particles in group; groups identified using a fixed-length friends-of-friends algorithm with $l = 0.42\bar{n}^{-1/3}$(including groups of one). (ii) *[dotted line]* Masses estimated dynamically using Eq. (3.2); groups identified using a fixed-length friends-of-friends algorithm with $l = 0.36\bar{n}^{-1/3}$.

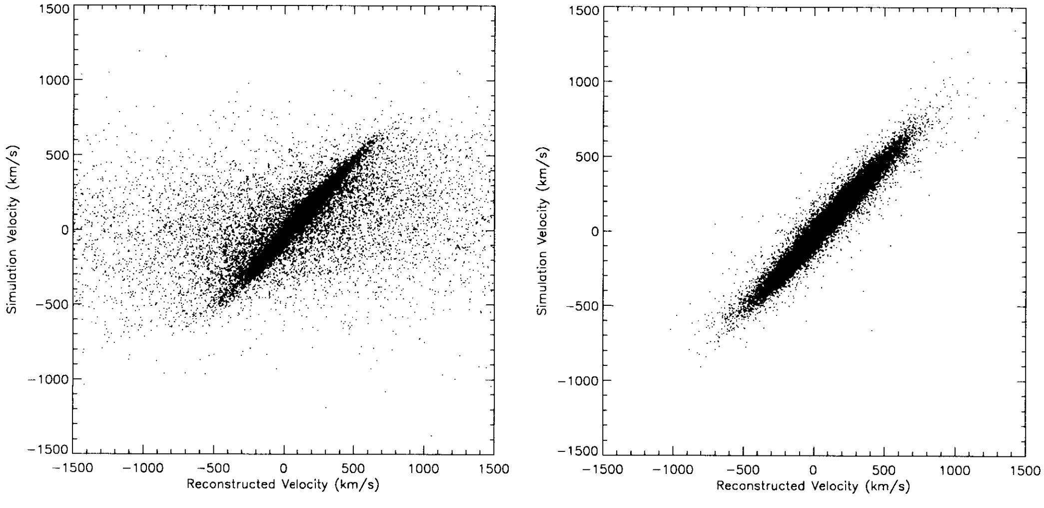

(a) (b)

Figure 4.3 Reconstruction of velocities of individual galaxies compared with groups. The peculiar velocities, reconstructed using linear perturbation theory, are shown for both individual galaxies and for groups of galaxies. (a) The predicted peculiar velocities of individual galaxies inside a sphere of radius $75/h$ Mpc are computed using all other galaxies as mass tracers. The scatter is extremely large since galaxies in clusters exhibit high non-linear motion and the approximation breaks down. Note that the minimizing Δ results in an unphysically small estimate for β, so the value used in (b) is implemented here. (b) The predicted peculiar velocities of groups of galaxies (including groups of one) inside a sphere of radius $75/h$ Mpc are computed using all groups of one or more members as tracers of the density-field ($\Delta = 38.5$ km s^{-1} in this case). Each point represents one cartesian component of the reconstructed velocity, plotted against the corresponding component of the peculiar velocity extracted from the simulation. The masses and distances are taken directly from the simulation and groups are identified using a fixed-length friends-of-friends algorithm with $l = 0.42\bar{n}^{-1/3}$.

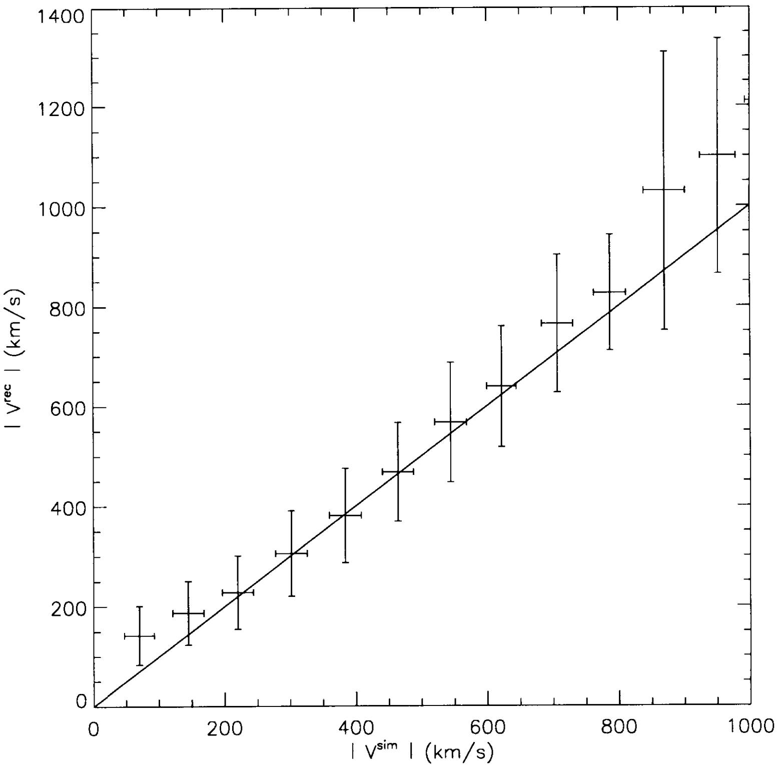

Figure 4.4 Prediction of the magnitude of the peculiar velocity. The magnitude of the reconstructed velocity ($|\mathbf{v}^{\mathrm{rec}}|$) is plotted as a function of the magnitude of the corresponding mean group velocity extracted from the simulation ($|\mathbf{v}^{\mathrm{sim}}|$). The line $|\mathbf{v}^{\mathrm{rec}}| = |\mathbf{v}^{\mathrm{sim}}|$ is overlaid on the figure. There is a small correlation between the error in the magnitude and $|\mathbf{v}^{\mathrm{sim}}|$. The plot is constructed using groups of 5 or more members as tracers of the density field.

4.3 Estimate of Errors

Under the idealized assumptions listed in §4.2.1 above, we have demonstrated that it is possible to optimize the reconstruction of peculiar velocities obtained through the application of gravitational instability theory (§1.3). In this section, we discuss the precision to which one can use the linear approximation to ascertain the peculiar velocity of a group.

Using all groups with 5 or more members as tracers of the density field, we estimate the peculiar velocity of every group with at least 5 members using Eq. (3.22). Figure 4.4 shows the magnitude of the reconstructed peculiar velocity ($|\mathbf{v}^{\mathrm{rec}}|$) plotted against the magnitude of the peculiar velocity extracted from the simulation ($|\mathbf{v}^{\mathrm{sim}}|$). Averaged over all peculiar velocities, we find $|\mathbf{v}^{\mathrm{rec}}| - |\mathbf{v}^{\mathrm{sim}}| = 14 \pm 99$ km s^{-1}, which is consistent with zero, as expected. The uncertainty is small compared with the r.m.s. magnitude of group peculiar velocities (438 km s^{-1}). With the exception of the increase at $\sim$ 1000 km s^{-1}, the absolute error only varies marginally over the entire range of peculiar velocities. This implies that gravitational instability theory cannot be applied to predict very small peculiar velocities ($\lesssim$ 100 km s^{-1}), and, on the other end of the spectrum, the linear approximation begins to break down for velocities $\gtrsim$ 1000 km s^{-1}. This stability in the uncertainty over the intermediate range further suggests that any uncertainty in the direction of the predicted peculiar velocity will decrease when applied to groups with larger velocities (so long as linear theory remains valid).

Such a limitation has been observed in the real Universe (e.g., Tonry et al., 2000) as a result of density perturbations acting over cosmic time to perturb the Hubble flow on small scales (e.g., Peebles, 1976a). Efforts to measure the magnitude of this cosmic thermal velocity have determined values typically in the range of $\sim$ 190 km s^{-1} (Tonry et al., 2000) to $\sim$ 300 km s^{-1} (Giovanelli et al., 1998), although, on small scales, evidence suggests the dispersion of galaxies about their local flow-field is closer to $\sim$ 125 km s^{-1} (Davis et al., 1997). The derived value of 100 km s^{-1} represents a lower-bound to this thermal component and we will use it to understand the limitations of the flow-field model in Chapters 5 and 6.

In Figure 4.5, we show the uncertainty in direction as a function of the magnitude of the peculiar velocity. The line shows an empirical fit to an equation of the form

$$\sigma_\theta = \frac{v_0}{|\mathbf{v}^{\rm sim}|} + \alpha \tag{4.2}$$

where a least squares fit gives v_0 = 4014 km s^{-1} and $\alpha = 4.2°$. Note that this functional form will diverge for small $|\mathbf{v}^{\rm sim}|$, which is unphysical, but is a reasonable approximation for $|\mathbf{v}^{\rm sim}| \gtrsim 100$ km s^{-1}.

4.4 Mass and Distance Estimates

The results presented in §4.2 above represent an idealized scenario, with the assumptions noted in §4.2.1. While we do not intend to examine all of the assumptions in this chapter, we will discuss the results of relaxing two of the assumptions: the knowledge of the precise distance to the group, and its mass.

4.4.1 Mass Estimators

Although we cannot directly measure the masses of groups of galaxies observationally, the dynamics allow for an estimate of the mass without the necessity to make assumptions based on the number of observed members or the luminosity of the group by using an estimator such as the projected mass estimator (Bahcall & Tremaine, 1981) described in §3.1.3.

In the absence of interlopers, the relative error on the estimated mass decreases when considering groups with larger numbers of members (see Figure 4.6). However, we have seen in §4.2.3 above that, *if* the masses are known, including even the smallest groups produces the most reliable reconstruction of the peculiar velocities. The crucial question is whether including small groups will improve the reconstruction

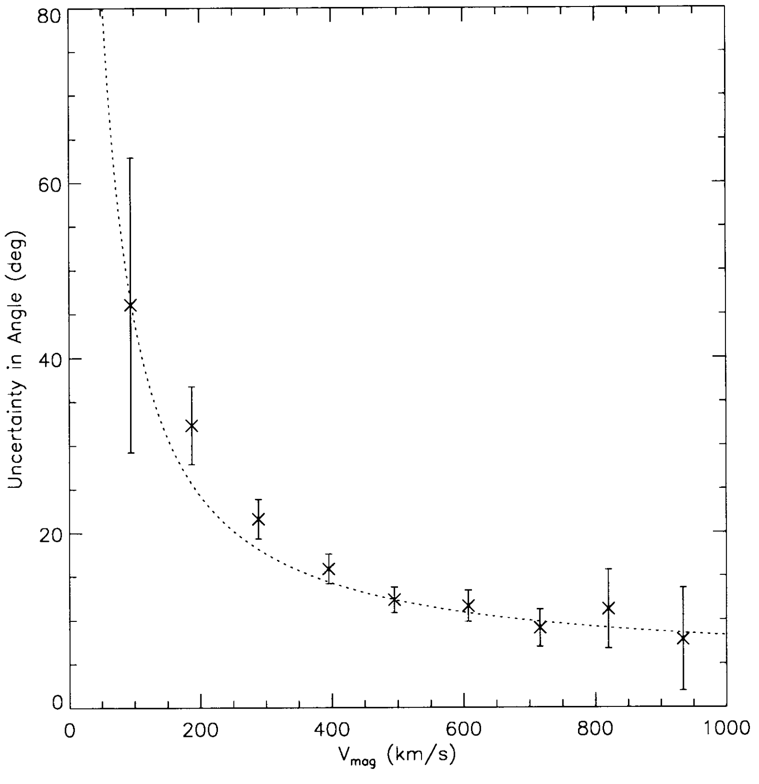

Figure 4.5 Uncertainty in direction of reconstructed peculiar velocities. The figure shows the uncertainty at 68% confidence. The error bars represent 2σ from Poisson statistics. The dotted line shows an empirical fit to an equation of the form (4.2). It is clear that the uncertainty in angle decreases with larger observed peculiar velocities.

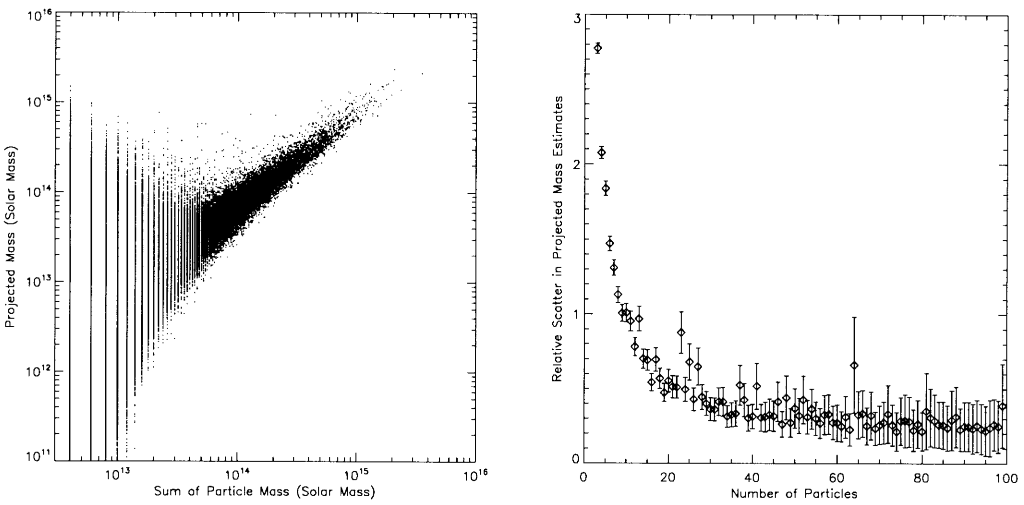

(a) Projected Mass

(b) Relative Scatter

Figure 4.6 Reliability of the Projected Mass estimator. Panel (a) shows the mass estimated from the projected mass estimator as a function of the summed mass of the particles. Panel (b) shows the scatter (defined by the standard deviation divided by the mean) in the estimated values for the projected mass as a function of the number of particles in the group. The error bars assume Poisson statistics, and are shown at the 5σ level. The uncertainty in the estimated mass may be as much as 100% if there are fewer than 10 particles tracing the mass, and the scatter appears to converge at $\sim 20\%$

of the flow-field, and, if so, how small? As noted in §4.2.3, the masses in small groups are significantly overestimated in comparison with nearby groups with similar numbers of members in the real Universe. This exercise will allow an estimate of the point at which the errors in the mass estimates become sufficiently small that their usefulness as a tracer of the density-field outweights the associated errors. In Figure 4.1, the dotted line shows Δ as a function of the linking length for velocities reconstructed using groups of at least 5 members. The linking length that minimizes Δ is $l = 0.36\bar{n}^{-1/3}$, which we will use to construct a group catalog in our analysis below.

We repeat the analysis of §4.2.3 to ascertain the optimal group size. The results are shown by the dotted line in Figure 4.2. As one might expect, the results suggest that including mass estimates from binaries is not sensible, and, if attempting to understand the motions of large groups, only the most massive groups need be modeled. The transition region (which here begins at groups of at least 4–5 members) is not necessarily applicable to groups of galaxies in the real Universe, since these groups represent significantly more massive structures than nearby groups of 5 members observed. We note that in this idealized case, the velocities can be reconstructed to an uncertainty given by $\Delta \sim 55$ km s^{-1}, which does not depend significantly on the minimum group size (above ~ 4). While the uncertainty in the estimated peculiar velocity is $\sim 20\%$ larger than velocities reconstructed using ideal masses, we conclude that the use of the projected mass estimator will not significantly impact our ability to model the (linear) dynamics.

4.4.2 Distance Estimates

While numerous methods are available for estimating distances to galaxies, each is only applicable over a limited range, and often depends on the properties of the galaxy in question. With the availability of redshift estimates, it is possible, in principle, to revise the distance estimates such that the peculiar velocities predicted from the flow-field are self-consistent. We discussed the application of such a technique in §3.2.6, but here we determine the optimal improvement we expect from the application of this technique, under the idealized assumption of an observer at rest with respect to the Hubble flow, considering groups with known masses identified in real-space (as discussed in §4.2.1 above).

We adapt the procedure of §3.2.6 for use under these idealized assumptions, as described below:

1. Initially assume the peculiar velocities of all groups are zero.

2. Subtract the group's line-of-sight peculiar velocity from the redshift to estimate the Hubble distance.

3. Estimate the peculiar velocities of the groups using Eq. (3.22) and repeat steps 2–3.

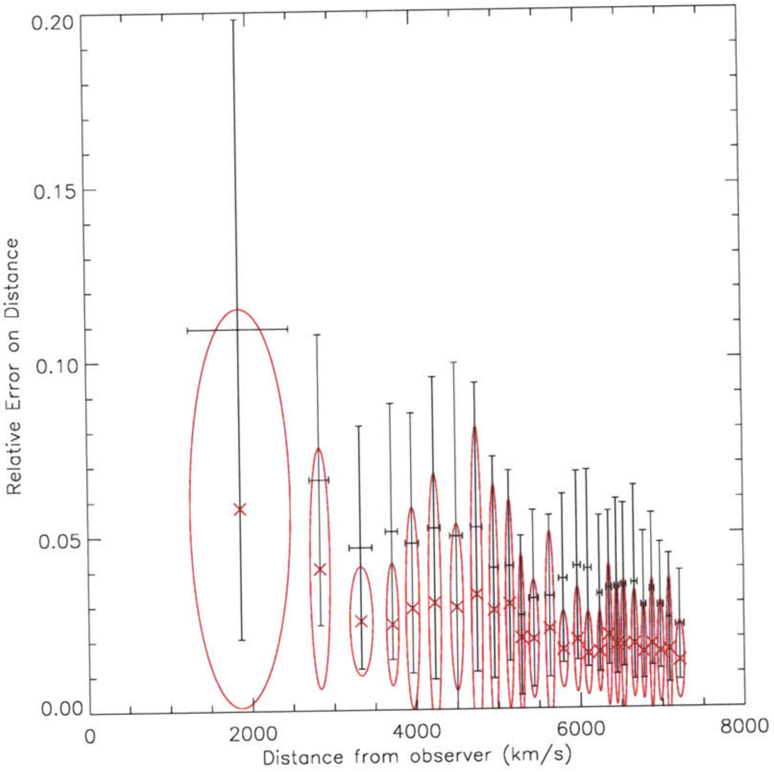

Figure 4.7 Error on distance estimate. The figure shows the relative error on the estimated distance from the center of the simulation to a group, computed (i) assuming the redshift is proportional to the distance (black vertical bars indicate 1σ errors), and (ii) by the iterative procedure discussed in §4.4.2 (red ellipses with centers marked with '$\times$' indicate 1σ errors). It is evident that applying the technique of §4.4.2 with accurate knowledge of the group mass, the error on the distance estimates to groups can be reduced by approximately 50 per cent.

Figure 4.7 shows the relative error on the distance before and after the iterative distance-computation. The graph demonstrates a decrease in the error on the distance as a result of this procedure. The mean absolute error, assuming Hubble's law, is 207 km s^{-1}, which is reduced to 124 km s^{-1} after the iterative procedure. The mean relative error nearby (inside 3000 km s^{-1}) is reduced from 10% to 5%, and, for groups beyond 3000 km s^{-1}, is reduced from 4% to 2%. Therefore, if the masses of the groups are known accurately, as well as the motion of the observer, the application of this iterative technique to compute the distances/peculiar velocities reduces the error on the distance estimates by $\sim$ 50%. It is very difficult to test this prediction in the real Universe, however, since the estimated errors on distances beyond $\sim$ 3000 km s^{-1} are usually 10–20%, so we cannot know how well Hubble's law performs in reality, nor how good (or bad) the estimated distance is in comparison with the true distance. Uncertainties in distances of less than 5% are generally considered ideal, and therefore there is limited utility in applying this method beyond $\sim$ 6000 km s^{-1}, where peculiar velocities of the order of 300 km s^{-1} will only contribute 5% to the uncertainty in distance.

4.5 Summary

Using the $z = 0$ snapshot of the ΛCDM Hubble Volume simulation, we have tested the method employed to reconstruct peculiar velocities of galaxy groups, as described in §1.3. We have demonstrated that the peculiar velocities of groups of galaxies will have an expected minimum uncertainty of $\sim$ 100 km s^{-1} in their magnitude, under the idealized assumptions of accurate mass and distance estimates. When estimating group masses dynamically, it is clear that including two– or three–particle systems will reduce the utility of the flow-field due to increased errors in the estimated masses. The estimates of masses are reliable to within $\sim$ 20% when considering large systems (50 or more particles). It is evident that there is an intermediate scale, which appears to be on the low end of this range, where the inclusion of groups with large errors will allow the flows of similarly-sized groups to be studied in a meaningful manner. Since groups of 5 or more members in the simulation are almost an order of magnitude more massive than the LG, we cannot draw specific conclusions from this analysis.

The uncertainty in the direction of the peculiar velocity of a group decreases for larger peculiar velocities (up to a limit of $\sim$ 1000 km s^{-1}). If these results are applicable to the real Universe then the calculated LG motion with respect to the CMB, which has a velocity $\sim$ 627 km s^{-1} (e.g., Erdoğdu et al., 2006b), will have an uncertainty in its direction of $\sim$ 11° (68% confidence) if estimated using the techniques discussed in this chapter.

Without accurate redshift-independent distance estimates to the groups, the distances to groups can only be estimated from their redshifts. Using the technique discussed in §3.2.6, we have demonstrated here that one can improve estimates of the distances to groups by up to $\sim$ 50% over simple application of Hubble's law. This is under very idealized conditions, however, and with the uncertainties in group membership and masses that we will face when considering the 2MRS group catalog, in addition to the peculiar velocity of the LG itself, it is unlikely one could achieve this limit. We will discuss this further in the context of observed data in Chapter 5.

The analysis presented in this chapter has addressed the limitations of the technique we implement to construct the flow-field. Certainly there are additional sources of error that have not been modeled in this chapter, however due to the limitations of the simulation, we do not pursue this topic in the context of the Hubble Volume simulation. We instead turn to the 2MRS data and redshift-independent distance estimates to ascertain the observed limitations of the model.

Chapter 5

Estimating Distances using the Flow-field Model

In Chapter 3, we constructed a model of the flow-field that predicts the peculiar velocities of test masses given knowledge of their spatial locations. While this is indeed an insightful analysis tool, one of the most powerful uses for the model of the flow-field is the ability to estimate the distance to a galaxy or cluster with only angular position and redshift information. In this chapter we discuss the flow-field as a tool to estimate distances from three easily-measured observable quantities: right ascension, declination and redshift.

We begin by discussing the issue of degeneracy in the redshifts of test masses in the vicinity of galaxy clusters (§5.1). In §5.2, we present the method used to convert the flow-field model into a tool for estimating distances; we show the results in §5.3. Utilizing a sample of redshift-independent distance estimates to nearby galaxies to calibrate the model of the flow-field, we place limits on the parameter β (§5.4). We then use the model to estimate distances to galaxies in 2MRS and show the improvement expected from the use of the model of the flow-field over the application of Hubble's law (§5.5). In §5.6, we compare the estimated distances from the flow-field model with a sample of distance estimates from the *SFI++* data set. Finally, we summarize our conclusions in §5.7.

5.1 Redshift Degeneracies

Suppose there exists a spherical dark matter halo of mass M (which, for the purposes of this illustration, we will model as a point particle) at a distance $v_H = H_0 D$ from the origin (see Figure 5.1). In the figure, the filled circle indicates the location of the dark matter halo, and the open circle indicates a test particle at a distance R from the center of the halo ($R \ll D$) and an angle θ ($-\pi < \theta < \pi$) with respect to the line-of-sight, forming a plane with the dark matter halo and the observer. If this overdensity is the only inhomogeneity in an otherwise uniformly-dense Universe, then from Eq. (3.12), an observer at rest with respect to the Hubble flow located at the

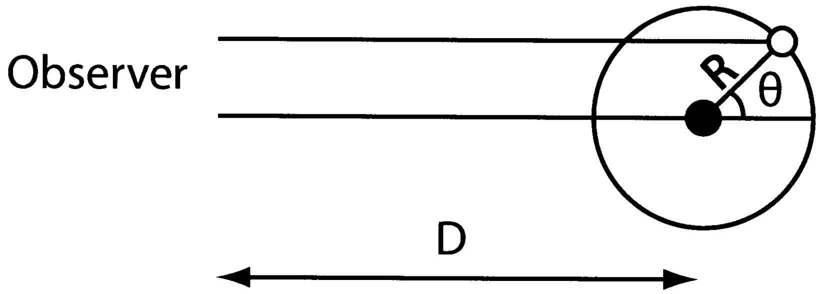

Figure 5.1 Illustration of components of redshift measurement near a dark matter halo. The filled circle indicates the center of the spherical mass. The open circle indicates the location of the test mass.

origin will measure the redshift of the test mass as

$$cz = H_0(D + R\cos\theta) - \alpha\frac{M}{R^2}\cos\theta \tag{5.1}$$

where $\alpha \equiv H_0\beta/(4\pi\bar{\rho})$, β is defined according to Eq. (1.7) and $\bar{\rho}$ is the background density. Objects with $-\pi/2 < \theta < \pi/2$ will therefore have redshifts smaller than that expected from the Hubble flow, and objects with $|\theta| > \pi/2$ will have redshifts larger than that expected from the Hubble flow.

For objects along the indicated line of sight (i.e. $R\sin\theta = s$, where s is constant), if s is sufficiently small, the equation will have multiple roots for fixed z, i.e. one redshift can correspond to multiple distances along the line of sight.

In this example, we have assumed the linear approximation holds. However, sufficiently close to the cluster, the motion becomes highly non-linear. Inside the core of a rich cluster, measured line-of-sight motions can exceed 10^3 km s^{-1}. While this example illustrates the principle of degeneracy in redshift-distance mapping in the vicinity of clusters, the reality is more complex and care must be taken when estimating the distance from the flow-field. We will discuss our approach in more detail below.

5.2 Method

We begin with a velocity-field constructed using the method of §3.3 that has been finely sampled in the radial direction at distances between 0 and 12,000 km s^{-1} at a finite number of angular coordinates distributed uniformly across the sky, and evaluate the velocity of the LS, $\mathbf{u}_{\rm pec}$ (i.e. the point located at the origin). At every grid point we record the distance from the origin, v_H (in units of velocity), and evaluate the quantity

$$cz = v_H + (\mathbf{v}_{\rm pec} - \mathbf{u}_{\rm pec}).\hat{\mathbf{r}} \tag{5.2}$$

where $\mathbf{v}_{\rm pec}$ is the predicted LR-frame peculiar velocity at each grid point. cz represents the predicted redshift, relative to the LS, of a test mass observed at the grid point; $\hat{\mathbf{r}}$ is a unit vector in the direction of the grid point from the origin.

We have now constructed a mapping between redshift and distance that can be inverted using an interpolation technique, however the mapping will suffer from the degeneracies described in §5.1 above. To remove the degeneracy, we follow a two-step process: firstly, we consider the non-linearities that may be encountered near the cores of galaxy clusters (§5.2.1) and, secondly, we remove the degeneracies in any remaining triple-valued regions (§5.2.2).

5.2.1 Cluster Cores

The motions of galaxies located in the cores of clusters are highly non-linear, and linear perturbation theory cannot be used to predict their peculiar velocities. When creating a map in redshift-space of galaxies associated with clusters, we find the dispersion in redshift-space is far greater than the angular extent of the cluster, creating so called *fingers of god* that point toward the observer (Jackson, 1972). Due to the non-singular form of the density profile assumed (§3.2.3), the flow-field model will contain few predictions of peculiar velocities that are sufficiently large to invalidate the approximation, however the model was not intended to predict velocities in the cores of clusters. Observationally, however, we find galaxies (for example) in the Virgo Cluster with peculiar velocities over 10^3 km s^{-1} above (and below) the mean heliocentric velocity of Virgo. Since the goal is to be able to use the model to predict distances to observed galaxies, the mapping from redshift to distance must allow for these motions in the non-linear regime.

When a galaxy is observed in the direction of the core of a cluster, and has a redshift close to the mean redshift of the cluster, it may still be far enough away to avoid susceptibility to the triple-value degeneracy described in §5.1. However we cannot distinguish whether it is moving in the Hubble flow, modified by the infall to the cluster, or located in the core of the cluster exercising non-linear motion. Without a redshift-independent distance estimate, we can do no better than to place it at one of two (or potentially three) possible locations, based on the available information from the flow-field.

The velocity dispersion of a group provides a measure to guide the choice, however groups with few observed members can have just as large velocity dispersions as groups with hundreds of observed members; in the former, the probability that one member is an interloper is significantly higher and this will also tend to increase the inferred velocity dispersion. What is required is a method that assigns a galaxy to the position of the group (rather than in front or behind) that accounts for the probabilities of observing the galaxy in these three regions. Approaches assigning the probabilities based on a combination of the luminosity function and overdensity have been used in the past (e.g., Strauss & Willick, 1995; Tonry et al., 2000); however in the case of group masses which are estimated dynamically, the estimated overdensity is not necessarily representative of the probability of observing a galaxy in the group. Here we propose a simple method based solely on the number of group members observed in the group and the measured velocity dispersion of the group, assigning a galaxy position to the center of the cluster if it lies "along the line-of-sight" to the cluster (see below), and has a redshift that satisfies $cz_{\mathrm{group}} - v_a(N,\sigma) < cz_{\mathrm{galaxy}} <$

$cz_{\rm group} + v_a(N, \sigma)$.

Assuming a normal distribution of line-of-sight velocities, we choose $v_a(N, \sigma)$ such that, had we applied the technique to the galaxies assigned to the group, we would assign at most 3 galaxies incorrectly, but at least 10 correctly. The choice these thresholds are arbitrary, but motivated by the observed length of the finger-of-god in the Virgo cluster, and capped at a minimum of 1σ. $v_a(N, \sigma)$ is therefore given by

$$v_a(N,\sigma) = \begin{cases} \sigma\sqrt{2}{\rm erf}^{-1}[N-3] & \text{if } N > 10 \\ \sigma & \text{otherwise} \end{cases} \tag{5.3}$$

where N is the number of member galaxies assigned to the group and σ is the measured velocity dispersion. ${\rm erf}^{-1}[z]$ is the inverse of the error function, such that

$${\rm erf}({\rm erf}^{-1}[z]) = z \tag{5.4}$$

where

$${\rm erf}[z] \equiv \frac{2}{\sqrt{\pi}} \int_0^z e^{-t^2} {\rm d}t \tag{5.5}$$

The second consideration is whether the galaxy is sufficiently close to the cluster that it should be considered along the line-of-sight to the group. We assume that a galaxy is sufficiently close if it lies no more than a (transverse) distance R_c from the identified center of the group, where we define R_c such that the average density contrast inside a sphere of radius R_c centered on the group is given by δ_c. This implies the following scaling relation:

$$R_c = R_F \left(\frac{M}{M_\odot}\right)^{1/3} \tag{5.6}$$

where R_F is a specified fiducial radius. We choose R_F such that R_c computed for Virgo corresponds to 6° at the distance of Virgo, which is motivated by the observed angular distribution of members of the Virgo cluster on the sky (see Figure 3.1).

If a member is not associated with the cluster core through this method, we place it at the distance implied by the flow-field, subject to §5.2.2 below.

5.2.2 Triple-valued Regions

Along each radial line, we have computed the observed redshift at finely sampled intervals in real-space distance traveling outward along the line. For a chosen redshift, we can test whether it is degenerate in distance by traveling along the line in an outward direction from the origin to find the distance where the value of the measured redshift is first crossed, and compare this with the distance obtained when travelling along the line in the inward direction from the edge of the sample. In the case of a degenerate redshift-distance mapping, the distances will differ.

Since the location of the central value in a triple-valued region depends heavily on the assumed potential of the cluster, we choose to place these galaxies at the center of the region as follows: For the value encountered first in the outward (inward) radial direction, we search at successively smaller (larger) redshifts to find the distance at which the redshift is no longer degenerate. We place the observed galaxy at the mean distance of these two points. At this stage, we have removed all degeneracies in the redshift-distance mapping and can invert the relation using an interpolation technique.

5.2.3 Application to an Observed Redshift

The prescription above decribes the method used to create a mapping from redshift to distance for spaced intervals in distance along a finite set of radial trajectories from the observer. When attempting to estimate the distance of an object with a measured angular position, we have two options:

1. Interpolate the result based on 4 surrounding radial trajectories — i.e. evaluate the distance at the corresponding redshift along the 4 surrounding trajectories (which essentially forms a rectangle on the sky) and then use 2-D interpolation to evaluate the distance for the measured right ascension and declination.[1]
2. Calculate the peculiar velocity at finely sampled distance intervals along the specified trajectory (i.e. line of sight to the target) and evaluate the distance according to the methods of this section.

While the former is the most practical method for extrapolating distances from a tabulated model, for the purposes of this Chapter we will utilize the second option for increased precision. Redshifts are sampled at 20 km s^{-1} intervals along the radial direction to the observed source, for a region spanning 2000 km s^{-1} above and below the observed redshift.

5.3 Results

For an object observed at redshift z ($z > 0$) with angular position (α, δ), we convert the position in redshift space (assuming radial coordinate cz) to cartesian supergalactic coordinates. We apply the method of §5.2 to provide distance estimates to points on a uniform grid within the supergalactic plane; the results are shown in Figures 5.2 and 5.3. The figures contain lines linking the "observed" position in redshift-space (the circles) to the predicted Hubble distance (H_0D). The resulting maps demonstrate the expected features: in the close proximity to clusters, objects are placed at the core of the cluster (due to the resolution of the map, this is only visible in the case of the Virgo Cluster at (SGX, SGY) $\sim$ (-250, 1200)). Farther from the cluster cores, we see the result of predicted infall (demonstrated clearly near Perseus-Pisces at (SGX, SGY) $\sim$ (4000, -2000)) — galaxies falling toward the cluster on the near (far) side will have higher (lower) redshifts than predicted by the Hubble flow, so their distances are closer (farther) than we expect from a redshift-inference. At

---

[1] Note that this requires sufficiently fine sampling such that the cluster cores are larger than the spacing between radial trajectories at the approximate distance considered.

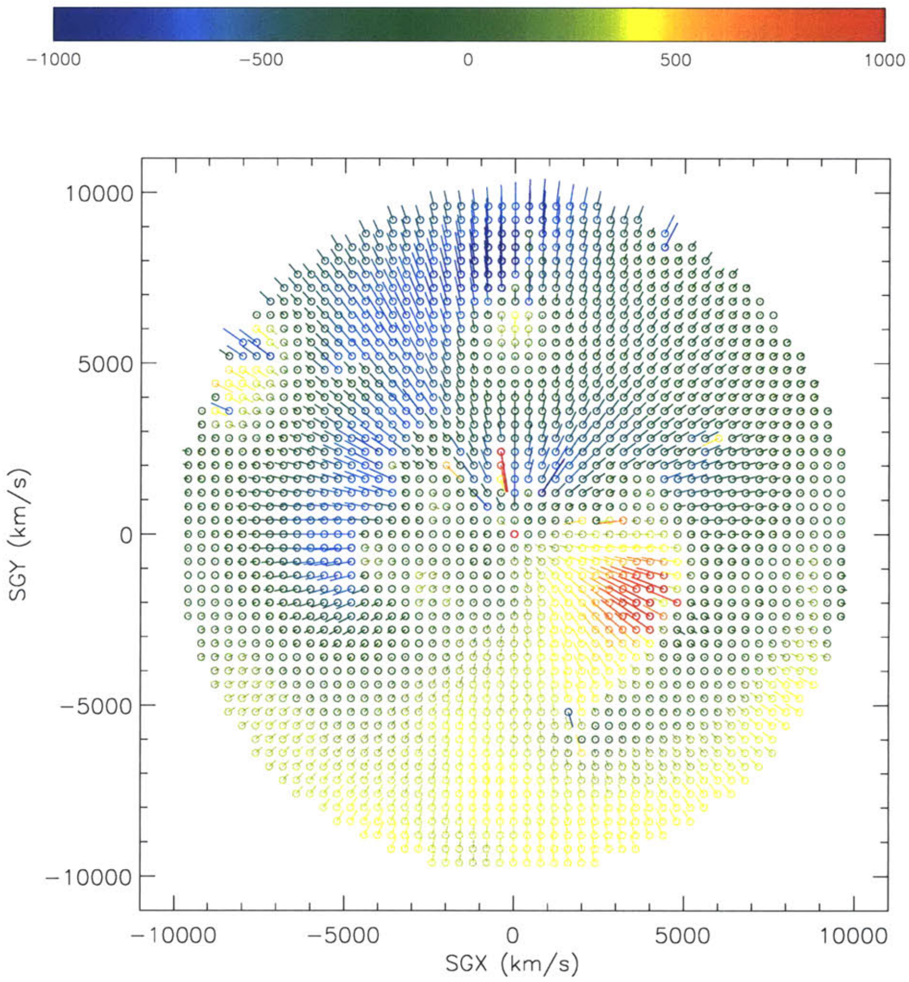

Figure 5.2 Estimating distances in the supergalactic plane (CMC). For a galaxy that lies in the supergalactic plane, with coordinates (SGX, SGY) computed from the corresponding polar coordinates where the radial coordinate equal to the LS-centric redshift, the distance is given by tracing the circle (position in redshift space) to the end of the line (position in real-space). The above plot is computed assuming the coherent mass correction. The color indicates the magnitude of the difference between the distance inferred simply from an LS-centric redshift and the distance predicted from the model — red (blue) indicates that the LS-centric distance is larger (smaller) than the predicted distance. In the vicinity of large clusters, the estimated distance for galaxies with velocities near the cluster redshift are placed at the distance of the center of the cluster. However, with the map resolution above, this is only visible for Virgo (SGX, SGY) $\sim$ (-250, 1200). Farther from large clusters, the infall can be seen by objects on the near (far) side being placed at lower (higher) distances than obtained from redshift-inference. The units of the indicated color scale are km s^{-1}.

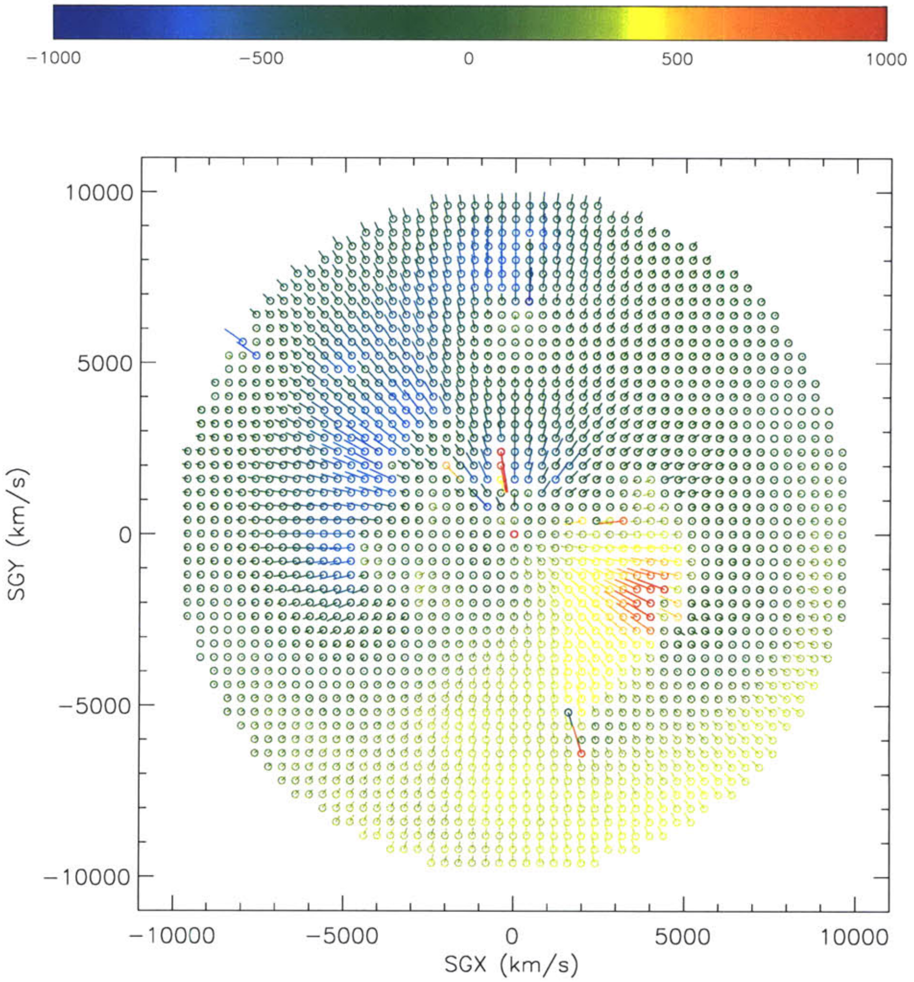

Figure 5.3 Estimating distances in the supergalactic plane (IMC). For a galaxy that lies in the supergalactic plane, with coordinates (SGX, SGY) computed from the corresponding polar coordinates with a radial coordinate equal to the LS-centric redshift, the distance is given by tracing the circle (position in redshift space) to the end of the line (position in real-space). The above plot is computed assuming the incoherent mass correction. The details of the figure are as Figure 5.2.

large scales, we see the effect of the predicted dipole on the result. Galaxies in the direction between Hydra and Virgo are assigned distances larger than their redshift implies, since their redshifts will be underestimates of the Hubble-flow (due the component of the LG motion in this direction). For galaxies in the opposing direction, the reverse is true. In the overall picture, the effects of the dipole component and infall toward clusters compete on small scales to obtain the predicted mapping. The difference between Figures 5.2 and 5.3 is small; the former predicts slightly larger corrections to the Hubble distance at large distances, and there is also a slight rotation in the direction of the dipole term (this will be discussed further in Chapter 6). The structures discussed in §3.3 above are observed in these maps. Note also that locally ($cz \lesssim 3000$ km s^{-1}), the redshift (recall that this is measured relative to the LS frame) provides a reasonable indicator of the Hubble distance, once corrected for infall into the Virgo cluster.

We show the effect of the mapping across the entire sky at successive shells in redshift-space in Figures 5.4 and 5.5. The figures show the mapping from redshift to distance as a function of angular position. While similar to Figures 3.14 and 3.15 in Chapter 3, these graphs represent a mapping from redshift-space to distance, instead of the inverse. The degeneracies in redshift discussed in §5.1 above dictate that a unique mapping is not possible in the vicinity of galaxy clusters, so the smooth variation in predicted peculiar velocities as a function of angular position seen in Figures 3.14 and 3.15 is not always present in Figures 5.4 and 5.5. Notice that the large-scale structure of Figures 3.14 and 3.15 is preserved and, as expected, as we reach the edge of the sample the mapping from redshift-space to real-space is observed as the subtraction of the LS dipole, perturbed by the density-field at the chosen redshift; the plots converge toward the inverse of the LS dipole (Figure 3.11) as the sample limit is approached.

Inside ~ 5000 km s^{-1}, Figures 5.4 and 5.5 express nearby identical features. At 1000 km s^{-1}, the green (very slightly blue) region coincident with the direction to the core of the Virgo cluster ($SGL \sim 100°$, $SGB \sim 0°$) indicates that objects in this region observed with a LS-centric velocity of 1000 km s^{-1} should be placed slightly farther (246 km s^{-1}, to be precise) than would be calculated using Hubble's law, resulting in the galaxies close to Virgo with a redshift of ~ 1000 km s^{-1} being placed at a distance equivalent to 1246 km s^{-1}. In the locations directly surrounding Virgo, we see the triple-valued region that places objects at the location of the Virgo Cluster. Farther from the cluster (noticeably as we look to lower latitudes), the model predicts infall of these objects into both Virgo and the Hydra-Centaurus region. According to the model predictions, due to the relative positions of the LG, Virgo, Hydra, and the observing target, objects observed with redshifts of 1000 km s^{-1} are actually farther from us than we would infer from Hubble's law, since their infall is directed toward the supergalactic plane and the dipole component from the LG motion is directed toward Hydra.

At 2000 km s^{-1} in redshift-space, this effect is amplified; in fact, with the relative positions described above, the line-of-sight components of the peculiar velocities at the dark-blue-indicated locations in the southern supergalactic hemisphere are actually negative relative to the LR frame, and the effect is amplified when subtracting the

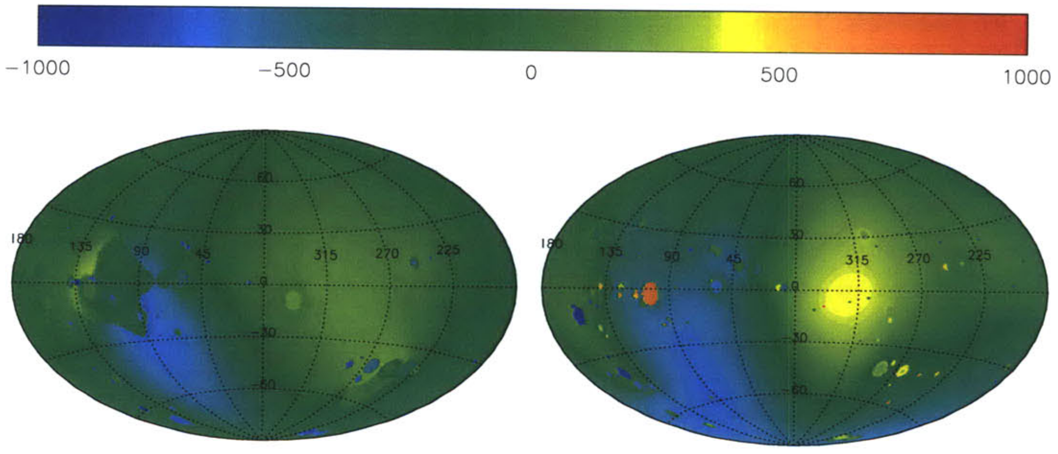

(a) $Z = 1000$ km s^{-1}

(b) $Z = 2000$ km s^{-1}

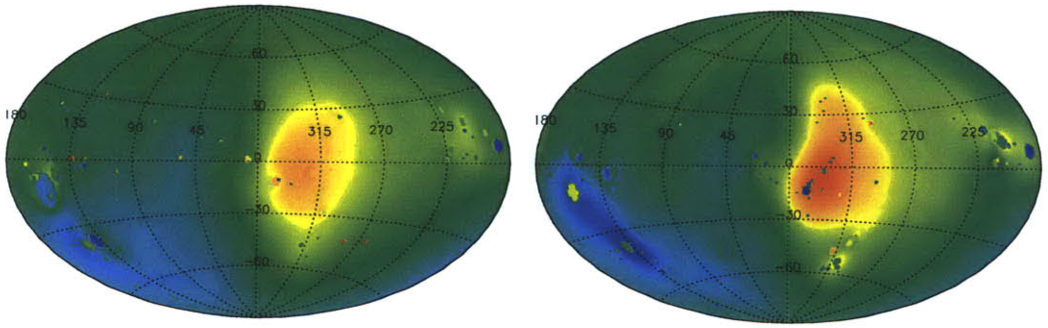

(c) $Z = 3000$ km s^{-1}

(d) $Z = 4000$ km s^{-1}

Figure 5.4 Estimated distance as a function of redshift and angular position (CMC). For concentric spherical shells at increasing LS-centric redshift, the plots show the difference between the distance derived from Hubble's law and the distance estimated from the model assuming the coherent mass correction. Blue shading indicates that a galaxy observed with the indicated redshift has a peculiar velocity (in the LS frame) toward the LG and should therefore be placed farther from the observer; red shading indicates that the galaxy has a peculiar velocity away from the LG (in the LS frame) and should be placed closer than would be inferred from the redshift distance. A green region indicates that the redshift distance will act as a good indicator of the distance to the object. The small "specs" visible on the plot are due to the collapsing of fingers-of-god for small groups. The units of the indicated color scale are km s^{-1}. See the text for details on the contents of the figure.

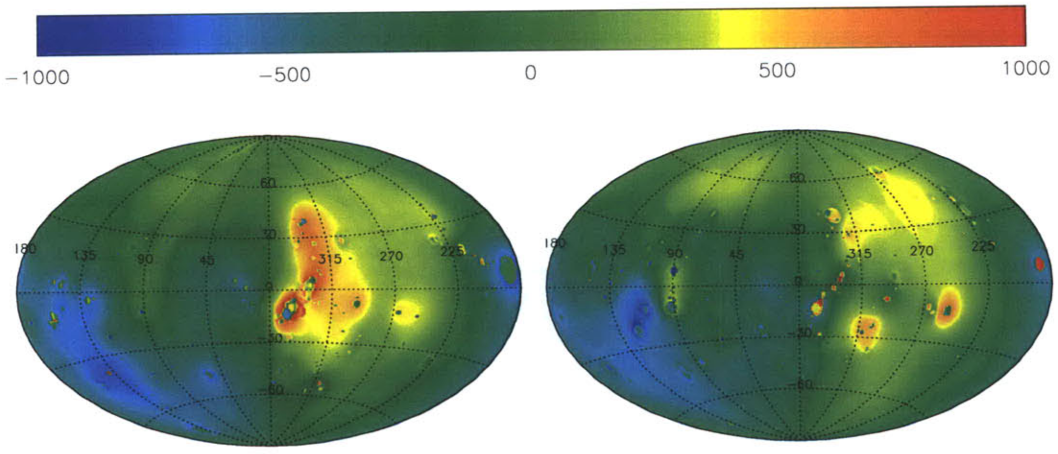

(e) $Z = 5000$ km s^{-1}

(f) $Z = 6000$ km s^{-1}

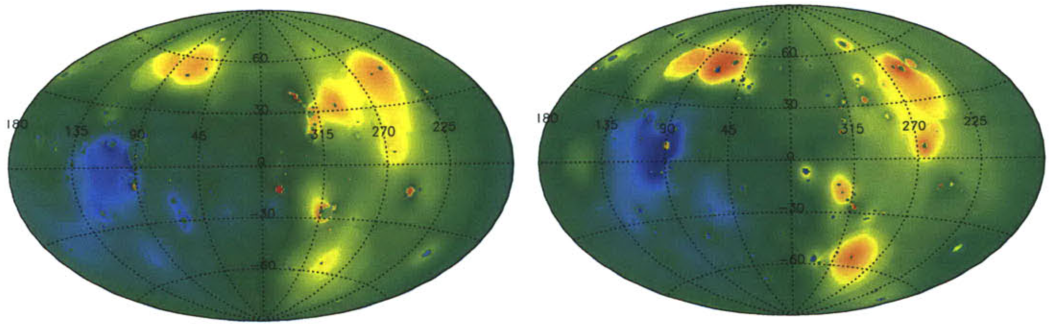

(g) $Z = 7000$ km s^{-1}

(h) $Z = 8000$ km s^{-1}

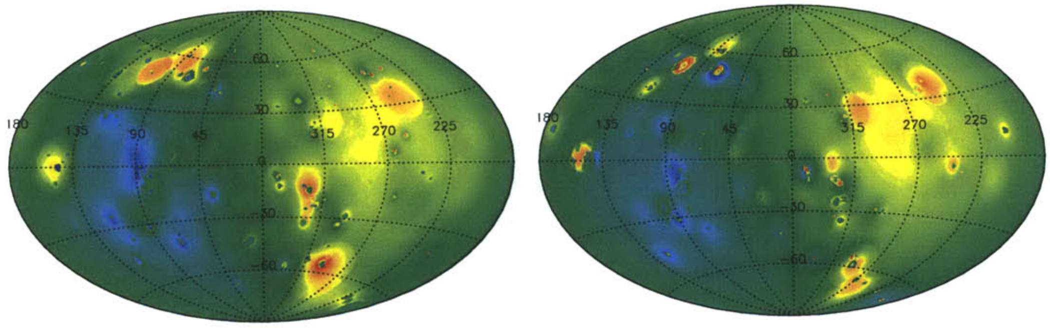

(i) $Z = 9000$ km s^{-1}

(j) $Z = 10000$ km s^{-1}

Figure 5.4 — *continued...*

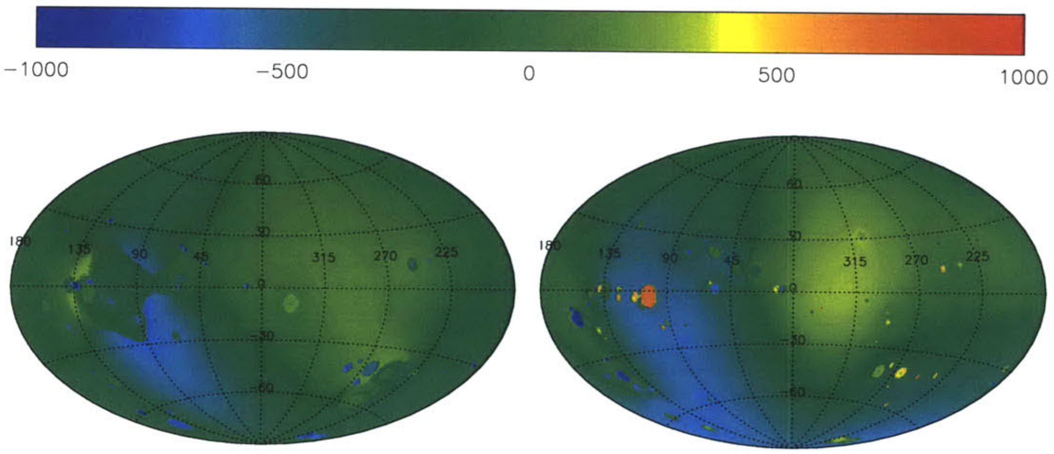

(a) $Z = 1000$ km s^{-1}

(b) $Z = 2000$ km s^{-1}

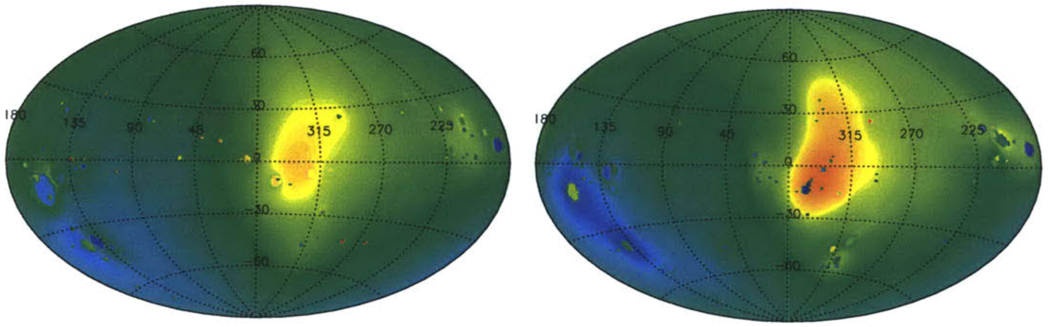

(c) $Z = 3000$ km s^{-1}

(d) $Z = 4000$ km s^{-1}

Figure 5.5 Estimated distance as a function of redshift and angular position (IMC). For concentric spherical shells at increasing LS-centric redshift, the plots show the difference between the distance derived from Hubble's law and the distance estimated from the model assuming the incoherent mass correction. The details are as Figure 5.4. See the text for details on the contents of the figure.

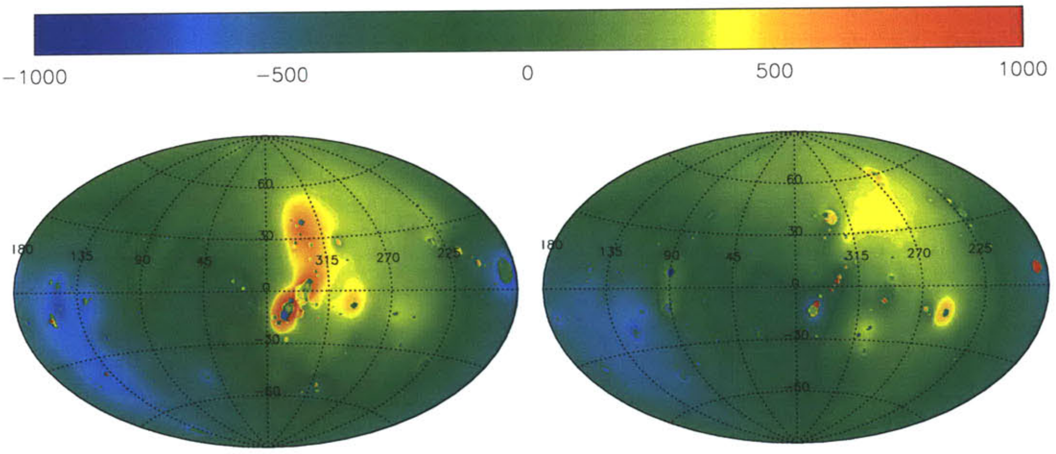

(e) $Z = 5000$ km s^{-1}

(f) $Z = 6000$ km s^{-1}

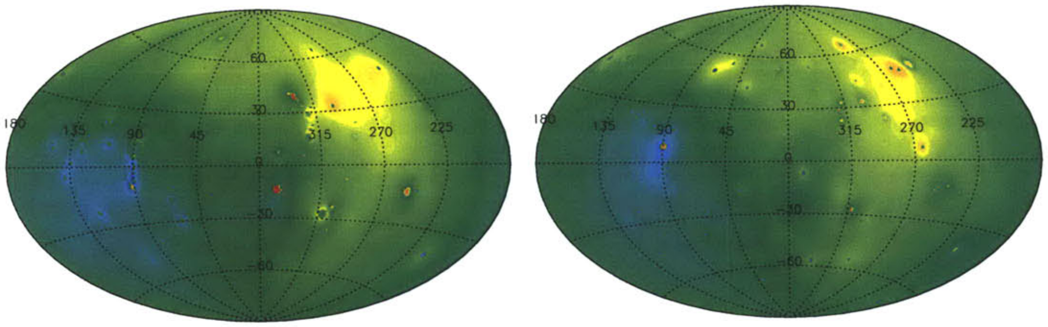

(g) $Z = 7000$ km s^{-1}

(h) $Z = 8000$ km s^{-1}

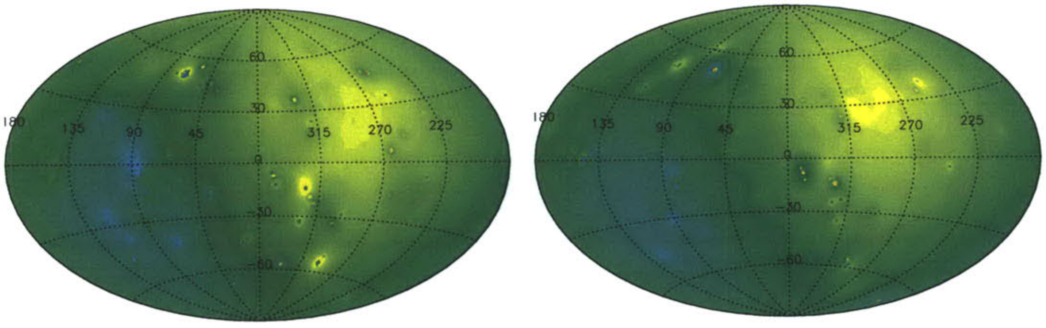

(i) $Z = 9000$ km s^{-1}

(j) $Z = 10000$ km s^{-1}

Figure 5.5 — *continued...*

motion of the LG. We observe that, at the core of the Virgo Cluster, galaxies observed with 2000 km s^{-1} velocities should be placed at the position of the Virgo center (indicated by the red shading); the yellow band surrounding Virgo represents the location of galaxies on the near-side of Virgo that are falling toward the cluster with sufficiently high velocities that a redshift-inference would overestimate their Hubble distances. In this plot we also notice that objects coincident with Centaurus ($SGL \sim 160°$, $SGB \sim -10°$) and Hydra ($SGL \sim 140°$, $SGB \sim -40°$) with observed 2000 km s^{-1} redshifts should be moved to the cores of the respective clusters.

Objects with LS-centric redshifts of 3000 km s^{-1} coincident with Centaurus are placed at the distance of the cluster (approximately 3500 km s^{-1}), and similarly with Hydra (although in this case the distance is overestimated – see §3.3). The surrounding green regions signify infall toward the group, where the velocity is directed such that the line-of-sight component of the infall cancels with the motion of the LG in the direction of Hydra. Since the physical distances between objects of the same angular separation naturally increase with the distance from the observer, the component of the infall of galaxies surrounding the large clusters (e.g., Hydra and Centaurus) is only aligned with the line-of-sight vector in the very close vicinity of the cluster; the infall of objects several degrees from the cluster will be directed toward the cluster, which is often better described by a tangent to the line-of-sight vector. Hence the LS dipole dominates the field away from the cluster centers. At 3000 km s^{-1}, we also observe the yellow/orange region near ($SGL \sim 330°$, $SGB \sim -10°$), in which galaxies are predicted to participate in infall toward the Perseus-Pisces region.

At 4000 km s^{-1}, beyond Hydra-Centaurus, the majority of the LG motion has been accounted for and is therefore clearly visible in the plot by the blue (yellow) shading toward (away) from the Virgo-Hydra direction. The core of, and triple-valued region around, the Perseus-Pisces cluster appears blue at ($SGL \sim 350°$, $SGB \sim -10°$); a similar feature is observed near the Norma Cluster at ($SGL \sim 190°$, $SGB \sim +5°$). The cores of Centaurus and Hydra are also observed.

At 5000 km s^{-1}, the Perseus-Pisces region appears green, since the cluster center is located not much farther than 5000 km s^{-1}, and the surrounding red region indicates infall toward this region. In Figure 5.4, we begin to see the core of the Coma Cluster at ($SGL \sim 90°$, $SGB \sim +10°$), which becomes more obvious as we approach 7000 km s^{-1}. At 8000 km s^{-1}, we observe the correction for galaxies in the Coma Cluster core. As we look to deeper slices in redshift space, the angular resolution required to resolve features increases, and as we progress toward 10,000 km s^{-1}, the clusters become successively smaller perturbations on the dipole term from the motion of the LG. The noticable differences between Figures 5.4 and 5.5 are due to the different bias corrections. In the far field, the application of the incoherent mass correction will result in negligible peculiar velocities for most test masses; the distortions due to the observed groups are significantly amplified in the case of the coherent mass correction.

Shapley and Hercules represent the largest distortions in the distant field. Near the edge of the sample, the distance obtained by simply correcting from the LS frame to the LR frame is expected to halve the relative error on the distance from a simple redshift-inference if we assume that the peculiar velocity of the LG is typical of galaxy group peculiar velocities. The small specs that are noticeable mostly on the deeper slices represent the fingers-of-god of small groups; the change in color indicates the necessity to move a galaxy observed at that redshift to the core of a cluster close to the line of sight. The reason there are an increased number at larger redshifts is simply due to the larger surface area of the shell.

5.4 Calibration with Redshift-independent Distance Estimates

So far, we have been proceeding under the apparently arbitrary choice of a value for β. The magnitudes of the peculiar velocities (of both external groups/galaxies and the LG) depend critically on this parameter, and therefore modifications to the choice of β would result in different estimated peculiar velocities at every point in the reconstructed flow-field. The predicted peculiar velocities in the LR frame are proportional to β. However, the construction of the density-field in a self-consistent manner (§3.2) will modify the distances to groups depending on the choice of β. In order to choose a value for β, we calibrate the model such that it optimally predicts the distances to nearby galaxies that have redshift-independent distance estimates from an alternative source. The reason for selecting *nearby* galaxies is that we constructed the flow-field in a self-consistent manner, such that the LG peculiar velocity can be accounted for within the sampled volume. It has been proposed that a significant source of attraction influencing the dynamics in the nearby Universe lies in the Shapley concentration (at $140/h$ Mpc), or potentially farther (e.g., Scaramella et al., 1989; Kocevski & Ebeling, 2006). If an attractor marginally outside the sampled volume (including Shapley) plays a significant role in the motions of galaxies, the self-consistent reconstruction will not predict reliable flows for regions where this external attractor dominates the flow. Locally, however, we expect that an attractor as far away as Shapley will have similar effects on the LG and on surrounding groups, and therefore by calibrating the model on small scales we still expect to obtain a meaningful estimate of β.

We calibrate the flow-field using known distances from the *Tully08* catalog (Tully et al. 2008, updated in Tully et al. 2008), which has grown from the *Nearby Galaxies Catalog* (Tully, 1988) and contains distance estimates for 1791 galaxies inside 3000 km s^{-1}. The galaxy distances are derived using four different methods, but have been calibrated to the distances set by the *Hubble Key Project* (Freedman et al., 2001). The catalog contains 51 Cepheid distances, 221 calibrated using the luminosity at the tip of the red giant branch (Karachentsev et al., 2004, 2006) (TRGB, see Lee et al., 1993; Sakai et al., 1996; Makarov et al., 2006), and 383 Surface Brightness Fluctuation (SBF, see Tonry & Schneider, 1988) distances (Tonry et al., 2001; Mei et al., 2007), with some overlap. In addition, the catalog includes 1432 Tully-Fisher (TF) distances (Tully & Fisher, 1977; Karachentsev et al., 2002). Errors are only reported for the TF distances; however, estimates of the error for quality distances are placed at 0.2 mag in the distance modulus, and 0.4 mag for SBF (Tully et al., 2008).

For each galaxy in the catalog, we use the method of §5.2 to estimate a distance to the galaxy for a given value of β. Distance estimates for galaxies in triple-valued regions, but outside cluster cores, will not be predicted accurately by the flow-field model and, due to both the errors on the reconstruction and the measurement errors, we expect significant scatter in the comparison. Before proceeding further, we need to gain an understanding of the errors in the predicted distances. We discuss these below in §5.4.1, then proceed to calibrate the model in §5.4.2. In §5.4.3 we discuss the implications on the clustering scales of dark matter.

5.4.1 Errors on Predicted Distances

The flow-field is constructed using the initial mass estimate, angular position, and estimated distance (generally from galaxy redshift measurements) to each group. While the angular position of each galaxy is known to high accuracy, the largest source of uncertainty in the position of the group center comes from missing member galaxies or including interlopers. We expect, however, that the errors on estimated distances and masses will have substantially more impact on the errors associated with the predicted peculiar velocities. Varying the initial distance to a group is expected to have little effect on the flow-field since, by its nature, it is constructed in a self-consistent manner. The error on the mass estimates, however, have contributions from the uncertainty in the group distance and velocity dispersion, as well as the finite number of elements from which the mass is estimated. The introduction of interlopers in the group will impact the mass estimate significantly through the estimated velocity dispersion.

We estimate the error on the mass using the results of §3.1.3. The scatter on the mass-to-light ratio has been characterized by Eq. (3.3). Assuming that this scatter is due entirely to the error on the estimated mass, we can model this error to understand its propagation into the reconstructed velocities.[2] We make the assumption that the error on the initial distance estimate is given by the standard error of the mean redshift, and is normally distributed.[3] We further assume that the mass is drawn from a normal distribution where the width is defined such that a fraction $\Delta_{M/L}(N)$ falls between the 32$^{\text{nd}}$ and 68th percentiles, consistent with the definition of $\Delta_{M/L}(N)$. The errors are then propagated using a Monte-Carlo technique: we randomly draw mass and distance estimates for each group, and compute the resulting converged flow-field according to §3.2. At the distance provided from the redshift-independent estimate for each source in the *Tully08* catalog, and corresponding angular position, we compute the line-of-sight component of the predicted peculiar velocity. Repeating this procedure 100 times, we find the standard deviation in the computed line-of-

---

[2] Note that some variation is expected since the sizes and masses of groups with similar numbers of observed members may differ. The uncertainty estimated here is therefore likely to be an overestimate of the true value.

[3] Since we require the mass and distance to be positive quantities, we truncate the distribution at zero, and symmetrically for large mass/distance.

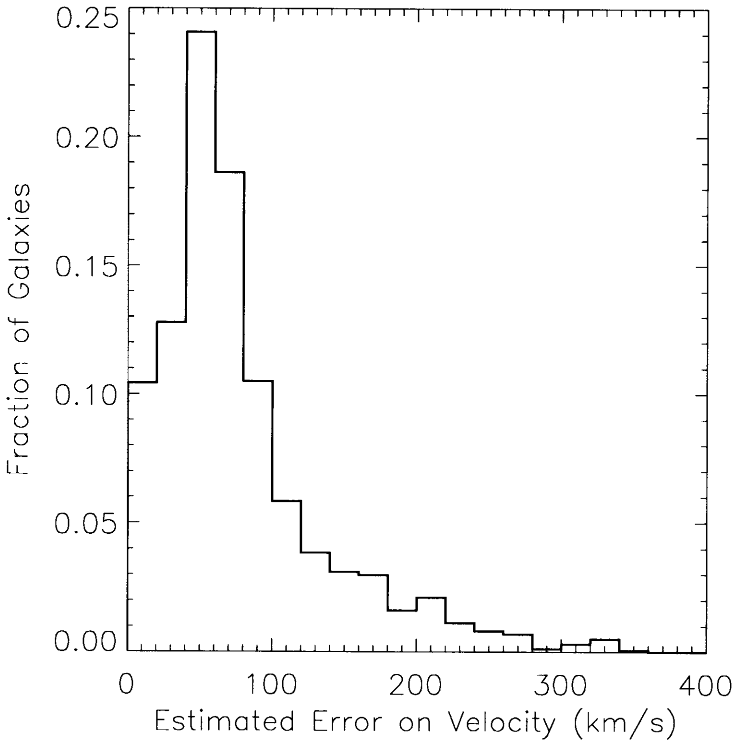

Figure 5.6 Estimated model errors on reconstructed peculiar velocities of *Tully08* galaxies. The graph shows the distribution of errors on the line-of-sight peculiar velocities computed from the flow-field for the locations of the galaxies in the *Tully08* catalog assuming $\beta = 0.17$ (CMC). The errors presented are derived from the uncertainty in the data and do not include errors associated with the approximation of linear perturbation theory. The r.m.s. model error on the velocity is 116 km s^{-1}.

sight peculiar velocities at each point, σ_i^{PV}, which will correspond approximately[4] to an error on the estimated distance. A histogram of the resulting values of σ_{PV} for $\beta = 0.17$ (CMC) is shown in Figure 5.6. Note that any difference between the CMC and IMC cases at the distances of these galaxies is the result of the chosen value of β. The r.m.s. model error is estimated to be 116 km s^{-1} for the CMC case and 131 km s^{-1} for the IMC case.

---

[4] An exact treatment would require the repeated evaluation of the distance at each point from the observed redshift (as §5.4.2). This is computationally intensive and the errors differ only in the locations of triple-valued regions and cluster cores, where the variation in the distance estimate only depends on the estimated flow-field location of the corresponding cluster. This approximate method will overestimate the errors in these regions.

5.4.2 Estimating β

To estimate the optimal value for the parameter β, for the flow-field, we minimize the quantity

$$\xi^2 = \sum_i \frac{(D_i^{\rm obs} - D_i^{\rm rec}[\beta])^2}{\sigma_i^{\rm obs\,2} + \sigma_i^{\rm PV\,2}} \tag{5.7}$$

where $D_i^{\rm obs}$ is the measured distance, $D_i^{\rm rec}$ is the predicted (reconstructed) distance, $\sigma_i^{\rm obs}$ is the estimated error on the observed distance, and $\sigma_i^{\rm PV}$ is the estimated error on the predicted distance.

However, before presenting the result, we note that it is essential to understand the sensitivity of the value of β to the raw data. With the same assumptions as specified in §5.4.1 above, we randomly draw values for the mass and distance to each group, re-compute the flow-field and estimate the peculiar velocities at the spatial locations of the *Tully08* galaxies using the modified flow-field. The procedure for determining the optimal value for β is repeated and the results are shown in Figure 5.7. For the coherent mass correction, we find that $\beta = 0.17^{+0.03}_{-0.01}$; for the incoherent mass correction, we obtain $\beta = 0.19^{+0.05}_{-0.03}$, justifying our choices of β used up to this point. Note that the two estimates are consistent with each other, and the uncertainty in β for the IMC case is larger than in the CMC case. This is likely to be due to the fact that distant groups (where the iterative procedure results in negligible fractional changes to their distances) contribute more significantly to the LG peculiar velocity in the CMC case (this will be demonstrated in Chapter 6). Note that this parameter estimation calibrates the proportionality constant between the gravitational acceleration and the peculiar velocity. The quoted errors on β are therefore only meaningful if the value of the mean mass density in groups ($\bar{\rho}_g$) is fixed (the proportionality constant is independent of the H_0). However, including the errors on the estimated density from §3.2.5 has a negligible impact on the reported 68% confidence limits. We discuss the interpretation of this result in §5.4.3 below.

5.4.3 Clustering Scales

Since dynamical considerations are used to estimate the masses of galaxy groups (see §3.1.3), we have a direct measure of the dark matter associated with clusters, interior to the contour specified by $\delta\rho/\rho = 80$. In §2.4.3, we noted that this density contrast threshold is likely to be significantly higher than the scale on which dark matter clusters. Therefore, the mass estimated within the chosen contour is expected to underestimate the total mass of the cluster. We investigate the magnitude of this effect below:

Analagous to Eq. (3.12), the peculiar velocity at location $\mathbf{r}$, induced by a perturbation in the dark matter density distribution, is given by

$$\mathbf{v}(\mathbf{r}) = \frac{H_0 f(\Omega_m)}{4\pi\Omega_m\rho_{\rm crit}} \sum_j{}' \left(\frac{\mathbf{r} - \mathbf{r}_j}{|\mathbf{r} - \mathbf{r}_j|^3}\right) \int_0^{|\mathbf{r}-\mathbf{r}_j|} 4\pi\tilde{\rho}_j(s')s'^2 {\rm d}s' \tag{5.8}$$

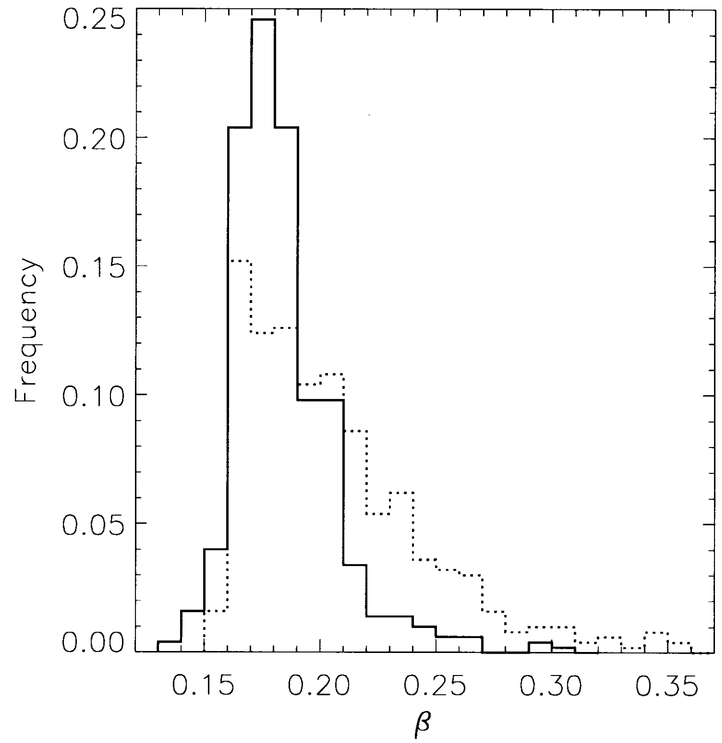

Figure 5.7 Result of Monte-Carlo error estimation on β. For 500 trials, we propagate random errors on the masses and distances of the groups used in the construction of the flow-field. In each case, we determine the value of β using the method of §5.4.2. The solid line represents the CMC case and the dotted line represents the IMC case. We find $\beta = 0.17^{+0.03}_{-0.01}$ when assuming the coherent mass correction and $\beta = 0.19^{+0.05}_{-0.03}$ when assuming the incoherent mass correction.

where $f(\Omega_m) \approx \Omega_m^{6/11}$, $\rho_{\rm crit} = 3H_0^2/(8\pi G)$ is the critical density, $\tilde{\rho}_j(r)$ represents the dark matter density profile of the $j^{\rm th}$ group, and the remaining parameters are defined as per Eq. (3.12). We allow for a constant of proportionality between the estimated mass and the total dark matter mass, f_M, such that

$$\int_0^\infty \tilde{\rho}_j(s')s'^2 {\rm d}s' = f_M \int_0^\infty \rho_j(s')s'^2 {\rm d}s' \tag{5.9}$$

where $\rho_j(r)$ is the assumed density profile defined according to Eq. (3.5). We can express f_M in terms of the estimated parameter β by equating Eq. (3.12) with Eq. (5.8),

$$f(\Omega_M)f_M = \beta\frac{\Omega_m\rho_{\rm crit}}{\bar{\rho}_g} \tag{5.10}$$

and we define the quantity $\tilde{\beta} = f(\Omega_M)f_M$. Using the WMAP5 result: $\Omega_m h^2 = 0.1358^{+0.0037}_{-0.0036}$ (Komatsu et al., 2009), we obtain $\tilde{\beta} = 2.3^{+0.4}_{-0.2}$ for the CMC model and $\tilde{\beta} = 2.6^{+0.7}_{-0.4}$ for the IMC model. Estimates of the redshift distortion parameter from galaxy-based reconstructions find values much smaller than the value of $\tilde{\beta}$ presented here. The PSCz dipole analysis (Rowan-Robinson et al., 2000) suggests a value $\beta = 0.75^{+0.11}_{-0.08}$ and, from 2MRS dipole analyses, Erdoğdu et al. (2006b) derive $\beta = 0.40 \pm 0.09$ and Erdoğdu et al. (2006a) find $\beta = 0.54 \pm 0.12$. Combining the WMAP5 value for $\Omega_m h^2$ with the Hubble constant $H_0 = 74.2 \pm 3.6$ km s^{-1} Mpc^{-1} (Riess et al., 2009), we find $f(\Omega_m) \approx \Omega_m^{6/11} = 0.466 \pm 0.024$. For the case $f_M = 1$, the amplitude of the predicted peculiar velocities are significantly smaller than the expectation from a WMAP5 cosmology. Since the value of β was calibrated using observational data, either the measured peculiar velocities are too large, or the estimated cluster masses are too small. For the reasons provided above, the expectation is that we have underestimated the masses of the clusters by considering only the mass at the peak of the density profile. To reconcile the observed values of $\tilde{\beta}$ with the expected value of $f(\Omega_m)$ requires an appropriate choice of f_M. For the CMC model, we find $f_M = 4.9^{+0.9}_{-0.5}$, and for the IMC model, we find $f_M = 5.6^{+1.5}_{-0.9}$. Note that the fraction of galaxies assigned to the identified groups with 5 or more members is 0.19 (see Figure 5.8), therefore the obtained values of f_M are consistent with a model where galaxies are weighted equally and correlated with the locations of the observed groups. Assuming that the density falls off as the inverse square of the distance from the group center (see §3.2.3), the ratio of the mass enclosed by the contours δ_1 and δ_2 is given by

$$\frac{M_2}{M_1} = \left(\frac{\delta_1}{\delta_2}\right)^{1/2} \tag{5.11}$$

We can use this result to interpret the appropriate cut-off scale. Since the mass estimates were derived from groups identified above a density contrast $\delta\rho/\rho = 80$, this implies that a lower threshold of $\delta\rho/\rho \sim 3$ sets the scale for the clustering of dark matter.

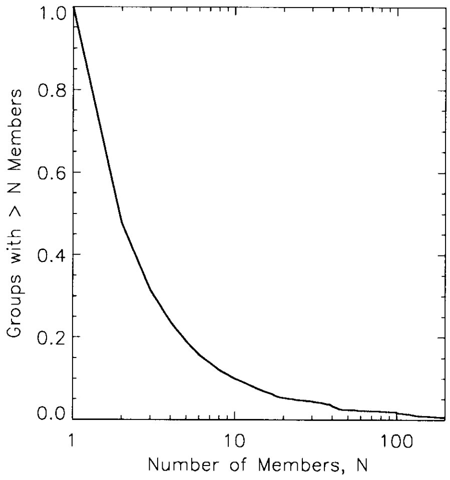

Figure 5.8 Fraction of galaxies in groups. The graph shows the fraction of 2MRS galaxies with LS-centric redshifts below 12,000 km s^{-1} in groups with at least N members as a function of the N. The fraction corresponding to $N = 5$ is 0.19. The groups are identified with a minimum density contrast, $\delta\rho/\rho = 80$.

5.5 Distances to 2MRS Galaxies

Using the method of §5.2, the calibrated model of the flow-field can be applied to estimate distances to galaxies in 2MRS. In this section, we examine the results of such an application. We restrict our discussion to the case of the coherent mass correction, noting that both the coherent and incoherent mass corrections produce nearly identical results over relevant distance range. Using the redshifts of 29,659 galaxies inside 10,000 km s^{-1}, we estimate their distances (according to §5.2) and the associated errors (according to §5.4.1). In addition, we expect a thermal contribution to the peculiar velocity as discussed in §4.3 on the order of 100–200 km s^{-1}.

In Figure 5.9, we demonstrate the effect of applying the flow-field model to estimate distances to galaxies near the supergalactic plane. Galaxies with -1000 km s^{-1} $< SGZ <$ $+1000$ km s^{-1} are plotted at both their redshift-space locations (i.e. before the application of the model) and at their real-space locations as predicted by the model. Most noticeably, we observe that the reconstructed real-space map has collapsed the *fingers-of-god* present in the redshift-space map. To understand the utility of the model, we consider the potential improvement in the distances to galaxies estimated by the model compared with the application of Hubble's law. In Figure 5.10, we show the redshifts of galaxies as a function of the distances predicted by the model; this demonstrates the difference between the distance obtained using Hubble's law and the flow-field model. Note that the prominent vertical bands are the result of collapsing the fingers-of-god associated with clusters in redshift-space. It is clear that in the vicinity of large clusters Hubble's law will perform poorly as an estimator of the distance to the group.

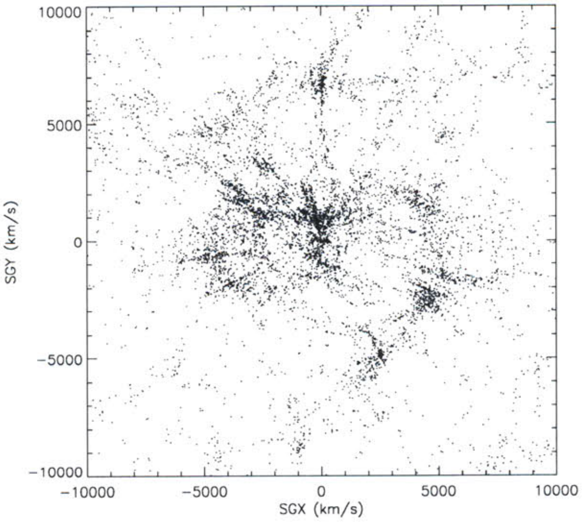

(a) 2MRS galaxies in redshift-space

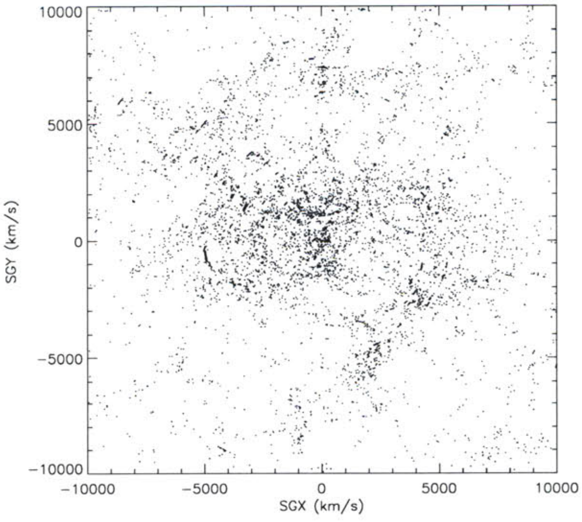

(b) 2MRS galaxies in real-space

Figure 5.9 Galaxies in 2MRS in redshift-space and real-space. Galaxies with $-1000 \text{ km s}^{-1} < SGZ < +1000 \text{ km s}^{-1}$ and $cz < 10,000 \text{ km s}^{-1}$ are shown in supergalactic coordinates. In panel (a), the locations indicate positions in redshift-space. In panel (b), the locations indicate the reconstructed real-space positions. Notice that the *fingers-of-god* have been collapsed to the cores of the clusters. The figure was produced assuming the coherent mass correction with $\beta = 0.17$.

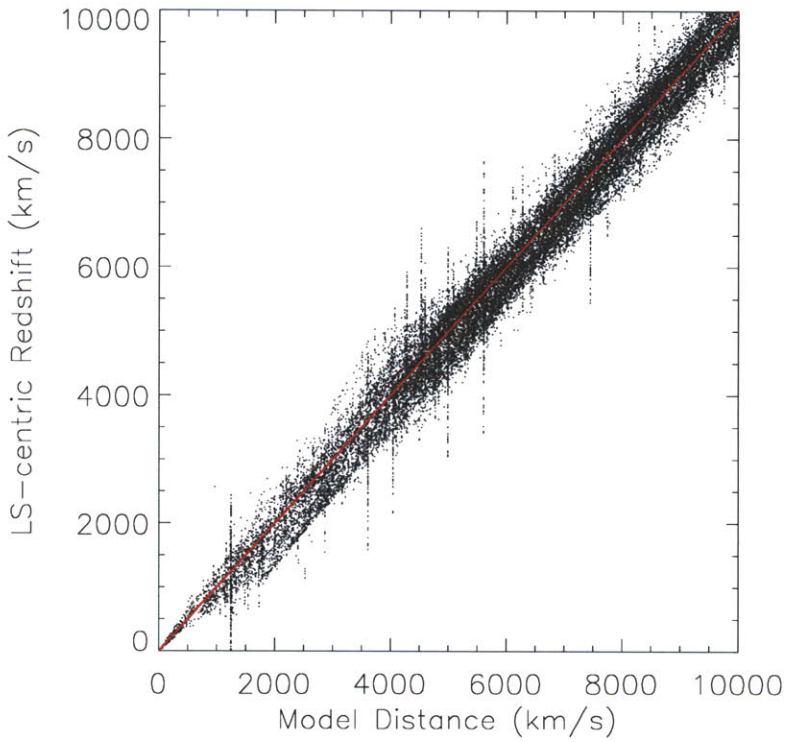

Figure 5.10 Distances predicted by Hubble's law and flow-field model for 2MRS galaxies. The graph shows the redshift relative to the LS frame as a function of the distance to the galaxy. If the model of the flow-field is accurate, it is clear that in the vicinity of large clusters (identified by the vertical bands) Hubble's law will perform poorly as an estimator of the distance to the group.

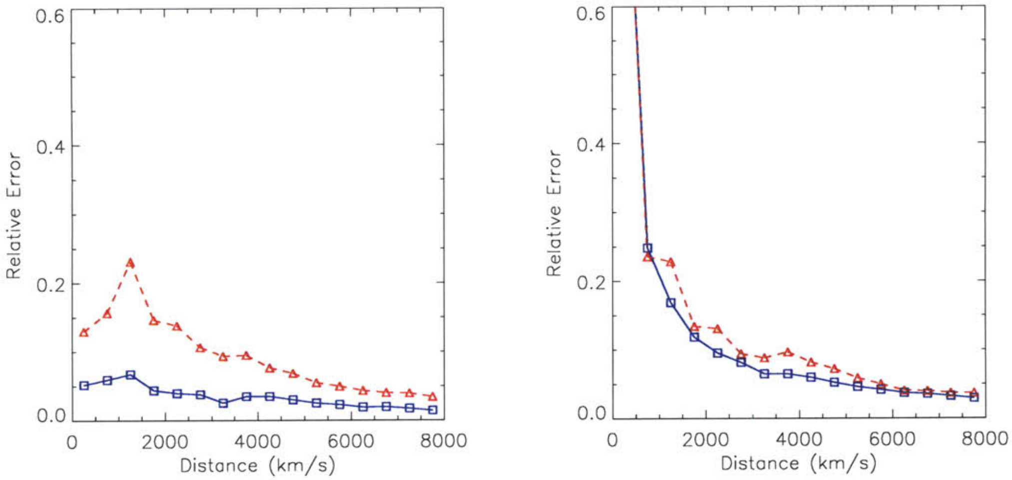

(a) (b)

Figure 5.11 Effect of using the flow-field model to estimate distances to 2MRS galaxies. The red (dashed) line shows the relative error obtained by using Hubble's law if the distance estimate from the flow-field is correct. The blue (solid) line shows the relative uncertainty in the distance estimate from the flow-field. In panel (a) thermal errors have been neglected. In the absence of thermal errors, the flow-field offers a significant improvement over Hubble's law. In panel (b) we include a 187 km s^{-1} km s^{-1} thermal contribution to the peculiar velocity. The model offers improvement of $\sim 30\%$ over distances beyond $\sim$ 1000 km s^{-1} in this case.

Under the assumption that the model correctly predicts the distance, we compute the relative error in the distance implied by Hubble's law:

$$\varepsilon_z = (cz - H_0 D_{\rm model})/(H_0 D_{\rm model}) \tag{5.12}$$

where z is the LS-centric redshift of the galaxy and $D_{\rm model}$ is the distance estimated from the model. We also compute the relative uncertainty in the distance estimate, neglecting the thermal contributions at this time.

$$\varepsilon_D = \sigma_{\rm PV}/D_{\rm model} \tag{5.13}$$

where $\sigma_{\rm PV}$ is the uncertainty in the model distance from §5.4.1. The quantities ε_z and ε_D are plotted in Figure 5.11(a). Notice that the model is expected to improve the relative error significantly nearby, especially in the vicinity of clusters. In Figure 5.11(b), we include a thermal velocity of 187 km s^{-1} (Tonry et al., 2000). It is clear that very nearby (within $\sim$ 500 km s^{-1}), the model of the flow-field can offer little to no improvement over Hubble's law, but beyond $\sim$ 1000 km s^{-1}, we notice the flow-field reduces the observed error by $\sim 30\%$,[5] and provides significant improvement at the distance of the Virgo Cluster (by virtue of the density of galaxies at that redshift appearing in Virgo itself). Estimates of the error below $\sim 5\%$ are generally considered very good, and a redshift-inference will achieve this limit for typical peculiar velocities up to a few hundred km s^{-1} by ~ 6000 km s^{-1}, as can be seen in the figure.

In the next section, we will attempt to perform a similar comparison using redshift-independent estimates. However, errors on the measured distances make it hard to interpret beyond a very narrow range.

5.6 Reliability of Distance Estimates

So far in this chapter, we have constructed and calibrated a tool for estimating the distances using only angular position and redshift information. It is desirable to test the tool against available redshift-independent distance estimates. We choose to examine distances from the *SFI++* catalog (Springob et al. 2007, updated in Springob et al. 2009). The catalog includes 4861 distances to spiral galaxies derived using the TF relation with I-band photometry, and either 21-cm or optical velocity-widths (see Masters et al., 2006). The distances probe much deeper than the *Tully08* catalog utilized in §5.4 above and provide a consistent sample that can be used to test the model out to scales of ~ 6000 km s^{-1}. In fact, the catalog contains galaxies with much higher redshifts; however, with methods currently available, errors on the distance estimates typically vary from 10–20% (TF distances are generally on the higher end of that range). Since typical peculiar velocities are a few hundred km s^{-1}, it is difficult to test the reconstructed flow-field beyond this scale. The discussion in this section is restricted to the CMC case. Since the CMC and IMC models of the flow-field are in good agreement inside 5,000 km s^{-1} (where the TF distance estimates are useful), the conclusions of this section are applicable to both the CMC and IMC models.

Given the angular position and LS-centric redshift for each galaxy, we use the method of §5.2 to estimate the distance ($D_{\rm model}$) to the galaxy in question. Using a similar approach to §5.5 above, we compare this estimate with the distance reported in the catalog ($D_{\rm measured}$) and compute a relative error on the predicted distance,

$$\epsilon_p = (D_{\rm model} - D_{\rm measured})/D_{\rm measured} \qquad (5.14)$$

We also compute the relative error on the distance that would be obtained if one simply assumes that the LS-centric redshift (z) is proportional to the distance,

$$\epsilon_z = (cz - H_0 D_{\rm measured})/(H_0 D_{\rm measured}) \qquad (5.15)$$

The distances to the galaxies as computed by the model and also from the redshift-independent measurement are shown in Figure 5.12.

---

[5] Note that the model errors have been overestimated in the vicinity of clusters; see §5.4.1 for details.

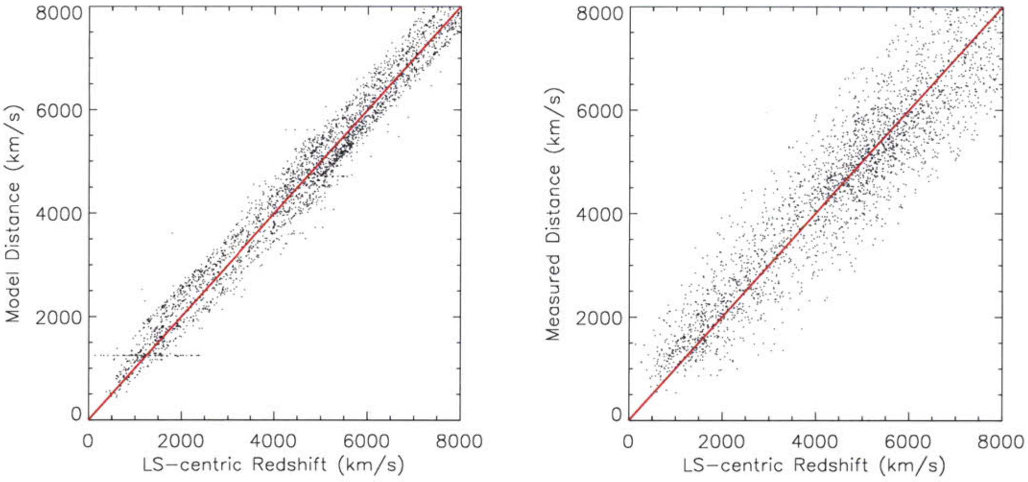

(a) Flow-field Model

(b) Measured Distance

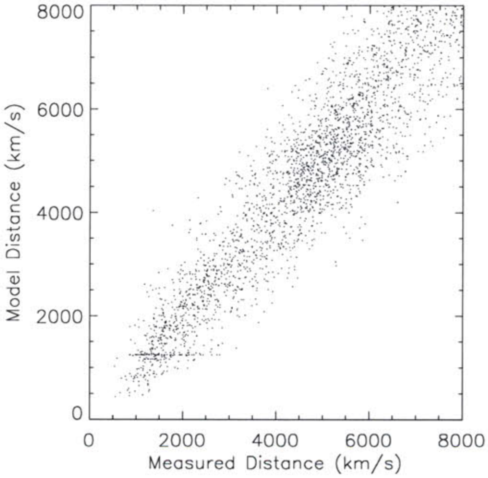

(c) Model vs. Measured

Figure 5.12 Distances to galaxies as predicted by the flow-field model. (a) shows the model distance and (b) shows the measured distance, plotted as a function of LS-centric redshift. (c) compares the model distance with the measured distance, although more detailed comparisons are available in Figures 5.13 and 5.14. The horizontal bands visible to an extent in these plots (though most prominent in panel (a)) indicate the locations of clusters, where the best available distance estimate is obtained by placing the galaxy at the distance of the center of the cluster. The solid lines show the prediction of Hubble's law.

The prominent horizontal bands in Figure 5.12(a) are present because the best available distance estimate to galaxies in the vicinity of massive clusters are obtained by placing the galaxy at the distance to the center of the cluster to avoid the degeneracies discussed in §5.2.1 above. The bands are less obvious in Figure 5.12(b), since galaxies that are falling into the cluster, but are not virialized members, will have distances in the foreground or background of the galaxy, that can often not be distinguished by the model. In Figure 5.12(c), the scatter is notably large due to uncertainties in both the model and the 15–20% errors in the TF distance estimates. We examine the content of this figure in more detail below.

To assess the reliability of using the flow-field model to estimate distances to galaxies, we examine both ϵ_p and ϵ_z as a function of the distance to the galaxy. In §5.4.1, we demonstrated that the estimated errors on predicted peculiar velocities are $\sim$ 116 km s^{-1} due to uncertainties in the distances, mass, and galaxy membership of the groups used to construct the flow-field. From §4.3, we found that linear perturbation theory, when applied to galaxy groups, can only recover velocities to within $\sim$ 100 km s^{-1}, if the masses and locations are known precisely. We are therefore subject to typical errors on the predicted peculiar velocity of $\sim$ 150 km s^{-1}, which means that nearby the relative error will be large. Figure 5.13 shows the mean value[6] of ϵ in each distance bin as function of distance; it is evident that, overall, the flow-field model offers a slight improvement over a simple redshift inference for redshifts less than $\sim$ 4000 km s^{-1}, although to gain a more insightful understanding, it is helpful to examine the performance of the model at different regions on the sky.

Figure 5.14 shows the relative error on the estimated distances obtained using both the flow-field model and Hubble's law (as in Figure 5.13), but computed using only the galaxies inside the specified range[7] of right-ascension and declination. Note that we also plot a thermal scatter of 187 km s^{-1} (black line) (Tonry et al., 2000) to demonstrate the expected limit. We discuss these plots below:

(a) **$09^{\mathrm{h}} < \alpha < 21^{\mathrm{h}}$, $45° < \delta < 90°$:** In this region above the Virgo cluster, the infall toward the supergalactic plane is predicted to dominate the flow. The model does not offer any advantage over Hubble's law inside 2000 km s^{-1} (in fact, Hubble's law actually performs better), and this can be understood by revisiting the assumption that the model is self-consistent, which we will discuss below.

(b) **$21^{\mathrm{h}} < \alpha < 03^{\mathrm{h}}$, $45° < \delta < 90°$:** The region contains a portion of the galactic plane and has few point tracers. The large peculiar velocity of the (few) nearby galaxies is not well predicted by the flow-field model, and both the model and Hubble's law perform poorly.

(c) **$15^{\mathrm{h}} < \alpha < 21^{\mathrm{h}}$, $0° < \delta < 45°$:** This region contains the galactic center, and so has very few tracers. The flow-field model generally outperforms Hubble's law

---

[6] For consistency with Figure 5.14, we exclude the 10% most extreme data points in each bin, in an effort to prevent single high-peculiar velocity galaxies dominating the statistics of small sample sizes in each bin.

[7] The ranges chosen coincide with those suggested by Masters (2005).

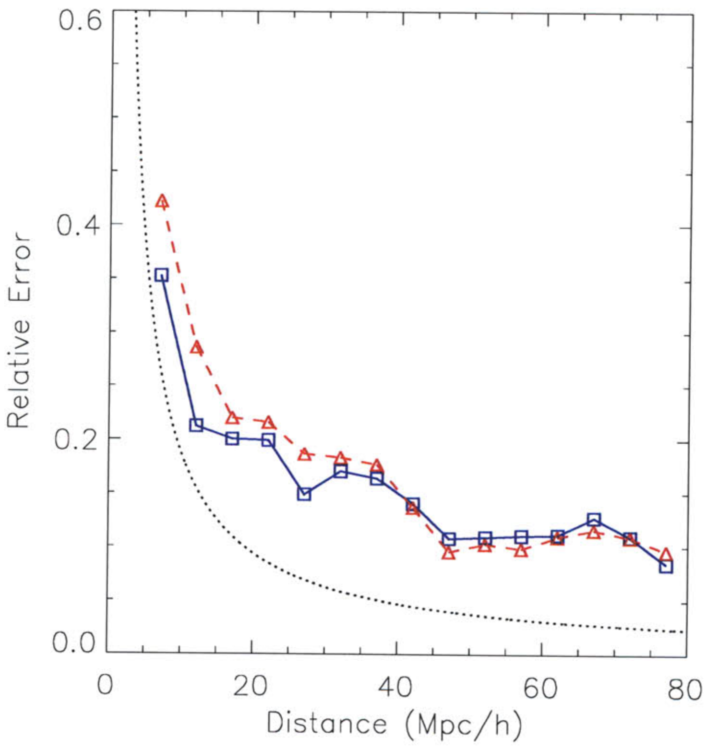

Figure 5.13 Relative error on distance for flow-field model vs. Hubble's law. The squares and (blue) solid line represent the distance estimate derived from the flow-field model. The triangles and (red) dashed line show the distance estimates derived assuming Hubble's law applied to the LS-centric redshift. Averaged over all available distance measurements, the application of the flow-field model offers a small, but noticeable improvement over the application of Hubble's law in reducing the error on the estimated distance for objects inside $\sim$ 4000 km s^{-1}. The black line represents an uncertainty of 187 km s^{-1} km s^{-1} in the measurement.

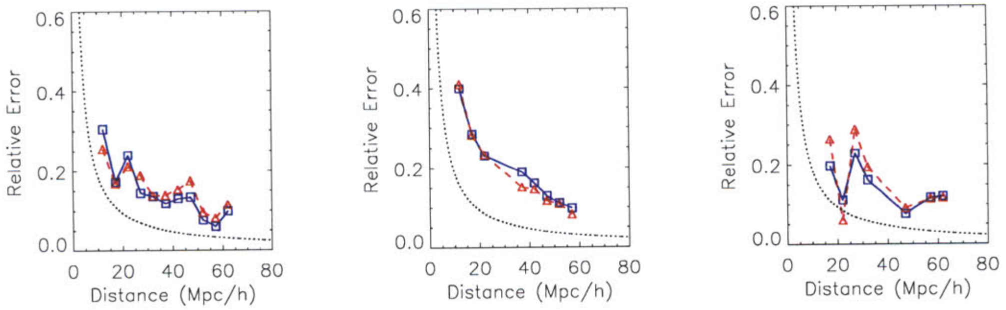

(a) $09^h \rightarrow 21^h$ $45° \rightarrow 90°$ (b) $21^h \rightarrow 03^h$ $45° \rightarrow 90°$ (c) $15^h \rightarrow 21^h$ $0° \rightarrow 45°$

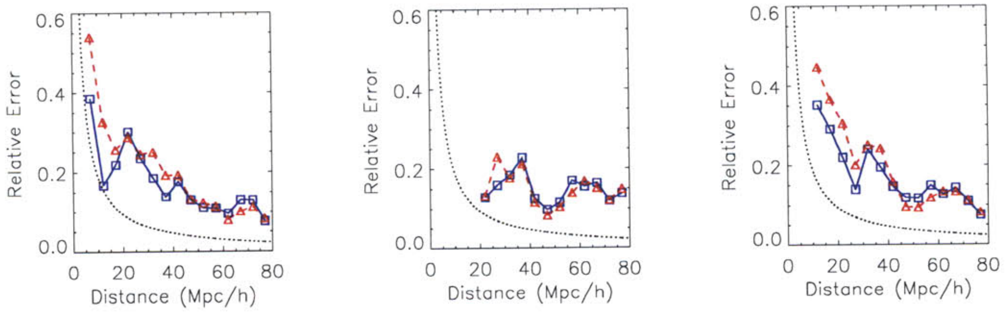

(d) $09^h \rightarrow 15^h$ $0° \rightarrow 45°$ (e) $03^h \rightarrow 09^h$ $0° \rightarrow 45°$ (f) $21^h \rightarrow 03^h$ $0° \rightarrow 45°$

Figure 5.14 Relative error on distance for different portions of the sky. The right-ascension (α) and declination (δ) are indicated below the plots. The squares and (blue) solid line represent the distance estimate derived from the flow-field model. The triangles and (red) dashed line show the distance estimates derived assuming Hubble's law applied to the LS-centric redshift. The black (dotted) line represents an uncertainty of 187 km s^{-1} km s^{-1}, typical of a thermal contribution to the error. The performance of the flow-field model depends upon the location.

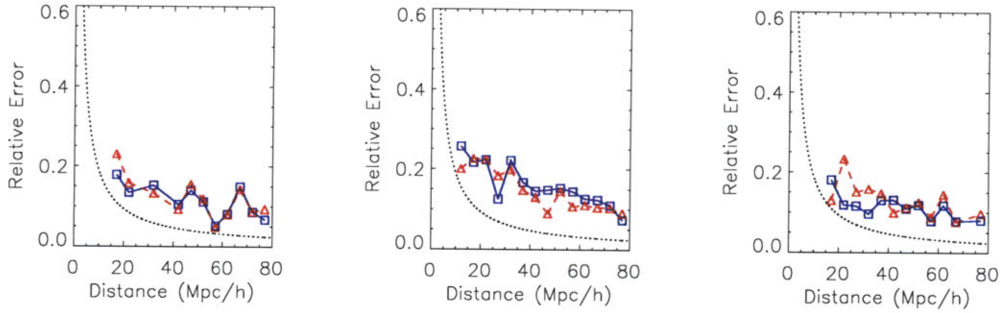

(g) $15^h \rightarrow 21^h$ $-45^\circ \rightarrow 0^\circ$ (h) $09^h \rightarrow 15^h$ $-45^\circ \rightarrow 0^\circ$ (i) $03^h \rightarrow 09^h$ $-45^\circ \rightarrow 0^\circ$

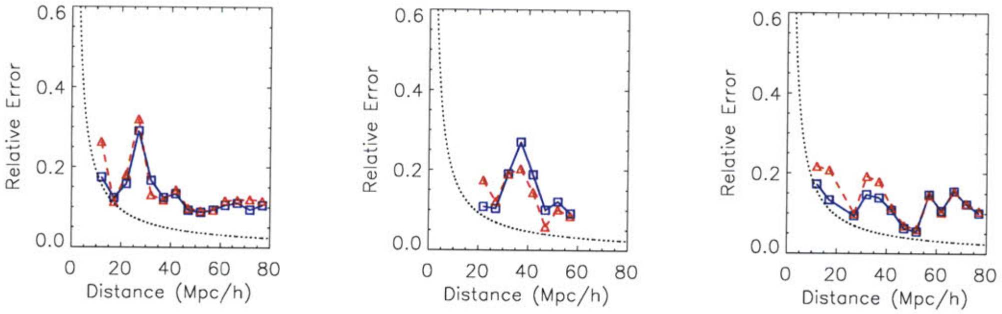

(j) $21^h \rightarrow 03^h$ $-45^\circ \rightarrow 0^\circ$ (k) $09^h \rightarrow 21^h$ $-90^\circ \rightarrow -45^\circ$ (l) $21^h \rightarrow 09^h$ $-90^\circ \rightarrow -45^\circ$

Figure 5.14 — *continued...*

here, except at 2000 km s^{-1}, where the prediction of Hubble's law drops below the thermal limit.

(d) **$09^h < \alpha < 15^h$, $0° < \delta < 45°$:** This region contains the Virgo cluster, as well as the Coma cluster toward the end of the plotted region. The flow-field model generally performs well here, especially at low redshifts in correcting for the infall velocities near Virgo, and achieving the model limit.

(e) **$03^h < \alpha < 09^h$, $0° < \delta < 45°$:** This region contains a portion of the galactic plane. The flow-field offers a slight improvement over Hubble's law inside 3000 km s^{-1}, but neither perform well beyond this scale.

(f) **$21^h < \alpha < 03^h$, $0° < \delta < 45°$:** The flow-field provides significantly better distance estimates than Hubble's law inside 4000 km s^{-1}, which contains the Perseus-Pisces foreground. The infall into the supercluster is well modeled by the flow-field.

(g) **$15^h < \alpha < 21^h$, $-45° < \delta < 0°$:** There are few velocity tracers in this region since it contains the galactic center. For the tracers that are available, both Hubble's law and the flow-field reproduce the distances reasonably well.

(h) **$09^h < \alpha < 15^h$, $-45° < \delta < 0°$:** This region contains the Hydra-Centaurus supercluster. Hubble's law generally outperforms the flow-field model in this region, except in the very foreground of the cluster, where the flow-field accounts for the infall. The reasoning is likely due to the inability of the flow-field to correctly predict the high peculiar velocity of Hydra (see §3.3), resulting in the erroneous placement of the group. Behind the group, the flow-field predicts backside-infall into the group, whereas it has been suggested that flows toward Shapley should dominate this region of space. We discuss this in more detail below.

(i) **$03^h < \alpha < 09^h$, $-45° < \delta < 0°$:** The flow-field performs reasonably well here, attaining estimates close to the thermal limit inside $\sim$ 4000 km s^{-1}.

(j) **$21^h < \alpha < 03^h$, $-45° < \delta < 0°$:** The large peculiar velocities nearby, due to the infall into the Virgo cluster (which is on the opposite side of the sky), are modeled to an extent by the flow-field, which reaches the model limits at $\sim$ 1000 km s^{-1}. At $\sim$ 2500 km s^{-1}, both Hubble's law and the model perform poorly.

(k) **$09^h < \alpha < 21^h$, $-90° < \delta < -45°$:** The galactic plane obscures a portion of this region, and the low number density gives rise to the large fluctuations in the figure. Hubble's law outperforms the flow-field model in this region.

(l) **$21^h < \alpha < 09^h$, $-90° < \delta < -45°$:** The flow-field generally performs well here, attaining the model limit and offering improvement over application of Hubble's law over the entire distance range.

It is clear that the model performs well in certain regions and poorly in others, and it is also evident that we do not see as distinct an improvement as demonstrated in §5.5. The primary reasons for this are as follows: Firstly, the uncertainties in the TF distance estimates (15–20%) mean that these errors will significantly affect the baseline in the plot, dominating the scatter potentially as nearby as ~ 3000 km s^{-1}. Secondly, the target selection of galaxies is biased against detecting galaxies in clusters, because galaxies close together on the sky are within the beam width for 21cm radio observations making their spectra difficult to separate. The vicinity of clusters is where the flow-field model performs best, since it is in these regions that we expect the largest deviation from the Hubble flow. In general, however, it is clear from Figure 5.13 that the flow-field offers a slight advantage over Hubble's law in predicting distances inside 4000 km s^{-1}.

The poor performance of the model in the regions behind Virgo and also behind Hydra-Centaurus may be due to the self-consistent nature of the model. While the region directly behind Hydra is explicable in part by the assigned location of the Hydra cluster (see §3.3), the model predicts back-infall far beyond where it is observed. By the construction of the model, we have implicitly assumed that peculiar velocities can be reconstructed using the observed groups inside the sampled volume. If there is significant mass just beyond 12,000 km s^{-1} in the direction of the Shapley concentration, the peculiar velocities behind Hydra-Centaurus and far from Virgo would be expected to stream toward Shapley, instead of the backside-infall that the model predicts. Very nearby, we expect the model to perform reasonably well in obtaining distance estimates, and we have shown that it offers a small improvement over Hubble's law inside ~ 4000 km s^{-1}. Thus, poor distance estimates in the discussed regions are suggestive of a significant contribution to the dynamics from just beyond the $120/h$ Mpc limit of the sample. The Shapley concentration has received many nominations as a candidate for the missing mass (e.g., Scaramella et al., 1989; Branchini & Plionis, 1996). If the source of the mass was significantly farther away, as calculations of the LG dipole from X-ray clusters imply (e.g., Kocevski & Ebeling, 2006), then we would expect the flow-field to perform well over a larger volume.

5.7 Summary

In this chapter, we have presented a method that will allow a mapping solely from angular position and redshift measurements of groups to estimates of their real-space distances, under the assumption that the flow-field model is robust. We estimated the errors from uncertainties in the mass and initial distance estimates contribute 116 km s^{-1}–131 km s^{-1} (r.m.s.) to the uncertainty in the reconstructed line-of-sight peculiar velocity. By calibrating the flow-field model using distance estimates to nearby galaxies, we obtain an estimate of the parameter $\tilde{\beta}$ for the identified galaxy groups. Under the assumption that the distribution of the unobserved mass is correlated with the observed groups, we obtain $\tilde{\beta} = 2.3^{+0.4}_{-0.2}$. Alternatively, assuming that the unobserved mass is distributed isotropically, we find $\tilde{\beta} = 2.6^{+0.7}_{-0.4}$. These values are consistent with each other, and provide lower and upper bounds to the value of

$\tilde{\beta}$ expected from the true distribution of the unobserved mass. By comparing the constraints from the calibration of the models with expectations from a WMAP5 cosmology, we demonstrate that the clustering scales of dark matter are set by $\delta\rho/\rho \sim 3$, much larger than the scales on which we have identified galaxy groups.

We showed the potential improvement on distance estimates to galaxies in 2MRS is expected to be $\sim 30\%$, and higher in the vicinity of massive clusters. Comparing the predicted distances with the *SFI++* sample demonstrates its utility in an improvement over Hubble's law inside ~ 4000 km s^{-1}, although the level of improvement is dependent on the region in question. The failure to predict distances accurately in the background of Hydra-Centaurus suggests evidence for attraction toward a massive concentration just beyond the sampled volume. This is consistent with previous suggestions (e.g., Scaramella et al., 1991; Branchini & Plionis, 1996; Kocevski & Ebeling, 2006) for a significant mass concentration in the vicinity of Shapley.

Chapter 6

Reconciling the Flow-field Model with the CMB

The model of the flow-field developed in Chapter 3 provides predictions of the peculiar velocities in inside 12,000 km s^{-1}. In Chapter 5, we calibrated the flow-field such that the distances predicted to nearby galaxies provided the best match with a sample of redshift-independent measurements. In this chapter, we take a closer look at the peculiar velocity predicted at the location of the Local Group (LG), i.e. the LG dipole.

We begin with a brief discussion of the dipole in the Cosmic Microwave Background (CMB, §6.1) and ascertain its value in the reference frame of the Local Sheet (LS). We then proceed to break down the LG dipole to understand the contributions to its predicted motion (§6.2). In §6.3, we discuss the necessary steps to reconcile the two values, and finally summarize our conclusions in §6.4.

Note that, throughout this chapter, we will use the galactic coordinate system for consistency with the literature on this subject.

6.1 Dipole in the Cosmic Microwave Background

Efforts to reconstruct the LG dipole from galaxies in 2MASS (Maller et al., 2003) and 2MRS (Erdoğdu et al., 2006b; Lavaux et al., 2008) have produced results that are both inconsistent with the CMB and highly dependent on the reconstruction method. The relatively recent work by Erdoğdu et al. (2006b) attempts four different reconstructions for the LG dipole. A flux-weighted reconstruction in the LG frame suggests a LG dipole 21° ± 8° from the CMB result. When performing the reconstruction, using redshifts relative to the CMB reference-frame as distance indicators, the result increases to 26° ± 8°. Flux-weighted reconstructions necessarily assume an intrinsic mass-to-light ratio, which, without information on the location or morphological type of the galaxy, may not be a valid assumption. The reconstructions using a number-weighted technique in the same paper suggest a LG velocity more than 35° from the CMB, and since the majority of distances are estimated from redshifts, different results are obtained when assuming the distances are given by the application of Hubble's law to the LG-centric redshift instead of CMB-centric values.

From the work in the previous chapters, it is evident that neither choice is ideal, and while the LG reference frame allows the use of Hubble's law locally, a different reference frame will provide better distance estimates beyond $\sim$ 3000–4000 km s^{-1}. The more recent reconstruction from 2MRS by Lavaux et al. (2008) predicts the LG velocity $\sim 50°$ from the CMB direction at $100h^{-1}$ Mpc, with an estimated error of 22° (95% confidence) associated with the reconstruction method.

It is clear that the reconstruction technique can have a significant impact on the derived dipole direction and magnitude. In this work, we remove the assumptions of equal weighting of galaxies, or intrinsic galaxy mass-to-light ratios, by utilizing dynamical mass estimates obtained from galaxies in identified groups.

Analysis of the 5-year WMAP data indicates the Sun is moving at a velocity of 369.0 ± 0.9 km s^{-1} toward ($b = 48.26° \pm 0.03°$, $l = 263.99° \pm 0.14°$) (Hinshaw et al., 2009). According to (Tully et al., 2008), the Sun has a velocity of 318 ± 20 km s^{-1} toward ($l = 96° \pm 4°$, $b = -1° \pm 4°$) in the reference frame of the LS (which is very closely related to the LG reference frame – see §3.1.2). Combining these results, we find that the LS is moving with a velocity of 627 ± 21 km s^{-1} towards ($b = 27° \pm 2°$, $l = 270° \pm 3°$) in the reference frame of the CMB.

6.2 Local Group Peculiar Velocity

In §4.3, we demonstrated that the application of linear perturbation theory to estimate a group's peculiar velocity will have an inherent uncertainty of $\sim$ 100 km s^{-1} in its magnitude. This implies that the uncertainty in the direction is reduced for groups with larger peculiar velocities, and the results of the simulation showed that the uncertainty follows the approximate form of Eq. (4.2). For a peculiar velocity with a magnitude of 627 km s^{-1} (i.e. the velocity of the LS in the rest frame of the CMB), Eq. (4.2) implies that the uncertainty in direction from linear perturbation theory (where we have scaled the velocity by the r.m.s. values provided in §4.3 and §3.3) is 11° (68% confidence) for the model constructed assuming the coherent mass correction (CMC), and 10° (68% confidence) for the model constructed assuming the incoherent mass correction (IMC). While the estimate of this uncertainty depends on the applicability of the Hubble Volume simulation to our sample (see the discussion of limitations in §4.2.1), the thermal velocity contributing to this effect is observed in practice, so we are justified in applying the results of §4.3. Using the revised distance and mass estimates from the procedure described in §3.2, we can examine more closely the contributions toward the LG peculiar velocity.

6.2.1 Contributions to the Local Group Peculiar Motion

While we noted the direction of the LG dipole to lie between the Virgo Cluster and Hydra in Chapter 3 (Figure 3.11), in this section we will examine the contributions to the resultant dipole vector. Figure 6.2.1 shows the cartesian galactic components of the LG peculiar velocity constructed from groups of galaxies inside concentric spheres of radius D as a function of D. The closest significant contribution arises from the Virgo cluster at $\sim$ 1250 km s^{-1}, pulling the LG toward the galactic north pole. Including the contribution from all groups inside the distance to the Virgo Cluster, the LG peculiar velocity is predicted to have reached $\sim$ 150 km s^{-1} in the direction of Virgo, in agreement with (although slightly on the low-end of) results in the literature, where estimates generally range from 130–250 km s^{-1} (e.g., Tonry et al., 2000; Bureau et al., 1996). The y–component decreases steadily between 2000 and 3500 km s^{-1}, due to contributions from smaller groups in the foreground of the Hydra-Centaurus supercluster. The sharp drop at $\sim$ 3600 km s^{-1} is due to the attraction of Hydra-Centaurus, which also increases the x–component. The ridge that increases the magnitude of the velocity at $\sim$ 5000 kms, followed shortly by a drop at $\sim$ 5500 km s^{-1}, is due to the tug of war between the Perseus-Pisces supercluster and the Norma cluster (Abell 3627) on almost the opposite side of the sky. Both are in the southern galactic hemisphere and so both act to decrease the z–component of the velocity.

Up to this point, the features predicted assuming either the coherent or incoherent mass corrections are similar. As we include groups at larger distances, the selection function falls rapidly, so the difference between the two models becomes apparent. For the IMC case, we distribute the unobserved mass isotropically. As such, the dipole is expected to converge since the anisotropies in the distribution will be small and decrease as we look to larger distances. Indeed, this is what we observe in Figure 6.1(b), although only 61% of the magnitude observed with respect to the CMB is recovered. For the CMC case, however, we assume that the missing mass is distributed according the observed group distribution, so we only expect convergence if the distribution of groups is sufficiently isotropic on large scales. In Figure 6.1(a), beyond $\sim$ 5500 km s^{-1} the magnitude of the dipole remains relatively steady until a small increase is observed in the z–component due to the Coma Cluster at $\sim$ 7500 km s^{-1}. The y– and z–components increase slowly as contributions are included up to the 12,000 km s^{-1} sample limit, and the x–component slowly decreases. While the magnitude does not change significantly, there is evidence for a rotation in the direction. By 10,600 km s^{-1}, the magnitude of the dipole has converged to within 5° of its final value, although the graph is suggestive that the dipole will continue to grow beyond the sampled 12,000 km s^{-1} volume. Additionally, we have only recovered 70% of the magnitude of the observed velocity with respect to the CMB.

In Figures 6.2 we show the offset between the LG direction and the CMB direction as we include groups in successively deeper concentric shells. The offset drops as close as 8–10° to the CMB direction (which is within the uncertainty of the modeling technique) after including the Norma Cluster, but before adding Perseus-Pisces. This feature can be seen more clearly in Figure 6.3, where the direction of the reconstructed LG peculiar velocity is shown on a walking plot. A similar feature was observed in the 2MRS galaxy-based reconstruction of Erdoğdu et al. (2006b). As we include groups at larger distances, however, the direction is drawn farther from the CMB. The effect is significantly more pronounced in the CMC case than the IMC case. The CMC case suggests little evidence for convergence; however, the convergence observed in the IMC case is expected by construction. The true distribution of the unobserved

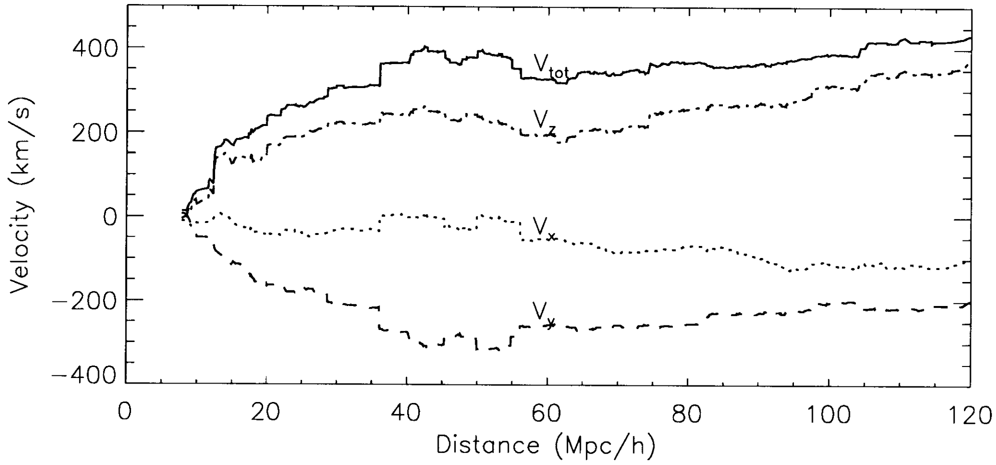

(a) Coherent Mass Correction

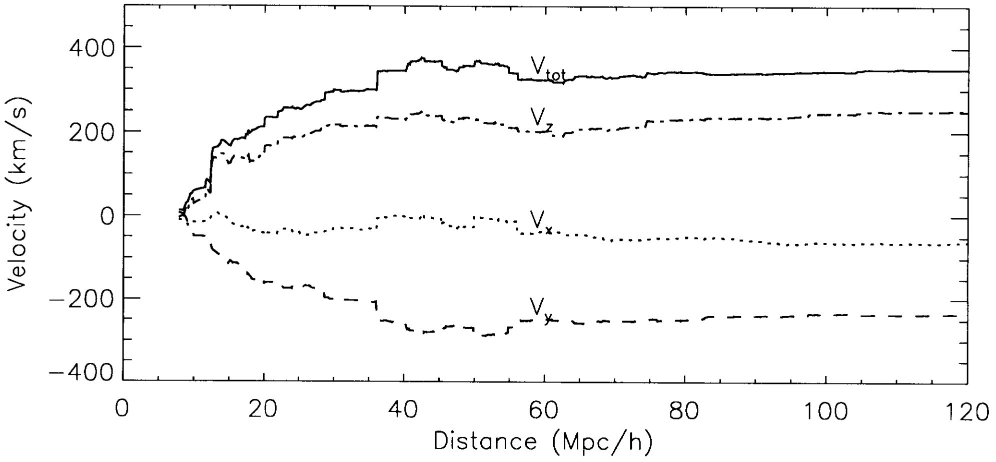

(b) Incoherent Mass Correction

Figure 6.1 Local Group dipole: Convergence with distance. The peculiar velocity of the LG is reconstructed from groups inside a sphere of the indicated radius, centered on the origin. Panel (a) shows the case for the coherent mass correction and panel (b) for the incoherent mass correction. The features of both figures are similar to $\sim$ 6000 km s^{-1}, after which the CMC case demonstrates a rotation in the direction, but the IMC case appears to converge.

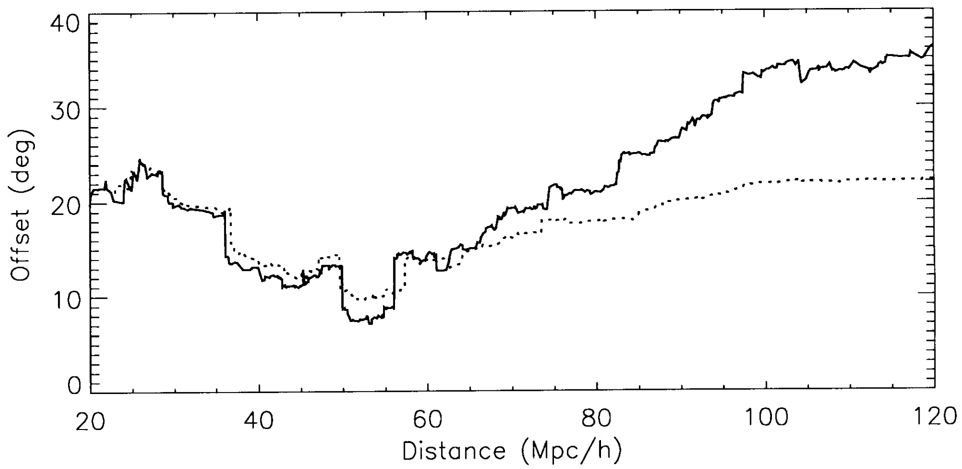

Figure 6.2 Angular offset from CMB dipole. The angular separation between the LG and CMB directions are plotted as we include groups in successively deeper concentric spheres. The solid (dotted) line shows the result assuming the coherent (incoherent) mass correction. The dip at $\sim$ 5000 km s^{-1} to 8° (10° in the IMC case) from the CMB is due to the inclusion of the Norma cluster, but adding Perseus-Pisces brings the angular separation back to 15°. The inclusion of groups at larger distances acts to pull the direction farther from that implied by the CMB. The CMC case continues to deviate from the CMB result, whereas the IMC case converges to a separation approximately 23° from the dipole in the CMB.

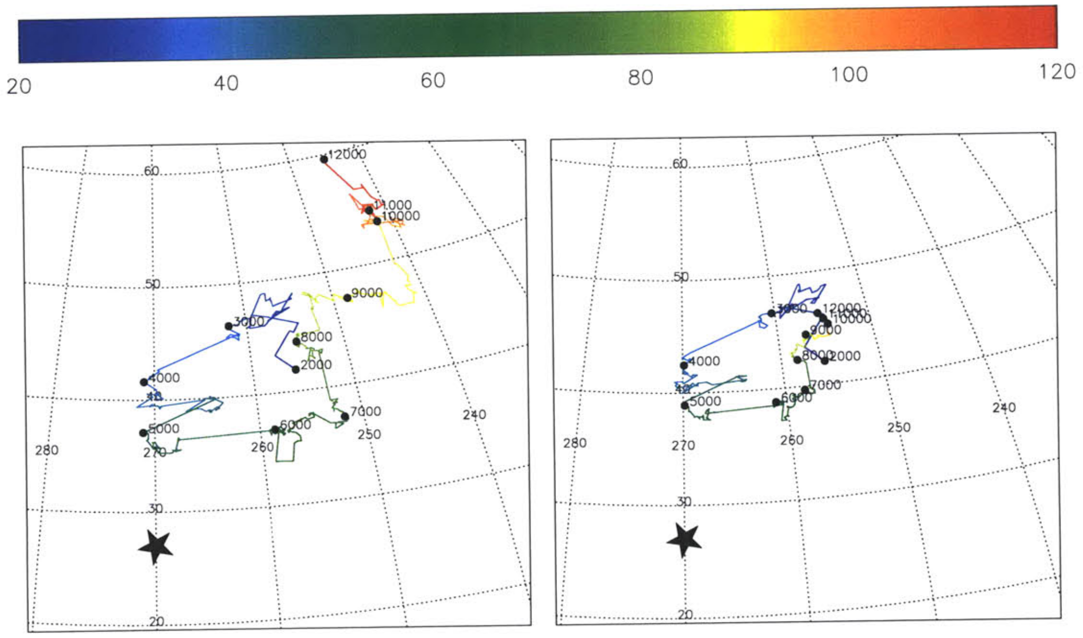

(a) Coherent Mass Correction

(b) Incoherent Mass Correction

Figure 6.3 Walking plot of Local Group peculiar velocity. The figure shows the reconstructed direction of the LS in the LR frame as groups at larger distances are included in the reconstruction. The map is an Aitoff projection in galactic coordinates. Panel (a) shows the case for the coherent mass correction and panel (b) for the incoherent mass correction. Circles are placed at 1,000 km s^{-1} intervals (in real-space distance) between 2,000 km s^{-1} and 12,000 km s^{-1} (the distances in km s^{-1} are indicated on the plot). The color indicates the distance inside which groups are included in the reconstruction, from blue ($20/h$ Mpc) to red ($120/h$ Mpc). The star indicates the expectation from the CMB. As seen in Figure 6.2, the IMC case results in convergence at approximately 23° from the CMB, whereas the CMC case shows no sign of convergence.

mass is likely to fall somewhere between these two extremes. Due to the fact that the CMC case does not appear to converge within the sampled volume, and only 60–70% of the expected magnitude has been recovered, we find no evidence to suggest that the dipole has converged inside 12,000 km s^{-1}.

In this work, we chose to consider groups of 5 or more members, a choice somewhat arbitrary, but motivated by the results of Chapters 2 and 4. In Figure 6.4, we can see the effect on the LG dipole had we chosen to restrict our sample to a higher threshold. The plot shows the resulting LG peculiar velocity when we include only groups with more than N_m members as a function of N_m. While the largest groups have a significant impact on the LG peculiar velocity, the contribution from a large number of small groups impacts the resulting dipole direction and magnitude significantly in both the CMC and IMC cases. The contribution to the LG peculiar velocity from small groups is the primary difference between the reconstruction presented here and a galaxy-based model. When assigning galaxies equal weights, one underestimates the masses of groups where only the brightest members are observed, relying on the selection function to redistribute the mass appropriately. Here, we use additional information on the mass estimates of the groups (from the dynamics), which is discarded in a galaxy-based reconstruction.

The potential problem with this technique is that the smallest groups are more prone to uncertainties in the mass estimates through interloper contamination. To test the effect this has on the resulting LG peculiar velocity, we show the angular offset from the direction obtained when including all groups to 12,000 km s^{-1}, as we include groups in decreasing order of size (Figure 6.5, solid line). The dashed line in the figure shows the result of removing groups beyond 9,000 km s^{-1} from the calculation. If the smallest groups at the largest distances were contributing significantly to the LG peculiar velocity, the two lines would diverge as we decrease the group size. Instead, we observe a discrepancy at $N_m = 40$, which corresponds to assignment of mass at the location of the Hercules Supercluster. The difference is more pronounced in the CMC case since the large distance of the supercluster means that the associated bias correction is large. To ascertain the true mass correlated with the location of the supercluster requires a deeper redshift survey. However, it is clear that while the reconstructed LG peculiar velocity depends on the choice of the bias correction, it is not significantly influenced by small groups near the sample limit.

We also ask the question, "How many attractors are required to reproduce the observed dipole at the location of the LG?" Figure 6.6 shows the resulting LG peculiar velocity constructed by adding the groups in decreasing order according to the acceleration at the LG due to their presence. For the CMC case, we find that 90% (95%) of the magnitude can be accounted for with a model of 163 (316) attractors, whereas the angle can be recovered to within 10° using a model of 91 attractors. For the IMC case, the numbers are notably smaller: 90% (95%) of the magnitude can be accounted for with a model of 68 (205) attractors, and the angle can be recovered to within 10° using a model of just 43 attractors.

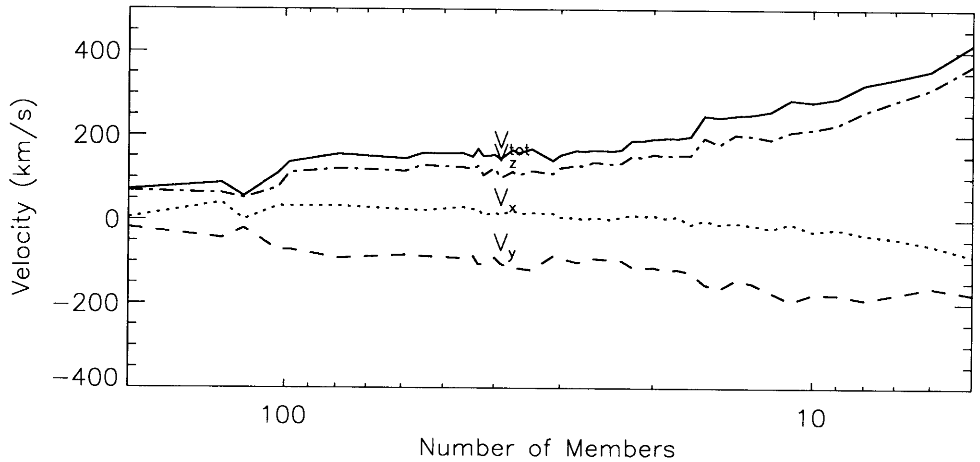

(a) Coherent Mass Correction

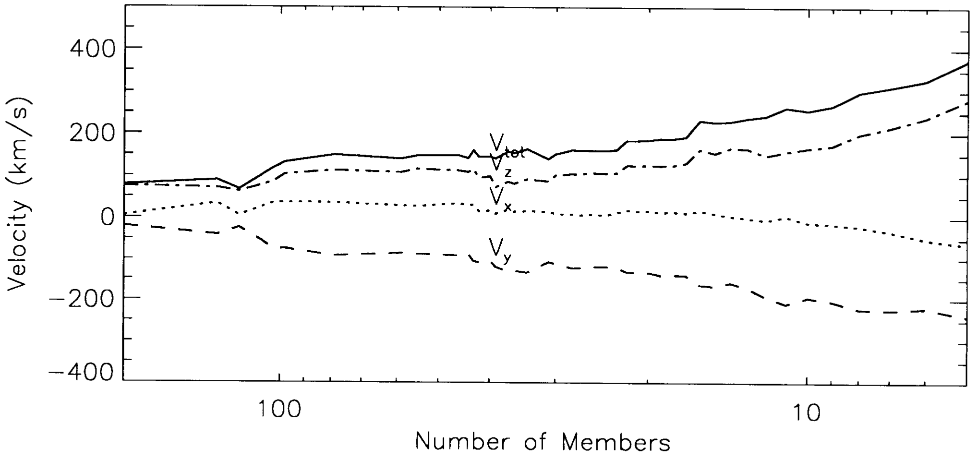

(b) Incoherent Mass Correction

Figure 6.4 Local Group dipole: Convergence with group size. The figure shows the peculiar velocity of the LG, reconstructed from groups containing N_m or more members, plotted as a decreasing function of N_m. Panel (a) shows the case for the coherent mass correction and panel (b) for the incoherent mass correction. In both cases, the contribution from small groups is not negligible.

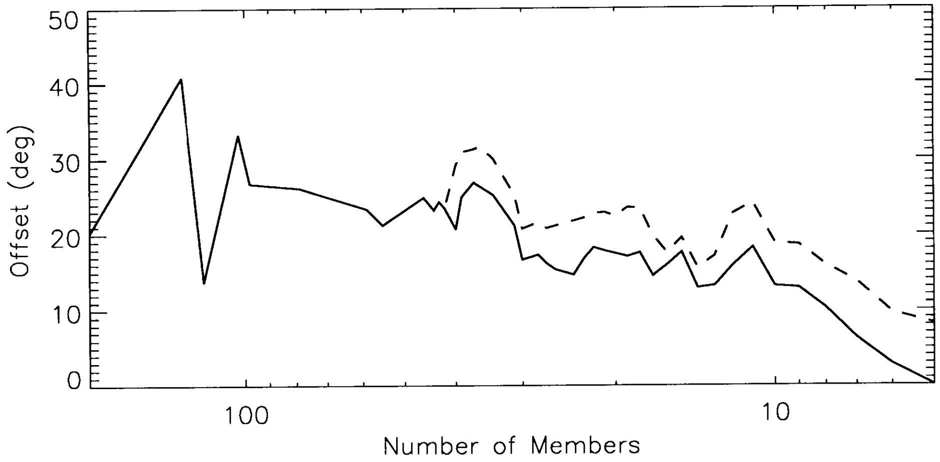

(a) Coherent Mass Correction

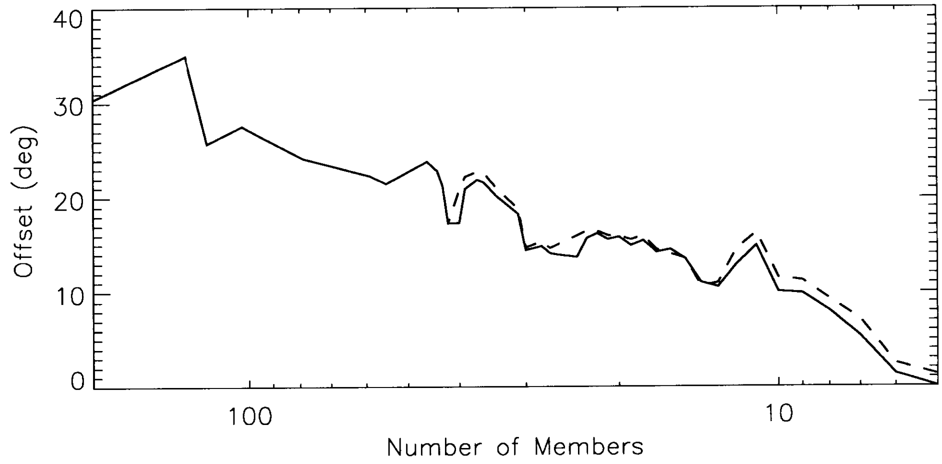

(b) Incoherent Mass Correction

Figure 6.5 Local Group dipole: Convergence of angular direction with minimum group size. The graph shows the angular offset between the direction of the LG dipole when using all groups of 5 or more members, and the direction obtained when only considering groups of N_m members, as a decreasing function of N_m. Panel (a) shows the case for the coherent mass correction, and panel (b) for the incoherent mass correction. The dashed line shows the result using all groups inside 12,000 km s^{-1}; the dashed line restricts the analysis to groups inside 9,000 km s^{-1}. The discrepancy occurs primarily by missing the Hercules Supercluster, rather than by a prominent effect from the selection bias in small groups. The discrepancy is notably smaller in panel (b) because Hercules lies near the edge of the sample.

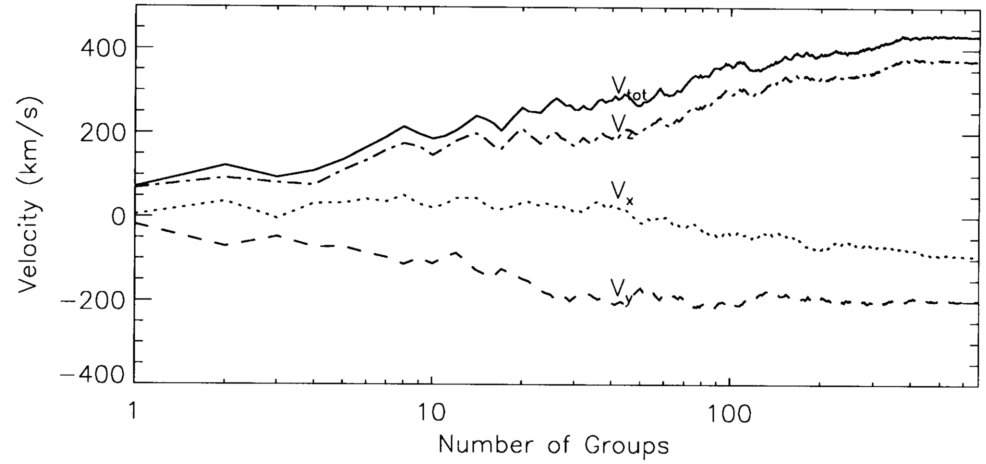

(a) Coherent Mass Correction

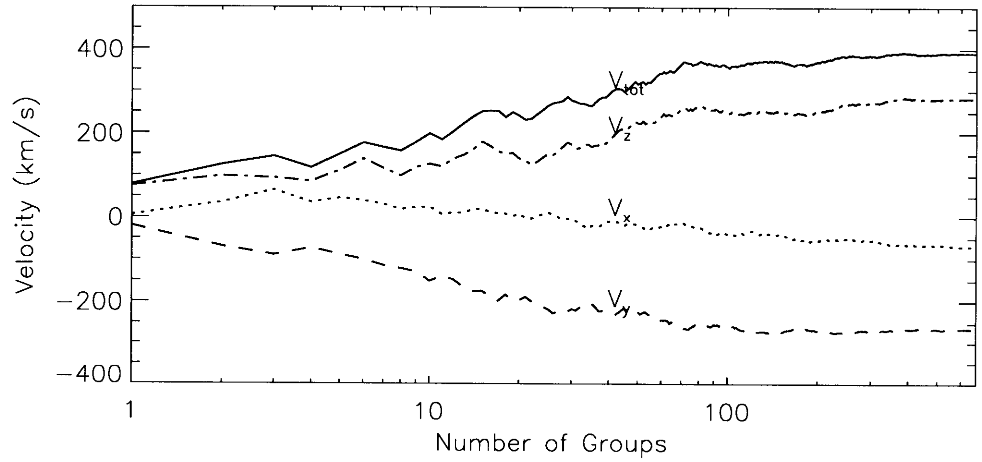

(b) Incoherent Mass Correction

Figure 6.6 Local Group dipole: Groups contributing to the flow. The figure shows the peculiar velocity of the LG, reconstructed by adding groups sequentially according to their contribution to LG peculiar velocity. Panel (a) shows the case for the coherent mass correction and panel (b) for the incoherent mass correction. For the CMC case, 90% of the magnitude of the LG peculiar velocity can be reconstructed using 163 groups, and using 91 groups we can reconstruct the predicted direction to within 10°. For the IMC case, 90% of the magnitude of the LG peculiar velocity can be reconstructed using just 68 groups, and just 43 groups are required to reconstruct the predicted direction to within 10°.

6.2.2 Direction of the Local Group Peculiar Velocity

Having established the underlying contributions to the LG peculiar velocity, we turn to examine the resulting direction of motion. In Figure 6.7, we plot (in galactic coordinates) the galaxy groups in 2MRS, sized according to their relative contribution to the LG peculiar velocity. The resulting direction of motion of the LG in the LR frame is indicated on the plot, along with the direction of the LG's motion with respect to the CMB. We consider the cases of the coherent mass correction and incoherent mass correction in turn. For the CMC case, we assume $\beta = 0.17$ and compute motion of the LS in the LR frame to be 439 ± 65 km s^{-1} towards ($l = 244° \pm 16°$, $b = 59° \pm 7°$), which corresponds to a LG motion of 442 ± 67 km s^{-1} towards ($l = 247° \pm 18°$, $b = 63° \pm 7°$), according to the definition of the LG reference frame in terms of the solar motion (Courteau & van den Bergh, 1999). The error in angle corresponds to 12° at 68% confidence, which has been calculated by propagating the uncertainty in mass, distance estimates, and membership to the groups using the Monte-Carlo method described in §5.4.1. Additionally, for a peculiar velocity of 92% of the r.m.s. group velocity, we estimate the error resulting from the application of linear perturbation theory to galaxy groups to be 14° (68% confidence) in the same manner as §6.2 above. The resulting peculiar velocity of the LS in the LR frame lies $36° \pm 18°$from the direction inferred from the CMB, inconsistent at 95% confidence.

For the IMC case, we assume $\beta = 0.19$ and compute motion of the LS in the LR frame to be 387 ± 54 km s^{-1} towards ($l = 255° \pm 8°$, $b = 46° \pm 4°$), which corresponds to a LG motion of 386 ± 54 km s^{-1} towards ($l = 259° \pm 7°$, $b = 50° \pm 4°$). The error in angle corresponds to 6° at 68% confidence. The errors are smaller than in the CMC case, where uncertainties in the bias correction are correlated with uncertainties in the group mass estimates. Additionally, for a peculiar velocity of 101% of the r.m.s. value, we estimate the error resulting from the application of linear perturbation theory to galaxy groups to be 13° (68% confidence) using the same procedure as above. The resulting peculiar velocity of the LS in the LR frame lies $23° \pm 14°$from the direction inferred from the CMB, inconsistent at 90% confidence. Due to the inherent uncertainty in the appropriate choice of bias correction, we have presented upper and lower limits on the discrepancy between the CMB dipole and the LG peculiar velocity computed from groups of galaxies in 2MRS.

Previous efforts to reconstruct the direction of the LG dipole have reached similar conclusions, although with the exception of the most recent work by Lavaux et al. (2008), most have found the direction lies within $\sim$ 30° of the dipole. The results found here lie at the high end of this range; while this method has fewer physical assumptions, its susceptibility to interloper contamination of groups drives the errors much higher than other techniques. As discussed above, the large number of groups with a small number of members contribute significantly to the LG peculiar velocity. While this partially explains the larger discrepancy observed with the CMB than obtained in earlier works, we have propagated the errors using a Monte-Carlo technique, and the conclusion of inconsistency with the CMB remains robust.

The IMC result is in very good agreement with the 2MASS flux-weighted reconstruction of Maller et al. (2003), who obtain ($l = 264.5° \pm 2°$, $b = 43.5° \pm 4°$). In

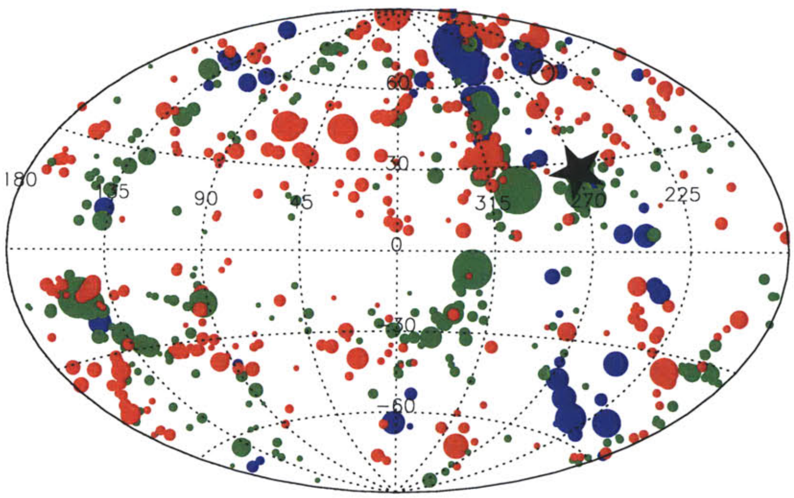

(a) Coherent Mass Correction

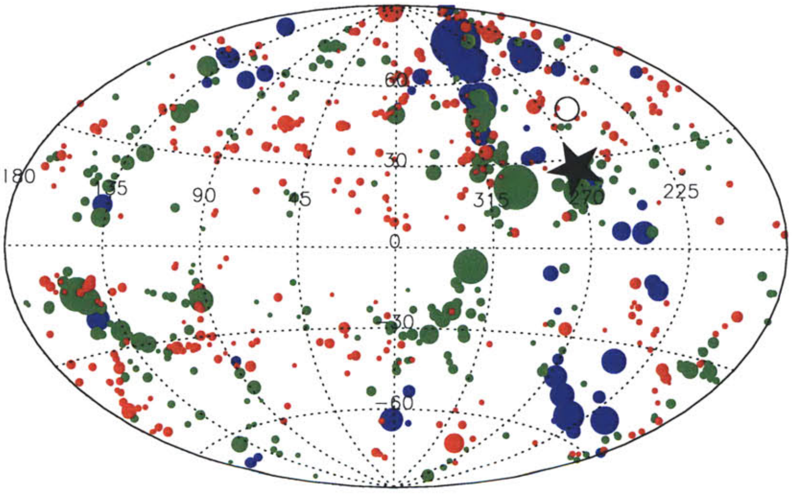

(b) Incoherent Mass Correction

Figure 6.7 Groups contributing to LG peculiar velocity. The figure shows the locations of the identified groups in galactic coordinates (Aitoff projection); the radii of the circles scale linearly with the group's contribution to the LG peculiar velocity. The color indicates the distance to the group: red $cz > 6,000$ km s^{-1}; green: $2000 < cz < 6000$ km s^{-1}; blue: $cz < 2000$ km s^{-1}. The location of the predicted LG dipole is shown by the open circle, and the star represents the direction inferred from the CMB. Panels (a) and (b) show the reconstructions for the coherent and incoherent mass corrections, respectively.

this case, no attempt to correct for the selection bias is used, since redshifts are not incorporated into the analysis. This result also lies within 1σ of the 2MRS-based flux-weighted reconstruction of Erdoğdu et al. (2006b), who find ($l = 251° \pm 12°$, $b = 37° \pm 10°$). A number-weighted reconstruction in the same paper ($l = 231°$, $b = 42°$) lies at a significantly lower galactic longitude, and likely differs because of the difference in weighting of the distant groups. The result is also within 1σ of the 1.2 Jy *IRAS* dipole (Webster et al., 1997), but inconsistent with the PSCz dipole of Rowan-Robinson et al. (2000), which differs from previous *IRAS* results. The CMC result, however, lies 2σ from the previous reconstructions with 2MASS and 2MRS. The discrepancy is due to the larger weight assigned to groups beyond $60/h$ Mpc including, most notably, the Hercules supercluster. Based on an analysis of X-ray clusters, Kocevski et al. (2004) suggest that Hercules and Shapley both contribute to the LG peculiar velocity, and that the observed convergence in previous work at $\sim 60/h$ Mpc is coincidental. Including clusters out to $z \sim 0.2$, they find the dipole diverges from the CMB result, and do not find convergence until they have included groups as distant as $\sim 200/h$ Mpc. Since we probe the mass distribution to 12,000 km s^{-1}, the divergence we observe is consistent with their findings, although a deeper survey is required to accurately trace the mass distribution at 12,000 km s^{-1}.

6.3 Bulk Flows

The errors on the reconstructed LG dipole are largely due to the effect of interlopers on mass estimates of smaller groups. However, the direction of the reconstructed LG peculiar velocity is inconsistent with the direction one interprets from analysis of the dipole in the CMB between above the 90% confidence level. Whilst there are several possible explanations for this discrepancy, in this section we consider the implication of assuming the model is indeed correct.

From Eq. (1.8), the reconstructed peculiar velocity is proportional to the quantity β. The estimated distances to groups obtained by constructing a self-consistent model of the flow-field (§3.2.6) therefore depend weakly on β. In the analysis below, we propagate the errors on the obtained value of β (§5.4.2), but do not re-compute the distances to groups in each case. This has a negligible effect on the reconstructed peculiar velocity of the LG over the small range of β that corresponds to its uncertainty.

When we first introduced the concept of the LR frame in §3.2.2, we noted the possibility that the LR frame and CMB rest frame may not be equivalent. The LG peculiar velocity reconstructed from inhomogeneities in the density-field, measured in the LR frame, differs *significantly* in magnitude and direction to the peculiar velocity inferred from the dipole in the CMB. With the hypothesis that the model is valid, this necessarily implies that the LR frame (and therefore the entire modeled volume) has a net velocity with respect to the CMB. Such hypotheses are commonly referred to in the literature as bulk flows; below we compute the magnitude and direction of the bulk flow of the LR frame with respect to the rest frame of the CMB.

If the LS has a peculiar velocity relative to the LR frame of $\mathbf{u}_{\rm pec}^{\rm (LR)}$, the velocity of the LS relative to the rest frame of the CMB is given by

$$\mathbf{u}_{\mathrm{pec}}^{(\mathrm{CMB})} = \mathbf{u}_{\mathrm{pec}}^{(\mathrm{LR})} + \mathbf{B} \tag{6.1}$$

where $\mathbf{B}$ is the velocity of the LR frame with respect to the CMB frame. From §6.2.2, for the coherent mass correction, we have

$$\mathbf{u}_{\mathrm{pec}}^{(\mathrm{LR})} = (-97 \pm 54)\hat{\mathbf{x}} + (-201 \pm 54)\hat{\mathbf{y}} + (378 \pm 72)\hat{\mathbf{z}} \text{ km s}^{-1} \tag{6.2}$$

(in galactic coordinates) where we have considered only the errors associated with the uncertainty in the model and neglected the possible contribution from a thermal component. From §6.1

$$\mathbf{u}_{\mathrm{pec}}^{(\mathrm{CMB})} = (2 \pm 22)\hat{\mathbf{x}} + (-561 \pm 20)\hat{\mathbf{y}} + (281 \pm 22)\hat{\mathbf{z}} \text{ km s}^{-1} \tag{6.3}$$

Subtracting, we find

$$\mathbf{B} = (99 \pm 58)\hat{\mathbf{x}} + (-360 \pm 55)\hat{\mathbf{y}} + (-97 \pm 75)\hat{\mathbf{z}} \text{ km s}^{-1} \tag{6.4}$$

If we propagate the error in the estimate of β through Monte-Carlo simulations, we obtain

$$\mathbf{B} = (97 \pm 64)\hat{\mathbf{x}} + (-358 \pm 70)\hat{\mathbf{y}} + (-91 \pm 70)\hat{\mathbf{z}} \text{ km s}^{-1} \tag{6.5}$$

which corresponds to a motion of 395 ± 59 km s^{-1} in a direction ($l = 286° \pm 11°$, $b = -14° \pm 11°$).

For the case of the incoherent mass correction,

$$\mathbf{u}_{\mathrm{pec}}^{(\mathrm{LR})} = (-67 \pm 32)\hat{\mathbf{x}} + (-258 \pm 46)\hat{\mathbf{y}} + (279 \pm 39)\hat{\mathbf{z}} \text{ km s}^{-1} \tag{6.6}$$

Propagating the uncertainty in β, we obtain

$$\mathbf{B} = (62 \pm 65)\hat{\mathbf{x}} + (-331 \pm 79)\hat{\mathbf{y}} + (36 \pm 72)\hat{\mathbf{z}} \text{ km s}^{-1} \tag{6.7}$$

which corresponds to a motion of 339 ± 73 km s^{-1} in a direction ($l = 281° \pm 13°$, $b = 6° \pm 12°$).

Recently, Watkins et al. (2009), who combine data from peculiar velocity surveys, find the bulk flow within a Gaussian window of $50/h$ Mpc to be 407 ± 81 km s^{-1} toward ($l = 287° \pm 9°$, $b = 8° \pm 6°$). This agrees with our IMC result to within 1σ and our CMC result within 2σ. Such a large bulk flow is certainly unexpected from cosmological arguments. From analysis of a ΛCDM cosmological model, using WMAP5 parameters, Watkins et al. (2009) conclude that the probability of observing a bulk flow of ~ 400 km s^{-1} is less than 1%. We discuss the implications of this result in Chapter 7.

Note that, in our analysis, the bulk flow is calculated based on the predicted motion solely of the LG, calibrated such that the flow-field model reproduces peculiar velocity measurements inside 3000 km s^{-1}. The bulk flows predicted under both the CMC and IMC assumptions of the unobserved mass distribution are of a similar magnitude, and both overlap with the Zone of Avoidance. The proximity of their directions to the galactic plane is suggestive that the poorly sampled region at low galactic latitudes may contain structures with sufficient mass to account for at least part of this motion. Certainly, in the past, the hunt for the Great Attractor took a significant turn when the early estimate of the mass of the Norma Cluster at $b \sim -10°$ was revised (Kraan-Korteweg et al., 1996).

While the inclusion of a massive structure within this region would alter the flow-field model derived in Chapter 3, an order of magnitude estimate suggests that a structure $\sim 10^{13} M_{\odot}$ at 1 Mpc, $\sim 3 \times 10^{15} M_{\odot}$ at 20 Mpc, or $\sim 2 \times 10^{17} M_{\odot}$ beyond the sample limit, would be required to give rise to the necessary motion. Similar estimates have been proposed by Loeb & Narayan (2008). Since Virgo subtends $\sim 12°$ on the sky, it would be very surprising if a structure at a similar distance, but several times more massive, was not visible in 2MRS. Similarly, a small galaxy group behind the galactic plane would subtend an angle much larger than the Zone of Avoidance, so the favored option would be that of a massive structure (or series of multiple structures) beyond $\sim 12,000$ km s^{-1}.

6.4 Summary

In this chapter, we have examined the peculiar motion of the LG as predicted by the flow-field constructed from 2MRS galaxy groups. While the errors in the reconstructed peculiar velocity are large due to the potential for interlopers to alter the dynamically estimated masses, a careful treatment demonstrates that the discrepancy between the LG motion and the motion expected from the dipole in the CMB is significant above the 90% confidence level. We observe that, by only including groups inside $60/h$ Mpc, the direction of the CMB dipole can be reproduced within the model errors, but adding more distant groups pulls the direction significantly farther from the CMB. Even at 12,000 km s^{-1}, we have only recovered 60–70% of the magnitude of the observed velocity and there is little evidence to suggest the dipole has converged.

Under the assumption that, locally, the flow-field can be predicted using the observed and identified groups of galaxies in 2MRS, we have demonstrated that a possible solution is the bulk motion of the sampled volume toward a direction very close to the galactic plane. While the possibility that undersampled regions inside the volume may contribute to the inconsistency has been examined, we note that contributions from outside the volume, which have been frequently suggested in the literature (e.g., Scaramella et al., 1991; Branchini & Plionis, 1996; Kocevski & Ebeling, 2006), remain likely candidates.

Chapter 7

Conclusions

In this thesis, I have presented a new approach to modeling the flows in the nearby Universe. Utilizing recent data from the Two Micron All-Sky Redshift Survey (2MRS, Huchra et al., 2009), I have constructed self-consistent density and velocity fields, tracing the underlying mass distribution through identified groups of galaxies. Early efforts to model the flows consisted of only a few "attractors" in an effort to understand the large motion of the Local Group (LG) in the reference frame of the Cosmic Microwave Background (CMB) (e.g., Lynden-Bell et al., 1989; Han & Mould, 1990), but since then the models have become significantly more complex with the completion of the first nearly all-sky flux-limited redshift surveys (e.g., Strauss et al., 1992; Branchini et al., 1999, using *IRAS*-selected samples). With the completion of the 2MRS $K_s < 11.25$ survey, a reconstruction of the density and velocity fields by Erdoğdu et al. (2006a) presented the first model that mapped to low galactic latitudes without the biased selection of spiral galaxies from which the *IRAS* and optically-selected samples suffered. At $\sim 2\mu$m, 2MASS also provides a better tracer of the baryonic mass than surveys conducted in the B-band or at 60μm. Although models based upon cluster samples have been considered in the past (e.g., Branchini & Plionis, 1996; Scaramella, 1995), the flow-field constructed from groups of galaxies in 2MRS provides the first complete model constructed from an all-sky flux-limited sample using dynamical mass estimates to trace the density-field.

I presented two group catalogs constructed from the 2MRS $K_s < 11.25$ source data at different density contrasts ($\delta\rho/\rho = 12$ and $\delta\rho/\rho = 80$). Groups were identified using an adaptation of the percolation algorithm of Huchra & Geller (1982), and properties of the groups derived. The mass functions agree with Press-Schechter theory (Press & Schechter, 1974) at the 2σ–level, and the distribution of velocity dispersions agree with the groups identified in the earlier CfAN catalog(Ramella et al., 1997). Combining the 2MRS-derived K_s-band luminosity density with the group mass-to-light ratios, the former catalog provides a value of the matter density parameter consistent with the 3-year WMAP results (Spergel et al., 2007), which is underestimated in the latter. The implication is that dark matter is likely to cluster on scales larger than $\delta\rho/\rho \sim 100$, and closer to $\delta\rho/\rho \sim 10$, although the potential for the LDC catalog to have overestimated the masses through inclusion of interlopers is noted. The identification of known clusters is more robust in the catalog constructed at the higher density contrast (HDC), motivating its use in the construction of a model of the flow-field.

I utilized the 2MRS $K_s < 11.75$ source data to construct a catalog of groups at a density contrast threshold of $\delta\rho/\rho = 80$, which forms the basis for a model of the flow-field inside 12,000 km s^{-1}. Using dynamical mass estimates and allowing for a linear bias between the inferred cluster masses and underlying dark matter distribution, I presented a method to estimate distances to groups such that the density and velocity fields are self-consistent. On application to 2MRS, I predict significant infall in the vicinity of Virgo, Perseus-Pisces, Hydra-Centaurus, Coma, Norma and Hercules. The Shapley concentration, which lies just outside the modeled volume, distorts the flow toward the limit of the sample. I noted that 8–15% of galaxy groups are expected to have velocities larger than than the 627 km s^{-1}, observed as the LG velocity with respect to the reference frame of the Cosmic Microwave Background (CMB). Subtracting the motion of the Local Sheet (LS) from the predicted flows, I constructed maps of the estimated LS-centric line-of-sight peculiar velocities as a function of spatial position.

I compared the 2MRS Groups (2MG) velocity-field with the PSCz velocity-field of Branchini et al. (1999) and the 2MRS galaxy-based velocity-field of Erdoğdu et al. (2006a). I find that the 2MG velocity-field predicts higher infall into the known rich clusters than the PSCz model — an expected result since the *IRAS*-selected samples are biased toward the detection of star-forming galaxies and therefore underestimate the overdensities of rich clusters. I find good agreement between the models constructed from galaxy groups and 2MRS galaxies. Both 2MRS-based models predict backside-infall into the Norma region, a feature that is absent from the PSCz model.

Using the $z = 0$ snapshot of the ΛCDM Hubble Volume simulation, I tested the reconstruction of peculiar velocities in the linear regime and demonstrated that the peculiar velocities of groups of galaxies will have an uncertainty of $\sim$ 100 km s^{-1} in their magnitude, under the idealized assumptions of accurate mass and distance estimates, consistent with the expectations of a cosmic thermal component to the velocity. I noted that the uncertainty in the direction of the peculiar velocity of a group decreases for larger peculiar velocities, until the non-linear regime is approached. If the results from the analysis of the simulation are applicable to the real Universe, then uncertainties in the linear approximation prevent alignment between the LG and CMB dipoles to better than 11° at 68% confidence. I demonstrated that the methods suggested to improve the distance estimates to groups by utilizing a self-consistent approach to modeling the flow-field can achieve up to a 50% improvement over a simple application of Hubble's law, in the absence of uncertainties in the mass estimates of groups and sufficient sample depth.

I presented a method that will allow a mapping from the angular position and redshift measurements of groups to an estimated distance, under the assumption that the flow-field model is robust. I used distance estimates to nearby galaxies to calibrate the amplitude of the velocities predicted by the flow-field model, and obtained estimates of the constant of proportionality between the measured density perturbations and the induced velocity. For the assumption that the unobserved mass is correlated with observed groups, I find $\tilde{\beta} = 2.3^{+0.4}_{-0.2}$. Assuming the unobserved mass is distributed isotropically, I find $\tilde{\beta} = 2.6^{+0.7}_{-0.4}$. Both values are consistent with each other, and provide upper and lower limits to the expected value for the true distribution. By comparing these values with a WMAP5 cosmology, I find the scale on which dark matter clusters is set by $\delta\rho/\rho \sim 3$.

The application of this method to galaxies in 2MRS demonstrates that, if the model is reliable, the utilization of the flow-field should improve distance estimates typically by ~ 30% over an estimation based upon Hubble's law when applied to galaxies beyond ~ 1000 km s^{-1}, and is predicted to perform significantly better in the vicinity of clusters. Comparing the model predictions for galaxy distances with estimates from the *SFI++* sample demonstrates its utility in an improvement over Hubble's law by ~ 5–50% inside ~ 4000 km s^{-1} (depending on the region in question), although uncertainties in the measurements and the biased target selection hinder our ability to draw accurate conclusions. The failure to predict distances accurately in the background of the Hydra cluster suggests evidence for attraction toward a massive concentration just beyond the sampled volume, such as the Shapley concentration (e.g., Scaramella et al., 1991; Branchini & Plionis, 1996; Kocevski & Ebeling, 2006), or a structure masked by the galactic plane.

I examined in detail the peculiar velocity of the LG as predicted by the flow-field and find a discrepancy depends on the assumption of the distribution of the unobserved mass. I consider the two extremes of the distribution: where the unobserved mass is distributed entirely isotropically, in which case I find a discrepancy between the LG and CMB directions of $23° \pm 14°$, and where the mass is distributed in the same manner as the observed groups, in which case I find a discrepancy of $36° \pm 18°$. These results bracket the expected offset from the true distribution of the unobserved mass, and both imply that the discrepancy between the observed and predicted directions is significant above the 90% confidence-level. Additionally, I are only able to account for 60–70% of the magnitude of the velocity of the LG in the CMB frame. Under the assumption that, locally, the flow-field can be predicted using the observed and identified groups of galaxies in 2MRS, I have demonstrated that a possible solution is the bulk motion of the sampled volume toward a direction that lies very close to the galactic plane. While the possibility that undersampled regions inside 12,000 km s^{-1} may contribute to the inconsistency has been considered, I note that contributions from outside the volume, as suggested above, form likely candidates for the solution.

Since the model of the flow-field performs reasonably well inside ~ 3000 km s^{-1}, discrepancies beyond this volume, in addition to the unexplained contribution to the dipole observed in the CMB, imply that our understanding of the dynamics and mass distribution beyond ~ 3000 km s^{-1} is less than desired. To understand where the sources of error may lie, I revisit some of the assumptions in the model of the flow-field:

(i) **Zone of avoidance**

The galactic plane was populated using a random-sampling technique to avoid edge-effects near the plane, however 2MRS contains few redshifts below $|b| = 5°$, and many initially included in the catalog turned out to be foreground objects (e.g., stars in the plane of the Milky Way). The undersampled region is sufficiently large that multiple groups behind the galactic plane would certainly alter the predicted motion of the LG, and, as implied in this work and the efforts of others (e.g. Watkins et al., 2009; Hoffman et al., 2001), an attractor (or multiple attractors) in this direction would account for the predicted bulk motions.

(ii) **Selection function**
The selection function of the $K_s < 11.75$ survey for galaxy groups begins to turn over $\sim 60/h$ Mpc, although I expect to find (and do find, as far as is possible to tell) all *known* massive structures inside a volume limited by a radius almost twice as deep. If one (or several) massive group(s) is (are) undersampled beyond the limit set by the selection function, the resulting effect could certainly account for the discrepancy with the CMB.

(iii) **ΛCDM Cosmology**
Expectations from ΛCDM cosmology indicate the dipole is expected to have converged by $120/h$ Mpc (e.g., Lavaux et al., 2008; Watkins et al., 2009). If our understanding of the cosmology is inaccurate, then our expectations for the scales of convergence may be invalid. Efforts to explore the effects of modified theories of gravity on the reconstructed motion of the LG (Crook et al., 2009) have not been able to resolve the discrepancy, however the subject is far from closed.

(iv) **Linear bias**
I assumed a model of linear bias throughout this analysis, however depedencies of bias on halo mass, luminosity and scale are being explored (e.g. Somerville et al., 2001). Such modifications to the bias could certainly alter the predictions of the flow-field model and warrant considerable investigation.

(v) **Dynamical mass estimates**
Our treatment of the errors associated with the dynamical mass estimates is routed in the assumption that variation in the mass-to-light ratios of similarly-sized groups is due to uncertainty in the mass. While I expect this to put conservative limits on the uncertainty in the mass, if the errors are dominated by interloper contamination, it is difficult to model the errors on the mass reliably and in a consistent manner.

(vi) **Interpretation of the CMB dipole**
While it is generally accepted that the dipole in the CMB is a measure of the heliocentric peculiar motion, alternative cosmological theories have been proposed (e.g., Paczynski & Piran, 1990) that allow for a dipole component in the spatial temperature distribution without the necessity for a peculiar motion with respect to the Hubble flow.

While the requirements to advance the field by investigating these possibilities vary from the investigation of alternative theoretical frameworks to deeper, fainter redshift surveys, I note that additional approaches to the problem can be considered with the data in hand. Methods for reconstructing the density-field using spherical harmonic decomposition and Wiener filtering (e.g., Webster et al., 1997; Schmoldt et al., 1999; Erdoğdu et al., 2006a) have proven successful in adapting the smoothing scale to compensate for the lack of information in poorly-sampled regions such as the zone of avoidance. With the functional form of the mass-to-light ratio as a function of group size provided in this thesis, a model constructed from the galaxy density-field with galaxy masses estimated based on group membership and K_s-band fluxes will provide a reliable method to trace the density-field. The comparison between such a model and a flux-weighted reconstruction would allow for further study of the bias parameter for galaxies.

Additionally, 2MASS $K_s < 11.75$ galaxies at low galactic latitudes without optical redshifts are being targeted in an HI survey of the galactic plane (Huchra et al., 2009). Such a survey expects to obtain redshifts to HI-rich inclined spiral galaxies within ~ 5000 km s^{-1}, and will allow us to understand if poor sampling behind the galactic plane is indeed the root of the discrepancy between the predicted motion of the LG and the CMB dipole.

With sufficient precision, a peculiar-velocity survey based on 2MRS targets will allow us to trace the observed flows directly. HI observations in nearly-edge-on spiral galaxies for locations outside the Arecibo declination range have recently been obtained (see the 2MASS Tully-Fisher Survey (2MTF), Masters et al., 2007). By calibrating the Tully-Fisher relation (Tully & Fisher, 1977) in the 2MASS J, H, and K_s-band (Masters et al., 2008), in conjunction with this work, 2MTF will provide the best available tool for understanding the bias between the dark matter and observed light.

On a closing note, I leave the reader with a map of Abell Clusters with measured redshifts beyond 10,000 km s^{-1} (Figure 7.1). There are two distinct overdensities: one is the Shapley Supercluster at $\sim 130/h$ Mpc ($l \sim 310°$, $b \sim 29°$), and the other is the Horologium-Reticulum Supercluster at $\sim 180/h$ Mpc ($l \sim 262°$, $b \sim -54°$). Interestingly, the bulk motion predicted here is in a direction half way between the two, which can be accounted for with a mass of $\sim 2 \times 10^{17} M_\odot$ in Shapley and an additional $\sim 4 \times 10^{17} M_\odot$ in Horologium-Reticulum. I suggest that further investigation into the mass of these superclusters is likely to be very revealing.

Presenting a new approach to mapping the density-field in this thesis, I have taken a step forward in our understanding of the dynamics of galaxies in the nearby Universe. With the rapid advancement in the available data and tools for analysis, our inability to explain the dipole observed in the Cosmic Microwave Background only becomes more puzzling over time.

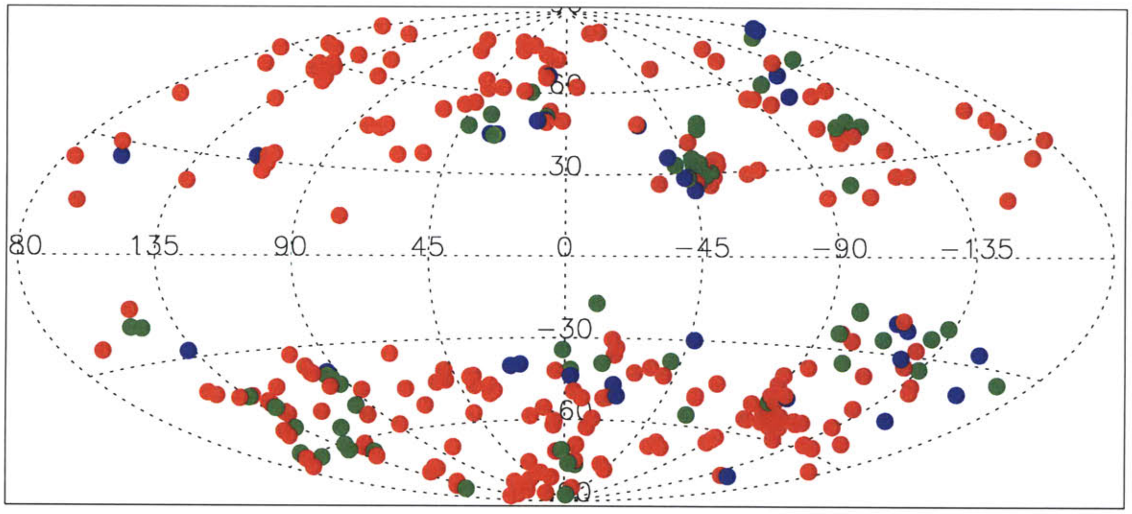

Figure 7.1 Distant Abell Clusters. The figure shows Abell clusters with measured redshifts greater than 10,000 km s^{-1} in galactic coordinates. The blue points correspond to $10,000 < cz < 12,000$ km s^{-1}, the green to $12,000 < cz < 15,000$ km s^{-1}, and the red to $cz > 15,000$ km s^{-1}. The two largest overdensities are the Shapley concentration at $\sim 130/h$ Mpc ($l \sim 310°$, $b \sim 29°$) and the Horologium-Reticulum Supercluster at $\sim 180/h$ Mpc ($l \sim 262°$, $b \sim -54°$). The predicted bulk flow lies in a direction half way between the two.

Appendix A

Group Catalogs

Table A.1. Low-density-contrast (LDC) catalog of groups in the 2MASS Redshift Survey

#	RA	Dec	Members[a]	Distance[b] (Mpc)	V_G[c] (km/s)	σ_P[d] (km/s)	R_P[e] (Mpc)	$\log\left[\frac{M_V}{M_\odot}\right]$[f]	$\log\left[\frac{M_P}{M_\odot}\right]$[g]	$\log\left[\frac{M_P/L}{M_\odot/L_\odot}\right]$[i]	a[j] (′)	η[k]	ϕ[l] (°)
1	$00^h00^m55.2^s$	$+28^\circ12'37''$	3 (0)	121.75	9001	190.5	2.95	14.069	14.233	2.143	48		
2	$00^h05^m31.5^s$	$+27^\circ29'37''$	3 (0)	102.61	7590	86.8	1.95	13.207	13.206	1.498	29		
3	$00^h05^m41.8^s$	$+05^\circ09'11''$	3 (0)	71.94	5340	41.0	0.64	12.072	11.974	0.594	15		
4	$00^h08^m29.8^s$	$+32^\circ53'28''$	7 (0)	66.41	4885	108.7	1.34	13.241	13.293	1.426	39	0.38	34
5	$00^h10^m21.2^s$	$+28^\circ18'59''$	3 (0)	110.50	8176	134.7	2.38	13.675	13.789	1.954	37		
6	$00^h10^m33.0^s$	$+47^\circ50'05''$	20 (0)	70.90	5168	146.8	1.80	13.629	13.875	1.588	135	0.36	69
7	$00^h11^m45.6^s$	$-57^\circ03'15''$	4 (0)	132.89	9662	167.8	0.88	13.432	13.682	1.253	31		
8	$00^h12^m14.6^s$	$+22^\circ07'46''$	4 (0)	82.43	6108	178.7	1.00	13.545	13.875	2.138	54		
9	$00^h13^m05.5^s$	$+30^\circ57'12''$	3 (0)	65.04	4792	61.3	0.56	12.360	12.424	0.969	12		
10	$00^h15^m31.8^s$	$-07^\circ11'35''$	5 (0)	73.36	5449	159.3	0.51	13.148	13.391	1.433	14	0.43	80

[a] No. of group members (including those generated from the population of the plane). The number derived from the galactic-plane population is contained in parentheses.

[b] Mean (corrected) group distance.

[c] Mean heliocentric group velocity.

[d] Line-of-sight velocity dispersion.

[e] Projected virial radius.

[f] Log of the virial mass in solar units.

[g] Log of the projected mass in solar units.

[i] Log of the (projected) mass-to-light ratio in solar units.

[j] Semi-major axis of the ellipse fit to the group at the 75th-percentile level (measured in arcminutes).

[k] Axis-ratio of ellipse fit to the group members.

[l] Position angle of semi-major axis of ellipse fit to the group members; measured from north toward east.

Note. — The complete version of this table is available in the electronic version of Crook et al. (2008). The above table represents a sample for guidance. This catalog has been produced using parameters (D_0, V_0) = (1.04 Mpc, 399 km s^{-1}), corresponding to the density contrast $\delta\rho/\rho = 12$. We assume $h = 0.73$ where a value is required.

Table A.2. High-density-contrast (HDC) catalog of groups in the 2MASS Redshift Survey

#	RA	Dec	Members[a]	Distance[b] (Mpc)	V_G[c] (km/s)	σ_P[d] (km/s)	R_P[e] (Mpc)	$\log\left[\frac{M_V}{M_\odot}\right]$[f]	$\log\left[\frac{M_P}{M_\odot}\right]$[g]	$\log\left[\frac{M_P/L}{M_\odot/L_\odot}\right]$[i]	a[j] (′)	η[k]	ϕ[l] (°)	Corresponding Group #[n]
1	$00^h05^m31.5^s$	+27°29′37″	3 (0)	102.61	7590	86.8	1.95	13.207	13.206	1.498	29			2
2	$00^h05^m41.8^s$	+05°09′11″	3 (0)	71.94	5340	41.0	0.64	12.072	11.974	0.594	15			3
3	$00^h06^m10.8^s$	+47°00′59″	4 (0)	70.80	5162	158.1	0.56	13.183	13.544	1.970	33			6
4	$00^h09^m11.3^s$	+33°07′36″	6 (0)	66.25	4873	113.9	1.05	13.174	13.328	1.488	23	0.69	46	4
5	$00^h11^m45.6^s$	−57°03′15″	4 (0)	132.89	9662	167.8	0.88	13.432	13.682	1.253	31			7
6	$00^h13^m05.5^s$	+30°57′12″	3 (0)	65.04	4792	61.3	0.56	12.360	12.424	0.969	12			9
7	$00^h13^m10.0^s$	−23°11′51″	3 (0)	6.70	465	88.5	0.53	12.656	12.734	3.147	115			26
8	$00^h14^m38.5^s$	+28°35′08″	4 (0)	96.68	7154	244.4	1.01	13.822	13.845	2.099	33			12
9	$00^h14^m45.7^s$	−07°13′44″	4 (0)	73.70	5473	173.1	0.33	13.037	13.053	1.123	9			10
10	$00^h16^m21.7^s$	+48°09′12″	11 (0)	70.97	5175	162.5	0.77	13.351	13.611	1.612	43	0.99	92	6

Note. — The complete version of this table is available in the electronic version of Crook et al. (2008). The above table represents a sample for guidance. This catalog has been produced using parameters (D_0, V_0) = (0.56 Mpc, 350 km s^{-1}), corresponding to the density contrast $\delta\rho/\rho = 80$. We assume $h = 0.73$ where a value is required.

[a] No. of group members (including those generated from the population of the plane). The number derived from the galactic-plane population is contained in parentheses.

[b] Mean (corrected) group distance.

[c] Mean heliocentric group velocity.

[d] Line-of-sight velocity dispersion.

[e] Projected virial radius.

[f] Log of the virial mass in solar units.

[g] Log of the projected mass in solar units.

[i] Log of the (projected) mass-to-light ratio in solar units.

[j] Semi-major axis of the ellipse fit to the group at the 75th–percentile level (measured in arcminutes).

[k] Axis-ratio of ellipse fit to the group members.

[l] Position angle of semi-major axis of ellipse fit to the group members; measured from north toward east.

[n] Group number from LDC catalog that encompasses all members of this group.

Table A.3. Groups in the LDC catalog with 50 or more members

#	RA	Dec	Members[a]	Distance[b] (Mpc)	V_G[c] (km/s)	σ_P[d] (km/s)	R_P[e] (Mpc)	$\log\left[\frac{M_V}{M_\odot}\right]$[f]	$\log\left[\frac{M_P}{M_\odot}\right]$[g]	$\log\left[\frac{M_P/L}{M_\odot/L_\odot}\right]$[i]	Identified With[j]
904	$12^h32^m57.8^s$	$+07^\circ56'31''$	300 (0)	19.28	1349	645.1	2.97	15.132	15.246	2.196	Virgo
224	$03^h08^m47.2^s$	$+41^\circ46'28''$	300 (0)	72.51	5332	1015.8	4.93	15.746	15.955	2.408	Perseus-Pisces (A426, A347)
1172	$16^h10^m37.4^s$	$-59^\circ52'21''$	214 (41)	69.11	4846	790.5	4.32	15.471	15.684	2.226	Norma (A3627)
729	$10^h27^m34.5^s$	$-29^\circ19'43''$	210 (0)	46.17	3269	613.1	5.06	15.319	15.590	2.436	Hydra (A1060)
916	$12^h50^m04.8^s$	$-42^\circ17'17''$	183 (0)	52.33	3314	651.1	4.11	15.281	15.365	2.035	Centaurus (A3526)
867	$12^h07^m37.1^s$	$+46^\circ37'45''$	138 (0)	15.98	1005	438.9	3.83	14.908	15.181	2.600	Ursa Major S
1323	$18^h58^m54.0^s$	$-62^\circ15'06''$	97 (0)	62.63	4403	350.1	3.42	14.663	14.849	1.772	
74	$01^h15^m09.0^s$	$+32^\circ47'16''$	97 (0)	67.54	5002	432.1	3.32	14.832	15.071	1.977	
926	$12^h58^m53.8^s$	$+27^\circ53'23''$	84 (0)	100.24	6842	648.0	3.31	15.183	15.271	1.916	Coma (A1656)
996	$13^h39^m39.0^s$	$-31^\circ01'54''$	83 (0)	58.90	4330	478.6	3.20	14.904	15.190	2.225	Centaurus (A3574)
279	$04^h03^m46.3^s$	$+51^\circ49'25''$	81 (76)	71.59	5225	511.0	5.93	15.230	15.236	2.240	
921	$12^h54^m53.8^s$	$-11^\circ13'56''$	80 (0)	62.01	4252	443.0	3.31	14.852	15.184	2.263	
1520	$22^h28^m34.8^s$	$+35^\circ40'15''$	76 (0)	84.62	6143	532.0	4.23	15.118	15.445	2.295	
836	$11^h44^m33.8^s$	$+20^\circ10'32''$	59 (0)	95.55	6535	539.7	1.99	14.802	14.847	1.736	Coma (A1367)
251	$03^h36^m29.0^s$	$-20^\circ06'51''$	59 (0)	22.13	1651	253.5	2.15	14.180	14.347	2.093	Eridanus
293	$04^h14^m23.7^s$	$+36^\circ58'31''$	51 (0)	81.93	6017	286.1	3.49	14.496	14.810	1.867	

[a] No. of group members (including those generated from the population of the plane). The number derived from the galactic-plane population is contained in parentheses.

[b] Mean (corrected) group distance.

[c] Mean heliocentric group velocity.

[d] Line-of-sight velocity dispersion.

[e] Projected virial radius.

[f] Log of the virial mass in solar units.

[g] Log of the projected mass in solar units.

[i] Log of the (projected) mass-to-light ratio in solar units.

[j] Composition of group based on known galaxy clusters and superclusters (lists only those groups that appear in HDC catalog with 25 or more members).

Note. — The LDC group catalog was created using $(D_0, V_0) = (1.04$ Mpc, 399 km s$^{-1})$, corresponding to a density contrast $\delta\rho/\rho = 12$. We assume $h = 0.73$ where a value is required.

Table A.4. Groups in the HDC catalog with 25 or more members

#	RA	Dec	Members[a]	Distance[b] (Mpc)	V_G[c] (km/s)	σ_P[d] (km/s)	R_P[e] (Mpc)	$\log\left[\frac{M_V}{M_\odot}\right]$[f]	$\log\left[\frac{M_P}{M_\odot}\right]$[g]	$\log\left[\frac{M_P/L}{M_\odot/L_\odot}\right]$[i]	Corresponding Group #[j]	Identified With[k]
720	$12^h29^m03.5^s$	$+10^\circ23'36''$	205 (0)	19.93	1389	659.5	2.10	15.000	15.149	2.234	904	Virgo
219	$03^h17^m43.1^s$	$+41^\circ31'27''$	117 (0)	74.35	5467	1060.9	1.62	15.301	15.351	2.173	224	Perseus-Pisces (A426)
941	$16^h15^m53.1^s$	$-60^\circ54'29''$	90 (0)	69.67	4887	827.4	1.46	15.039	14.997	1.892	1172	Norma (A3627)
730	$12^h46^m44.0^s$	$-41^\circ11'54''$	88 (0)	55.35	3509	757.1	1.72	15.033	15.093	2.080	916	Centaurus (A3526)
706	$12^h14^m45.5^s$	$+41^\circ46'20''$	85 (0)	11.94	795	253.0	2.10	14.168	14.477	2.200	867	Ursa Major S
596	$10^h36^m02.4^s$	$-27^\circ37'57''$	55 (0)	51.46	3622	556.6	1.11	14.578	14.572	1.984	729	Hydra (A1060)
745	$12^h59^m21.0^s$	$+27^\circ59'04''$	49 (0)	102.60	7012	588.0	2.00	14.880	14.886	1.713	926	Coma (A1656)
1048	$18^h47^m27.0^s$	$-63^\circ26'33''$	48 (0)	63.04	4432	326.1	1.62	14.277	14.310	1.562	1323	
672	$11^h44^m35.4^s$	$+19^\circ58'45''$	42 (0)	95.31	6517	614.5	1.22	14.701	14.775	1.813	836	Coma (A1367)
236	$03^h37^m50.2^s$	$-20^\circ21'37''$	42 (0)	21.92	1635	241.1	1.42	13.957	14.045	2.000	251	Eridanus
234	$03^h34^m56.0^s$	$-35^\circ04'23''$	42 (0)	18.95	1426	286.4	0.99	13.949	14.063	1.737	249	Fornax I
99	$01^h53^m36.6^s$	$+36^\circ17'59''$	39 (0)	66.12	4891	412.0	1.55	14.461	14.466	1.810	115	Perseus-Pisces (A262)
70	$01^h23^m18.6^s$	$+33^\circ34'59''$	35 (0)	66.89	4953	526.0	1.01	14.486	14.429	1.806	74	
185	$02^h53^m39.6^s$	$+41^\circ36'14''$	33 (0)	70.91	5220	583.5	1.44	14.730	14.777	2.256	224	
840	$14^h01^m44.9^s$	$-33^\circ56'00''$	32 (0)	55.16	4182	331.4	1.50	14.257	14.331	1.932	1024	
75	$01^h26^m52.1^s$	$-01^\circ30'24''$	32 (0)	70.96	5311	424.5	1.10	14.337	14.458	1.869	89	A194
587	$10^h30^m25.5^s$	$-35^\circ20'24''$	30 (0)	40.47	2928	383.0	0.69	14.047	13.935	1.660	729	
736	$12^h52^m38.0^s$	$-08^\circ57'53''$	29 (0)	59.59	4070	350.8	1.34	14.258	14.367	1.984	921	
137	$02^h25^m24.5^s$	$+42^\circ05'38''$	29 (0)	76.52	5642	563.1	1.36	14.675	14.801	2.210	224	Perseus-Pisces (A347)
53	$01^h09^m52.6^s$	$+32^\circ43'06''$	29 (0)	68.38	5064	368.8	1.30	14.286	14.442	1.848	74	
284	$04^h22^m27.8^s$	$+36^\circ43'26''$	28 (0)	82.20	6032	266.6	1.79	14.145	14.255	1.560	293	
741	$12^h56^m09.5^s$	$-13^\circ37'44''$	27 (0)	65.56	4510	319.2	1.34	14.175	14.529	1.967	921	
821	$13^h48^m34.0^s$	$-30^\circ20'51''$	26 (0)	64.85	4611	422.6	1.11	14.336	14.286	1.732	996	Centaurus (A3574)

[a] No. of group members (including those generated from the population of the plane). The number derived from the galactic-plane population is contained in parentheses.

[b] Mean (corrected) group distance.

[c] Mean heliocentric group velocity.

[d] Line-of-sight velocity dispersion.

[e] Projected virial radius.

[f] Log of the virial mass in solar units.

[g] Log of the projected mass in solar units.

[i] Log of the (projected) mass-to-light ratio in solar units.

[j] Group number from LDC catalog that encompasses all members of this group.

[k] Composition of group based on known galaxy clusters and superclusters.

Note. — The HDC group catalog was created using $(D_0, V_0) = (0.56\ \mathrm{Mpc}, 350\ \mathrm{km\ s^{-1}})$, corresponding to a density contrast $\delta\rho/\rho = 80$. We assume $h = 0.73$ where a value is required.

Table A.5 Groups in the LDC catalog and their members

Name	RA	Dec	V_{h}[a] (km/s)	m_K[b]	Distance[c] (Mpc)	Corresponding Group #[d]
Group 1						
000433.73+2818059	$00^h04^m33.6^s$	+28°18′06″	8785	10.62	118.79	None
235828.41+2802025	$23^h58^m28.3^s$	+28°02′03″	9145	10.94	123.72	None
235943.72+2817251	$23^h59^m43.6^s$	+28°17′25″	9073	10.71	122.74	None
Group 2						
000329.22+2721063	$00^h03^m29.1^s$	+27°21′06″	7690	11.02	103.97	1
000548.43+2726579	$00^h05^m48.3^s$	+27°26′58″	7531	10.95	101.81	1
000717.10+2740421	$00^h07^m17.1^s$	+27°40′42″	7550	11.13	102.05	1
Group 3						
000457.78+0507245	$00^h04^m57.8^s$	+05°07′24″	5357	11.19	72.17	2
000527.66+0513204	$00^h05^m27.6^s$	+05°13′20″	5294	10.08	71.31	2
000640.35+0506483	$00^h06^m40.3^s$	+05°06′48″	5371	11.22	72.34	2
Group 4						
000424.49+3128193	$00^h04^m24.5^s$	+31°28′19″	4958	11.14	67.36	None
000719.51+3236334	$00^h07^m19.5^s$	+32°36′33″	5074	9.95	68.93	4
000801.63+3304148	$00^h08^m01.6^s$	+33°04′15″	4904	10.31	66.66	4
000847.72+3326000	$00^h08^m47.7^s$	+33°26′00″	4811	9.89	65.43	4
000932.70+3318310	$00^h09^m32.7^s$	+33°18′31″	4901	9.55	66.62	4
001040.87+3258592	$00^h10^m40.8^s$	+32°58′59″	4788	10.66	65.08	4
001046.88+3321102	$00^h10^m46.8^s$	+33°21′10″	4765	10.47	64.79	4
Group 5						
000948.17+2749564	$00^h09^m48.2^s$	+27°49′56″	8315	10.85	112.37	None
001001.99+2812364	$00^h10^m02.0^s$	+28°12′36″	8168	11.19	110.39	None
001114.22+2854233	$00^h11^m14.2^s$	+28°54′23″	8046	10.98	108.75	None

---

[a] Heliocentric velocity.

[b] Corrected distance, assuming $h = 0.73$.

[c] Apparent K magnitude.

[d] Corresponding group number assigned to this galaxy when in the HDC catalog.

Note. — The complete version of this table is available in the electronic version of Crook et al. (2008). The table above is only intended as a guide to its content. The LDC group catalog was created using (D_0, V_0) = (1.04 Mpc, 399 km s^{-1}), corresponding to a density contrast $\delta\rho/\rho = 12$. Galaxies with names including the text *SimGal* are galaxies generated by the population of the galactic plane and are not observed galaxies.

Table A.6 Groups in the HDC catalog and their members

Name	RA	Dec	V_h[a] (km/s)	m_K[b]	Distance[c] (Mpc)	Corresponding Group #[d]
Group 1						
000329.22+2721063	$00^h03^m29.1^s$	$+27^\circ21'06''$	7690	11.02	103.97	2
000548.43+2726579	$00^h05^m48.3^s$	$+27^\circ26'58''$	7531	10.95	101.81	2
000717.10+2740421	$00^h07^m17.1^s$	$+27^\circ40'42''$	7550	11.13	102.05	2
Group 2						
000457.78+0507245	$00^h04^m57.8^s$	$+05^\circ07'24''$	5357	11.19	72.17	3
000527.66+0513204	$00^h05^m27.6^s$	$+05^\circ13'20''$	5294	10.08	71.31	3
000640.35+0506483	$00^h06^m40.3^s$	$+05^\circ06'48''$	5371	11.22	72.34	3
Group 3						
000426.65+4729250	$00^h04^m26.6^s$	$+47^\circ29'25''$	5269	10.52	72.27	6
000527.96+4632371	$00^h05^m28.0^s$	$+46^\circ32'37''$	4971	11.02	68.21	6
000723.79+4702265	$00^h07^m23.8^s$	$+47^\circ02'27''$	5313	9.93	72.81	6
000724.58+4659195	$00^h07^m24.6^s$	$+46^\circ59'20''$	5097	10.87	69.91	6
Group 4						
000719.51+3236334	$00^h07^m19.5^s$	$+32^\circ36'33''$	5074	9.95	68.93	4
000801.63+3304148	$00^h08^m01.6^s$	$+33^\circ04'15''$	4904	10.31	66.66	4
000847.72+3326000	$00^h08^m47.7^s$	$+33^\circ26'00''$	4811	9.89	65.43	4
000932.70+3318310	$00^h09^m32.7^s$	$+33^\circ18'31''$	4901	9.55	66.62	4
001040.87+3258592	$00^h10^m40.8^s$	$+32^\circ58'59''$	4788	10.66	65.08	4
001046.88+3321102	$00^h10^m46.8^s$	$+33^\circ21'10''$	4765	10.47	64.79	4
Group 5						
000959.29-5701148	$00^h09^m59.2^s$	$-57^\circ01'15''$	9457	9.98	130.09	7
001025.24-5659209	$00^h10^m25.2^s$	$-56^\circ59'21''$	9595	10.92	131.97	7
001122.90-5657264	$00^h11^m22.8^s$	$-56^\circ57'26''$	9809	10.73	134.88	7
001516.47-5714412	$00^h15^m16.5^s$	$-57^\circ14'41''$	9790	11.13	134.62	7

---

[a] Heliocentric velocity.

[b] Corrected distance, assuming $h = 0.73$.

[c] Apparent K magnitude.

[d] Corresponding group number assigned to this galaxy in the LDC catalog.

Note. — The complete version of this table is available in the electronic version of Crook et al. (2008). The table above is only intended as a guide to its content. The HDC group catalog was created using (D_0, V_0) = (0.56 Mpc, 350 km s^{-1}), corresponding to a density contrast $\delta\rho/\rho = 80$.

Appendix B

Reconstructed Density-field

Table B.1: Attractors defining the density-field (CMC)

Distance[a]	N_{m}[b]	SGX[a]	SGY[a]	SGZ[a]	α	δ	$\log\left(\frac{M}{M_\odot}\right)$	w[c]
787	7	728	-268	-125	$02^{\mathrm{h}}35^{\mathrm{m}}37^{\mathrm{s}}$	+37°30′06″	12.635	1.01
832	7	-46	750	-356	$10^{\mathrm{h}}49^{\mathrm{m}}23^{\mathrm{s}}$	+12°51′53″	12.229	1.01
851	6	-461	-463	-544	$04^{\mathrm{h}}53^{\mathrm{m}}07^{\mathrm{s}}$	-60°56′02″	11.919	1.01
887	6	-92	835	-284	$11^{\mathrm{h}}18^{\mathrm{m}}57^{\mathrm{s}}$	+13°06′17″	13.083	1.01
912	5	-178	-448	-773	$05^{\mathrm{h}}09^{\mathrm{m}}12^{\mathrm{s}}$	-37°31′36″	12.844	1.01
947	17	-545	772	-52	$12^{\mathrm{h}}52^{\mathrm{m}}09^{\mathrm{s}}$	-09°16′51″	13.169	1.01
969	6	-882	373	-141	$13^{\mathrm{h}}05^{\mathrm{m}}20^{\mathrm{s}}$	-41°14′01″	12.008	1.01
982	8	-546	435	-689	$10^{\mathrm{h}}04^{\mathrm{m}}15^{\mathrm{s}}$	-28°39′58″	12.457	1.01
996	13	-286	-677	-671	$03^{\mathrm{h}}58^{\mathrm{m}}47^{\mathrm{s}}$	-46°13′34″	12.896	1.01
1062	13	86	1058	13	$12^{\mathrm{h}}21^{\mathrm{m}}02^{\mathrm{s}}$	+30°02′55″	12.582	1.01
1159	6	-479	1006	316	$13^{\mathrm{h}}55^{\mathrm{m}}06^{\mathrm{s}}$	+05°10′14″	12.576	1.02
1165	12	-470	1062	-79	$12^{\mathrm{h}}37^{\mathrm{m}}12^{\mathrm{s}}$	+01°25′49″	13.122	1.02
1181	15	353	1126	36	$12^{\mathrm{h}}05^{\mathrm{m}}40^{\mathrm{s}}$	+42°27′48″	12.741	1.02
1231	12	-381	-1142	255	$22^{\mathrm{h}}58^{\mathrm{m}}14^{\mathrm{s}}$	-37°30′34″	13.020	1.02
1246	198	-283	1212	-58	$12^{\mathrm{h}}29^{\mathrm{m}}53^{\mathrm{s}}$	+12°02′48″	13.820	1.02
1265	23	-492	1164	-24	$12^{\mathrm{h}}46^{\mathrm{m}}56^{\mathrm{s}}$	+03°05′25″	13.242	1.02
1337	13	-601	-829	-858	$04^{\mathrm{h}}17^{\mathrm{m}}58^{\mathrm{s}}$	-55°51′31″	13.076	1.02
1337	7	-1007	878	13	$13^{\mathrm{h}}23^{\mathrm{m}}01^{\mathrm{s}}$	-21°24′45″	13.005	1.02
1375	7	694	1181	106	$11^{\mathrm{h}}52^{\mathrm{m}}42^{\mathrm{s}}$	+55°34′46″	12.984	1.02
1375	5	107	-1069	-857	$03^{\mathrm{h}}17^{\mathrm{m}}52^{\mathrm{s}}$	-25°47′57″	12.626	1.02
1375	6	491	1125	-618	$09^{\mathrm{h}}46^{\mathrm{m}}27^{\mathrm{s}}$	+32°29′39″	12.477	1.02
1381	9	-1006	798	-507	$11^{\mathrm{h}}49^{\mathrm{m}}44^{\mathrm{s}}$	-28°39′59″	12.810	1.02
1407	5	-637	1046	691	$14^{\mathrm{h}}53^{\mathrm{m}}25^{\mathrm{s}}$	+03°32′34″	11.663	1.02
1433	5	482	-1289	-397	$01^{\mathrm{h}}51^{\mathrm{m}}23^{\mathrm{s}}$	-09°48′33″	12.445	1.03
1440	8	550	-1155	-659	$02^{\mathrm{h}}39^{\mathrm{m}}38^{\mathrm{s}}$	-07°58′07″	12.240	1.03
1487	40	-126	-1099	-993	$03^{\mathrm{h}}37^{\mathrm{m}}07^{\mathrm{s}}$	-34°49′42″	13.469	1.03
1514	11	1481	311	30	$03^{\mathrm{h}}51^{\mathrm{m}}06^{\mathrm{s}}$	+69°32′41″	13.041	1.03
1528	7	-74	1468	-413	$11^{\mathrm{h}}25^{\mathrm{m}}12^{\mathrm{s}}$	+17°15′32″	12.897	1.03
1543	8	-36	1472	-458	$11^{\mathrm{h}}16^{\mathrm{m}}43^{\mathrm{s}}$	+17°57′34″	12.840	1.03
1550	5	-440	520	-1391	$08^{\mathrm{h}}43^{\mathrm{m}}17^{\mathrm{s}}$	-20°07′37″	12.332	1.03
1564	5	776	1357	12	$11^{\mathrm{h}}29^{\mathrm{m}}36^{\mathrm{s}}$	+53°19′30″	12.688	1.03

Continued on next page...

Table B.1 – Continued

Distance^a	$N_{\mathrm{m}}{}^b$	SGX^a	SGY^a	SGZ^a	α	δ	$\log\left(\frac{M}{M_\odot}\right)$	w^c
1564	9	-990	1105	-492	$11^{\mathrm{h}}57^{\mathrm{m}}30^{\mathrm{s}}$	-19°09′31″	11.731	1.03
1593	5	-191	-1225	-999	$03^{\mathrm{h}}23^{\mathrm{m}}53^{\mathrm{s}}$	-37°06′58″	11.769	1.03
1601	7	-1201	-490	-937	$07^{\mathrm{h}}34^{\mathrm{m}}30^{\mathrm{s}}$	-69°30′56″	11.985	1.03
1613	7	-581	-1494	176	$23^{\mathrm{h}}17^{\mathrm{m}}05^{\mathrm{s}}$	-42°42′44″	11.728	1.03
1676	12	-266	-192	-1643	$06^{\mathrm{h}}46^{\mathrm{m}}47^{\mathrm{s}}$	-26°51′18″	13.173	1.03
1719	6	-861	-1431	402	$22^{\mathrm{h}}12^{\mathrm{m}}42^{\mathrm{s}}$	-46°32′11″	12.647	1.04
1723	6	-92	-1112	-1312	$04^{\mathrm{h}}11^{\mathrm{m}}49^{\mathrm{s}}$	-31°57′30″	12.671	1.04
1731	14	-539	328	-1611	$08^{\mathrm{h}}15^{\mathrm{m}}26^{\mathrm{s}}$	-26°03′47″	13.319	1.04
1755	8	649	-1596	-330	$01^{\mathrm{h}}32^{\mathrm{m}}23^{\mathrm{s}}$	-07°00′17″	12.260	1.04
1761	9	-982	1461	19	$13^{\mathrm{h}}05^{\mathrm{m}}34^{\mathrm{s}}$	-07°01′41″	13.227	1.04
1763	7	993	1451	129	$11^{\mathrm{h}}39^{\mathrm{m}}55^{\mathrm{s}}$	+59°08′11″	12.253	1.04
1771	5	1088	1366	289	$12^{\mathrm{h}}09^{\mathrm{m}}11^{\mathrm{s}}$	+64°48′22″	12.494	1.04
1771	5	-794	1442	651	$14^{\mathrm{h}}20^{\mathrm{m}}43^{\mathrm{s}}$	+03°34′27″	12.233	1.04
1771	5	896	-1225	911	$23^{\mathrm{h}}01^{\mathrm{m}}36^{\mathrm{s}}$	+16°11′03″	12.456	1.04
1788	43	290	-1279	-1214	$03^{\mathrm{h}}36^{\mathrm{m}}40^{\mathrm{s}}$	-20°31′29″	13.539	1.04
1813	9	-1397	1013	-554	$12^{\mathrm{h}}08^{\mathrm{m}}09^{\mathrm{s}}$	-30°28′38″	12.888	1.04
1821	6	-1569	-180	-906	$10^{\mathrm{h}}10^{\mathrm{m}}13^{\mathrm{s}}$	-66°54′00″	12.939	1.04
1863	5	-1514	1085	-60	$13^{\mathrm{h}}19^{\mathrm{m}}40^{\mathrm{s}}$	-27°20′51″	12.610	1.04
1898	10	-410	-144	-1847	$07^{\mathrm{h}}02^{\mathrm{m}}20^{\mathrm{s}}$	-28°51′55″	13.058	1.05
1924	8	961	1522	677	$13^{\mathrm{h}}51^{\mathrm{m}}32^{\mathrm{s}}$	+59°56′16″	13.155	1.05
1924	6	816	1575	743	$14^{\mathrm{h}}04^{\mathrm{m}}37^{\mathrm{s}}$	+55°14′11″	13.067	1.05
1995	6	519	1852	-529	$10^{\mathrm{h}}50^{\mathrm{m}}53^{\mathrm{s}}$	+33°24′30″	12.161	1.05
1996	34	-628	1879	-240	$12^{\mathrm{h}}19^{\mathrm{m}}37^{\mathrm{s}}$	+05°44′18″	13.302	1.05
1997	9	-948	386	-1714	$08^{\mathrm{h}}45^{\mathrm{m}}34^{\mathrm{s}}$	-33°57′60″	13.230	1.05
1997	6	-1164	1615	-147	$12^{\mathrm{h}}48^{\mathrm{m}}42^{\mathrm{s}}$	-10°07′21″	12.607	1.05
2006	12	-955	1412	1056	$15^{\mathrm{h}}05^{\mathrm{m}}09^{\mathrm{s}}$	+01°56′52″	13.233	1.05
2006	11	1471	1286	452	$12^{\mathrm{h}}20^{\mathrm{m}}11^{\mathrm{s}}$	+75°29′54″	13.258	1.05
2043	5	365	1908	-632	$10^{\mathrm{h}}51^{\mathrm{m}}12^{\mathrm{s}}$	+28°04′49″	12.614	1.05
2142	9	1302	-1693	-162	$01^{\mathrm{h}}24^{\mathrm{m}}12^{\mathrm{s}}$	+09°28′32″	12.625	1.06
2174	5	-1725	-128	-1317	$09^{\mathrm{h}}27^{\mathrm{m}}18^{\mathrm{s}}$	-60°50′09″	11.375	1.06
2189	6	1520	1477	544	$12^{\mathrm{h}}46^{\mathrm{m}}58^{\mathrm{s}}$	+72°49′59″	12.954	1.06
2199	30	-1512	1595	14	$13^{\mathrm{h}}15^{\mathrm{m}}29^{\mathrm{s}}$	-16°15′22″	13.612	1.06
2253	6	-1825	949	918	$15^{\mathrm{h}}19^{\mathrm{m}}22^{\mathrm{s}}$	-24°02′22″	13.125	1.07
2282	17	-1333	875	-1631	$09^{\mathrm{h}}57^{\mathrm{m}}08^{\mathrm{s}}$	-32°11′42″	13.354	1.07
2388	5	-2003	-1004	823	$18^{\mathrm{h}}56^{\mathrm{m}}10^{\mathrm{s}}$	-54°07′17″	12.435	1.07
2401	8	-140	1271	-2031	$08^{\mathrm{h}}55^{\mathrm{m}}15^{\mathrm{s}}$	-03°01′01″	12.690	1.07
2401	7	2293	-530	-475	$03^{\mathrm{h}}04^{\mathrm{m}}39^{\mathrm{s}}$	+42°26′26″	13.188	1.07
2418	15	2100	1097	481	$07^{\mathrm{h}}53^{\mathrm{m}}59^{\mathrm{s}}$	+85°38′00″	13.303	1.08
2433	7	1887	-1511	-273	$01^{\mathrm{h}}50^{\mathrm{m}}12^{\mathrm{s}}$	+21°49′47″	12.698	1.08
2434	5	-2168	1022	-425	$12^{\mathrm{h}}54^{\mathrm{m}}09^{\mathrm{s}}$	-39°24′02″	12.556	1.08
2452	12	-779	-2090	1018	$22^{\mathrm{h}}02^{\mathrm{m}}60^{\mathrm{s}}$	-31°48′39″	12.707	1.08
2468	10	-1873	644	-1471	$10^{\mathrm{h}}29^{\mathrm{m}}30^{\mathrm{s}}$	-44°44′13″	12.880	1.08
2497	7	-1756	-1457	1012	$20^{\mathrm{h}}08^{\mathrm{m}}23^{\mathrm{s}}$	-48°18′43″	12.885	1.08
2518	12	2492	355	52	$03^{\mathrm{h}}22^{\mathrm{m}}54^{\mathrm{s}}$	+66°49′23″	13.443	1.08
2525	7	370	2202	-1176	$10^{\mathrm{h}}17^{\mathrm{m}}06^{\mathrm{s}}$	+21°59′40″	12.432	1.08
2546	10	-2475	589	-94	$13^{\mathrm{h}}55^{\mathrm{m}}09^{\mathrm{s}}$	-48°28′40″	12.900	1.08
2564	12	-1926	1095	-1290	$11^{\mathrm{h}}09^{\mathrm{m}}56^{\mathrm{s}}$	-36°54′08″	13.064	1.09
2596	9	1456	2147	75	$11^{\mathrm{h}}23^{\mathrm{m}}09^{\mathrm{s}}$	+57°48′05″	13.535	1.09

Continued on next page...

Table B.1 – Continued

Distance^a	$N_{\mathrm{m}}{}^b$	SGX^a	SGY^a	SGZ^a	α	δ	$\log\left(\frac{M}{M_\odot}\right)$	w^c
2608	8	-1348	1188	-1889	$09^{h}57^{m}01^{s}$	-26°31′12″	12.597	1.09
2632	6	-1856	-1865	73	$22^{h}09^{m}11^{s}$	-64°41′13″	12.750	1.09
2657	6	1472	-1816	-1263	$02^{h}57^{m}43^{s}$	+03°11′41″	12.577	1.09
2674	12	-2477	942	-360	$13^{h}11^{m}25^{s}$	-43°08′05″	13.340	1.09
2681	5	-2533	-666	569	$17^{h}22^{m}24^{s}$	-59°42′55″	12.904	1.09
2731	10	-522	2664	-290	$12^{h}13^{m}57^{s}$	+12°59′33″	13.274	1.10
2788	5	-2020	1921	-57	$13^{h}12^{m}44^{s}$	-19°32′60″	12.256	1.10
2795	6	908	2300	1301	$14^{h}33^{m}04^{s}$	+49°22′47″	12.620	1.10
2800	6	-2037	-1910	208	$21^{h}38^{m}48^{s}$	-64°04′33″	12.311	1.10
2804	9	-2421	1201	-747	$12^{h}25^{m}39^{s}$	-39°14′26″	12.926	1.10
2810	18	526	2574	996	$13^{h}51^{m}34^{s}$	+40°33′25″	13.144	1.11
2835	5	-2368	586	-1444	$10^{h}57^{m}48^{s}$	-50°16′25″	11.647	1.11
2851	7	-2186	1822	-165	$13^{h}08^{m}16^{s}$	-23°44′50″	12.652	1.11
2859	6	-2722	793	-368	$13^{h}19^{m}54^{s}$	-47°25′28″	12.642	1.11
2866	43	-1933	1146	-1778	$10^{h}30^{m}13^{s}$	-35°17′47″	13.924	1.11
2896	5	-2170	-1893	309	$21^{h}13^{m}45^{s}$	-63°46′40″	12.573	1.11
2926	5	-1705	2250	770	$14^{h}05^{m}42^{s}$	-05°49′17″	12.755	1.11
2927	12	-2448	-1338	885	$19^{h}10^{m}22^{s}$	-56°37′13″	13.084	1.11
2937	7	-2372	-166	-1723	$09^{h}36^{m}52^{s}$	-61°33′44″	12.885	1.12
2982	5	-1932	2267	127	$13^{h}20^{m}05^{s}$	-12°45′31″	11.912	1.12
2985	20	-2463	1658	-311	$13^{h}03^{m}38^{s}$	-30°04′40″	13.429	1.12
3055	5	2468	467	1737	$21^{h}10^{m}08^{s}$	+66°22′07″	12.787	1.13
3084	6	-2804	-1277	132	$18^{h}30^{m}03^{s}$	-71°44′09″	12.944	1.13
3088	12	1334	-2464	1296	$23^{h}20^{m}45^{s}$	+08°16′09″	13.284	1.13
3113	6	1450	-1322	-2416	$04^{h}30^{m}56^{s}$	+00°31′60″	12.574	1.13
3165	14	-2246	1037	-1973	$10^{h}24^{m}58^{s}$	-39°47′40″	12.865	1.14
3203	5	1898	2498	641	$12^{h}31^{m}18^{s}$	+64°06′29″	12.653	1.14
3208	6	-1972	1180	-2239	$10^{h}02^{m}05^{s}$	-34°06′57″	12.535	1.14
3271	10	-2219	-885	-2234	$07^{h}24^{m}40^{s}$	-62°19′39″	12.257	1.15
3345	16	1698	-1509	-2455	$04^{h}18^{m}34^{s}$	+02°36′03″	13.408	1.15
3397	5	-2397	1360	-1985	$10^{h}42^{m}20^{s}$	-36°29′41″	12.881	1.16
3408	5	2243	63	2565	$20^{h}39^{m}38^{s}$	+51°10′17″	11.832	1.16
3439	15	-2685	2097	-468	$12^{h}51^{m}05^{s}$	-26°37′37″	13.122	1.16
3452	6	-1936	2858	-32	$13^{h}01^{m}16^{s}$	-07°31′35″	12.875	1.17
3462	5	-2642	1824	1296	$14^{h}57^{m}49^{s}$	-19°17′21″	12.970	1.17
3469	5	-2969	-1779	229	$19^{h}47^{m}52^{s}$	-70°00′15″	13.063	1.17
3478	6	1252	-1293	-2976	$04^{h}56^{m}22^{s}$	-04°38′15″	12.121	1.17
3507	10	3339	-961	-477	$02^{h}39^{m}39^{s}$	+41°46′04″	12.838	1.17
3529	5	513	3485	-206	$11^{h}57^{m}18^{s}$	+32°13′02″	11.659	1.17
3535	5	-345	3434	-760	$11^{h}42^{m}08^{s}$	+15°54′48″	11.918	1.18
3551	5	196	2589	-2422	$09^{h}33^{m}39^{s}$	+10°06′57″	12.379	1.18
3571	5	1211	-3116	-1254	$02^{h}09^{m}41^{s}$	-10°11′03″	11.810	1.18
3588	5	3309	-1352	-310	$02^{h}12^{m}03^{s}$	+37°34′30″	12.586	1.18
3591	8	2764	-2089	-944	$02^{h}27^{m}40^{s}$	+20°02′18″	12.995	1.18
3595	9	1561	-2153	-2419	$03^{h}47^{m}05^{s}$	-03°42′06″	13.054	1.18
3602	5	473	3307	1346	$13^{h}58^{m}34^{s}$	+37°27′35″	13.271	1.18
3610	103	-3235	1420	-739	$12^{h}46^{m}42^{s}$	-41°14′07″	14.591	1.18
3632	5	-3545	500	-613	$13^{h}18^{m}31^{s}$	-55°52′14″	11.336	1.19

Continued on next page. . .

Table B.1 – Continued

Distance^a	$N_\mathrm{m}{}^b$	SGX^a	SGY^a	SGZ^a	α	δ	$\log\left(\frac{M}{M_\odot}\right)$	w^c
3638	5	2796	-645	-2236	$04^{h}40^{m}57^{s}$	+24°50′12″	12.169	1.19
3646	5	1147	-2797	-2037	$03^{h}03^{m}57^{s}$	-12°03′43″	12.781	1.19
3653	14	-3086	-1747	876	$19^{h}19^{m}03^{s}$	-60°15′42″	13.539	1.19
3655	7	-237	3561	-787	$11^{h}39^{m}17^{s}$	+17°40′20″	12.322	1.19
3679	10	-1823	2069	-2435	$10^{h}19^{m}21^{s}$	-21°25′14″	12.968	1.19
3716	5	1554	2736	1977	$15^{h}12^{m}01^{s}$	+55°06′36″	12.795	1.20
3723	8	3322	-1516	-724	$02^{h}34^{m}50^{s}$	+32°48′34″	12.872	1.20
3739	5	1560	-2447	-2357	$03^{h}31^{m}46^{s}$	-05°15′33″	12.553	1.20
3747	5	0	-1964	3190	$20^{h}47^{m}01^{s}$	+00°20′12″	11.674	1.20
3751	18	-3294	1794	-25	$13^{h}36^{m}10^{s}$	-33°37′02″	13.081	1.20
3766	5	-2548	-2739	-430	$23^{h}26^{m}51^{s}$	-67°48′60″	12.805	1.20
3807	8	-3186	-2079	154	$20^{h}17^{m}48^{s}$	-70°47′22″	13.332	1.21
3814	5	-3446	-1464	727	$18^{h}25^{m}12^{s}$	-63°04′59″	12.877	1.21
3899	9	3575	-967	-1218	$03^{h}27^{m}10^{s}$	+36°49′21″	12.767	1.22
3919	5	2218	3208	379	$11^{h}48^{m}56^{s}$	+59°53′41″	12.905	1.22
3920	6	-3860	625	-280	$13^{h}53^{m}05^{s}$	-53°05′17″	13.047	1.22
3927	7	3242	2213	53	$08^{h}47^{m}58^{s}$	+73°10′41″	12.968	1.22
3995	5	1826	-3520	486	$00^{h}29^{m}05^{s}$	+02°48′48″	12.226	1.23
4013	19	1530	-1856	-3213	$04^{h}31^{m}31^{s}$	-04°57′38″	13.696	1.24
4043	79	-2435	2077	-2469	$10^{h}36^{m}19^{s}$	-27°39′48″	14.177	1.24
4059	9	304	4046	-110	$12^{h}11^{m}37^{s}$	+28°59′55″	12.108	1.24
4072	13	3626	-1604	-926	$02^{h}44^{m}21^{s}$	+32°28′31″	13.462	1.24
4077	30	-2325	3342	-209	$12^{h}52^{m}40^{s}$	-08°51′52″	13.825	1.24
4132	6	-3040	-1569	-2316	$06^{h}46^{m}05^{s}$	-71°35′51″	12.862	1.25
4135	5	368	3792	1607	$14^{h}03^{m}51^{s}$	+35°06′58″	12.871	1.25
4152	7	3512	2215	33	$08^{h}19^{m}22^{s}$	+73°43′07″	12.718	1.26
4174	6	103	2462	-3368	$08^{h}59^{m}48^{s}$	+03°12′04″	12.791	1.26
4178	6	1169	-1841	-3563	$04^{h}47^{m}35^{s}$	-10°17′34″	12.567	1.26
4186	5	3883	-1009	-1197	$03^{h}22^{m}21^{s}$	+38°12′41″	12.172	1.26
4194	5	-3922	1415	-451	$13^{h}21^{m}10^{s}$	-43°39′53″	12.876	1.26
4194	10	-1829	2273	-3012	$09^{h}59^{m}57^{s}$	-19°45′03″	13.121	1.26
4207	11	-3535	2279	-89	$13^{h}26^{m}16^{s}$	-29°50′45″	13.061	1.26
4221	8	3950	1458	-300	$05^{h}44^{m}13^{s}$	+69°16′39″	12.807	1.27
4236	39	-3781	1879	332	$14^{h}01^{m}51^{s}$	-33°54′56″	13.794	1.27
4239	11	2972	-1190	2778	$22^{h}09^{m}53^{s}$	+41°24′28″	12.896	1.27
4240	5	3932	-1092	-1152	$03^{h}16^{m}06^{s}$	+37°57′53″	12.233	1.27
4260	14	1649	-1616	-3580	$04^{h}51^{m}35^{s}$	-03°14′04″	13.167	1.27
4261	7	1417	-3580	-1825	$02^{h}29^{m}01^{s}$	-10°55′47″	12.668	1.27
4277	5	1516	-3194	-2407	$03^{h}07^{m}11^{s}$	-09°36′52″	12.803	1.27
4278	46	-3795	-1792	829	$18^{h}44^{m}53^{s}$	-63°05′20″	13.885	1.27
4280	59	3881	-1798	-156	$01^{h}53^{m}43^{s}$	+36°15′39″	13.972	1.27
4281	6	1213	-3594	-1985	$02^{h}35^{m}58^{s}$	-13°57′53″	12.645	1.27
4313	7	459	3736	2105	$14^{h}35^{m}03^{s}$	+36°32′17″	12.982	1.28
4313	5	-4068	-1211	767	$17^{h}30^{m}04^{s}$	-62°15′57″	13.125	1.28
4328	5	-1057	-2659	-3247	$04^{h}27^{m}40^{s}$	-42°37′24″	12.603	1.28
4336	8	3966	1662	-559	$06^{h}17^{m}51^{s}$	+66°35′19″	12.820	1.28
4398	6	3751	-972	-2079	$04^{h}05^{m}50^{s}$	+30°49′23″	13.295	1.29
4404	5	1791	2471	-3175	$08^{h}16^{m}55^{s}$	+23°19′59″	12.597	1.29

Continued on next page...

Table B.1 – Continued

Distance^a	$N_{\rm m}{}^b$	SGX^a	SGY^a	SGZ^a	α	δ	$\log\left(\frac{M}{M_\odot}\right)$	w^c
4417	5	1243	2858	-3129	$08^{\rm h}49^{\rm m}56^{\rm s}$	+19°09′48″	12.703	1.30
4418	6	2187	-3263	2020	$23^{\rm h}15^{\rm m}27^{\rm s}$	+13°31′15″	13.300	1.30
4427	6	1487	-1972	-3673	$04^{\rm h}40^{\rm m}42^{\rm s}$	-07°14′31″	13.176	1.30
4431	5	4	4272	-1177	$11^{\rm h}21^{\rm m}40^{\rm s}$	+20°01′04″	13.046	1.30
4438	7	-3804	2286	65	$13^{\rm h}37^{\rm m}58^{\rm s}$	-30°55′09″	12.740	1.30
4459	5	-2523	-2227	-2925	$05^{\rm h}18^{\rm m}13^{\rm s}$	-61°35′07″	12.890	1.30
4473	5	-4304	-1208	154	$16^{\rm h}47^{\rm m}01^{\rm s}$	-69°21′27″	12.610	1.31
4488	9	-362	3963	2076	$14^{\rm h}28^{\rm m}47^{\rm s}$	+25°44′12″	13.068	1.31
4499	5	-2551	2557	-2681	$10^{\rm h}40^{\rm m}51^{\rm s}$	-23°58′33″	12.841	1.31
4505	9	4328	-431	-1173	$03^{\rm h}45^{\rm m}20^{\rm s}$	+45°45′32″	13.210	1.31
4525	6	3603	-2356	1394	$00^{\rm h}09^{\rm m}11^{\rm s}$	+33°07′36″	12.795	1.31
4528	31	4309	-1134	-809	$02^{\rm h}54^{\rm m}35^{\rm s}$	+41°37′37″	14.318	1.32
4540	23	-3485	-2582	1340	$20^{\rm h}04^{\rm m}04^{\rm s}$	-55°38′46″	13.952	1.32
4545	5	-2759	-3235	1603	$21^{\rm h}05^{\rm m}37^{\rm s}$	-47°08′13″	12.736	1.32
4551	6	3604	-2693	687	$00^{\rm h}48^{\rm m}35^{\rm s}$	+28°00′40″	12.830	1.32
4555	5	3832	-1476	1971	$23^{\rm h}32^{\rm m}04^{\rm s}$	+44°41′12″	12.915	1.32
4559	9	134	4535	-448	$11^{\rm h}58^{\rm m}16^{\rm s}$	+25°10′16″	12.595	1.32
4560	5	1515	-3739	-2125	$02^{\rm h}39^{\rm m}02^{\rm s}$	-11°01′55″	12.667	1.32
4562	8	548	2168	-3977	$08^{\rm h}22^{\rm m}35^{\rm s}$	+04°05′55″	12.689	1.32
4564	7	3266	-1568	2774	$22^{\rm h}31^{\rm m}31^{\rm s}$	+39°21′03″	13.232	1.32
4589	7	-2681	3615	-894	$12^{\rm h}21^{\rm m}48^{\rm s}$	-12°37′25″	12.819	1.33
4594	44	3997	-2253	236	$01^{\rm h}23^{\rm m}14^{\rm s}$	+33°36′07″	13.876	1.33
4615	12	1938	-1541	-3894	$04^{\rm h}58^{\rm m}40^{\rm s}$	-00°33′30″	13.389	1.33
4655	6	4270	1694	-751	$06^{\rm h}10^{\rm m}40^{\rm s}$	+64°32′55″	13.177	1.34
4674	7	3255	-1060	-3182	$04^{\rm h}43^{\rm m}50^{\rm s}$	+18°34′53″	12.855	1.34
4687	5	-2454	-3577	1773	$21^{\rm h}25^{\rm m}39^{\rm s}$	-42°32′46″	13.137	1.34
4697	10	3785	-2710	-631	$02^{\rm h}00^{\rm m}02^{\rm s}$	+24°14′37″	12.755	1.35
4701	5	1578	-3492	-2722	$03^{\rm h}10^{\rm m}58^{\rm s}$	-10°42′59″	12.611	1.35
4709	10	3469	-2408	2083	$23^{\rm h}29^{\rm m}13^{\rm s}$	+32°22′37″	13.270	1.35
4716	11	381	1074	4576	$18^{\rm h}12^{\rm m}09^{\rm s}$	+25°28′34″	12.594	1.35
4732	15	4517	1401	143	$04^{\rm h}39^{\rm m}21^{\rm s}$	+73°20′30″	13.524	1.35
4732	5	-2257	3383	-2419	$11^{\rm h}01^{\rm m}04^{\rm s}$	-14°03′25″	12.844	1.35
4736	5	-1633	2450	-3709	$09^{\rm h}35^{\rm m}23^{\rm s}$	-16°42′14″	12.908	1.35
4737	6	1915	-2191	-3738	$04^{\rm h}28^{\rm m}52^{\rm s}$	-03°38′42″	12.937	1.35
4742	5	-4334	-1750	799	$18^{\rm h}14^{\rm m}28^{\rm s}$	-64°12′14″	13.311	1.35
4753	15	4310	1939	499	$06^{\rm h}03^{\rm m}03^{\rm s}$	+80°05′05″	13.688	1.36
4773	37	-3033	3672	-309	$12^{\rm h}54^{\rm m}43^{\rm s}$	-13°36′41″	14.089	1.36
4780	5	3932	-2649	604	$00^{\rm h}57^{\rm m}54^{\rm s}$	+30°22′23″	12.100	1.36
4817	8	169	460	4792	$18^{\rm h}37^{\rm m}58^{\rm s}$	+19°55′13″	12.765	1.37
4831	9	1519	-2206	-4021	$04^{\rm h}40^{\rm m}07^{\rm s}$	-08°38′06″	13.342	1.37
4833	39	-4146	2469	259	$13^{\rm h}48^{\rm m}06^{\rm s}$	-30°23′27″	13.822	1.37
4839	6	4575	-888	-1303	$03^{\rm h}29^{\rm m}10^{\rm s}$	+41°32′54″	12.996	1.37
4843	11	4554	-668	-1506	$03^{\rm h}48^{\rm m}08^{\rm s}$	+41°50′38″	13.507	1.37
4861	5	-4746	1046	104	$14^{\rm h}15^{\rm m}58^{\rm s}$	-48°00′45″	12.751	1.38
4876	5	1760	2905	-3499	$08^{\rm h}29^{\rm m}42^{\rm s}$	+21°51′16″	13.221	1.38
4907	6	2385	-2308	-3613	$04^{\rm h}16^{\rm m}30^{\rm s}$	+01°01′41″	13.037	1.38
4908	7	-3040	-3472	1670	$21^{\rm h}04^{\rm m}41^{\rm s}$	-48°09′58″	12.818	1.39
4916	7	-2787	-3531	1982	$21^{\rm h}05^{\rm m}08^{\rm s}$	-43°25′54″	12.604	1.39

Continued on next page...

Table B.1 – Continued

Distance[a]	N_m[b]	SGX[a]	SGY[a]	SGZ[a]	α	δ	$\log\left(\frac{M}{M_\odot}\right)$	w[c]
4917	5	4289	2239	-875	$07^{h}05^{m}05^{s}$	+64°00′26″	12.297	1.39
4923	6	3805	-929	-2983	$04^{h}37^{m}10^{s}$	+24°54′22″	12.114	1.39
4963	5	1524	-2132	4215	$21^{h}08^{m}05^{s}$	+18°05′01″	12.245	1.40
4973	6	4117	-2711	-647	$02^{h}02^{m}35^{s}$	+26°23′50″	12.424	1.40
4987	5	-2171	3572	-2720	$10^{h}50^{m}13^{s}$	-12°27′22″	12.836	1.40
4991	132	-4909	-663	606	$16^{h}12^{m}20^{s}$	-60°40′24″	14.613	1.40
5017	5	4846	1146	-605	$04^{h}51^{m}36^{s}$	+63°52′52″	13.186	1.41
5017	7	-1091	-4301	-2340	$02^{h}29^{m}24^{s}$	-42°57′27″	12.826	1.41
5019	5	-2087	2331	-3924	$09^{h}36^{m}21^{s}$	-21°46′45″	13.138	1.41
5022	8	3372	-3636	-792	$01^{h}49^{m}00^{s}$	+13°02′16″	13.040	1.41
5036	5	1669	2371	-4117	$08^{h}01^{m}03^{s}$	+15°26′31″	12.528	1.41
5050	6	1110	-2556	4211	$21^{h}11^{m}54^{s}$	+11°26′21″	12.297	1.41
5050	5	-3393	1653	-3356	$10^{h}10^{m}42^{s}$	-38°12′48″	12.944	1.41
5053	9	-2754	-3104	-2883	$04^{h}07^{m}38^{s}$	-62°35′03″	13.410	1.41
5056	7	-3009	1173	-3889	$09^{h}23^{m}37^{s}$	-38°26′40″	12.708	1.42
5058	7	-4759	-1713	-52	$17^{h}18^{m}38^{s}$	-73°31′29″	13.120	1.42
5063	6	3819	-1931	2705	$22^{h}58^{m}32^{s}$	+39°08′26″	13.147	1.42
5086	39	2297	-4481	-712	$01^{h}26^{m}46^{s}$	-01°30′25″	13.896	1.42
5093	11	2412	-4468	402	$00^{h}39^{m}37^{s}$	+03°03′48″	12.498	1.42
5105	6	2575	4110	-1593	$09^{h}49^{m}40^{s}$	+44°04′09″	11.976	1.43
5114	5	4798	1752	258	$05^{h}07^{m}54^{s}$	+75°43′23″	12.886	1.43
5129	5	-2739	-3824	2045	$21^{h}16^{m}50^{s}$	-42°13′29″	12.915	1.43
5160	5	-3705	1728	-3148	$10^{h}30^{m}13^{s}$	-39°49′35″	12.893	1.44
5173	9	4130	-2957	982	$00^{h}39^{m}39^{s}$	+29°37′45″	13.303	1.44
5174	5	2488	-4281	1499	$23^{h}53^{m}36^{s}$	+07°56′21″	12.676	1.44
5179	5	2804	-2483	-3576	$04^{h}06^{m}00^{s}$	+04°15′13″	12.877	1.44
5198	6	5063	813	-851	$04^{h}33^{m}14^{s}$	+59°33′45″	13.285	1.45
5203	5	-3781	-2595	-2457	$04^{h}57^{m}30^{s}$	-75°29′17″	12.503	1.45
5205	5	4716	-1468	1642	$00^{h}14^{m}12^{s}$	+48°11′27″	12.555	1.45
5212	7	-1351	3565	-3553	$10^{h}03^{m}30^{s}$	-06°35′36″	12.408	1.45
5229	5	3022	-4099	-1187	$01^{h}56^{m}36^{s}$	+05°45′60″	12.790	1.45
5267	11	84	1038	5162	$18^{h}13^{m}06^{s}$	+21°20′13″	13.329	1.46
5269	5	-3160	-3079	2879	$20^{h}11^{m}12^{s}$	-38°17′16″	12.814	1.46
5271	5	2396	4580	1032	$12^{h}44^{m}31^{s}$	+54°49′49″	12.868	1.46
5278	5	-1095	4753	2015	$14^{h}10^{m}58^{s}$	+18°06′05″	13.287	1.46
5287	9	-4452	2817	427	$13^{h}52^{m}21^{s}$	-28°23′24″	13.391	1.47
5287	6	4716	-2390	58	$01^{h}37^{m}42^{s}$	+35°18′13″	12.892	1.47
5301	13	-309	-5173	-1113	$01^{h}13^{m}58^{s}$	-31°42′51″	13.643	1.47
5301	7	4643	-2512	-481	$02^{h}01^{m}20^{s}$	+31°48′33″	13.041	1.47
5303	8	-1307	1040	-5033	$08^{h}07^{m}04^{s}$	-22°39′46″	13.608	1.47
5304	7	1974	-4919	-196	$00^{h}58^{m}16^{s}$	-04°58′49″	12.848	1.47
5313	12	-4491	2764	-641	$13^{h}02^{m}03^{s}$	-32°33′44″	13.250	1.47
5336	6	3569	-572	-3925	$05^{h}16^{m}18^{s}$	+19°21′03″	13.087	1.48
5336	42	4549	-2744	505	$01^{h}09^{m}34^{s}$	+32°40′24″	13.959	1.48
5338	17	1973	3005	-3946	$08^{h}20^{m}20^{s}$	+21°05′21″	13.348	1.48
5369	5	908	4709	2413	$14^{h}22^{m}44^{s}$	+40°03′26″	13.232	1.49
5399	5	-3054	-3188	-3108	$04^{h}20^{m}23^{s}$	-63°42′40″	12.861	1.49
5401	6	4796	-1600	1900	$00^{h}00^{m}52^{s}$	+47°10′44″	12.882	1.49

Continued on next page...

Table B.1 – Continued

Distance^a	$N_\mathrm{m}{}^b$	SGX^a	SGY^a	SGZ^a	α	δ	$\log\left(\frac{M}{M_\odot}\right)$	w^c
5401	6	3131	-2602	-3549	$03^\mathrm{h}59^\mathrm{m}08^\mathrm{s}$	+06°36′51″	12.934	1.49
5412	6	3579	3710	-1648	$08^\mathrm{h}58^\mathrm{m}03^\mathrm{s}$	+51°23′42″	12.865	1.50
5414	14	4425	-1822	2532	$23^\mathrm{h}20^\mathrm{m}03^\mathrm{s}$	+43°22′19″	13.326	1.50
5453	9	-3592	-3258	2494	$20^\mathrm{h}14^\mathrm{m}06^\mathrm{s}$	-44°25′52″	13.269	1.51
5459	21	5187	-1618	-528	$02^\mathrm{h}25^\mathrm{m}45^\mathrm{s}$	+41°43′39″	13.671	1.51
5471	18	-3039	-2900	3504	$19^\mathrm{h}57^\mathrm{m}19^\mathrm{s}$	-32°11′34″	13.251	1.51
5473	10	-4186	-2443	2542	$19^\mathrm{h}14^\mathrm{m}40^\mathrm{s}$	-46°27′09″	13.075	1.51
5479	5	2840	2937	3651	$16^\mathrm{h}59^\mathrm{m}27^\mathrm{s}$	+58°59′04″	13.057	1.51
5482	31	3680	-2092	3482	$22^\mathrm{h}24^\mathrm{m}18^\mathrm{s}$	+35°56′34″	14.323	1.51
5498	6	-585	-5283	-1404	$01^\mathrm{h}24^\mathrm{m}13^\mathrm{s}$	-34°57′31″	12.969	1.52
5505	7	-2158	-3471	3687	$20^\mathrm{h}37^\mathrm{m}12^\mathrm{s}$	-25°16′47″	12.718	1.52
5511	7	2521	-4883	-411	$01^\mathrm{h}12^\mathrm{m}26^\mathrm{s}$	-00°20′05″	12.820	1.52
5515	5	693	5276	1446	$13^\mathrm{h}25^\mathrm{m}22^\mathrm{s}$	+36°07′39″	12.998	1.52
5534	7	2397	-3676	-3370	$03^\mathrm{h}26^\mathrm{m}14^\mathrm{s}$	-04°22′51″	12.977	1.53
5548	5	2267	-4672	1951	$23^\mathrm{h}34^\mathrm{m}55^\mathrm{s}$	+04°57′01″	11.892	1.53
5561	6	40	-1828	5251	$20^\mathrm{h}04^\mathrm{m}49^\mathrm{s}$	+06°56′36″	12.829	1.53
5585	5	1229	4187	3486	$15^\mathrm{h}29^\mathrm{m}19^\mathrm{s}$	+42°51′28″	13.010	1.54
5591	14	3923	-3764	1303	$00^\mathrm{h}21^\mathrm{m}19^\mathrm{s}$	+22°16′60″	13.073	1.54
5601	11	-5063	-2380	-272	$18^\mathrm{h}32^\mathrm{m}19^\mathrm{s}$	-77°00′55″	13.132	1.54
5604	6	3146	3004	-3533	$07^\mathrm{h}58^\mathrm{m}34^\mathrm{s}$	+32°53′19″	12.667	1.54
5608	120	5319	-1164	-1341	$03^\mathrm{h}17^\mathrm{m}19^\mathrm{s}$	+41°35′07″	14.709	1.55
5615	6	-907	-5335	-1495	$01^\mathrm{h}25^\mathrm{m}01^\mathrm{s}$	-38°14′09″	12.700	1.55
5624	5	-218	-3276	4566	$20^\mathrm{h}56^\mathrm{m}24^\mathrm{s}$	-03°38′21″	12.847	1.55
5640	5	3875	-607	-4052	$05^\mathrm{h}13^\mathrm{m}10^\mathrm{s}$	+20°34′48″	12.908	1.55
5641	8	4774	-1293	-2711	$04^\mathrm{h}05^\mathrm{m}53^\mathrm{s}$	+30°04′11″	13.494	1.55
5656	5	-4143	-3382	1840	$20^\mathrm{h}16^\mathrm{m}31^\mathrm{s}$	-53°05′60″	12.495	1.56
5660	7	3389	-169	-4530	$05^\mathrm{h}43^\mathrm{m}40^\mathrm{s}$	+16°39′10″	13.363	1.56
5662	11	-3891	1696	-3747	$10^\mathrm{h}09^\mathrm{m}20^\mathrm{s}$	-40°00′58″	13.278	1.56
5682	7	-3015	-2674	4005	$19^\mathrm{h}43^\mathrm{m}23^\mathrm{s}$	-27°55′32″	12.912	1.56
5718	5	5395	1821	-516	$05^\mathrm{h}31^\mathrm{m}28^\mathrm{s}$	+67°43′24″	13.164	1.57
5738	12	-4321	3768	238	$13^\mathrm{h}30^\mathrm{m}17^\mathrm{s}$	-20°51′44″	12.942	1.58
5749	7	-1833	2342	-4920	$09^\mathrm{h}05^\mathrm{m}00^\mathrm{s}$	-19°22′46″	12.970	1.58
5758	8	-407	-2828	4999	$20^\mathrm{h}31^\mathrm{m}27^\mathrm{s}$	-02°05′46″	13.328	1.59
5765	6	-2722	5072	309	$13^\mathrm{h}08^\mathrm{m}47^\mathrm{s}$	-00°52′04″	12.849	1.59
5778	5	4458	2470	-2724	$07^\mathrm{h}07^\mathrm{m}56^\mathrm{s}$	+46°05′49″	13.039	1.59
5783	5	-1317	-5328	-1820	$01^\mathrm{h}37^\mathrm{m}50^\mathrm{s}$	-42°35′08″	12.529	1.59
5785	5	4128	-1063	3910	$21^\mathrm{h}50^\mathrm{m}58^\mathrm{s}$	+45°59′50″	12.235	1.59
5794	5	-5687	612	-924	$13^\mathrm{h}25^\mathrm{m}39^\mathrm{s}$	-57°33′03″	12.339	1.60
5794	6	1096	4938	2825	$14^\mathrm{h}36^\mathrm{m}11^\mathrm{s}$	+41°20′51″	13.244	1.60
5795	7	4200	-1288	3779	$22^\mathrm{h}04^\mathrm{m}52^\mathrm{s}$	+44°54′03″	12.666	1.60
5801	8	3661	-3909	-2228	$02^\mathrm{h}41^\mathrm{m}07^\mathrm{s}$	+08°41′15″	12.959	1.60
5815	5	1146	-5608	-1025	$01^\mathrm{h}19^\mathrm{m}20^\mathrm{s}$	-16°56′21″	12.383	1.60
5822	5	4050	-3203	2689	$23^\mathrm{h}22^\mathrm{m}35^\mathrm{s}$	+29°15′26″	12.845	1.60
5829	15	-3620	-3255	3205	$20^\mathrm{h}01^\mathrm{m}34^\mathrm{s}$	-38°44′54″	13.707	1.61
5835	5	-5675	-821	1079	$16^\mathrm{h}33^\mathrm{m}05^\mathrm{s}$	-58°03′12″	12.937	1.61
5871	6	1378	4290	3763	$15^\mathrm{h}37^\mathrm{m}37^\mathrm{s}$	+43°34′34″	12.984	1.62
5884	7	2053	-5502	-352	$01^\mathrm{h}01^\mathrm{m}49^\mathrm{s}$	-06°41′22″	12.957	1.62
5891	6	-2610	5011	-1667	$11^\mathrm{h}52^\mathrm{m}39^\mathrm{s}$	-05°22′59″	12.614	1.62

Continued on next page...

Table B.1 – Continued

Distance[a]	$N_{\rm m}$[b]	SGX[a]	SGY[a]	SGZ[a]	α	δ	$\log\left(\frac{M}{M_\odot}\right)$	w[c]
5903	5	-3250	1867	4560	$16^{h}46^{m}11^{s}$	-07°27′43″	12.862	1.63
5903	7	-4192	-3648	1990	$20^{h}25^{m}10^{s}$	-51°47′55″	12.849	1.63
5916	5	-4570	-1980	3193	$18^{h}41^{m}27^{s}$	-41°32′18″	12.113	1.63
5918	10	-4969	1195	-2984	$10^{h}59^{m}28^{s}$	-50°40′19″	12.998	1.63
5921	6	2238	-5465	428	$00^{h}34^{m}30^{s}$	-02°53′09″	13.205	1.63
5940	13	-2091	5225	1899	$14^{h}02^{m}40^{s}$	+09°13′26″	13.280	1.64
5953	9	915	5417	2290	$14^{h}01^{m}41^{s}$	+38°49′20″	13.085	1.64
5962	5	2985	-4375	-2737	$02^{h}48^{m}25^{s}$	-00°25′23″	12.372	1.64
5965	5	1770	-5696	-2	$00^{h}45^{m}06^{s}$	-08°50′35″	12.575	1.65
5974	6	-4938	3308	600	$13^{h}54^{m}45^{s}$	-26°35′43″	12.666	1.65
5977	9	3288	3350	3699	$16^{h}42^{m}51^{s}$	+61°53′44″	13.071	1.65
5984	5	2767	-3978	-3510	$03^{h}21^{m}43^{s}$	-02°35′42″	13.231	1.65
5986	10	5409	2565	15	$06^{h}38^{m}56^{s}$	+74°24′01″	13.210	1.65
6017	16	4740	2643	-2597	$07^{h}09^{m}45^{s}$	+48°37′59″	13.470	1.66
6021	7	1932	4088	3976	$15^{h}57^{m}42^{s}$	+48°17′08″	12.384	1.66
6039	5	-5884	-1069	842	$16^{h}34^{m}35^{s}$	-61°23′19″	12.787	1.67
6055	5	-3776	-3019	3645	$19^{h}43^{m}09^{s}$	-36°02′14″	12.986	1.67
6077	10	3162	-4609	-2385	$02^{h}32^{m}28^{s}$	+00°58′15″	13.481	1.68
6081	11	-5917	715	-1208	$13^{h}07^{m}55^{s}$	-57°20′59″	13.435	1.68
6101	17	4089	-2120	4001	$22^{h}15^{m}12^{s}$	+37°18′60″	13.500	1.69
6109	15	-1837	-5647	-1434	$01^{h}08^{m}46^{s}$	-45°59′10″	14.257	1.69
6177	5	-4674	-2420	-3232	$06^{h}43^{m}33^{s}$	-74°07′56″	12.492	1.71
6206	5	4958	-3449	1422	$00^{h}29^{m}53^{s}$	+30°49′25″	12.982	1.72
6218	5	-932	2153	-5758	$08^{h}26^{m}11^{s}$	-13°23′19″	12.241	1.73
6225	5	4788	3000	-2611	$07^{h}26^{m}16^{s}$	+49°07′06″	12.652	1.73
6246	27	5546	-705	-2784	$04^{h}22^{m}09^{s}$	+36°35′51″	13.633	1.74
6252	5	5658	-1076	-2431	$03^{h}58^{m}12^{s}$	+36°55′54″	12.555	1.74
6255	11	5938	-1667	-1038	$02^{h}48^{m}39^{s}$	+41°13′17″	13.494	1.74
6277	55	-228	6169	-1137	$11^{h}44^{m}38^{s}$	+19°56′07″	14.202	1.75
6289	8	5005	3471	-1568	$07^{h}57^{m}31^{s}$	+58°45′27″	13.184	1.75
6293	5	-3600	-4015	3243	$20^{h}30^{m}53^{s}$	-38°50′28″	12.318	1.75
6317	11	-1332	4198	-4528	$09^{h}50^{m}08^{s}$	-05°12′45″	13.483	1.76
6345	6	-88	6339	-265	$12^{h}15^{m}22^{s}$	+23°53′23″	12.875	1.77
6377	10	4891	-2070	-3529	$04^{h}03^{m}16^{s}$	+21°50′11″	13.116	1.78
6378	5	6097	-1792	-533	$02^{h}24^{m}23^{s}$	+42°54′25″	12.826	1.78
6392	14	32	6358	659	$12^{h}49^{m}23^{s}$	+27°18′46″	13.549	1.79
6417	22	-3045	5122	-2381	$11^{h}34^{m}41^{s}$	-09°37′28″	14.004	1.80
6420	12	-5368	3398	923	$14^{h}07^{m}36^{s}$	-27°03′04″	13.665	1.80
6453	6	-1934	-5797	-2070	$01^{h}38^{m}11^{s}$	-46°55′26″	12.938	1.81
6453	11	-2288	5892	-1298	$12^{h}04^{m}40^{s}$	+01°48′14″	13.388	1.81
6468	8	-1212	6155	-1576	$11^{h}43^{m}01^{s}$	+10°23′48″	12.990	1.81
6516	6	4417	1198	-4637	$06^{h}19^{m}12^{s}$	+28°03′47″	13.060	1.83
6550	7	-1721	-1405	-6162	$06^{h}33^{m}59^{s}$	-34°58′10″	13.100	1.85
6562	7	806	1876	6236	$18^{h}01^{m}46^{s}$	+29°04′03″	13.233	1.85
6574	9	1035	6103	-2212	$10^{h}47^{m}20^{s}$	+26°16′26″	12.876	1.85
6583	8	5135	2609	-3187	$06^{h}57^{m}27^{s}$	+45°19′48″	13.302	1.86
6592	11	4485	-2108	4345	$22^{h}11^{m}56^{s}$	+38°53′37″	13.734	1.86
6604	13	-1964	2076	5953	$17^{h}16^{m}24^{s}$	+07°02′27″	13.125	1.87

Continued on next page...

Table B.1 – Continued

Distance^a	$N_{\rm m}{}^b$	SGX^a	SGY^a	SGZ^a	α	δ	$\log\left(\frac{M}{M_\odot}\right)$	w^c
6623	5	-4266	5042	484	$13^{\rm h}26^{\rm m}42^{\rm s}$	-12°03′34″	12.631	1.87
6633	23	5304	2940	-2686	$07^{\rm h}09^{\rm m}40^{\rm s}$	+50°19′09″	13.595	1.88
6636	7	2143	-6022	1783	$23^{\rm h}47^{\rm m}34^{\rm s}$	-02°10′15″	13.089	1.88
6641	5	2745	5989	-827	$11^{\rm h}03^{\rm m}45^{\rm s}$	+45°11′06″	13.230	1.88
6648	7	-1328	4710	-4500	$10^{\rm h}00^{\rm m}38^{\rm s}$	-02°57′44″	13.395	1.88
6649	7	-107	-5605	-3574	$02^{\rm h}50^{\rm m}26^{\rm s}$	-31°23′47″	12.683	1.88
6652	11	4494	-2832	4003	$22^{\rm h}37^{\rm m}27^{\rm s}$	+34°14′26″	13.245	1.89
6659	7	414	5035	-4338	$09^{\rm h}41^{\rm m}06^{\rm s}$	+11°37′24″	13.447	1.89
6669	13	4540	-3168	3717	$22^{\rm h}53^{\rm m}06^{\rm s}$	+32°16′42″	13.029	1.89
6686	7	3595	-4933	-2726	$02^{\rm h}37^{\rm m}58^{\rm s}$	+02°05′56″	13.289	1.90
6689	9	4913	-3874	2365	$23^{\rm h}53^{\rm m}36^{\rm s}$	+28°43′02″	12.927	1.90
6693	8	6447	-1557	900	$01^{\rm h}22^{\rm m}12^{\rm s}$	+50°03′52″	13.510	1.90
6715	5	6443	-1769	-668	$02^{\rm h}31^{\rm m}23^{\rm s}$	+43°23′37″	12.875	1.91
6723	10	113	6710	-395	$12^{\rm h}08^{\rm m}50^{\rm s}$	+25°15′02″	13.171	1.91
6742	6	-2326	5944	2173	$14^{\rm h}02^{\rm m}51^{\rm s}$	+09°39′53″	12.987	1.92
6746	5	-1927	1698	6238	$17^{\rm h}31^{\rm m}52^{\rm s}$	+06°26′09″	12.601	1.92
6748	5	-1247	6301	-2070	$11^{\rm h}28^{\rm m}43^{\rm s}$	+09°05′25″	11.612	1.92
6764	8	5338	3429	2342	$15^{\rm h}28^{\rm m}16^{\rm s}$	+82°30′05″	13.127	1.93
6771	5	-4243	-4359	2973	$20^{\rm h}33^{\rm m}01^{\rm s}$	-44°12′16″	13.252	1.93
6793	15	-5340	1707	-3836	$10^{\rm h}40^{\rm m}16^{\rm s}$	-46°16′22″	13.514	1.94
6811	5	79	6755	-865	$11^{\rm h}53^{\rm m}02^{\rm s}$	+23°38′13″	13.366	1.95
6815	14	4648	-3742	3291	$23^{\rm h}16^{\rm m}13^{\rm s}$	+28°53′24″	13.598	1.95
6830	36	4064	-4517	-3120	$02^{\rm h}56^{\rm m}53^{\rm s}$	+06°03′36″	14.108	1.96
6834	10	6139	-972	-2841	$04^{\rm h}09^{\rm m}52^{\rm s}$	+36°54′58″	13.550	1.96
6855	6	-3673	-4655	3439	$20^{\rm h}46^{\rm m}59^{\rm s}$	-38°06′54″	12.983	1.97
6857	11	-2179	-6304	-1591	$01^{\rm h}06^{\rm m}57^{\rm s}$	-46°58′10″	13.491	1.97
6880	6	3392	-5033	-3240	$02^{\rm h}50^{\rm m}59^{\rm s}$	-00°55′53″	12.675	1.98
6906	17	2902	5246	-3427	$09^{\rm h}20^{\rm m}12^{\rm s}$	+33°36′59″	13.860	1.99
6919	14	-5822	3515	1273	$14^{\rm h}19^{\rm m}21^{\rm s}$	-27°13′42″	13.516	2.00
6924	5	-154	6768	-1455	$11^{\rm h}36^{\rm m}42^{\rm s}$	+20°03′41″	12.858	2.00
6944	17	5391	-3952	1880	$00^{\rm h}17^{\rm m}33^{\rm s}$	+29°53′35″	13.880	2.01
6947	9	5244	4509	644	$10^{\rm h}34^{\rm m}43^{\rm s}$	+72°34′59″	13.337	2.01
6948	7	-4179	5477	896	$13^{\rm h}35^{\rm m}45^{\rm s}$	-08°21′53″	13.483	2.01
7008	5	6698	-1986	-550	$02^{\rm h}22^{\rm m}35^{\rm s}$	+42°55′08″	12.742	2.04
7029	5	-1273	4501	-5246	$09^{\rm h}39^{\rm m}06^{\rm s}$	-04°47′55″	12.404	2.05
7038	16	-2080	6580	1377	$13^{\rm h}29^{\rm m}37^{\rm s}$	+11°29′23″	13.614	2.05
7041	5	6536	-1279	-2286	$03^{\rm h}42^{\rm m}20^{\rm s}$	+39°21′50″	12.861	2.05
7052	18	-4952	5016	206	$13^{\rm h}22^{\rm m}05^{\rm s}$	-16°59′52″	13.535	2.06
7058	8	-2564	6088	2487	$14^{\rm h}11^{\rm m}23^{\rm s}$	+08°45′09″	13.200	2.06
7062	7	-5268	4670	-553	$13^{\rm h}01^{\rm m}23^{\rm s}$	-22°22′23″	13.518	2.06
7075	5	-1878	-6562	-1861	$01^{\rm h}19^{\rm m}43^{\rm s}$	-44°15′11″	13.364	2.07
7132	17	-243	7048	-1059	$11^{\rm h}52^{\rm m}00^{\rm s}$	+20°44′36″	13.553	2.10
7141	6	-3448	977	6176	$17^{\rm h}35^{\rm m}27^{\rm s}$	-07°05′17″	13.046	2.10
7161	13	2850	6170	-2255	$10^{\rm h}13^{\rm m}52^{\rm s}$	+38°50′40″	13.617	2.11
7209	5	-4080	5940	215	$13^{\rm h}10^{\rm m}26^{\rm s}$	-07°15′33″	12.486	2.14
7218	5	2988	5835	-3019	$09^{\rm h}42^{\rm m}44^{\rm s}$	+36°10′29″	13.068	2.14
7219	5	-4531	-5099	2363	$21^{\rm h}05^{\rm m}16^{\rm s}$	-49°02′29″	12.910	2.14
7227	5	-3304	5784	-2803	$11^{\rm h}29^{\rm m}45^{\rm s}$	-08°57′53″	12.949	2.14

Continued on next page...

Table B.1 – Continued

Distance[a]	N_{m}[b]	SGX[a]	SGY[a]	SGZ[a]	α	δ	$\log\left(\frac{M}{M_\odot}\right)$	w[c]
7237	5	-6667	2467	1354	$14^{h}42^{m}27^{s}$	-36°40′05″	12.984	2.15
7237	7	1928	-6020	-3523	$02^{h}41^{m}31^{s}$	-15°00′00″	13.091	2.15
7263	5	77	7262	-91	$12^{h}20^{m}28^{s}$	+25°45′19″	13.190	2.16
7265	8	7044	-1749	320	$01^{h}51^{m}42^{s}$	+48°06′04″	13.388	2.16
7283	8	-5735	451	4465	$17^{h}04^{m}12^{s}$	-29°05′31″	13.412	2.17
7293	9	3094	-5283	3963	$22^{h}50^{m}07^{s}$	+11°39′55″	13.749	2.18
7298	7	7111	992	1306	$01^{h}52^{m}40^{s}$	+71°11′20″	12.769	2.18
7300	5	2805	5415	-4012	$09^{h}13^{m}51^{s}$	+30°02′04″	12.859	2.18
7305	5	5361	4857	1016	$11^{h}15^{m}44^{s}$	+72°48′03″	13.249	2.19
7329	5	7170	-1300	-782	$02^{h}47^{m}43^{s}$	+47°34′49″	11.812	2.20
7337	5	-2108	-2931	6387	$19^{h}49^{m}04^{s}$	-10°33′37″	12.312	2.20
7345	5	-1268	4617	-5569	$09^{h}34^{m}48^{s}$	-04°51′13″	12.515	2.21
7353	5	-4258	-3144	5104	$19^{h}28^{m}03^{s}$	-29°38′26″	12.315	2.21
7363	5	6865	-742	-2555	$04^{h}04^{m}13^{s}$	+41°47′25″	12.676	2.22
7374	12	-2376	-4295	5502	$20^{h}29^{m}15^{s}$	-18°59′35″	13.822	2.22
7375	5	2981	-2176	-6384	$05^{h}09^{m}30^{s}$	-00°42′50″	13.080	2.22
7380	8	-3044	6546	1527	$13^{h}39^{m}31^{s}$	+04°38′11″	12.810	2.22
7384	8	-5552	4861	241	$13^{h}28^{m}06^{s}$	-20°54′47″	12.940	2.23
7416	6	-3162	5978	-3042	$11^{h}22^{m}38^{s}$	-07°38′20″	12.956	2.24
7447	98	48	7370	1068	$12^{h}59^{m}28^{s}$	+27°57′26″	14.645	2.26
7474	6	4658	-4226	4037	$22^{h}58^{m}26^{s}$	+26°09′54″	13.446	2.28
7511	12	5321	-4437	2901	$23^{h}43^{m}45^{s}$	+27°30′19″	13.549	2.30
7530	5	-6988	1182	2542	$15^{h}50^{m}11^{s}$	-39°52′37″	12.341	2.31
7535	5	2033	-6622	2964	$23^{h}15^{m}47^{s}$	-02°09′54″	13.148	2.31
7536	5	-3151	-6642	-1657	$00^{h}56^{m}34^{s}$	-52°55′19″	13.454	2.31
7556	5	-5320	4048	3521	$15^{h}14^{m}52^{s}$	-14°32′18″	12.336	2.32
7569	9	-2942	6371	2835	$14^{h}18^{m}30^{s}$	+07°19′01″	13.478	2.33
7581	5	-7032	2278	1683	$14^{h}57^{m}09^{s}$	-37°37′14″	13.428	2.34
7585	7	4573	4188	4367	$16^{h}41^{m}08^{s}$	+65°49′39″	13.096	2.34
7595	5	-4530	5927	1424	$13^{h}48^{m}54^{s}$	-07°23′42″	13.489	2.35
7605	22	-4956	-2985	-4936	$06^{h}21^{m}49^{s}$	-64°55′02″	14.019	2.35
7609	6	2934	-4841	5085	$22^{h}14^{m}12^{s}$	+13°54′58″	13.176	2.36
7614	7	3734	5581	-3588	$09^{h}09^{m}06^{s}$	+37°32′55″	13.171	2.36
7622	5	2134	3795	6256	$17^{h}11^{m}34^{s}$	+42°37′01″	12.746	2.36
7623	7	583	7270	2218	$13^{h}35^{m}34^{s}$	+33°37′23″	13.447	2.36
7648	6	5324	-5171	-1845	$02^{h}11^{m}58^{s}$	+14°10′13″	12.775	2.38
7664	13	4544	776	6123	$19^{h}58^{m}11^{s}$	+50°25′03″	13.016	2.39
7690	9	4912	-4886	-3337	$02^{h}55^{m}41^{s}$	+09°14′26″	13.609	2.40
7706	7	-4141	-6158	-2077	$01^{h}10^{m}50^{s}$	-61°29′48″	12.895	2.42
7709	5	-2528	7115	1555	$13^{h}32^{m}56^{s}$	+09°39′19″	13.363	2.42
7742	28	-436	7688	-799	$12^{h}04^{m}20^{s}$	+20°26′33″	13.863	2.44
7798	6	981	-5860	5049	$22^{h}02^{m}23^{s}$	-02°12′08″	12.527	2.47
7825	7	5042	-4370	4087	$23^{h}04^{m}02^{s}$	+27°12′57″	12.556	2.49
7829	5	-2573	6754	3009	$14^{h}17^{m}29^{s}$	+10°59′26″	13.389	2.49
7869	18	-1442	-5217	5711	$21^{h}02^{m}33^{s}$	-14°13′43″	13.709	2.52
7887	8	4704	5084	-3771	$08^{h}33^{m}06^{s}$	+41°22′35″	13.232	2.53
7900	13	-3589	6100	3509	$14^{h}40^{m}48^{s}$	+03°25′26″	13.643	2.54
7925	10	-5097	1872	5772	$16^{h}50^{m}59^{s}$	-14°49′18″	13.248	2.56

Continued on next page...

Table B.1 – Continued

Distance^a	$N_m{}^b$	SGX^a	SGY^a	SGZ^a	α	δ	$\log\left(\frac{M}{M_\odot}\right)$	w^c
7929	16	-718	-7844	904	$23^h48^m50^s$	-28°07′34″	13.652	2.56
7931	7	3372	7133	-811	$11^h08^m08^s$	+46°24′59″	12.401	2.56
7935	5	-4268	6369	2042	$14^h00^m29^s$	-02°51′13″	12.890	2.57
7936	7	-4061	5677	-3776	$11^h11^m43^s$	-15°15′39″	13.241	2.57
7941	6	1096	-3275	7150	$20^h39^m02^s$	+10°42′52″	13.536	2.57
7945	5	-2826	6715	-3168	$11^h20^m40^s$	-02°59′19″	13.031	2.57
7976	9	5265	3735	4684	$17^h35^m59^s$	+68°14′30″	13.271	2.59
7986	5	3577	6959	-1600	$10^h35^m00^s$	+44°51′50″	12.777	2.60
8041	7	-6222	1082	4978	$16^h50^m07^s$	-26°12′04″	12.900	2.64
8050	6	-4926	3797	5111	$15^h56^m18^s$	-08°48′56″	12.864	2.65
8063	6	4710	963	6473	$19^h50^m49^s$	+50°32′29″	12.966	2.66
8082	6	721	7812	-1941	$11^h18^m36^s$	+25°14′22″	13.302	2.67
8104	18	6258	4732	-2026	$08^h13^m59^s$	+58°01′58″	13.551	2.69
8123	5	-4952	3103	5642	$16^h20^m52^s$	-09°59′43″	12.785	2.70
8128	5	-6307	4387	-2652	$12^h03^m04^s$	-31°42′60″	12.904	2.71
8136	6	-3376	1948	7142	$17^h20^m54^s$	-00°59′29″	13.040	2.71
8138	5	-3487	6217	-3925	$11^h05^m36^s$	-09°55′18″	12.200	2.71
8141	5	3610	-2088	-6991	$05^h13^m46^s$	+02°16′28″	13.002	2.71
8147	7	-2594	-5085	5813	$20^h40^m42^s$	-20°25′03″	12.605	2.72
8157	7	5218	-4873	3944	$23^h14^m58^s$	+25°13′12″	12.687	2.73
8165	7	4914	3299	5624	$18^h09^m47^s$	+61°27′32″	12.952	2.73
8171	5	2843	-5116	5701	$22^h03^m47^s$	+12°43′54″	13.245	2.74
8210	6	5876	-4921	2942	$23^h51^m25^s$	+27°11′10″	12.782	2.77
8223	5	6136	-4782	-2663	$02^h40^m26^s$	+17°49′26″	13.418	2.78
8237	5	2583	-4358	-6495	$04^h21^m02^s$	-09°47′14″	11.615	2.79
8250	16	8057	-1481	-979	$02^h50^m44^s$	+47°05′56″	14.067	2.80
8253	6	5086	6452	-778	$10^h22^m21^s$	+57°13′56″	12.812	2.80
8269	5	4188	-1362	6998	$20^h45^m41^s$	+36°30′49″	12.982	2.81
8275	26	1598	5047	6359	$16^h28^m37^s$	+39°30′05″	14.185	2.82
8277	7	2165	-4701	-6459	$04^h15^m12^s$	-13°15′28″	13.086	2.82
8289	5	4560	-1749	6697	$21^h06^m46^s$	+37°02′40″	12.753	2.83
8290	10	-2140	-7751	2014	$22^h56^m51^s$	-33°53′33″	13.252	2.83
8290	8	6256	-4868	2427	$00^h10^m27^s$	+28°32′35″	13.335	2.83
8294	13	803	7903	2384	$13^h33^m46^s$	+34°44′34″	13.376	2.83
8297	5	2664	6487	4434	$15^h01^m21^s$	+49°10′26″	12.950	2.84
8301	8	2498	4060	6796	$17^h15^m37^s$	+43°41′22″	13.729	2.84
8311	7	-2164	7441	3004	$14^h08^m08^s$	+14°54′37″	13.189	2.85
8325	6	2621	1957	7655	$18^h34^m27^s$	+38°24′04″	13.271	2.86
8328	5	3492	-3509	-6697	$04^h37^m34^s$	-02°07′13″	12.837	2.86
8333	5	5392	-5703	-2801	$02^h30^m20^s$	+09°58′23″	12.972	2.87
8339	7	-960	-5475	6216	$21^h07^m12^s$	-10°18′38″	13.458	2.87
8342	5	3449	-6087	-4544	$03^h05^m37^s$	-05°57′57″	13.333	2.87
8393	8	1704	6016	-5599	$09^h16^m20^s$	+17°33′43″	13.258	2.92
8399	10	-6036	737	5792	$17^h12^m06^s$	-23°16′13″	13.729	2.92
8403	5	4620	4054	5730	$17^h27^m22^s$	+59°55′11″	13.147	2.93
8405	5	-5518	1792	6080	$16^h54^m08^s$	-16°10′24″	11.552	2.93
8490	5	3687	3285	-6905	$07^h32^m12^s$	+18°39′59″	13.251	3.00
8500	6	5877	-5195	-3275	$02^h49^m07^s$	+13°15′56″	13.392	3.01

Continued on next page...

Table B.1 – Continued

Distance^a	$N_m{}^b$	SGX^a	SGY^a	SGZ^a	α	δ	$\log\left(\frac{M}{M_\odot}\right)$	w^c
8525	5	-872	-8443	790	$23^h52^m57^s$	-29°11′43″	13.008	3.03
8546	12	2246	-4379	-6986	$04^h30^m30^s$	-12°23′11″	13.892	3.05
8551	5	-1526	8376	-793	$12^h16^m04^s$	+13°56′47″	12.871	3.06
8587	5	-3942	6362	4209	$14^h53^m35^s$	+03°08′21″	13.311	3.09
8600	6	-1090	-8150	-2518	$01^h34^m14^s$	-36°30′18″	13.028	3.10
8635	6	-2883	6455	-4958	$10^h37^m04^s$	-07°02′50″	12.991	3.14
8639	9	477	8626	7	$12^h20^m15^s$	+28°25′26″	13.545	3.14
8687	5	-3124	6696	4568	$14^h56^m55^s$	+09°22′37″	12.582	3.19
8693	13	6001	-3555	5187	$22^h38^m32^s$	+35°32′08″	13.787	3.19
8695	5	1053	4154	-7565	$08^h23^m04^s$	+04°13′53″	13.074	3.19
8703	20	4357	-1836	-7306	$05^h17^m02^s$	+06°31′38″	13.970	3.20
8715	7	-2832	7356	3716	$14^h28^m09^s$	+11°22′49″	13.363	3.21
8721	5	3483	6898	-4041	$09^h33^m55^s$	+33°54′56″	12.998	3.22
8734	6	5255	3814	5840	$17^h53^m16^s$	+62°29′34″	13.521	3.23
8735	5	-3626	-3127	-7306	$06^h08^m41^s$	-47°32′27″	12.656	3.23
8739	8	2588	2087	-8081	$07^h13^m56^s$	+06°09′46″	13.567	3.24
8805	6	-4951	-6406	3461	$21^h09^m35^s$	-43°38′26″	12.565	3.30
8819	6	-2728	-1700	-8213	$06^h45^m02^s$	-36°58′18″	12.868	3.32
8827	8	2093	6440	-5662	$09^h17^m41^s$	+20°05′41″	13.571	3.33
8828	9	-979	-8756	552	$23^h59^m36^s$	-30°15′47″	13.133	3.33
8835	5	-1496	-5795	6498	$21^h01^m53^s$	-13°10′60″	12.876	3.34
8845	8	3883	-6287	-4861	$03^h08^m51^s$	-04°18′38″	13.206	3.35
8853	5	6376	-5160	3329	$23^h47^m01^s$	+28°12′20″	12.825	3.35
8855	9	1784	5115	7004	$16^h40^m33^s$	+39°27′33″	12.893	3.36
8856	6	-2751	-8175	-2008	$01^h05^m34^s$	-46°28′03″	13.030	3.36
8889	13	6295	-4022	-4818	$03^h41^m17^s$	+15°38′15″	13.724	3.39
8901	6	859	8059	3680	$14^h11^m19^s$	+35°41′13″	12.351	3.41
8908	7	-1231	8339	2880	$13^h52^m50^s$	+21°42′14″	13.203	3.41
8929	7	-3386	5333	-6311	$10^h02^m16^s$	-15°11′32″	12.873	3.44
8942	8	6481	-5043	-3539	$02^h57^m15^s$	+16°00′15″	13.068	3.45
8948	6	-3542	7357	-3659	$11^h20^m60^s$	-05°42′07″	13.568	3.46
8977	5	3266	-5170	6571	$21^h53^m38^s$	+15°21′35″	12.468	3.49
8978	8	-3776	2157	7855	$17^h20^m03^s$	-01°17′31″	13.462	3.49
9008	17	7012	5056	-2532	$08^h00^m54^s$	+56°39′43″	13.861	3.53
9016	9	1004	5716	6899	$16^h17^m53^s$	+35°06′18″	13.304	3.53
9020	6	3500	5695	-6056	$08^h37^m41^s$	+25°02′50″	12.843	3.54
9029	5	3424	-7171	-4287	$02^h44^m02^s$	-08°10′26″	13.493	3.55
9054	9	-7651	4726	-1040	$13^h03^m30^s$	-32°23′22″	13.168	3.58
9072	5	-4273	-6531	4624	$21^h03^m37^s$	-35°12′44″	12.912	3.60
9085	14	7276	-4958	-2237	$02^h28^m31^s$	+22°55′44″	14.067	3.61
9098	8	-4083	7173	3825	$14^h34^m12^s$	+03°43′51″	13.477	3.63
9100	5	-4638	-7744	-1151	$00^h10^m50^s$	-56°58′36″	12.812	3.63
9104	6	-6847	4662	-3778	$11^h37^m33^s$	-32°44′56″	12.660	3.64
9143	8	8744	-1876	-1904	$03^h10^m04^s$	+42°49′53″	13.704	3.68
9144	6	3808	-3936	-7323	$04^h35^m38^s$	-02°26′03″	13.340	3.69
9157	7	-6192	958	6676	$17^h15^m39^s$	-19°54′40″	13.413	3.70
9170	15	-3185	-814	-8561	$07^h16^m24^s$	-36°10′15″	14.008	3.72
9189	10	4673	4381	6589	$17^h29^m09^s$	+56°48′29″	13.815	3.74

Continued on next page...

Table B.1 – Continued

Distance^{a}	$N_{\mathrm{m}}{}^{b}$	SGX^{a}	SGY^{a}	SGZ^{a}	α	δ	$\log\left(\frac{M}{M_{\odot}}\right)$	w^{c}
9201	7	3893	8023	2264	$13^{h}06^{m}17^{s}$	+53°37′58″	13.094	3.76
9229	8	-3433	5232	-6783	$09^{h}52^{m}55^{s}$	-16°03′23″	13.208	3.79
9250	5	3844	8359	962	$12^{h}15^{m}12^{s}$	+50°41′39″	13.475	3.82
9253	5	54	9074	-1806	$11^{h}37^{m}34^{s}$	+21°52′57″	12.844	3.82
9263	5	6338	1733	-6529	$06^{h}19^{m}02^{s}$	+28°37′30″	13.103	3.83
9310	8	-2114	-7380	5267	$21^{h}39^{m}48^{s}$	-22°29′12″	13.122	3.90
9311	24	2243	-4696	-7720	$04^{h}34^{m}41^{s}$	-13°28′51″	13.837	3.90
9322	5	6850	-5339	3386	$23^{h}51^{m}04^{s}$	+29°05′02″	13.060	3.91
9323	10	-2653	-2423	-8602	$06^{h}24^{m}24^{s}$	-37°20′40″	13.513	3.91
9367	5	6771	1276	-6345	$06^{h}01^{m}41^{s}$	+29°52′18″	13.578	3.97
9370	5	-6351	1554	6710	$17^{h}01^{m}29^{s}$	-18°36′51″	12.953	3.98
9381	10	9218	-1500	-886	$02^{h}47^{m}19^{s}$	+48°49′49″	13.846	3.99
9383	7	635	9349	-491	$12^{h}06^{m}03^{s}$	+28°07′36″	13.723	3.99
9385	5	-2464	7149	-5559	$10^{h}27^{m}41^{s}$	-03°26′31″	13.169	4.00
9390	7	4084	5283	6601	$16^{h}48^{m}32^{s}$	+53°45′17″	13.381	4.00
9396	17	6541	-5575	3798	$23^{h}38^{m}28^{s}$	+27°03′47″	13.338	4.01
9418	5	2289	6668	-6245	$09^{h}10^{m}34^{s}$	+19°29′16″	13.325	4.04
9452	5	-7406	5860	382	$13^{h}33^{m}43^{s}$	-23°29′14″	13.093	4.09
9453	7	-4831	4722	6612	$16^{h}05^{m}05^{s}$	-02°06′51″	13.621	4.09
9459	7	260	4606	8257	$17^{h}00^{m}21^{s}$	+27°57′49″	13.423	4.10
9463	6	8000	-4664	-1948	$02^{h}26^{m}12^{s}$	+27°29′09″	13.516	4.11
9536	17	-767	8961	3169	$13^{h}52^{m}50^{s}$	+25°03′27″	13.605	4.21
9536	7	-2808	-6890	5964	$21^{h}11^{m}34^{s}$	-23°13′21″	13.159	4.21
9544	5	-30	8173	-4928	$10^{h}23^{m}08^{s}$	+12°58′52″	13.535	4.22
9558	5	4808	-5892	5790	$22^{h}36^{m}34^{s}$	+19°27′56″	12.668	4.25
9568	6	696	9445	-1362	$11^{h}43^{m}43^{s}$	+26°34′57″	13.280	4.26
9639	7	-3609	7619	-4673	$11^{h}01^{m}44^{s}$	-06°36′37″	13.050	4.37
9645	5	7796	-1755	5400	$22^{h}35^{m}24^{s}$	+50°22′23″	13.350	4.38
9706	20	-1910	6041	7352	$16^{h}04^{m}42^{s}$	+17°35′47″	13.980	4.48
9737	7	-7315	6354	952	$13^{h}43^{m}33^{s}$	-19°57′07″	13.164	4.53
9746	40	2077	5974	7414	$16^{h}27^{m}50^{s}$	+40°44′06″	14.421	4.54
9808	11	-3412	5840	-7103	$09^{h}55^{m}35^{s}$	-13°55′21″	13.579	4.65
9843	5	-3242	4839	7934	$16^{h}29^{m}29^{s}$	+08°20′52″	13.615	4.71
9866	7	6866	-5911	-3904	$02^{h}52^{m}43^{s}$	+13°38′23″	13.138	4.75
9922	7	-9083	3989	-106	$13^{h}42^{m}59^{s}$	-38°17′01″	13.580	4.84
9939	5	-406	8504	-5129	$10^{h}27^{m}11^{s}$	+11°03′43″	12.221	4.88
9947	7	-3918	7025	5851	$15^{h}17^{m}06^{s}$	+07°02′31″	13.411	4.89
9947	5	3521	-6052	-7065	$03^{h}54^{m}00^{s}$	-08°30′56″	13.034	4.89
9957	5	-8823	4520	936	$14^{h}04^{m}29^{s}$	-32°55′43″	13.296	4.91
9969	9	9678	-1888	-1467	$02^{h}56^{m}54^{s}$	+45°41′31″	13.913	4.93
9975	6	-4202	-9012	-791	$00^{h}06^{m}05^{s}$	-50°31′47″	13.423	4.94
10015	9	1791	9810	-926	$11^{h}45^{m}14^{s}$	+33°18′17″	13.549	5.02
10026	5	-286	7251	6918	$15^{h}40^{m}59^{s}$	+28°11′07″	13.250	5.04
10046	6	5008	-2122	-8446	$05^{h}17^{m}14^{s}$	+06°24′01″	12.873	5.08
10057	5	7658	-4721	4495	$23^{h}28^{m}13^{s}$	+35°10′23″	12.330	5.10
10098	5	8393	-5169	-2193	$02^{h}26^{m}21^{s}$	+25°58′53″	13.483	5.18
10104	6	2530	-5193	-8290	$04^{h}31^{m}14^{s}$	-13°06′15″	13.572	5.19
10107	5	2982	-8354	-4845	$02^{h}40^{m}46^{s}$	-13°17′17″	12.943	5.20

Continued on next page. . .

Table B.1 – Continued

Distance^a	$N_{\rm m}{}^b$	SGX^a	SGY^a	SGZ^a	α	δ	$\log\left(\frac{M}{M_\odot}\right)$	w^c
10118	5	-1125	-3917	-9261	$05^{\rm h}34^{\rm m}13^{\rm s}$	-30°38′33″	12.978	5.22
10139	5	-4646	8666	2472	$13^{\rm h}51^{\rm m}16^{\rm s}$	+02°09′10″	12.943	5.26
10141	5	2652	7636	-6123	$09^{\rm h}23^{\rm m}42^{\rm s}$	+22°37′57″	13.089	5.27
10146	5	-14	-4135	-9265	$05^{\rm h}20^{\rm m}11^{\rm s}$	-25°02′23″	13.236	5.28
10152	7	7716	-5035	-4261	$03^{\rm h}11^{\rm m}08^{\rm s}$	+19°11′45″	13.666	5.29
10154	9	245	5017	8824	$16^{\rm h}58^{\rm m}04^{\rm s}$	+27°54′16″	13.497	5.29
10156	7	-4633	3238	8438	$16^{\rm h}57^{\rm m}56^{\rm s}$	-01°48′23″	13.600	5.30
10240	5	-3201	-2220	-9470	$06^{\rm h}39^{\rm m}04^{\rm s}$	-37°47′41″	12.668	5.47
10263	7	9053	-4811	-467	$01^{\rm h}50^{\rm m}37^{\rm s}$	+33°09′34″	13.425	5.52
10306	7	7450	-5865	-4038	$02^{\rm h}55^{\rm m}48^{\rm s}$	+15°50′16″	13.346	5.62
10340	5	-361	9000	-5078	$10^{\rm h}32^{\rm m}35^{\rm s}$	+12°07′42″	13.213	5.69
10369	5	-9181	-4395	1975	$18^{\rm h}47^{\rm m}26^{\rm s}$	-63°17′42″	13.487	5.76
10379	5	6626	-5317	-5962	$03^{\rm h}39^{\rm m}01^{\rm s}$	+10°04′48″	13.692	5.78
10396	6	-4656	7412	5608	$15^{\rm h}06^{\rm m}35^{\rm s}$	+03°46′14″	13.254	5.82
10401	5	4855	9198	-100	$11^{\rm h}29^{\rm m}20^{\rm s}$	+51°09′27″	13.439	5.83
10430	16	-8581	5929	-34	$13^{\rm h}28^{\rm m}13^{\rm s}$	-27°47′10″	14.403	5.90
10438	8	-492	-3283	-9896	$05^{\rm h}47^{\rm m}49^{\rm s}$	-25°36′34″	13.417	5.92
10460	5	2916	6196	7907	$16^{\rm h}36^{\rm m}36^{\rm s}$	+44°20′37″	13.168	5.98
10496	8	8121	6023	2814	$12^{\rm h}56^{\rm m}50^{\rm s}$	+80°15′40″	13.184	6.06
10500	7	8930	4029	-3776	$06^{\rm h}41^{\rm m}31^{\rm s}$	+53°09′11″	13.201	6.07
10531	12	1628	10081	-2575	$11^{\rm h}10^{\rm m}06^{\rm s}$	+28°31′19″	14.045	6.15
10547	9	-2375	6566	7904	$16^{\rm h}02^{\rm m}18^{\rm s}$	+16°00′31″	13.698	6.19
10614	5	8708	-5585	-2372	$02^{\rm h}25^{\rm m}58^{\rm s}$	+24°53′45″	12.710	6.36
10630	6	10264	-2109	-1790	$03^{\rm h}00^{\rm m}59^{\rm s}$	+44°32′45″	13.138	6.41
10642	7	8547	-1758	6091	$22^{\rm h}28^{\rm m}25^{\rm s}$	+50°55′27″	13.041	6.44
10644	11	-10319	1112	2360	$15^{\rm h}33^{\rm m}44^{\rm s}$	-46°56′53″	13.647	6.44
10663	6	1388	6565	8286	$16^{\rm h}24^{\rm m}55^{\rm s}$	+35°55′19″	13.593	6.49
10735	5	-854	7835	7288	$15^{\rm h}36^{\rm m}20^{\rm s}$	+25°21′06″	12.822	6.69
10771	6	700	5304	9348	$17^{\rm h}01^{\rm m}14^{\rm s}$	+30°08′48″	13.698	6.80
10807	17	2053	-5207	-9244	$04^{\rm h}45^{\rm m}11^{\rm s}$	-15°55′41″	14.269	6.90
10810	7	5463	-7663	5319	$23^{\rm h}07^{\rm m}19^{\rm s}$	+15°21′30″	13.385	6.91
10839	5	-9666	4791	-1042	$13^{\rm h}15^{\rm m}16^{\rm s}$	-37°14′20″	12.922	6.99
10841	6	-8752	6246	1384	$13^{\rm h}58^{\rm m}34^{\rm s}$	-24°28′13″	13.111	7.00
10888	5	9177	-5424	-2217	$02^{\rm h}25^{\rm m}02^{\rm s}$	+27°14′14″	13.323	7.14
10925	6	-8305	6622	2556	$14^{\rm h}18^{\rm m}36^{\rm s}$	-19°23′15″	12.623	7.26
10943	6	-4019	7628	6738	$15^{\rm h}23^{\rm m}47^{\rm s}$	+08°34′18″	13.494	7.32
10955	9	2494	10516	-1789	$11^{\rm h}21^{\rm m}22^{\rm s}$	+34°18′26″	13.118	7.36
10957	6	6129	-7113	5647	$23^{\rm h}03^{\rm m}36^{\rm s}$	+20°04′44″	12.639	7.36
10959	7	-4747	7537	6384	$15^{\rm h}18^{\rm m}09^{\rm s}$	+04°32′45″	13.441	7.37
10989	11	-1328	9943	-4486	$11^{\rm h}00^{\rm m}15^{\rm s}$	+09°58′33″	13.711	7.46
11000	5	-10061	4445	22	$13^{\rm h}46^{\rm m}16^{\rm s}$	-37°55′06″	12.952	7.50
11059	5	8240	7341	702	$10^{\rm h}26^{\rm m}02^{\rm s}$	+70°44′47″	13.692	7.70
11138	9	-3731	-7974	6823	$21^{\rm h}07^{\rm m}01^{\rm s}$	-25°27′21″	13.959	7.98
11233	6	-2328	-3221	-10506	$06^{\rm h}09^{\rm m}25^{\rm s}$	-33°42′10″	13.428	8.32
11253	6	-9159	-6260	-1885	$22^{\rm h}25^{\rm m}59^{\rm s}$	-80°11′33″	13.395	8.40
11259	5	5066	9911	1694	$12^{\rm h}27^{\rm m}43^{\rm s}$	+53°42′31″	13.574	8.42
11263	10	-543	-3778	-10596	$05^{\rm h}42^{\rm m}39^{\rm s}$	-26°06′50″	13.385	8.43
11343	5	2546	5398	9645	$17^{\rm h}15^{\rm m}57^{\rm s}$	+38°53′20″	13.489	8.75

Continued on next page...

Table B.1 – Continued

Distance[a]	N_m[b]	SGX[a]	SGY[a]	SGZ[a]	α	δ	$\log\left(\frac{M}{M_\odot}\right)$	w[c]
11349	6	10609	-1507	-3738	$03^h53^m22^s$	+41°15′56″	13.340	8.78
11379	6	10007	-5391	-531	$01^h50^m23^s$	+32°49′41″	13.231	8.90
11394	5	-705	-1985	-11198	$06^h22^m53^s$	-23°12′49″	13.334	8.96
11434	6	9472	5025	-3968	$07^h04^m34^s$	+53°57′13″	13.011	9.13
11434	7	6876	-7590	5085	$23^h23^m50^s$	+20°44′10″	13.792	9.13
11441	5	-9534	6223	1127	$13^h55^m21^s$	-27°16′44″	13.047	9.16
11453	7	888	11089	2725	$13^h20^m40^s$	+33°07′14″	13.519	9.21
11609	5	-10699	4503	-143	$13^h44^m05^s$	-39°08′48″	12.953	9.91
11718	11	-5109	8209	6620	$15^h13^m07^s$	+04°26′60″	13.460	10.45
11729	6	-175	5370	10426	$17^h05^m28^s$	+25°05′38″	13.775	10.50
11747	5	-563	-3633	-11157	$05^h49^m12^s$	-25°32′13″	13.203	10.60
11855	9	-10412	5650	439	$13^h47^m37^s$	-32°51′41″	13.624	11.17
11878	5	5059	9043	5807	$14^h52^m04^s$	+55°40′42″	12.213	11.30
11963	14	-2239	7423	9110	$16^h06^m03^s$	+18°06′57″	14.175	11.79
11994	8	9463	5707	4662	$16^h52^m10^s$	+81°36′00″	12.946	11.98
12072	5	-3212	8930	-7461	$10^h21^m17^s$	-04°33′38″	12.272	12.46
12083	5	10512	3758	-4624	$06^h14^m55^s$	+51°13′08″	13.169	12.53
12188	5	2140	10755	-5319	$10^h20^m26^s$	+24°18′18″	13.456	13.22
12234	14	-3027	10432	-5626	$10^h58^m45^s$	+01°35′40″	13.663	13.54

[a] Distances are given in km s^{-1}.

[b] Number of observed member-galaxies assigned to the group.

[c] The inverse of the radial selection function evaluated at the distance of the group.

The above table contains the group positions and mass estimates after the iterative procedure has been applied. The flow-field was calculated assuming the coherent mass correction.

Table B.2: Attractors defining the density-field (IMC)

Distance^a	$N_{\rm m}{}^b$	SGX^a	SGY^a	SGZ^a	α	δ	$\log\left(\frac{M}{M_\odot}\right)$
787	7	728	-268	-125	$02^{\rm h}35^{\rm m}37^{\rm s}$	+37°30′06″	12.635
832	7	-46	750	-356	$10^{\rm h}49^{\rm m}23^{\rm s}$	+12°51′53″	12.229
851	6	-461	-463	-544	$04^{\rm h}53^{\rm m}07^{\rm s}$	-60°56′02″	11.919
887	6	-92	835	-284	$11^{\rm h}18^{\rm m}57^{\rm s}$	+13°06′17″	13.083
912	5	-178	-448	-773	$05^{\rm h}09^{\rm m}12^{\rm s}$	-37°31′36″	12.844
947	17	-545	772	-52	$12^{\rm h}52^{\rm m}09^{\rm s}$	-09°16′51″	13.169
969	6	-882	373	-141	$13^{\rm h}05^{\rm m}20^{\rm s}$	-41°14′01″	12.008
982	8	-546	435	-689	$10^{\rm h}04^{\rm m}15^{\rm s}$	-28°39′58″	12.457
996	13	-286	-677	-671	$03^{\rm h}58^{\rm m}47^{\rm s}$	-46°13′34″	12.896
1062	13	86	1058	13	$12^{\rm h}21^{\rm m}02^{\rm s}$	+30°02′55″	12.582
1159	6	-479	1006	316	$13^{\rm h}55^{\rm m}06^{\rm s}$	+05°10′14″	12.576
1165	12	-470	1062	-79	$12^{\rm h}37^{\rm m}12^{\rm s}$	+01°25′49″	13.122
1181	15	353	1126	36	$12^{\rm h}05^{\rm m}40^{\rm s}$	+42°27′48″	12.741
1231	12	-381	-1142	255	$22^{\rm h}58^{\rm m}14^{\rm s}$	-37°30′34″	13.020
1246	198	-283	1212	-58	$12^{\rm h}29^{\rm m}53^{\rm s}$	+12°02′48″	13.820
1265	23	-492	1164	-24	$12^{\rm h}46^{\rm m}56^{\rm s}$	+03°05′25″	13.242
1337	13	-601	-829	-858	$04^{\rm h}17^{\rm m}58^{\rm s}$	-55°51′31″	13.076
1337	7	-1007	878	13	$13^{\rm h}23^{\rm m}01^{\rm s}$	-21°24′45″	13.005
1375	7	694	1181	106	$11^{\rm h}52^{\rm m}42^{\rm s}$	+55°34′46″	12.984
1375	5	107	-1069	-857	$03^{\rm h}17^{\rm m}52^{\rm s}$	-25°47′57″	12.626
1375	6	491	1125	-618	$09^{\rm h}46^{\rm m}27^{\rm s}$	+32°29′39″	12.477
1381	9	-1006	798	-507	$11^{\rm h}49^{\rm m}44^{\rm s}$	-28°39′59″	12.810
1407	5	-637	1046	691	$14^{\rm h}53^{\rm m}25^{\rm s}$	+03°32′34″	11.663
1433	5	482	-1289	-397	$01^{\rm h}51^{\rm m}23^{\rm s}$	-09°48′33″	12.445
1440	8	550	-1155	-659	$02^{\rm h}39^{\rm m}38^{\rm s}$	-07°58′07″	12.240
1487	40	-126	-1099	-993	$03^{\rm h}37^{\rm m}07^{\rm s}$	-34°49′42″	13.469
1514	11	1481	311	30	$03^{\rm h}51^{\rm m}06^{\rm s}$	+69°32′41″	13.041
1528	7	-74	1468	-413	$11^{\rm h}25^{\rm m}12^{\rm s}$	+17°15′32″	12.897
1543	8	-36	1472	-458	$11^{\rm h}16^{\rm m}43^{\rm s}$	+17°57′34″	12.840
1550	5	-440	520	-1391	$08^{\rm h}43^{\rm m}17^{\rm s}$	-20°07′37″	12.332
1564	5	776	1357	12	$11^{\rm h}29^{\rm m}36^{\rm s}$	+53°19′30″	12.688
1564	9	-990	1105	-492	$11^{\rm h}57^{\rm m}30^{\rm s}$	-19°09′31″	11.731
1593	5	-191	-1225	-999	$03^{\rm h}23^{\rm m}53^{\rm s}$	-37°06′58″	11.769
1601	7	-1201	-490	-937	$07^{\rm h}34^{\rm m}30^{\rm s}$	-69°30′56″	11.985
1613	7	-581	-1494	176	$23^{\rm h}17^{\rm m}05^{\rm s}$	-42°42′44″	11.728
1676	12	-266	-192	-1643	$06^{\rm h}46^{\rm m}47^{\rm s}$	-26°51′18″	13.173
1704	7	960	1402	125	$11^{\rm h}39^{\rm m}55^{\rm s}$	+59°08′11″	12.238
1719	6	-861	-1431	402	$22^{\rm h}12^{\rm m}42^{\rm s}$	-46°32′11″	12.647
1723	6	-92	-1112	-1312	$04^{\rm h}11^{\rm m}49^{\rm s}$	-31°57′30″	12.671
1731	14	-539	328	-1611	$08^{\rm h}15^{\rm m}26^{\rm s}$	-26°03′47″	13.319
1755	8	649	-1596	-330	$01^{\rm h}32^{\rm m}23^{\rm s}$	-07°00′17″	12.260
1761	9	-982	1461	19	$13^{\rm h}05^{\rm m}34^{\rm s}$	-07°01′41″	13.227
1771	5	1088	1366	289	$12^{\rm h}09^{\rm m}11^{\rm s}$	+64°48′22″	12.494
1771	5	-794	1442	651	$14^{\rm h}20^{\rm m}43^{\rm s}$	+03°34′27″	12.233
1771	5	896	-1225	911	$23^{\rm h}01^{\rm m}36^{\rm s}$	+16°11′03″	12.456
1788	43	290	-1279	-1214	$03^{\rm h}36^{\rm m}40^{\rm s}$	-20°31′29″	13.539
1813	9	-1397	1013	-554	$12^{\rm h}08^{\rm m}09^{\rm s}$	-30°28′38″	12.888

Continued on next page...

Table B.2 – Continued

Distance^{a}	$N_{\rm m}{}^{b}$	SGX^{a}	SGY^{a}	SGZ^{a}	α	δ	$\log\left(\frac{M}{M_{\odot}}\right)$
1821	6	-1569	-180	-906	$10^{h}10^{m}13^{s}$	-66°54′00″	12.939
1898	10	-410	-144	-1847	$07^{h}02^{m}20^{s}$	-28°51′55″	13.058
1924	8	961	1522	677	$13^{h}51^{m}32^{s}$	+59°56′16″	13.155
1924	6	816	1575	743	$14^{h}04^{m}37^{s}$	+55°14′11″	13.067
1929	5	-1567	1123	-62	$13^{h}19^{m}40^{s}$	-27°20′51″	12.625
1995	6	519	1852	-529	$10^{h}50^{m}53^{s}$	+33°24′30″	12.161
1996	34	-628	1879	-240	$12^{h}19^{m}37^{s}$	+05°44′18″	13.302
1997	9	-948	386	-1714	$08^{h}45^{m}34^{s}$	-33°57′60″	13.230
1997	6	-1164	1615	-147	$12^{h}48^{m}42^{s}$	-10°07′21″	12.607
2006	12	-955	1412	1056	$15^{h}05^{m}09^{s}$	+01°56′52″	13.233
2006	11	1471	1286	452	$12^{h}20^{m}11^{s}$	+75°29′54″	13.258
2043	5	365	1908	-632	$10^{h}51^{m}12^{s}$	+28°04′49″	12.614
2178	5	-1728	-128	-1319	$09^{h}27^{m}18^{s}$	-60°50′09″	11.376
2189	6	1520	1477	544	$12^{h}46^{m}58^{s}$	+72°49′59″	12.954
2199	30	-1512	1595	14	$13^{h}15^{m}29^{s}$	-16°15′22″	13.612
2253	6	-1825	949	918	$15^{h}19^{m}22^{s}$	-24°02′22″	13.125
2267	9	1378	-1791	-172	$01^{h}24^{m}12^{s}$	+09°28′32″	12.649
2282	17	-1333	875	-1631	$09^{h}57^{m}08^{s}$	-32°11′42″	13.354
2313	15	2009	1049	460	$07^{h}53^{m}59^{s}$	+85°38′00″	13.284
2401	8	-140	1271	-2031	$08^{h}55^{m}15^{s}$	-03°01′01″	12.690
2412	5	-2023	-1014	831	$18^{h}56^{m}10^{s}$	-54°07′17″	12.439
2463	12	-783	-2100	1023	$22^{h}02^{m}60^{s}$	-31°48′39″	12.709
2468	10	-1873	644	-1471	$10^{h}29^{m}30^{s}$	-44°44′13″	12.880
2489	12	2463	351	52	$03^{h}22^{m}54^{s}$	+66°49′23″	13.437
2490	5	-2218	1046	-434	$12^{h}54^{m}09^{s}$	-39°24′02″	12.566
2496	7	2384	-551	-494	$03^{h}04^{m}39^{s}$	+42°26′26″	13.205
2513	7	-1767	-1466	1019	$20^{h}08^{m}23^{s}$	-48°18′43″	12.887
2525	7	370	2202	-1176	$10^{h}17^{m}06^{s}$	+21°59′40″	12.432
2570	12	-1930	1098	-1293	$11^{h}09^{m}56^{s}$	-36°54′08″	13.065
2576	7	1998	-1600	-289	$01^{h}50^{m}12^{s}$	+21°49′47″	12.723
2596	9	1456	2147	75	$11^{h}23^{m}09^{s}$	+57°48′05″	13.535
2602	10	-2529	602	-96	$13^{h}55^{m}09^{s}$	-48°28′40″	12.909
2608	8	-1348	1188	-1889	$09^{h}57^{m}01^{s}$	-26°31′12″	12.597
2678	6	-1888	-1898	74	$22^{h}09^{m}11^{s}$	-64°41′13″	12.757
2706	5	-2557	-672	575	$17^{h}22^{m}24^{s}$	-59°42′55″	12.908
2731	10	-522	2664	-290	$12^{h}13^{m}57^{s}$	+12°59′33″	13.274
2735	12	-2533	963	-368	$13^{h}11^{m}25^{s}$	-43°08′05″	13.350
2795	6	908	2300	1301	$14^{h}33^{m}04^{s}$	+49°22′47″	12.620
2827	6	1566	-1932	-1343	$02^{h}57^{m}43^{s}$	+03°11′41″	12.603
2831	5	-2365	585	-1442	$10^{h}57^{m}48^{s}$	-50°16′25″	11.646
2832	18	530	2594	1004	$13^{h}51^{m}34^{s}$	+40°33′25″	13.147
2854	6	-2076	-1946	212	$21^{h}38^{m}48^{s}$	-64°04′33″	12.319
2856	5	-2069	1968	-58	$13^{h}12^{m}44^{s}$	-19°32′60″	12.266
2861	43	-1930	1144	-1775	$10^{h}30^{m}13^{s}$	-35°17′47″	13.924
2866	9	-2475	1228	-764	$12^{h}25^{m}39^{s}$	-39°14′26″	12.936
2916	5	2356	446	1658	$21^{h}10^{m}08^{s}$	+66°22′07″	12.767
2922	6	-2782	811	-376	$13^{h}19^{m}54^{s}$	-47°25′28″	12.652
2929	7	-2366	-166	-1719	$09^{h}36^{m}52^{s}$	-61°33′44″	12.884

Continued on next page...

Table B.2 – Continued

Distance^a	$N_m{}^b$	SGX^a	SGY^a	SGZ^a	α	δ	$\log\left(\frac{M}{M_\odot}\right)$
2934	7	-2250	1875	-170	$13^h08^m16^s$	-23°44′50″	12.665
2953	5	-2213	-1930	315	$21^h13^m45^s$	-63°46′40″	12.581
2970	12	-2484	-1358	898	$19^h10^m22^s$	-56°37′13″	13.090
2994	5	-1745	2301	788	$14^h05^m42^s$	-05°49′17″	12.765
3068	5	-1988	2333	131	$13^h20^m05^s$	-12°45′31″	11.924
3074	20	-2536	1707	-320	$13^h03^m38^s$	-30°04′40″	13.442
3118	6	-2834	-1291	133	$18^h30^m03^s$	-71°44′09″	12.949
3124	12	1350	-2493	1311	$23^h20^m45^s$	+08°16′09″	13.288
3125	5	1852	2437	625	$12^h31^m18^s$	+64°06′29″	12.642
3165	14	-2246	1037	-1973	$10^h24^m58^s$	-39°47′40″	12.865
3192	6	-1962	1174	-2227	$10^h02^m05^s$	-34°06′57″	12.533
3265	6	1521	-1387	-2534	$04^h30^m56^s$	+00°31′60″	12.595
3270	10	-2218	-884	-2234	$07^h24^m40^s$	-62°19′39″	12.257
3281	5	2159	61	2470	$20^h39^m38^s$	+51°10′17″	11.816
3386	5	-2389	1356	-1979	$10^h42^m20^s$	-36°29′41″	12.880
3485	5	192	2542	-2377	$09^h33^m39^s$	+10°06′57″	12.372
3500	15	-2732	2135	-476	$12^h51^m05^s$	-26°37′37″	13.130
3506	16	1780	-1582	-2573	$04^h18^m34^s$	+02°36′03″	13.428
3516	5	-3009	-1804	232	$19^h47^m52^s$	-70°00′15″	13.069
3520	6	-1974	2914	-33	$13^h01^m16^s$	-07°31′35″	12.883
3525	5	-2689	1857	1319	$14^h57^m49^s$	-19°17′21″	12.978
3558	5	518	3514	-208	$11^h57^m18^s$	+32°13′02″	11.663
3577	5	-349	3476	-770	$11^h42^m08^s$	+15°54′48″	11.924
3616	6	1301	-1344	-3094	$04^h56^m22^s$	-04°38′15″	12.138
3644	5	479	3345	1362	$13^h58^m34^s$	+37°27′35″	13.276
3653	5	-3565	503	-616	$13^h18^m31^s$	-55°52′14″	11.339
3657	10	-1812	2057	-2420	$10^h19^m21^s$	-21°25′14″	12.966
3664	10	3489	-1004	-499	$02^h39^m39^s$	+41°46′04″	12.857
3670	5	1535	2702	1952	$15^h12^m01^s$	+55°06′36″	12.790
3676	103	-3295	1446	-752	$12^h46^m42^s$	-41°14′07″	14.600
3686	7	-239	3591	-794	$11^h39^m17^s$	+17°40′20″	12.326
3696	5	0	-1937	3147	$20^h47^m01^s$	+00°20′12″	11.668
3709	5	1258	-3237	-1302	$02^h09^m41^s$	-10°11′03″	11.826
3712	14	-3136	-1775	890	$19^h19^m03^s$	-60°15′42″	13.546
3736	5	2872	-662	-2296	$04^h40^m57^s$	+24°50′12″	12.180
3751	5	3459	-1413	-324	$02^h12^m03^s$	+37°34′30″	12.605
3773	9	1639	-2259	-2539	$03^h47^m05^s$	-03°42′06″	13.075
3774	8	2905	-2196	-992	$02^h27^m40^s$	+20°02′18″	13.016
3778	7	3120	2130	51	$08^h47^m58^s$	+73°10′41″	12.952
3800	5	-2570	-2764	-434	$23^h26^m51^s$	-67°48′60″	12.808
3802	5	1197	-2917	-2124	$03^h03^m57^s$	-12°03′43″	12.799
3819	5	2161	3126	370	$11^h48^m56^s$	+59°53′41″	12.894
3850	8	-3222	-2103	156	$20^h17^m48^s$	-70°47′22″	13.337
3866	18	-3395	1849	-26	$13^h36^m10^s$	-33°37′02″	13.094
3867	5	-3494	-1484	737	$18^h25^m12^s$	-63°04′59″	12.883
3913	5	1633	-2561	-2467	$03^h31^m46^s$	-05°15′33″	12.573
3916	8	3494	-1594	-762	$02^h34^m50^s$	+32°48′34″	12.894
3967	6	-3906	632	-283	$13^h53^m05^s$	-53°05′17″	13.053

Continued on next page...

Table B.2 – Continued

Distance^a	$N_{\rm m}{}^b$	SGX^a	SGY^a	SGZ^a	α	δ	$\log\left(\frac{M}{M_\odot}\right)$
3992	7	3377	2130	32	$08^{\rm h}19^{\rm m}22^{\rm s}$	+73°43′07″	12.701
4010	79	-2416	2060	-2449	$10^{\rm h}36^{\rm m}19^{\rm s}$	-27°39′48″	14.173
4061	5	1856	-3578	494	$00^{\rm h}29^{\rm m}05^{\rm s}$	+02°48′48″	12.233
4065	9	3728	-1008	-1270	$03^{\rm h}27^{\rm m}10^{\rm s}$	+36°49′21″	12.785
4083	6	101	2409	-3295	$08^{\rm h}59^{\rm m}48^{\rm s}$	+03°12′04″	12.782
4107	8	3843	1418	-292	$05^{\rm h}44^{\rm m}13^{\rm s}$	+69°16′39″	12.796
4122	9	309	4109	-112	$12^{\rm h}11^{\rm m}37^{\rm s}$	+28°59′55″	12.115
4132	10	-1802	2240	-2967	$09^{\rm h}59^{\rm m}57^{\rm s}$	-19°45′03″	13.115
4137	30	-2360	3391	-212	$12^{\rm h}52^{\rm m}40^{\rm s}$	-08°51′52″	13.832
4147	6	-3052	-1575	-2325	$06^{\rm h}46^{\rm m}05^{\rm s}$	-71°35′51″	12.863
4186	19	1595	-1936	-3351	$04^{\rm h}31^{\rm m}31^{\rm s}$	-04°57′38″	13.715
4194	5	373	3846	1630	$14^{\rm h}03^{\rm m}51^{\rm s}$	+35°06′58″	12.878
4215	8	3855	1615	-543	$06^{\rm h}17^{\rm m}51^{\rm s}$	+66°35′19″	12.808
4237	11	2971	-1189	2777	$22^{\rm h}09^{\rm m}53^{\rm s}$	+41°24′28″	12.896
4248	5	-3973	1433	-457	$13^{\rm h}21^{\rm m}10^{\rm s}$	-43°39′53″	12.882
4298	13	3827	-1693	-977	$02^{\rm h}44^{\rm m}21^{\rm s}$	+32°28′31″	13.485
4307	46	-3820	-1804	834	$18^{\rm h}44^{\rm m}53^{\rm s}$	-63°05′20″	13.888
4309	5	1753	2418	-3106	$08^{\rm h}16^{\rm m}55^{\rm s}$	+23°19′59″	12.588
4327	11	-3636	2344	-92	$13^{\rm h}26^{\rm m}16^{\rm s}$	-29°50′45″	13.074
4337	7	461	3756	2117	$14^{\rm h}35^{\rm m}03^{\rm s}$	+36°32′17″	12.984
4338	5	1221	2807	-3073	$08^{\rm h}49^{\rm m}56^{\rm s}$	+19°09′48″	12.695
4340	39	-3874	1925	341	$14^{\rm h}01^{\rm m}51^{\rm s}$	-33°54′56″	13.805
4342	6	1215	-1914	-3703	$04^{\rm h}47^{\rm m}35^{\rm s}$	-10°17′34″	12.584
4357	5	4041	-1050	-1246	$03^{\rm h}22^{\rm m}21^{\rm s}$	+38°12′41″	12.189
4376	14	1694	-1659	-3677	$04^{\rm h}51^{\rm m}35^{\rm s}$	-03°14′04″	13.179
4390	5	-4140	-1233	781	$17^{\rm h}30^{\rm m}04^{\rm s}$	-62°15′57″	13.133
4404	6	1247	-3697	-2042	$02^{\rm h}35^{\rm m}58^{\rm s}$	-13°57′53″	12.657
4409	7	1466	-3705	-1888	$02^{\rm h}29^{\rm m}01^{\rm s}$	-10°55′47″	12.683
4421	5	-1080	-2716	-3316	$04^{\rm h}27^{\rm m}40^{\rm s}$	-42°37′24″	12.612
4424	5	4102	-1139	-1202	$03^{\rm h}16^{\rm m}06^{\rm s}$	+37°57′53″	12.251
4434	6	2195	-3276	2027	$23^{\rm h}15^{\rm m}27^{\rm s}$	+13°31′15″	13.301
4442	5	1574	-3317	-2499	$03^{\rm h}07^{\rm m}11^{\rm s}$	-09°36′52″	12.819
4445	8	534	2112	-3874	$08^{\rm h}22^{\rm m}35^{\rm s}$	+04°05′55″	12.677
4449	5	-2523	2529	-2652	$10^{\rm h}40^{\rm m}51^{\rm s}$	-23°58′33″	12.836
4474	5	4	4314	-1188	$11^{\rm h}21^{\rm m}40^{\rm s}$	+20°01′04″	13.051
4491	59	4072	-1886	-163	$01^{\rm h}53^{\rm m}43^{\rm s}$	+36°15′39″	13.993
4507	5	-2550	-2251	-2956	$05^{\rm h}18^{\rm m}13^{\rm s}$	-61°35′07″	12.895
4511	6	4138	1642	-728	$06^{\rm h}10^{\rm m}40^{\rm s}$	+64°32′55″	13.163
4514	6	3850	-998	-2134	$04^{\rm h}05^{\rm m}50^{\rm s}$	+30°49′23″	13.306
4551	9	-367	4018	2104	$14^{\rm h}28^{\rm m}47^{\rm s}$	+25°44′12″	13.074
4553	5	-4381	-1229	156	$16^{\rm h}47^{\rm m}01^{\rm s}$	-69°21′27″	12.617
4557	7	-3906	2347	67	$13^{\rm h}37^{\rm m}58^{\rm s}$	-30°55′09″	12.752
4558	23	-3499	-2593	1345	$20^{\rm h}04^{\rm m}04^{\rm s}$	-55°38′46″	13.954
4562	5	3838	-1478	1974	$23^{\rm h}32^{\rm m}04^{\rm s}$	+44°41′12″	12.916
4569	15	4144	1864	480	$06^{\rm h}03^{\rm m}03^{\rm s}$	+80°05′05″	13.671
4578	15	4371	1356	139	$04^{\rm h}39^{\rm m}21^{\rm s}$	+73°20′30″	13.509
4589	6	1542	-2044	-3807	$04^{\rm h}40^{\rm m}42^{\rm s}$	-07°14′31″	13.191
4598	9	4417	-440	-1197	$03^{\rm h}45^{\rm m}20^{\rm s}$	+45°45′32″	13.219

Continued on next page...

Table B.2 – Continued

Distance[a]	$N_{\rm m}$[b]	SGX[a]	SGY[a]	SGZ[a]	α	δ	$\log\left(\frac{M}{M_\odot}\right)$
4604	7	3295	-1582	2799	$22^{\rm h}31^{\rm m}31^{\rm s}$	+39°21′03″	13.236
4620	7	-2699	3640	-900	$12^{\rm h}21^{\rm m}48^{\rm s}$	-12°37′25″	12.822
4625	5	-2808	-3293	1632	$21^{\rm h}05^{\rm m}37^{\rm s}$	-47°08′13″	12.744
4630	6	3687	-2410	1426	$00^{\rm h}09^{\rm m}11^{\rm s}$	+33°07′36″	12.805
4657	5	-1606	2409	-3648	$09^{\rm h}35^{\rm m}23^{\rm s}$	-16°42′14″	12.901
4662	9	137	4638	-458	$11^{\rm h}58^{\rm m}16^{\rm s}$	+25°10′16″	12.605
4668	44	4061	-2289	239	$01^{\rm h}23^{\rm m}14^{\rm s}$	+33°36′07″	13.882
4676	5	1554	-3834	-2179	$02^{\rm h}39^{\rm m}02^{\rm s}$	-11°01′55″	12.678
4692	6	3716	-2776	708	$00^{\rm h}48^{\rm m}35^{\rm s}$	+28°00′40″	12.843
4710	12	1977	-1573	-3974	$04^{\rm h}58^{\rm m}40^{\rm s}$	-00°33′30″	13.398
4715	31	4486	-1180	-842	$02^{\rm h}54^{\rm m}35^{\rm s}$	+41°37′37″	14.336
4715	5	-2249	3371	-2410	$11^{\rm h}01^{\rm m}04^{\rm s}$	-14°03′25″	12.843
4718	11	381	1074	4578	$18^{\rm h}12^{\rm m}09^{\rm s}$	+25°28′34″	12.594
4741	5	-4333	-1750	799	$18^{\rm h}14^{\rm m}28^{\rm s}$	-64°12′14″	13.310
4757	5	4149	2166	-847	$07^{\rm h}05^{\rm m}05^{\rm s}$	+64°00′26″	12.283
4758	8	167	454	4733	$18^{\rm h}37^{\rm m}58^{\rm s}$	+19°55′13″	12.759
4758	5	-2491	-3632	1800	$21^{\rm h}25^{\rm m}39^{\rm s}$	-42°32′46″	13.143
4760	7	3315	-1080	-3241	$04^{\rm h}43^{\rm m}50^{\rm s}$	+18°34′53″	12.863
4779	5	1725	2847	-3429	$08^{\rm h}29^{\rm m}42^{\rm s}$	+21°51′16″	13.213
4786	10	3526	-2447	2117	$23^{\rm h}29^{\rm m}13^{\rm s}$	+32°22′37″	13.277
4809	37	-3056	3700	-312	$12^{\rm h}54^{\rm m}43^{\rm s}$	-13°36′41″	14.092
4850	5	1628	-3603	-2808	$03^{\rm h}10^{\rm m}58^{\rm s}$	-10°42′59″	12.625
4862	10	3917	-2804	-653	$02^{\rm h}00^{\rm m}02^{\rm s}$	+24°14′37″	12.770
4871	5	1496	-2093	4136	$21^{\rm h}08^{\rm m}05^{\rm s}$	+18°05′01″	12.237
4879	5	4713	1114	-588	$04^{\rm h}51^{\rm m}36^{\rm s}$	+63°52′52″	13.174
4893	6	1978	-2263	-3861	$04^{\rm h}28^{\rm m}52^{\rm s}$	-03°38′42″	12.951
4896	5	4028	-2714	619	$00^{\rm h}57^{\rm m}54^{\rm s}$	+30°22′23″	12.111
4910	5	1627	2312	-4014	$08^{\rm h}01^{\rm m}03^{\rm s}$	+15°26′31″	12.517
4913	5	4609	1683	247	$05^{\rm h}07^{\rm m}54^{\rm s}$	+75°43′23″	12.868
4915	5	-4798	1058	105	$14^{\rm h}15^{\rm m}58^{\rm s}$	-48°00′45″	12.756
4926	5	-2144	3529	-2686	$10^{\rm h}50^{\rm m}13^{\rm s}$	-12°27′22″	12.831
4935	5	-2052	2292	-3859	$09^{\rm h}36^{\rm m}21^{\rm s}$	-21°46′45″	13.131
4937	11	4642	-681	-1535	$03^{\rm h}48^{\rm m}08^{\rm s}$	+41°50′38″	13.515
4945	39	-4243	2526	265	$13^{\rm h}48^{\rm m}06^{\rm s}$	-30°23′27″	13.833
4956	7	-3070	-3506	1686	$21^{\rm h}04^{\rm m}41^{\rm s}$	-48°09′58″	12.822
4964	132	-4883	-659	603	$16^{\rm h}12^{\rm m}20^{\rm s}$	-60°40′24″	14.611
4969	7	-2817	-3569	2003	$21^{\rm h}05^{\rm m}08^{\rm s}$	-43°25′54″	12.609
4973	9	1563	-2271	-4139	$04^{\rm h}40^{\rm m}07^{\rm s}$	-08°38′06″	13.355
4979	6	1095	-2520	4152	$21^{\rm h}11^{\rm m}54^{\rm s}$	+11°26′21″	12.290
4987	6	3854	-941	-3021	$04^{\rm h}37^{\rm m}10^{\rm s}$	+24°54′22″	12.119
5004	7	-2978	1161	-3849	$09^{\rm h}23^{\rm m}37^{\rm s}$	-38°26′40″	12.704
5006	5	-3363	1638	-3326	$10^{\rm h}10^{\rm m}42^{\rm s}$	-38°12′48″	12.940
5037	6	4906	787	-825	$04^{\rm h}33^{\rm m}14^{\rm s}$	+59°33′45″	13.271
5045	6	2545	4061	-1574	$09^{\rm h}49^{\rm m}40^{\rm s}$	+44°04′09″	11.971
5053	7	-4754	-1711	-52	$17^{\rm h}18^{\rm m}38^{\rm s}$	-73°31′29″	13.120
5055	6	4779	-927	-1361	$03^{\rm h}29^{\rm m}10^{\rm s}$	+41°32′54″	13.015
5073	6	2466	-2386	-3736	$04^{\rm h}16^{\rm m}30^{\rm s}$	+01°01′41″	13.051
5082	7	-1105	-4357	-2371	$02^{\rm h}29^{\rm m}24^{\rm s}$	-42°57′27″	12.831

Continued on next page...

Table B.2 – Continued

Distance^a	$N_m{}^b$	SGX^a	SGY^a	SGZ^a	α	δ	$\log\left(\frac{M}{M_\odot}\right)$
5092	11	2411	-4467	402	$00^h39^m37^s$	+03°03′48″	12.498
5100	9	-2780	-3133	-2909	$04^h07^m38^s$	-62°35′03″	13.414
5106	5	-3667	1710	-3115	$10^h30^m13^s$	-39°49′35″	12.889
5111	6	4232	-2787	-665	$02^h02^m35^s$	+26°23′50″	12.436
5126	6	3866	-1955	2738	$22^h58^m32^s$	+39°08′26″	13.152
5136	8	3449	-3718	-810	$01^h49^m00^s$	+13°02′16″	13.050
5136	39	2320	-4525	-719	$01^h26^m46^s$	-01°30′25″	13.900
5143	5	4659	-1450	1622	$00^h14^m12^s$	+48°11′27″	12.550
5168	7	-1340	3535	-3523	$10^h03^m30^s$	-06°35′36″	12.404
5172	5	-2762	-3856	2062	$21^h16^m50^s$	-42°13′29″	12.919
5187	5	2494	-4292	1503	$23^h53^m36^s$	+07°56′21″	12.677
5190	5	2359	4509	1017	$12^h44^m31^s$	+54°49′49″	12.862
5207	17	1924	2931	-3849	$08^h20^m20^s$	+21°05′21″	13.337
5234	5	-3803	-2611	-2472	$04^h57^m30^s$	-75°29′17″	12.506
5259	8	-1296	1031	-4991	$08^h07^m04^s$	-22°39′46″	13.604
5263	11	84	1038	5159	$18^h13^m06^s$	+21°20′13″	13.328
5284	6	4691	-1565	1858	$00^h00^m52^s$	+47°10′44″	12.872
5286	9	4220	-3021	1004	$00^h39^m39^s$	+29°37′45″	13.312
5288	7	1968	-4904	-196	$00^h58^m16^s$	-04°58′49″	12.846
5303	6	3507	3635	-1615	$08^h58^m03^s$	+51°23′42″	12.856
5336	5	3084	-4183	-1211	$01^h56^m36^s$	+05°45′60″	12.799
5337	6	3570	-572	-3926	$05^h16^m18^s$	+19°21′03″	13.087
5349	5	2896	-2565	-3693	$04^h06^m00^s$	+04°15′13″	12.890
5351	5	-1110	4819	2043	$14^h10^m58^s$	+18°06′05″	13.294
5356	5	-3212	-3130	2926	$20^h11^m12^s$	-38°17′16″	12.821
5361	14	4381	-1804	2507	$23^h20^m03^s$	+43°22′19″	13.322
5361	13	-313	-5232	-1125	$01^h13^m58^s$	-31°42′51″	13.647
5364	42	4572	-2758	508	$01^h09^m34^s$	+32°40′24″	13.961
5379	12	-4547	2799	-649	$13^h02^m03^s$	-32°33′44″	13.256
5382	6	4800	-2433	59	$01^h37^m42^s$	+35°18′13″	12.900
5388	9	-4538	2872	436	$13^h52^m21^s$	-28°23′24″	13.400
5410	5	914	4745	2431	$14^h22^m44^s$	+40°03′26″	13.235
5420	5	-3065	-3200	-3120	$04^h20^m23^s$	-63°42′40″	12.863
5430	7	4756	-2573	-492	$02^h01^m20^s$	+31°48′33″	13.051
5437	10	-4158	-2427	2526	$19^h14^m40^s$	-46°27′09″	13.072
5461	5	2831	2927	3639	$16^h59^m27^s$	+58°59′04″	13.055
5463	6	39	-1796	5159	$20^h04^m49^s$	+06°56′36″	12.821
5467	6	3069	2931	-3447	$07^h58^m34^s$	+32°53′19″	12.656
5477	7	2505	-4853	-408	$01^h12^m26^s$	-00°20′05″	12.817
5507	31	3697	-2102	3499	$22^h24^m18^s$	+35°56′34″	14.325
5514	9	-3632	-3294	2522	$20^h14^m06^s$	-44°25′52″	13.273
5518	5	5206	1757	-498	$05^h31^m28^s$	+67°43′24″	13.148
5521	6	-588	-5305	-1410	$01^h24^m13^s$	-34°57′31″	12.971
5532	18	-3073	-2933	3543	$19^h57^m19^s$	-32°11′34″	13.255
5552	5	2268	-4675	1952	$23^h34^m55^s$	+04°57′01″	11.892
5552	7	-2177	-3501	3718	$20^h37^m12^s$	-25°16′47″	12.722
5557	6	3222	-2678	-3651	$03^h59^m08^s$	+06°36′51″	12.947
5580	11	-5044	-2370	-271	$18^h32^m19^s$	-77°00′55″	13.131

Continued on next page...

Table B.2 – Continued

Distance^a	$N_{\rm m}{}^b$	SGX^a	SGY^a	SGZ^a	α	δ	$\log\left(\frac{M}{M_\odot}\right)$
5590	11	-3841	1674	-3699	$10^{\rm h}09^{\rm m}20^{\rm s}$	-40°00′58″	13.273
5595	7	3350	-167	-4478	$05^{\rm h}43^{\rm m}40^{\rm s}$	+16°39′10″	13.359
5596	5	703	5354	1467	$13^{\rm h}25^{\rm m}22^{\rm s}$	+36°07′39″	13.005
5597	5	3846	-602	-4022	$05^{\rm h}13^{\rm m}10^{\rm s}$	+20°34′48″	12.905
5614	21	5334	-1664	-543	$02^{\rm h}25^{\rm m}45^{\rm s}$	+41°43′39″	13.683
5628	5	4017	-1034	3804	$21^{\rm h}50^{\rm m}58^{\rm s}$	+45°59′50″	12.223
5639	5	-219	-3285	4578	$20^{\rm h}56^{\rm m}24^{\rm s}$	-03°38′21″	12.848
5644	14	3960	-3800	1316	$00^{\rm h}21^{\rm m}19^{\rm s}$	+22°16′60″	13.076
5649	7	4094	-1256	3684	$22^{\rm h}04^{\rm m}52^{\rm s}$	+44°54′03″	12.655
5661	5	-4147	-3385	1841	$20^{\rm h}16^{\rm m}31^{\rm s}$	-53°05′60″	12.495
5664	7	-1806	2307	-4847	$09^{\rm h}05^{\rm m}00^{\rm s}$	-19°22′46″	12.963
5675	7	-3011	-2671	4000	$19^{\rm h}43^{\rm m}23^{\rm s}$	-27°55′32″	12.912
5679	5	1250	4257	3545	$15^{\rm h}29^{\rm m}19^{\rm s}$	+42°51′28″	13.017
5699	6	-921	-5415	-1517	$01^{\rm h}25^{\rm m}01^{\rm s}$	-38°14′09″	12.707
5719	8	4840	-1311	-2749	$04^{\rm h}05^{\rm m}53^{\rm s}$	+30°04′11″	13.500
5730	5	4420	2449	-2701	$07^{\rm h}07^{\rm m}56^{\rm s}$	+46°05′49″	13.035
5733	120	5438	-1190	-1371	$03^{\rm h}17^{\rm m}19^{\rm s}$	+41°35′07″	14.718
5745	8	-407	-2822	4988	$20^{\rm h}31^{\rm m}27^{\rm s}$	-02°05′46″	13.327
5751	7	2491	-3821	-3503	$03^{\rm h}26^{\rm m}14^{\rm s}$	-04°22′51″	12.993
5759	6	-2719	5067	309	$13^{\rm h}08^{\rm m}47^{\rm s}$	-00°52′04″	12.849
5771	10	5214	2472	14	$06^{\rm h}38^{\rm m}56^{\rm s}$	+74°24′01″	13.194
5776	5	-5617	-813	1068	$16^{\rm h}33^{\rm m}05^{\rm s}$	-58°03′12″	12.932
5778	6	1093	4924	2817	$14^{\rm h}36^{\rm m}11^{\rm s}$	+41°20′51″	13.243
5794	5	1142	-5588	-1022	$01^{\rm h}19^{\rm m}20^{\rm s}$	-16°56′21″	12.381
5828	7	2033	-5450	-349	$01^{\rm h}01^{\rm m}49^{\rm s}$	-06°41′22″	12.953
5839	5	-5731	616	-932	$13^{\rm h}25^{\rm m}39^{\rm s}$	-57°33′03″	12.342
5846	12	-4401	3839	242	$13^{\rm h}30^{\rm m}17^{\rm s}$	-20°51′44″	12.950
5852	15	-3635	-3268	3218	$20^{\rm h}01^{\rm m}34^{\rm s}$	-38°44′54″	13.709
5861	5	-4527	-1962	3163	$18^{\rm h}41^{\rm m}27^{\rm s}$	-41°32′18″	12.109
5865	6	2217	-5413	424	$00^{\rm h}34^{\rm m}30^{\rm s}$	-02°53′09″	13.200
5873	10	-4931	1186	-2961	$10^{\rm h}59^{\rm m}28^{\rm s}$	-50°40′19″	12.995
5884	7	-4179	-3636	1983	$20^{\rm h}25^{\rm m}10^{\rm s}$	-51°47′55″	12.847
5908	5	1754	-5642	-2	$00^{\rm h}45^{\rm m}06^{\rm s}$	-08°50′35″	12.571
5911	5	-1346	-5446	-1861	$01^{\rm h}37^{\rm m}50^{\rm s}$	-42°35′08″	12.539
5914	6	-2620	5031	-1673	$11^{\rm h}52^{\rm m}39^{\rm s}$	-05°22′59″	12.616
5914	5	-3257	1870	4568	$16^{\rm h}46^{\rm m}11^{\rm s}$	-07°27′43″	12.863
5919	5	4117	-3256	2734	$23^{\rm h}22^{\rm m}35^{\rm s}$	+29°15′26″	12.852
5925	9	3259	3321	3667	$16^{\rm h}42^{\rm m}51^{\rm s}$	+61°53′44″	13.067
5927	16	4669	2604	-2558	$07^{\rm h}09^{\rm m}45^{\rm s}$	+48°37′59″	13.463
5938	9	912	5404	2285	$14^{\rm h}01^{\rm m}41^{\rm s}$	+38°49′20″	13.084
5946	6	1396	4345	3811	$15^{\rm h}37^{\rm m}37^{\rm s}$	+43°34′34″	12.989
5971	5	-5818	-1057	832	$16^{\rm h}34^{\rm m}35^{\rm s}$	-61°23′19″	12.782
6004	5	-3744	-2993	3614	$19^{\rm h}43^{\rm m}09^{\rm s}$	-36°02′14″	12.982
6039	13	-2126	5312	1931	$14^{\rm h}02^{\rm m}40^{\rm s}$	+09°13′26″	13.287
6047	8	3816	-4075	-2322	$02^{\rm h}41^{\rm m}07^{\rm s}$	+08°41′15″	12.977
6059	17	4061	-2105	3973	$22^{\rm h}15^{\rm m}12^{\rm s}$	+37°18′60″	13.497
6070	11	-5906	713	-1206	$13^{\rm h}07^{\rm m}55^{\rm s}$	-57°20′59″	13.434
6100	5	4692	2940	-2558	$07^{\rm h}26^{\rm m}16^{\rm s}$	+49°07′06″	12.643

Continued on next page...

Table B.2 – Continued

Distance^a	$N_m{}^b$	SGX^a	SGY^a	SGZ^a	α	δ	$\log\left(\frac{M}{M_\odot}\right)$
6105	7	1959	4145	4031	$15^h57^m42^s$	+48°17′08″	12.390
6140	5	-921	2126	-5686	$08^h26^m11^s$	-13°23′19″	12.236
6144	6	-5078	3402	618	$13^h54^m45^s$	-26°35′43″	12.679
6171	8	4910	3405	-1538	$07^h57^m31^s$	+58°45′27″	13.175
6192	5	2864	-4116	-3632	$03^h21^m43^s$	-02°35′42″	13.246
6193	5	3101	-4544	-2843	$02^h48^m25^s$	-00°25′23″	12.389
6220	5	-4707	-2436	-3255	$06^h43^m33^s$	-74°07′56″	12.496
6248	27	5548	-705	-2785	$04^h22^m09^s$	+36°35′51″	13.633
6262	10	3258	-4749	-2457	$02^h32^m28^s$	+00°58′15″	13.494
6265	15	-1884	-5791	-1471	$01^h08^m46^s$	-45°59′10″	14.268
6273	5	5012	-3487	1437	$00^h29^m53^s$	+30°49′25″	12.986
6276	5	5679	-1080	-2441	$03^h58^m12^s$	+36°55′54″	12.557
6302	11	5983	-1680	-1046	$02^h48^m39^s$	+41°13′17″	13.497
6308	11	-1330	4192	-4521	$09^h50^m08^s$	-05°12′45″	13.482
6322	11	-2241	5773	-1272	$12^h04^m40^s$	+01°48′14″	13.379
6334	5	-3624	-4041	3264	$20^h30^m53^s$	-38°50′28″	12.321
6361	22	-3018	5077	-2361	$11^h34^m41^s$	-09°37′28″	14.000
6398	6	4337	1176	-4554	$06^h19^m12^s$	+28°03′47″	13.052
6404	8	-1200	6094	-1560	$11^h43^m01^s$	+10°23′48″	12.986
6405	8	4996	2539	-3101	$06^h57^m27^s$	+45°19′48″	13.290
6415	55	-233	6304	-1163	$11^h44^m38^s$	+19°56′07″	14.212
6437	10	4937	-2090	-3563	$04^h03^m16^s$	+21°50′11″	13.120
6442	6	-1930	-5788	-2067	$01^h38^m11^s$	-46°55′26″	12.937
6448	23	5156	2858	-2611	$07^h09^m40^s$	+50°19′09″	13.583
6469	11	4402	-2068	4264	$22^h11^m56^s$	+38°53′37″	13.725
6490	5	6204	-1824	-543	$02^h24^m23^s$	+42°54′25″	12.834
6537	14	33	6502	674	$12^h49^m23^s$	+27°18′46″	13.559
6554	7	-1309	4643	-4436	$10^h00^m38^s$	-02°57′44″	13.389
6574	9	1035	6104	-2213	$10^h47^m20^s$	+26°16′26″	12.876
6575	5	2718	5931	-818	$11^h03^m45^s$	+45°11′06″	13.226
6591	12	-5511	3488	948	$14^h07^m36^s$	-27°03′04″	13.676
6603	8	5212	3348	2287	$15^h28^m16^s$	+82°30′05″	13.116
6604	6	-92	6598	-276	$12^h15^m22^s$	+23°53′23″	12.893
6605	7	2133	-5993	1775	$23^h47^m34^s$	-02°10′15″	13.087
6608	11	4464	-2813	3977	$22^h37^m27^s$	+34°14′26″	13.242
6620	7	411	5005	-4312	$09^h41^m06^s$	+11°37′24″	13.445
6625	7	814	1894	6296	$18^h01^m46^s$	+29°04′03″	13.237
6637	13	-1974	2087	5983	$17^h16^m24^s$	+07°02′27″	13.127
6646	5	-1228	6205	-2038	$11^h28^m43^s$	+09°05′25″	11.605
6652	8	6407	-1548	894	$01^h22^m12^s$	+50°03′52″	13.507
6658	13	4533	-3163	3711	$22^h53^m06^s$	+32°16′42″	13.028
6687	7	-107	-5638	-3595	$02^h50^m26^s$	-31°23′47″	12.685
6708	5	-4321	5107	490	$13^h26^m42^s$	-12°03′34″	12.637
6712	15	-5276	1687	-3790	$10^h40^m16^s$	-46°16′22″	13.509
6723	7	-1766	-1442	-6325	$06^h33^m59^s$	-34°58′10″	13.112
6724	5	-1921	1693	6218	$17^h31^m52^s$	+06°26′09″	12.599
6786	10	6096	-965	-2821	$04^h09^m52^s$	+36°54′58″	13.546
6793	5	-4256	-4373	2983	$20^h33^m01^s$	-44°12′16″	13.254

Continued on next page...

Table B.2 – Continued

Distance^a	$N_m{}^b$	SGX^a	SGY^a	SGZ^a	α	δ	$\log\left(\frac{M}{M_\odot}\right)$
6803	5	6527	-1793	-677	$02^h31^m23^s$	+43°23′37″	12.881
6810	7	3661	-5025	-2777	$02^h37^m58^s$	+02°05′56″	13.297
6837	9	5161	4438	634	$10^h34^m43^s$	+72°34′59″	13.330
6845	9	5027	-3964	2420	$23^h53^m36^s$	+28°43′02″	12.937
6846	6	-2362	6035	2206	$14^h02^m51^s$	+09°39′53″	12.994
6872	17	2888	5221	-3410	$09^h20^m12^s$	+33°36′59″	13.858
6876	14	4689	-3776	3321	$23^h16^m13^s$	+28°53′24″	13.601
6889	6	-3692	-4678	3456	$20^h46^m59^s$	-38°06′54″	12.985
6894	5	80	6838	-875	$11^h53^m02^s$	+23°38′13″	13.371
6932	17	5381	-3945	1877	$00^h17^m33^s$	+29°53′35″	13.879
6943	6	3423	-5079	-3269	$02^h50^m59^s$	-00°55′53″	12.678
6944	11	-2207	-6383	-1611	$01^h06^m57^s$	-46°58′10″	13.496
6945	16	-2052	6494	1359	$13^h29^m37^s$	+11°29′23″	13.608
6947	5	-1258	4448	-5185	$09^h39^m06^s$	-04°47′55″	12.399
6948	7	-4179	5478	896	$13^h35^m45^s$	-08°21′53″	13.483
6967	5	-154	6809	-1464	$11^h36^m42^s$	+20°03′41″	12.861
6989	10	117	6976	-410	$12^h08^m50^s$	+25°15′02″	13.188
7014	14	-5902	3563	1291	$14^h19^m21^s$	-27°13′42″	13.522
7027	5	2909	5681	-2939	$09^h42^m44^s$	+36°10′29″	13.057
7041	36	4189	-4656	-3216	$02^h56^m53^s$	+06°03′36″	14.121
7045	13	2804	6070	-2219	$10^h13^m52^s$	+38°50′40″	13.610
7062	5	6555	-1282	-2292	$03^h42^m20^s$	+39°21′50″	12.862
7063	5	-3997	5820	211	$13^h10^m26^s$	-07°15′33″	12.477
7068	5	2716	5243	-3885	$09^h13^m51^s$	+30°02′04″	12.845
7074	5	-1878	-6561	-1861	$01^h19^m43^s$	-44°15′11″	13.364
7081	5	6768	-2007	-555	$02^h22^m35^s$	+42°55′08″	12.747
7101	18	-4987	5051	208	$13^h22^m05^s$	-16°59′52″	13.538
7109	5	5217	4726	989	$11^h15^m44^s$	+72°48′03″	13.238
7118	7	6936	967	1274	$01^h52^m40^s$	+71°11′20″	12.758
7138	17	-243	7054	-1060	$11^h52^m00^s$	+20°44′36″	13.554
7146	5	-3267	5720	-2771	$11^h29^m45^s$	-08°57′53″	12.944
7152	7	-5335	4729	-560	$13^h01^m23^s$	-22°22′23″	13.524
7158	6	-3457	979	6190	$17^h35^m27^s$	-07°05′17″	13.047
7162	8	-2601	6177	2523	$14^h11^m23^s$	+08°45′09″	13.206
7201	8	-2971	6388	1490	$13^h39^m31^s$	+04°38′11″	12.800
7220	5	-4532	-5099	2363	$21^h05^m16^s$	-49°02′29″	12.909
7230	5	-1248	4545	-5482	$09^h34^m48^s$	-04°51′13″	12.509
7258	8	7037	-1748	320	$01^h51^m42^s$	+48°06′04″	13.387
7285	5	-2093	-2910	6342	$19^h49^m04^s$	-10°33′37″	12.309
7301	5	6807	-736	-2533	$04^h04^m13^s$	+41°47′25″	12.673
7311	5	-4234	-3126	5074	$19^h28^m03^s$	-29°38′26″	12.313
7311	7	1948	-6082	-3559	$02^h41^m31^s$	-15°00′00″	13.095
7314	8	-5760	453	4484	$17^h04^m12^s$	-29°05′31″	13.414
7322	6	-3122	5902	-3004	$11^h22^m38^s$	-07°38′20″	12.951
7325	9	3107	-5306	3981	$22^h50^m07^s$	+11°39′55″	13.751
7348	5	78	7347	-92	$12^h20^m28^s$	+25°45′19″	13.195
7353	98	48	7277	1054	$12^h59^m28^s$	+27°57′26″	14.639
7399	7	3629	5424	-3487	$09^h09^m06^s$	+37°32′55″	13.159

Continued on next page...

Table B.2 – Continued

Distance^{a}	$N_{\mathrm{m}}{}^{b}$	SGX^{a}	SGY^{a}	SGZ^{a}	α	δ	$\log\left(\frac{M}{M_{\odot}}\right)$
7401	5	-6818	2523	1385	$14^{h}42^{m}27^{s}$	-36°40′05″	12.994
7435	5	-2438	6862	1499	$13^{h}32^{m}56^{s}$	+09°39′19″	13.348
7454	8	-5605	4907	244	$13^{h}28^{m}06^{s}$	-20°54′47″	12.944
7476	5	-5264	4005	3483	$15^{h}14^{m}52^{s}$	-14°32′18″	12.332
7487	7	573	7140	2179	$13^{h}35^{m}34^{s}$	+33°37′23″	13.439
7490	12	-2414	-4363	5590	$20^{h}29^{m}15^{s}$	-18°59′35″	13.829
7499	6	4673	-4240	4051	$22^{h}58^{m}26^{s}$	+26°09′54″	13.448
7503	5	-4475	5855	1407	$13^{h}48^{m}54^{s}$	-07°23′42″	13.484
7509	5	-6969	1179	2535	$15^{h}50^{m}11^{s}$	-39°52′37″	12.340
7520	5	2029	-6609	2958	$23^{h}15^{m}47^{s}$	-02°09′54″	13.146
7536	7	4543	4161	4339	$16^{h}41^{m}08^{s}$	+65°49′39″	13.093
7549	5	7385	-1339	-805	$02^{h}47^{m}43^{s}$	+47°34′49″	11.825
7551	12	5349	-4461	2917	$23^{h}43^{m}45^{s}$	+27°30′19″	13.551
7568	13	4487	766	6046	$19^{h}58^{m}11^{s}$	+50°25′03″	13.010
7591	5	-3173	-6690	-1669	$00^{h}56^{m}34^{s}$	-52°55′19″	13.457
7599	5	-7048	2284	1687	$14^{h}57^{m}09^{s}$	-37°37′14″	13.429
7604	6	2932	-4837	5082	$22^{h}14^{m}12^{s}$	+13°54′58″	13.175
7624	28	-429	7571	-787	$12^{h}04^{m}20^{s}$	+20°26′33″	13.857
7627	9	-2964	6420	2857	$14^{h}18^{m}30^{s}$	+07°19′01″	13.481
7647	5	3091	-2256	-6620	$05^{h}09^{m}30^{s}$	-00°42′50″	13.096
7672	22	-4999	-3011	-4979	$06^{h}21^{m}49^{s}$	-64°55′02″	14.023
7681	8	4582	4951	-3673	$08^{h}33^{m}06^{s}$	+41°22′35″	13.221
7726	5	-4156	6202	1989	$14^{h}00^{m}29^{s}$	-02°51′13″	12.878
7731	5	-2541	6669	2972	$14^{h}17^{m}29^{s}$	+10°59′26″	13.384
7754	7	4996	-4330	4050	$23^{h}04^{m}02^{s}$	+27°12′57″	12.552
7775	7	-4178	-6213	-2096	$01^{h}10^{m}50^{s}$	-61°29′48″	12.898
7782	6	979	-5849	5040	$22^{h}02^{m}23^{s}$	-02°12′08″	12.526
7816	6	5441	-5284	-1885	$02^{h}11^{m}58^{s}$	+14°10′13″	12.784
7821	7	3325	7033	-799	$11^{h}08^{m}08^{s}$	+46°24′59″	12.395
7822	5	3504	6816	-1567	$10^{h}35^{m}00^{s}$	+44°51′50″	12.768
7835	9	5004	-4978	-3400	$02^{h}55^{m}41^{s}$	+09°14′26″	13.617
7844	7	-4014	5610	-3732	$11^{h}11^{m}43^{s}$	-15°15′39″	13.236
7859	9	5188	3681	4616	$17^{h}35^{m}59^{s}$	+68°14′30″	13.264
7873	6	1086	-3247	7089	$20^{h}39^{m}02^{s}$	+10°42′52″	13.532
7875	6	4600	941	6322	$19^{h}50^{m}49^{s}$	+50°32′29″	12.955
7898	5	-2809	6676	-3149	$11^{h}20^{m}40^{s}$	-02°59′19″	13.029
7975	10	-5129	1884	5809	$16^{h}50^{m}59^{s}$	-14°49′18″	13.251
7982	5	2235	3974	6551	$17^{h}11^{m}34^{s}$	+42°37′01″	12.766
8014	13	776	7636	2303	$13^{h}33^{m}46^{s}$	+34°44′34″	13.361
8040	13	-3653	6208	3571	$14^{h}40^{m}48^{s}$	+03°25′26″	13.651
8046	7	-6225	1082	4981	$16^{h}50^{m}07^{s}$	-26°12′04″	12.901
8055	18	-1476	-5341	5846	$21^{h}02^{m}33^{s}$	-14°13′43″	13.719
8065	6	-4935	3804	5121	$15^{h}56^{m}18^{s}$	-08°48′56″	12.865
8068	7	-2101	7223	2916	$14^{h}08^{m}08^{s}$	+14°54′37″	13.176
8081	5	-3463	6174	-3898	$11^{h}05^{m}36^{s}$	-09°55′18″	12.197
8081	18	6241	4719	-2020	$08^{h}13^{m}59^{s}$	+58°01′58″	13.550
8085	5	2813	-5062	5641	$22^{h}03^{m}47^{s}$	+12°43′54″	13.240
8086	16	-732	-8000	922	$23^{h}48^{m}50^{s}$	-28°07′34″	13.660

Continued on next page...

Table B.2 – Continued

Distance^a	$N_{\mathrm{m}}{}^b$	SGX^a	SGY^a	SGZ^a	α	δ	$\log\left(\frac{M}{M_\odot}\right)$
8110	6	4998	6341	-764	$10^{\mathrm{h}}22^{\mathrm{m}}21^{\mathrm{s}}$	+57°13′56″	12.805
8116	6	724	7845	-1949	$11^{\mathrm{h}}18^{\mathrm{m}}36^{\mathrm{s}}$	+25°14′22″	13.304
8121	5	-4951	3102	5640	$16^{\mathrm{h}}20^{\mathrm{m}}52^{\mathrm{s}}$	-09°59′43″	12.785
8129	5	-6308	4387	-2652	$12^{\mathrm{h}}03^{\mathrm{m}}04^{\mathrm{s}}$	-31°42′60″	12.905
8136	5	2612	6360	4348	$15^{\mathrm{h}}01^{\mathrm{m}}21^{\mathrm{s}}$	+49°10′26″	12.941
8137	5	4121	-1341	6887	$20^{\mathrm{h}}45^{\mathrm{m}}41^{\mathrm{s}}$	+36°30′49″	12.975
8138	7	5206	-4862	3935	$23^{\mathrm{h}}14^{\mathrm{m}}58^{\mathrm{s}}$	+25°13′12″	12.686
8154	6	2567	1917	7498	$18^{\mathrm{h}}34^{\mathrm{m}}27^{\mathrm{s}}$	+38°24′04″	13.262
8159	5	4488	-1721	6592	$21^{\mathrm{h}}06^{\mathrm{m}}46^{\mathrm{s}}$	+37°02′40″	12.746
8180	7	4923	3305	5635	$18^{\mathrm{h}}09^{\mathrm{m}}47^{\mathrm{s}}$	+61°27′32″	12.953
8194	7	-2608	-5114	5846	$20^{\mathrm{h}}40^{\mathrm{m}}42^{\mathrm{s}}$	-20°25′03″	12.607
8231	6	-3415	1970	7225	$17^{\mathrm{h}}20^{\mathrm{m}}54^{\mathrm{s}}$	-00°59′29″	13.045
8248	8	6224	-4844	2414	$00^{\mathrm{h}}10^{\mathrm{m}}27^{\mathrm{s}}$	+28°32′35″	13.332
8249	6	5904	-4944	2955	$23^{\mathrm{h}}51^{\mathrm{m}}25^{\mathrm{s}}$	+27°11′10″	12.784
8253	5	-1473	8084	-765	$12^{\mathrm{h}}16^{\mathrm{m}}04^{\mathrm{s}}$	+13°56′47″	12.855
8337	5	3697	-2139	-7160	$05^{\mathrm{h}}13^{\mathrm{m}}46^{\mathrm{s}}$	+02°16′28″	13.012
8353	7	-962	-5484	6227	$21^{\mathrm{h}}07^{\mathrm{m}}12^{\mathrm{s}}$	-10°18′38″	13.458
8357	5	-5487	1782	6046	$16^{\mathrm{h}}54^{\mathrm{m}}08^{\mathrm{s}}$	-16°10′24″	11.550
8369	10	-2160	-7825	2033	$22^{\mathrm{h}}56^{\mathrm{m}}51^{\mathrm{s}}$	-33°53′33″	13.256
8403	5	3649	3252	-6835	$07^{\mathrm{h}}32^{\mathrm{m}}12^{\mathrm{s}}$	+18°39′59″	13.247
8412	5	5443	-5757	-2827	$02^{\mathrm{h}}30^{\mathrm{m}}20^{\mathrm{s}}$	+09°58′23″	12.976
8430	10	-6059	740	5814	$17^{\mathrm{h}}12^{\mathrm{m}}06^{\mathrm{s}}$	-23°16′13″	13.731
8469	16	8271	-1521	-1005	$02^{\mathrm{h}}50^{\mathrm{m}}44^{\mathrm{s}}$	+47°05′56″	14.079
8488	8	2554	4151	6949	$17^{\mathrm{h}}15^{\mathrm{m}}37^{\mathrm{s}}$	+43°41′22″	13.739
8496	8	1725	6090	-5667	$09^{\mathrm{h}}16^{\mathrm{m}}20^{\mathrm{s}}$	+17°33′43″	13.264
8498	5	3514	-6200	-4629	$03^{\mathrm{h}}05^{\mathrm{m}}37^{\mathrm{s}}$	-05°57′57″	13.341
8500	5	3395	6724	-3939	$09^{\mathrm{h}}33^{\mathrm{m}}55^{\mathrm{s}}$	+33°54′56″	12.987
8503	6	5116	3713	5686	$17^{\mathrm{h}}53^{\mathrm{m}}16^{\mathrm{s}}$	+62°29′34″	13.509
8513	9	470	8500	7	$12^{\mathrm{h}}20^{\mathrm{m}}15^{\mathrm{s}}$	+28°25′26″	13.539
8521	7	-2769	7193	3634	$14^{\mathrm{h}}28^{\mathrm{m}}09^{\mathrm{s}}$	+11°22′49″	13.353
8534	5	4691	4117	5819	$17^{\mathrm{h}}27^{\mathrm{m}}22^{\mathrm{s}}$	+59°55′11″	13.153
8568	13	5915	-3504	5113	$22^{\mathrm{h}}38^{\mathrm{m}}32^{\mathrm{s}}$	+35°32′08″	13.780
8582	5	-878	-8499	796	$23^{\mathrm{h}}52^{\mathrm{m}}57^{\mathrm{s}}$	-29°11′43″	13.011
8586	5	6407	-4993	-2781	$02^{\mathrm{h}}40^{\mathrm{m}}26^{\mathrm{s}}$	+17°49′26″	13.434
8605	5	3608	-3626	-6920	$04^{\mathrm{h}}37^{\mathrm{m}}34^{\mathrm{s}}$	-02°07′13″	12.851
8614	5	1044	4116	-7495	$08^{\mathrm{h}}23^{\mathrm{m}}04^{\mathrm{s}}$	+04°13′53″	13.070
8627	6	-2880	6449	-4953	$10^{\mathrm{h}}37^{\mathrm{m}}04^{\mathrm{s}}$	-07°02′50″	12.991
8651	6	-1096	-8199	-2533	$01^{\mathrm{h}}34^{\mathrm{m}}14^{\mathrm{s}}$	-36°30′18″	13.030
8671	5	-3980	6424	4250	$14^{\mathrm{h}}53^{\mathrm{m}}35^{\mathrm{s}}$	+03°08′21″	13.316
8684	20	4347	-1833	-7291	$05^{\mathrm{h}}17^{\mathrm{m}}02^{\mathrm{s}}$	+06°31′38″	13.969
8686	6	6005	-5308	-3347	$02^{\mathrm{h}}49^{\mathrm{m}}07^{\mathrm{s}}$	+13°15′56″	13.401
8686	6	838	7864	3591	$14^{\mathrm{h}}11^{\mathrm{m}}19^{\mathrm{s}}$	+35°41′13″	12.340
8689	8	2574	2075	-8036	$07^{\mathrm{h}}13^{\mathrm{m}}56^{\mathrm{s}}$	+06°09′46″	13.565
8713	26	1683	5314	6696	$16^{\mathrm{h}}28^{\mathrm{m}}37^{\mathrm{s}}$	+39°30′05″	14.207
8731	7	-1206	8173	2823	$13^{\mathrm{h}}52^{\mathrm{m}}50^{\mathrm{s}}$	+21°42′14″	13.194
8774	9	-973	-8703	549	$23^{\mathrm{h}}59^{\mathrm{m}}36^{\mathrm{s}}$	-30°15′47″	13.130
8780	5	2754	-4645	-6923	$04^{\mathrm{h}}21^{\mathrm{m}}02^{\mathrm{s}}$	-09°47′14″	11.643
8781	8	2082	6406	-5632	$09^{\mathrm{h}}17^{\mathrm{m}}41^{\mathrm{s}}$	+20°05′41″	13.569

Continued on next page...

Table B.2 – Continued

Distance^a	$N_{\rm m}$^{b}	SGX^a	SGY^a	SGZ^a	α	δ	$\log\left(\frac{M}{M_\odot}\right)$
8786	8	3857	-6245	-4829	$03^{\rm h}08^{\rm m}51^{\rm s}$	-04°18′38″	13.203
8791	7	2300	-4993	-6860	$04^{\rm h}15^{\rm m}12^{\rm s}$	-13°15′28″	13.112
8797	5	-1489	-5770	6470	$21^{\rm h}01^{\rm m}53^{\rm s}$	-13°10′60″	12.874
8801	5	-3165	6784	4627	$14^{\rm h}56^{\rm m}55^{\rm s}$	+09°22′37″	12.588
8821	6	-3492	7253	-3607	$11^{\rm h}20^{\rm m}60^{\rm s}$	-05°42′07″	13.562
8822	17	6867	4952	-2480	$08^{\rm h}00^{\rm m}54^{\rm s}$	+56°39′43″	13.852
8850	5	-3674	-3168	-7402	$06^{\rm h}08^{\rm m}41^{\rm s}$	-47°32′27″	12.662
8876	6	3444	5603	-5959	$08^{\rm h}37^{\rm m}41^{\rm s}$	+25°02′50″	12.837
8879	6	-4992	-6460	3490	$21^{\rm h}09^{\rm m}35^{\rm s}$	-43°38′26″	12.569
8884	5	3233	-5116	6503	$21^{\rm h}53^{\rm m}38^{\rm s}$	+15°21′35″	12.463
8921	6	-2772	-8235	-2023	$01^{\rm h}05^{\rm m}34^{\rm s}$	-46°28′03″	13.034
8939	10	4545	4261	6409	$17^{\rm h}29^{\rm m}09^{\rm s}$	+56°48′29″	13.803
8967	5	6459	-5227	3372	$23^{\rm h}47^{\rm m}01^{\rm s}$	+28°12′20″	12.830
8969	8	-3772	2155	7847	$17^{\rm h}20^{\rm m}03^{\rm s}$	-01°17′31″	13.462
8971	8	-4027	7074	3772	$14^{\rm h}34^{\rm m}12^{\rm s}$	+03°43′51″	13.471
9023	7	-6102	944	6579	$17^{\rm h}15^{\rm m}39^{\rm s}$	-19°54′40″	13.406
9039	13	6400	-4089	-4899	$03^{\rm h}41^{\rm m}17^{\rm s}$	+15°38′15″	13.731
9047	5	3431	-7185	-4295	$02^{\rm h}44^{\rm m}02^{\rm s}$	-08°10′26″	13.494
9066	7	3943	5101	6373	$16^{\rm h}48^{\rm m}32^{\rm s}$	+53°45′17″	13.365
9067	6	-6819	4643	-3762	$11^{\rm h}37^{\rm m}33^{\rm s}$	-32°44′56″	12.658
9105	8	6599	-5135	-3603	$02^{\rm h}57^{\rm m}15^{\rm s}$	+16°00′15″	13.076
9117	7	-3457	5446	-6443	$10^{\rm h}02^{\rm m}16^{\rm s}$	-15°11′32″	12.882
9130	7	3863	7962	2246	$13^{\rm h}06^{\rm m}17^{\rm s}$	+53°37′58″	13.090
9148	7	619	9114	-479	$12^{\rm h}06^{\rm m}03^{\rm s}$	+28°07′36″	13.713
9161	12	2408	-4694	-7489	$04^{\rm h}30^{\rm m}30^{\rm s}$	-12°23′11″	13.922
9172	5	-6217	1522	6568	$17^{\rm h}01^{\rm m}29^{\rm s}$	-18°36′51″	12.943
9181	9	1850	5304	7262	$16^{\rm h}40^{\rm m}33^{\rm s}$	+39°27′33″	12.909
9196	5	2235	6511	-6097	$09^{\rm h}10^{\rm m}34^{\rm s}$	+19°29′16″	13.315
9198	6	-2845	-1773	-8566	$06^{\rm h}45^{\rm m}02^{\rm s}$	-36°58′18″	12.886
9208	5	53	9031	-1798	$11^{\rm h}37^{\rm m}34^{\rm s}$	+21°52′57″	12.843
9208	6	3834	-3963	-7374	$04^{\rm h}35^{\rm m}38^{\rm s}$	-02°26′03″	13.343
9216	15	-3201	-818	-8604	$07^{\rm h}16^{\rm m}24^{\rm s}$	-36°10′15″	14.010
9240	5	6322	1728	-6513	$06^{\rm h}19^{\rm m}02^{\rm s}$	+28°37′30″	13.102
9241	5	6790	-5293	3357	$23^{\rm h}51^{\rm m}04^{\rm s}$	+29°05′02″	13.056
9243	5	-4711	-7866	-1169	$00^{\rm h}10^{\rm m}50^{\rm s}$	-56°58′36″	12.819
9249	5	-4356	-6659	4715	$21^{\rm h}03^{\rm m}37^{\rm s}$	-35°12′44″	12.920
9251	5	3844	8359	962	$12^{\rm h}15^{\rm m}12^{\rm s}$	+50°41′39″	13.475
9272	9	1033	5878	7095	$16^{\rm h}17^{\rm m}53^{\rm s}$	+35°06′18″	13.316
9280	5	-2436	7069	-5497	$10^{\rm h}27^{\rm m}41^{\rm s}$	-03°26′31″	13.165
9281	5	6709	1265	-6287	$06^{\rm h}01^{\rm m}41^{\rm s}$	+29°52′18″	13.574
9297	8	8890	-1907	-1936	$03^{\rm h}10^{\rm m}04^{\rm s}$	+42°49′53″	13.712
9335	17	-751	8772	3102	$13^{\rm h}52^{\rm m}50^{\rm s}$	+25°03′27″	13.594
9354	8	-3480	5302	-6875	$09^{\rm h}52^{\rm m}55^{\rm s}$	-16°03′23″	13.214
9379	17	6528	-5565	3791	$23^{\rm h}38^{\rm m}28^{\rm s}$	+27°03′47″	13.337
9385	7	-4796	4688	6565	$16^{\rm h}05^{\rm m}05^{\rm s}$	-02°06′51″	13.618
9388	14	7519	-5124	-2312	$02^{\rm h}28^{\rm m}31^{\rm s}$	+22°55′44″	14.081
9434	9	-7973	4925	-1084	$13^{\rm h}03^{\rm m}30^{\rm s}$	-32°23′22″	13.186
9442	7	-3535	7463	-4577	$11^{\rm h}01^{\rm m}44^{\rm s}$	-06°36′37″	13.041

Continued on next page...

Table B.2 – Continued

Distance[a]	$N_{\rm m}$[b]	SGX[a]	SGY[a]	SGZ[a]	α	δ	$\log\left(\frac{M}{M_\odot}\right)$
9478	10	-2698	-2463	-8746	$06^h24^m24^s$	-37°20′40″	13.520
9502	6	691	9379	-1352	$11^h43^m43^s$	+26°34′57″	13.277
9524	8	-2163	-7550	5388	$21^h39^m48^s$	-22°29′12″	13.132
9529	10	9363	-1523	-899	$02^h47^m19^s$	+48°49′49″	13.853
9565	5	4811	-5896	5794	$22^h36^m34^s$	+19°27′56″	12.668
9631	9	9350	-1824	-1418	$02^h56^m54^s$	+45°41′31″	13.898
9635	5	7788	-1754	5394	$22^h35^m24^s$	+50°22′23″	13.350
9651	6	8159	-4756	-1987	$02^h26^m12^s$	+27°29′09″	13.525
9653	11	-3358	5747	-6991	$09^h55^m35^s$	-13°55′21″	13.572
9657	5	-31	8270	-4986	$10^h23^m08^s$	+12°58′52″	13.540
9728	5	-3204	4782	7842	$16^h29^m29^s$	+08°20′52″	13.610
9755	40	2079	5979	7421	$16^h27^m50^s$	+40°44′06″	14.422
9819	24	2365	-4953	-8141	$04^h34^m41^s$	-13°28′51″	13.860
9823	5	2738	5818	7425	$16^h36^m36^s$	+44°20′37″	13.141
9846	7	-2899	-7114	6158	$21^h11^m34^s$	-23°13′21″	13.172
9868	9	1764	9666	-913	$11^h45^m14^s$	+33°18′17″	13.543
9871	7	272	4806	8618	$17^h00^m21^s$	+27°57′49″	13.441
9888	5	3500	-6016	-7023	$03^h54^m00^s$	-08°30′56″	13.032
9889	5	-282	7152	6824	$15^h40^m59^s$	+28°11′07″	13.244
9896	7	-7435	6459	968	$13^h43^m33^s$	-19°57′07″	13.171
9898	5	2589	7453	-5977	$09^h23^m42^s$	+22°37′57″	13.078
9917	6	4944	-2095	-8337	$05^h17^m14^s$	+06°24′01″	12.868
9920	5	-405	8488	-5119	$10^h27^m11^s$	+11°03′43″	12.220
9936	7	6915	-5953	-3932	$02^h52^m43^s$	+13°38′23″	13.141
9982	5	7602	-4686	4461	$23^h28^m13^s$	+35°10′23″	12.326
10019	5	-4591	8564	2443	$13^h51^m16^s$	+02°09′10″	12.938
10061	7	-4589	3208	8358	$16^h57^m56^s$	-01°48′23″	13.596
10072	5	8372	-5155	-2188	$02^h26^m21^s$	+25°58′53″	13.482
10093	6	-4251	-9118	-800	$00^h06^m05^s$	-50°31′47″	13.428
10095	5	-7910	6258	408	$13^h33^m43^s$	-23°29′14″	13.122
10146	5	2994	-8386	-4863	$02^h40^m46^s$	-13°17′17″	12.945
10152	7	7339	-5777	-3978	$02^h55^m48^s$	+15°50′16″	13.340
10155	7	7719	-5037	-4262	$03^h11^m08^s$	+19°11′45″	13.665
10174	5	-355	8856	-4996	$10^h32^m35^s$	+12°07′42″	13.206
10185	5	-3184	-2209	-9419	$06^h39^m04^s$	-37°47′41″	12.666
10197	5	4759	9017	-98	$11^h29^m20^s$	+51°09′27″	13.431
10273	6	1338	6325	7983	$16^h24^m55^s$	+35°55′19″	13.577
10284	6	9929	-2040	-1732	$03^h00^m59^s$	+44°32′45″	13.118
10295	20	-2026	6407	7798	$16^h04^m42^s$	+17°35′47″	14.006
10324	7	-9452	4151	-110	$13^h42^m59^s$	-38°17′01″	13.597
10351	7	-4077	7310	6089	$15^h17^m06^s$	+07°02′31″	13.428
10354	8	8012	5942	2776	$12^h56^m50^s$	+80°15′40″	13.178
10357	5	6612	-5306	-5949	$03^h39^m01^s$	+10°04′48″	13.691
10363	5	-9182	4704	974	$14^h04^m29^s$	-32°55′43″	13.314
10393	7	9168	-4872	-473	$01^h50^m37^s$	+33°09′34″	13.430
10407	16	-8561	5916	-34	$13^h28^m13^s$	-27°47′10″	14.403
10417	6	2608	-5354	-8546	$04^h31^m14^s$	-13°06′15″	13.586
10425	12	1611	9979	-2549	$11^h10^m06^s$	+28°31′19″	14.040

Continued on next page...

Table B.2 – Continued

Distance^a	$N_{\mathrm{m}}{}^b$	SGX^a	SGY^a	SGZ^a	α	δ	$\log\left(\frac{M}{M_\odot}\right)$
10434	5	-15	-4252	-9528	$05^{h}20^{m}11^{s}$	-25°02′23″	13.248
10477	7	8414	-1731	5997	$22^{h}28^{m}25^{s}$	+50°55′27″	13.034
10479	5	-9279	-4442	1996	$18^{h}47^{m}26^{s}$	-63°17′42″	13.492
10494	7	8926	4027	-3774	$06^{h}41^{m}31^{s}$	+53°09′11″	13.201
10508	5	-836	7669	7134	$15^{h}36^{m}20^{s}$	+25°21′06″	12.812
10508	5	-1168	-4068	-9618	$05^{h}34^{m}13^{s}$	-30°38′33″	12.994
10515	5	8627	-5533	-2350	$02^{h}25^{m}58^{s}$	+24°53′45″	12.702
10536	6	685	5188	9144	$17^{h}01^{m}14^{s}$	+30°08′48″	13.689
10657	5	8982	-5308	-2170	$02^{h}25^{m}02^{s}$	+27°14′14″	13.317
10691	11	-10364	1117	2370	$15^{h}33^{m}44^{s}$	-46°56′53″	13.649
10705	6	-4794	7633	5774	$15^{h}06^{m}35^{s}$	+03°46′14″	13.266
10726	9	259	5300	9322	$16^{h}58^{m}04^{s}$	+27°54′16″	13.521
10809	5	-9639	4778	-1039	$13^{h}15^{m}16^{s}$	-37°14′20″	12.921
10825	9	2465	10391	-1768	$11^{h}21^{m}22^{s}$	+34°18′26″	13.110
10833	17	2058	-5220	-9266	$04^{h}45^{m}11^{s}$	-15°55′41″	14.270
10847	7	5482	-7689	5337	$23^{h}07^{m}19^{s}$	+15°21′30″	13.386
10876	6	-3995	7582	6697	$15^{h}23^{m}47^{s}$	+08°34′18″	13.492
10886	8	-513	-3424	-10320	$05^{h}47^{m}49^{s}$	-25°36′34″	13.436
10889	9	-2452	6780	8160	$16^{h}02^{m}18^{s}$	+16°00′31″	13.712
10891	6	-8279	6601	2548	$14^{h}18^{m}36^{s}$	-19°23′15″	12.622
10898	11	-1317	9861	-4449	$11^{h}00^{m}15^{s}$	+09°58′33″	13.708
10916	5	8134	7247	692	$10^{h}26^{m}02^{s}$	+70°44′47″	13.687
10958	6	-8847	6313	1399	$13^{h}58^{m}34^{s}$	-24°28′13″	13.115
11102	7	-4809	7635	6467	$15^{h}18^{m}09^{s}$	+04°32′45″	13.445
11107	5	4997	9777	1671	$12^{h}27^{m}43^{s}$	+53°42′31″	13.568
11180	6	6254	-7258	5762	$23^{h}03^{m}36^{s}$	+20°04′44″	12.648
11199	5	-10244	4525	22	$13^{h}46^{m}16^{s}$	-37°55′06″	12.958
11228	5	2521	5343	9547	$17^{h}15^{m}57^{s}$	+38°53′20″	13.484
11228	9	-3761	-8038	6878	$21^{h}07^{m}01^{s}$	-25°27′21″	13.962
11312	7	877	10952	2691	$13^{h}20^{m}40^{s}$	+33°07′14″	13.514
11313	6	10576	-1502	-3726	$03^{h}53^{m}22^{s}$	+41°15′56″	13.338
11326	6	-2348	-3248	-10593	$06^{h}09^{m}25^{s}$	-33°42′10″	13.431
11332	6	9388	4981	-3933	$07^{h}04^{m}34^{s}$	+53°57′13″	13.007
11379	6	10007	-5391	-531	$01^{h}50^{m}23^{s}$	+32°49′41″	13.231
11391	6	-9271	-6337	-1908	$22^{h}25^{m}59^{s}$	-80°11′33″	13.400
11411	5	-9509	6207	1124	$13^{h}55^{m}21^{s}$	-27°16′44″	13.044
11433	11	-4984	8009	6459	$15^{h}13^{m}07^{s}$	+04°26′60″	13.456
11457	7	6890	-7605	5095	$23^{h}23^{m}50^{s}$	+20°44′10″	13.792
11462	5	-10563	4446	-141	$13^{h}44^{m}05^{s}$	-39°08′48″	12.949
11464	5	-709	-1997	-11266	$06^{h}22^{m}53^{s}$	-23°12′49″	13.337
11513	10	-555	-3862	-10831	$05^{h}42^{m}39^{s}$	-26°06′50″	13.393
11632	6	-173	5325	10340	$17^{h}05^{m}28^{s}$	+25°05′38″	13.771
11728	5	4995	8928	5734	$14^{h}52^{m}04^{s}$	+55°40′42″	12.207
11832	5	-567	-3660	-11237	$05^{h}49^{m}12^{s}$	-25°32′13″	13.206
11854	9	-10412	5650	439	$13^{h}47^{m}37^{s}$	-32°51′41″	13.624
11859	8	9356	5643	4610	$16^{h}52^{m}10^{s}$	+81°36′00″	12.941
11863	14	-2220	7361	9034	$16^{h}06^{m}03^{s}$	+18°06′57″	14.171
11997	5	10437	3731	-4591	$06^{h}14^{m}55^{s}$	+51°13′08″	13.166

Continued on next page...

Table B.2 – Continued

Distance[a]	N_m[b]	SGX[a]	SGY[a]	SGZ[a]	α	δ	$\log\left(\frac{M}{M_\odot}\right)$
12023	5	-3199	8893	-7430	$10^h21^m17^s$	-04°33′38″	12.271
12080	5	2121	10660	-5272	$10^h20^m26^s$	+24°18′18″	13.452
12161	14	-3009	10370	-5593	$10^h58^m45^s$	+01°35′40″	13.660

[a] Distances are given in km s^{-1}.

[b] Number of observed member-galaxies assigned to the group.

The above table contains the group positions and mass estimates after the iterative procedure has been applied. The flow-field was calculated assuming the incoherent mass correction.

Bibliography

Aaronson, M., Bothun, G., Mould, J., Huchra, J., Schommer, R. A., & Cornell, M. E. 1986, ApJ, 302, 536

Aaronson, M., Huchra, J., Mould, J., Schechter, P. L., & Tully, R. B. 1982, ApJ, 258, 64

Aaronson, M., Mould, J., Huchra, J., Sullivan, III, W. T., Schommer, R. A., & Bothun, G. D. 1980, ApJ, 239, 12

Abell, G. O. 1958, ApJS, 3, 211

Abell, G. O., Corwin, Jr., H. G., & Olowin, R. P. 1989, ApJS, 70, 1

Bahcall, J. N., & Tremaine, S. 1981, ApJ, 244, 805

Baker, J. E., Davis, M., Strauss, M. A., Lahav, O., & Santiago, B. X. 1998, ApJ, 508, 6

Beichman, C. A., Neugebauer, G., Habing, H. J., Clegg, P. E., & Chester, T. J., eds. 1988, Infrared astronomical satellite (IRAS) catalogs and atlases. Volume 1: Explanatory supplement, Vol. 1

Bell, E. F., & de Jong, R. S. 2001, ApJ, 550, 212

Bell, E. F., McIntosh, D. H., Katz, N., & Weinberg, M. D. 2003, ApJS, 149, 289

Bennett, C. L., et al. 1993, Proceedings of the National Academy of Science, 90, 4766

Branchini, E., & Plionis, M. 1996, ApJ, 460, 569

Branchini, E., et al. 1999, MNRAS, 308, 1

Bureau, M., Mould, J. R., & Staveley-Smith, L. 1996, ApJ, 463, 60

Burstein, D., Davies, R. L., Dressler, A., Faber, S. M., & Lynden-Bell, D. 1986, in NATO ASIC Proc. 180: Galaxy Distances and Deviations from Universal Expansion, ed. B. F. Madore & R. B. Tully, 123–130

Chakravarti, Laha, & Roy. 1967, Handbook of Methods of Applied Statistics, Vol. I (John Wiley and Sons), 392–394

Colberg, J. M., et al. 2000, MNRAS, 319, 209

Colless, M., & Dunn, A. M. 1996, ApJ, 458, 435

Conklin, E. K. 1969, Nature, 222, 971

Corey, B. E., & Wilkinson, D. T. 1976, BAAS, 8, 351

Courteau, S., & van den Bergh, S. 1999, AJ, 118, 337

Cox, A. N. 2000, Allen's astrophysical quantities (Allen's astrophysical quantities, 4th ed. Publisher: New York: AIP Press; Springer, 2000. Editedy by Arthur N. Cox. ISBN: 0387987460)

Crook, A. C., Huchra, J. P., Martimbeau, N., Masters, K. L., Jarrett, T., & Macri, L. M. 2007, ApJ, 655, 790

—. 2008, ApJ, 685, 1320

Crook, A. C., Silvestri, A., & Zukin, P. 2009, submitted to MNRAS

Cutri, R., et al. 2003, IPAC, http://www.ipac.caltech.edu/2mass/

da Costa, L. N., Bernardi, M., Alonso, M. V., Wegner, G., Willmer, C. N. A., Pellegrini, P. S., Maia, M. A. G., & Zaroubi, S. 2000, ApJ, 537, L81

da Costa, L. N., et al. 1998, AJ, 116, 1

Davis, M., Miller, A., & White, S. D. M. 1997, ApJ, 490, 63

Davis, M., et al. 2003, in Discoveries and Research Prospects from 6- to 10-Meter-Class Telescopes II. Edited by Guhathakurta, Puragra. Proceedings of the SPIE, Volume 4834, pp. 161-172 (2003)., ed. P. Guhathakurta, 161–172

de Lapparent, V., Geller, M. J., & Huchra, J. P. 1991, ApJ, 369, 273

De Vaucouleurs, G. 1953, AJ, 58, 30

—. 1958, Nature, 182, 1478

—. 1975, Stars and stellar systems, 9, 557

Dekel, A., Bertschinger, E., Yahil, A., Strauss, M. A., Davis, M., & Huchra, J. P. 1993, ApJ, 412, 1

Diaferio, A., Kauffmann, G., Colberg, J. M., & White, S. D. M. 1999, MNRAS, 307, 537

Djorgovski, S., & Davis, M. 1987, ApJ, 313, 59

Dressler, A. 1991, Nature, 350, 391

Dressler, A., & Faber, S. M. 1990, ApJ, 354, 13

Dressler, A., Lynden-Bell, D., Burstein, D., Davies, R. L., Faber, S. M., Terlevich, R., & Wegner, G. 1987, ApJ, 313, 42

Eke, V. R., et al. 2004, MNRAS, 348, 866

Erdoğdu, P., et al. 2006a, MNRAS, 373, 45

—. 2006b, MNRAS, 368, 1515

Fabbri, R., Guidi, I., Melchiorri, F., & Natale, V. 1980, Physical Review Letters, 44, 1563

Faber, S. M., & Gallagher, J. S. 1979, ARA&A, 17, 135

Faber, S. M., & Jackson, R. E. 1976, ApJ, 204, 668

Falco, E. E., et al. 1999, VizieR Online Data Catalog, 611, 10438

Fisher, K. B., Huchra, J. P., Strauss, M. A., Davis, M., Yahil, A., & Schlegel, D. 1995, ApJS, 100, 69

Frederic, J. J. 1995a, ApJS, 97, 275

—. 1995b, ApJS, 97, 259

Freedman, W. L., et al. 2001, ApJ, 553, 47

Geller, M. J., & Huchra, J. P. 1983, ApJS, 52, 61

—. 1989, Science, 246, 897

Gerke, B. F., et al. 2005, ApJ, 625, 6

Giovanelli, R., Haynes, M. P., Freudling, W., da Costa, L. N., Salzer, J. J., & Wegner, G. 1998, ApJ, 505, L91

Giuricin, G., Marinoni, C., Ceriani, L., & Pisani, A. 2000, ApJ, 543, 178

Gunn, J. E., & Gott, J. R. I. 1972, ApJ, 176, 1

Han, M., & Mould, J. 1990, ApJ, 360, 448

Harmon, R. T., Lahav, O., & Meurs, E. J. A. 1987, MNRAS, 228, 5P

Heisler, J., Tremaine, S., & Bahcall, J. N. 1985, ApJ, 298, 8

Henry, P. S. 1971, Nature, 231, 516

Hinshaw, G., et al. 2009, ApJS, 180, 225

Hoffman, Y., Eldar, A., Zaroubi, S., & Dekel, A. 2001, ArXiv Astrophysics e-prints

Huchra, J., et al. 2005, in IAU Symposium No. 216, 170

Huchra, J. P., & Geller, M. J. 1982, ApJ, 257, 423

Huchra, J. P., Geller, M. J., & Corwin, H. G. 1995, ApJS, 99, 391

Huchra, J. P., Geller, M. J., de Lapparent, V., & Corwin, H. G. 1990, ApJS, 72, 433

Huchra, J. P., et al. 2009, In preparation

Hudson, M. J. 1993, MNRAS, 265, 43

Hughes, J. P. 1989, ApJ, 337, 21

Jackson, J. C. 1972, MNRAS, 156, 1P

Jarrett, T. H., Chester, T., Cutri, R., Schneider, S., Skrutskie, M., & Huchra, J. P. 2000, AJ, 119, 2498

Jenkins, A., Frenk, C. S., White, S. D. M., Colberg, J. M., Cole, S., Evrard, A. E., Couchman, H. M. P., & Yoshida, N. 2001, MNRAS, 321, 372

Kaiser, N. 1987, MNRAS, 227, 1

Kaiser, N., & Squires, G. 1993, ApJ, 404, 441

Karachentsev, I. D., Dolphin, A., Tully, R. B., Sharina, M., Makarova, L., Makarov, D., Karachentseva, V., Sakai, S., & Shaya, E. J. 2006, AJ, 131, 1361

Karachentsev, I. D., Karachentseva, V. E., Huchtmeier, W. K., & Makarov, D. I. 2004, AJ, 127, 2031

Karachentsev, I. D., Kashibadze, O. G., Makarov, D. I., & Tully, R. B. 2009, MNRAS, 393, 1265

Karachentsev, I. D., Mitronova, S. N., Karachentseva, V. E., Kudrya, Y. N., & Jarrett, T. H. 2002, A&A, 396, 431

Kennicutt, Jr., R. C., Tamblyn, P., & Congdon, C. E. 1994, ApJ, 435, 22

Kocevski, D. D., & Ebeling, H. 2006, ApJ, 645, 1043

Kocevski, D. D., Mullis, C. R., & Ebeling, H. 2004, ApJ, 608, 721

Kochanek, C. S., Pahre, M. A., Falco, E. E., Huchra, J. P., Mader, J., Jarrett, T. H., Chester, T., Cutri, R., & Schneider, S. E. 2001, ApJ, 560, 566

Kochanek, C. S., White, M., Huchra, J., Macri, L., Jarrett, T. H., Schneider, S. E., & Mader, J. 2003, ApJ, 585, 161

Komatsu, E., et al. 2009, ApJS, 180, 330

Kraan-Korteweg, R. C., Woudt, P. A., Cayatte, V., Fairall, A. P., Balkowski, C., & Henning, P. A. 1996, Nature, 379, 519

Lahav, O., Fisher, K. B., Hoffman, Y., Scharf, C. A., & Zaroubi, S. 1994, ApJ, 423, L93

Lahav, O., Lynden-Bell, D., & Rowan-Robinson, M. 1988, MNRAS, 234, 677

Lavaux, G., Tully, R. B., Mohayaee, R., & Colombi, S. 2008, arXiv:astro-ph/08103658

Lee, M. G., Freedman, W. L., & Madore, B. F. 1993, ApJ, 417, 553

Lineweaver, C. H., Tenorio, L., Smoot, G. F., Keegstra, P., Banday, A. J., & Lubin, P. 1996, ApJ, 470, 38

Loeb, A., & Narayan, R. 2008, MNRAS, 386, 2221

Lynden-Bell, D., Faber, S. M., Burstein, D., Davies, R. L., Dressler, A., Terlevich, R. J., & Wegner, G. 1988, ApJ, 326, 19

Lynden-Bell, D., Lahav, O., & Burstein, D. 1989, MNRAS, 241, 325

Makarov, D., Makarova, L., Rizzi, L., Tully, R. B., Dolphin, A. E., Sakai, S., & Shaya, E. J. 2006, AJ, 132, 2729

Maller, A. H., McIntosh, D. H., Katz, N., & Weinberg, M. D. 2003, ApJ, 598, L1

Marinoni, C., Davis, M., Newman, J. A., & Coil, A. L. 2002, ApJ, 580, 122

Martínez, H. J., Zandivarez, A., Merchán, M. E., & Domínguez, M. J. L. 2002, MNRAS, 337, 1441

Masters, K. L. 2005, PhD thesis, Cornell University, United States – New York

Masters, K. L., Haynes, M. P., & Giovanelli, R. 2004, ApJ, 607, L115

Masters, K. L., Huchra, J. P., Crook, A. C., Macri, L. M., Jarrett, T., Koribalski, B., Staveley-Smith, L., Jones, H., & Springob, C. M. 2007, in Bulletin of the American Astronomical Society, Vol. 38, Bulletin of the American Astronomical Society, 193

Masters, K. L., Springob, C. M., Haynes, M. P., & Giovanelli, R. 2006, ApJ, 653, 861

Masters, K. L., Springob, C. M., & Huchra, J. P. 2008, AJ, 135, 1738

Mathewson, D. S., Ford, V. L., & Buchhorn, M. 1992, ApJ, 389, L5

Mei, S., Blakeslee, J. P., Côté, P., Tonry, J. L., West, M. J., Ferrarese, L., Jordán, A., Peng, E. W., Anthony, A., & Merritt, D. 2007, ApJ, 655, 144

Meiksin, A., & Davis, M. 1986, AJ, 91, 191

Merchán, M., & Zandivarez, A. 2002, MNRAS, 335, 216

Merchán, M. E., & Zandivarez, A. 2005, ApJ, 630, 759

Mieske, S., Hilker, M., & Infante, L. 2005, A&A, 438, 103

Miller, C. J., et al. 2005, AJ, 130, 968

Mould, J. R., et al. 2000, ApJ, 529, 786

Navarro, J. F., Frenk, C. S., & White, S. D. M. 1997, ApJ, 490, 493

Nolthenius, R., & White, S. D. M. 1987, MNRAS, 225, 505

Norberg, P., et al. 2001, MNRAS, 328, 64

Paczynski, B., & Piran, T. 1990, ApJ, 364, 341

Peebles, P. J. E. 1967, ApJ, 147, 859

—. 1976a, ApJ, 205, L109+

—. 1976b, ApJ, 205, 318

—. 1980, The large-scale structure of the universe (Princeton University Press), 435

Peebles, P. J. E., & Wilkinson, D. T. 1968, Phys. Rev., 174, 2168

Peebles, P. J. E., & Yu, J. T. 1970, ApJ, 162, 815

Penzias, A. A., & Wilson, R. W. 1965, ApJ, 142, 419

Persic, M., Salucci, P., & Stel, F. 1996, MNRAS, 281, 27

Press, W. H., & Schechter, P. 1974, ApJ, 187, 425

Ramella, M., Geller, M. J., & Huchra, J. P. 1989, ApJ, 344, 57

Ramella, M., Geller, M. J., Pisani, A., & da Costa, L. N. 2002, AJ, 123, 2976

Ramella, M., Pisani, A., & Geller, M. J. 1997, AJ, 113, 483

Riess, A. G., et al. 2009, ApJ, 699, 539

Rowan-Robinson, M., et al. 2000, MNRAS, 314, 375

Rubin, V. C. 1951, AJ, 56, 47

Rubin, V. C., Burbidge, E. M., Burbidge, G. R., Crampin, D. J., & Prendergast, K. H. 1965, ApJ, 141, 759

Rubin, V. C., Thonnard, N., Ford, Jr., W. K., & Roberts, M. S. 1976, AJ, 81, 719

Sakai, S., Madore, B. F., & Freedman, W. L. 1996, ApJ, 461, 713

Santiago, B. X., Strauss, M. A., Lahav, O., Davis, M., Dressler, A., & Huchra, J. P. 1995, ApJ, 446, 457

Saunders, W., et al. 2000, MNRAS, 317, 55

Scaramella, R. 1995, Astrophysical Letters Communications, 32, 137

Scaramella, R., Baiesi-Pillastrini, G., Chincarini, G., Vettolani, G., & Zamorani, G. 1989, Nature, 338, 562

Scaramella, R., Vettolani, G., & Zamorani, G. 1991, ApJ, 376, L1

Schechter, P. 1976, ApJ, 203, 297

Schechter, P. L. 1980, AJ, 85, 801

Schipper, L., & King, I. R. 1978, ApJ, 220, 798

Schlegel, D. J., Finkbeiner, D. P., & Davis, M. 1998, ApJ, 500, 525

Schmoldt, I., et al. 1999, MNRAS, 304, 893

Seljak, U., & Zaldarriaga, M. 1996, ApJ, 469, 437

Shaya, E. J. 1984, ApJ, 280, 470

Shaya, E. J., Tully, R. B., & Pierce, M. J. 1992, ApJ, 391, 16

Sheth, R. K., & Tormen, G. 1999, MNRAS, 308, 119

Shu, C., Zhou, B., Bartelmann, M., Comerford, J. M., Huang, J.-S., & Mellier, Y. 2008, ApJ, 685, 70

Silk, J. 1968, ApJ, 151, 459

Skrutskie, M. F., et al. 2006, AJ, 131, 1163

Smoot, G. F., et al. 1992, ApJ, 396, L1

Somerville, R. S., Lemson, G., Sigad, Y., Dekel, A., Kauffmann, G., & White, S. D. M. 2001, MNRAS, 320, 289

Spergel, D. N., et al. 2007, ApJS, 170, 377

Springel, V., et al. 2005, Nature, 435, 629

Springob, C. M., Masters, K. L., Haynes, M. P., Giovanelli, R., & Marinoni, C. 2007, ApJS, 172, 599

—. 2009, ApJS, 182, 474

Strauss, M. A., & Davis, M. 1991, in ASP Conf. Ser. 15: Large-scale Structures and Peculiar Motions in the Universe, ed. D. W. Latham & L. A. N. da Costa, 53–+

Strauss, M. A., Davis, M., Yahil, A., & Huchra, J. P. 1990, ApJ, 361, 49

—. 1992, ApJ, 385, 421

Strauss, M. A., & Willick, J. A. 1995, Phys. Rep., 261, 271

Tammann, G. A., & Sandage, A. 1985, ApJ, 294, 81

Tonry, J., & Schneider, D. P. 1988, AJ, 96, 807

Tonry, J. L., Blakeslee, J. P., Ajhar, E. A., & Dressler, A. 2000, ApJ, 530, 625

Tonry, J. L., & Davis, M. 1981, ApJ, 246, 680

Tonry, J. L., Dressler, A., Blakeslee, J. P., Ajhar, E. A., Fletcher, A. B., Luppino, G. A., Metzger, M. R., & Moore, C. B. 2001, ApJ, 546, 681

Tully, R. B. 1988, Nearby galaxies catalog

Tully, R. B., & Fisher, J. R. 1977, A&A, 54, 661

Tully, R. B., Shaya, E. J., Karachentsev, I. D., Courtois, H. M., Kocevski, D. D., Rizzi, L., & Peel, A. 2008, ApJ, 676, 184

—. 2008, ApJ, 686, 1523

Turner, E. L., & Gott, J. R. 1976, ApJS, 32, 409

Tyson, J. A., Wenk, R. A., & Valdes, F. 1990, ApJ, 349, L1

Villumsen, J. V., & Strauss, M. A. 1987, ApJ, 322, 37

Wang, L., & Steinhardt, P. J. 1998, ApJ, 508, 483

Watkins, R., Feldman, H. A., & Hudson, M. J. 2009, MNRAS, 392, 743

Webster, M., Lahav, O., & Fisher, K. 1997, MNRAS, 287, 425

Weinmann, S. M., van den Bosch, F. C., Yang, X., & Mo, H. J. 2006, MNRAS, 366, 2

White, S. D. M., Navarro, J. F., Evrard, A. E., & Frenk, C. S. 1993, Nature, 366, 429

Willick, J. A. 1990, ApJ, 351, L5

Yahil, A., Sandage, A., & Tammann, G. A. 1980, ApJ, 242, 448

Yahil, A., Strauss, M. A., Davis, M., & Huchra, J. P. 1991, ApJ, 372, 380

Yahil, A., Tammann, G. A., & Sandage, A. 1977, ApJ, 217, 903

Yahil, A., Walker, D., & Rowan-Robinson, M. 1986, ApJ, 301, L1

Yang, X., Mo, H. J., van den Bosch, F. C., & Jing, Y. P. 2005, MNRAS, 356, 1293

Zaldarriaga, M., & Seljak, U. 2000, ApJS, 129, 431

Zaldarriaga, M., Seljak, U., & Bertschinger, E. 1998, ApJ, 494, 491

Zehavi, I., et al. 2002, ApJ, 571, 172

Zwicky, F. 1937, ApJ, 86, 217